HEINRICH HEINE
UNIVERSITÄT DÜSSELDORF

Non-equilibrium effects in colloidal mixtures caused by particle interactions and external potentials

Inaugural-Dissertation

zur

Erlangung des Doktorgrades der
Mathematisch-Naturwissenschaftlichen Fakultät
der Heinrich-Heine-Universität Düsseldorf

vorgelegt von

Ronja Franziska Capellmann
geboren in
Aachen

Düsseldorf, Juni 2017

Aus dem Institut für experimentelle Physik der kondensierten Materie, Lehrstuhl für Physik der weichen Materie
der Heinrich-Heine-Universität Düsseldorf

Gedruckt mit der Genehmigung der
Mathematisch-Naturwissenschaftlichen Fakultät der
Heinrich-Heine-Universität Düsseldorf

Berichterstatter:

1.: Prof. Dr. Stefan U. Egelhaaf

2.: Prof. Dr. Jan K. G. Dhont

Tag der mündlichen Prüfung: 25.07.2017

ABSTRACT

In equilibrium, hard-sphere colloids form a fluid or a crystal, or both phases coexist, depending on the concentration. However, particle-particle and particle-potential interactions can lead to non-equilibrium states, affecting the spatial arrangement and dynamics of the particles. Hence, studies on the phase behaviour and on non-equilibrium effects are of considerable scientific interest, but also of great industrial relevance. Colloidal suspensions are frequently used in foodstuff and consumer products industry.

In this thesis, two kinds of non-equilibrium situations are studied. Non-equilibrium caused by particle-particle interactions is considered as intrinsic non-equilibrium. The interactions can induce disorder-disorder transitions, e.g. from a fluid to a gel. The structure of gels could be reproduced by modelling the particle-particle interactions as equilibrium interactions. Furthermore, a structural transition from continuous to directed percolation in colloidal gels was found to be connected to the onset of a slowing-down of the dynamics, which is characteristic for gel formation.

Non-equilibrium due to external potentials is considered as extrinsic non-equilibrium. A new set-up for the generation of a modulated light field has been devised. If exposed to a sinusoidal potential, a binary colloidal mixture undergoes a disorder-order transition into a modulated liquid. Depending on the total packing fraction in the sample and the amplitude of the potential, homogenisation or partial demixing of the two particle species occurred. In addition, a slowing-down of the dynamics has been observed.

Particle-particle and particle-potential interactions can also be combined. Preliminary results, presented in an outlook, indicate that external potentials can order gel samples.

The main results of this thesis can be summarized as follows:

1. The structure of colloidal gels can be reproduced by modelling particle-particle interactions by equilibrium interactions.
2. The structural transition from continuous to directed percolation in colloidal gels is connected to the onset of a slowing-down of the dynamics.
3. An external sinusoidal potential leads to a disorder-order transition in binary colloidal mixtures.

This page has been left intentionally blank.

ZUSAMMENFASSUNG

Im Gleichgewicht bilden Kolloide, die wie harte Kugeln wechselwirken, je nach Konzentration eine Flüssigkeit, einen Kristall oder eine Koexistenz beider Phasen. Jedoch können Teilchen-Teilchen- oder Teilchen-Potential-Wechselwirkungen zu Nichtgleichgewichtszuständen führen, die die räumliche Anordnung und Dynamik der Teilchen verändern. Daher sind Untersuchungen des Phasenverhaltens und auch der Nichtgleichgewichtszustände von beträchtlichem wissenschaftlichen Interesse, aber auch von großer industrieller Bedeutung. Kolloide werden häufig in der Lebensmittel- und Konsumgüterindustrie verwendet.

In dieser Arbeit wurden zwei Arten von Nichtgleichgewicht untersucht. Ein Nichtgleichgewicht aufgrund von Wechselwirkungen zwischen den Kolloiden wird als intrinsisches Nichtgleichgewicht bezeichnet. Die Wechselwirkungen können Übergänge von einer ungeordneten Phase in eine andere bewirken, z. B. von einem Fluid zu einem Gel. Die Struktur von Gelen konnte reproduziert werden, indem die Teilchen-Teilchen-Wechselwirkungen durch Gleichgewichtswechselwirkungen modelliert wurden. Außerdem wurde in Gelen ein struktureller Übergang von kontinuierlicher zu gerichteter Perkolation beobachtet. Dieser ist mit dem Einsetzen der Verlangsamung der Dynamik, einem Merkmal der Gelbildung, verbunden.

Ein Nichtgleichgewicht aufgrund externer Potentiale wird als extrinsisches Nichtgleichgewicht bezeichnet. Es wurde ein neuer Aufbau zum Erzeugen eines modulierten Lichtfelds entwickelt. Werden binäre kolloidale Mischungen einem sinusförmigen Potential ausgesetzt, so wird ein Unordnung-Ordnung-Übergang zu einer modulierten Flüssigkeit beobachtet. Abhängig von der Packungsdichte und der Amplitude des Potentials traten Homogenisierung oder partielles Entmischen der Teilchensorten auf. Zudem wurde eine Verlangsamung der Dynamik beobachtet.

Teilchen-Teilchen- und Teilchen-Potential-Wechselwirkungen können auch kombiniert werden. Erste Experimente, vorgestellt in einem Ausblick, deuten darauf hin, dass äußere Potentiale Gel-Proben ordnen können.

Die wesentlichen Ergebnisse dieser Arbeit können wie folgt in drei Thesen zusammengefasst werden:

1. Die Struktur kolloidaler Gele kann reproduziert werden, indem die Teilchen--Teilchen-Wechselwirkungen als Gleichgewichtswechselwirkungen modelliert werden.
2. Der Übergang von kontinuierlicher Perkolation zu gerichteter Perkolation in kolloidalen Gelen ist mit dem Einsetzen der Verlangsamung der Dynamik verbunden.
3. Ein externes sinusförmiges Potential führt zu einem Übergang von Unordnung zu Ordnung in binären kolloidalen Mischungen.

This page has been left intentionally blank.

EIDESSTATTLICHE ERKLÄRUNG

Ich versichere an Eides Statt, dass die Dissertation von mir selbständig und ohne unzulässige fremde Hilfe unter Beachtung der „Grundsätze zur Sicherung guter wissenschaftlicher Praxis an der Heinrich-Heine-Universität Düsseldorf“ erstellt worden ist. Die Dissertation ist nicht in gleicher oder ähnlicher Form an einer anderen Fakultät vorgelegt worden. Das ist mein erster Promotionsversuch.

Unterschrift: .... Ort, Datum: ....

This page has been left intentionally blank.

DANKSAGUNG

Ich bedanke mich herzlich bei allen, die mich in den vergangenen Jahren während meiner Promotion unterstützt haben.

Besonderer Dank gilt meinem Doktorvater Prof. Dr. Stefan Egelhaaf für die umfassende Betreuung dieser Arbeit. Vielen Dank für das entgegengebrachte Vertrauen, die motivierenden Gespräche und die Möglichkeit, so viele wertvolle Erfahrungen zu machen und Neues zu lernen! Bei Prof. Dr. Jan Dhont bedanke ich mich für die Übernahme der Rolle des 2. Berichterstatters und die hilfreichen Tipps im Rahmen der Graduiertenschule BioSoft. Prof. Dr. Axel Görlitz danke ich für seine Tätigkeit als Mentor.

Herzlicher Dank gilt allen jetzigen und ehemaligen Kolleginnen und Kollegen am Lehrstuhl für Physik der weichen Materie, die mich unterstützt und immer gerne geholfen haben, und besonders

... Florian für die tolle Zusammenarbeit, die aufbauenden Worte und das Korrekturlesen auf Abruf.

... Marco für die langjährige Betreuung und die kurzfristige Hilfe auch über den Ozean hinweg.

... Dana und Jörg dafür, dass sie mich als Bachelorstudentin so nett aufgenommen und mir seitdem 9 Jahre lang mit Rat und Tat und Freude zur Seite gestanden haben.

Desweiteren bedanke ich mich herzlich bei Hanna, Kathrin und Michael, die immer für mich da sind.

Meine Eltern und Pascal haben alle Höhen und Tiefen der vergangenen Jahre sehr nah miterlebt. Danke, dass ihr mir, vor allem in den letzten Wochen und Tagen, den Rücken frei gehalten habt und ich mich bedingungslos auf eure Unterstützung verlassen kann!

Mein letzter Dank geht an meine liebe Oma Ruth, die mich so sehr lieb hat, dass sie es immer noch weiß.

Danke!

This page has been left intentionally blank.

CONTENTS

This page has been left intentionally blank.

BACKGROUND 1

1.1 Colloidal dispersions

Colloidal dispersions are frequently encountered in nature as well as in industry. We use them regularly in our daily life in the form of industrial products, like paint, toothpaste, ice cream, shaving foam and hair spray. Fog, smoke and milk represent examples of colloidal dispersions occurring in nature. All these materials are two-phase dispersions: matter in one phase (gas, fluid or solid) is dispersed in matter in another or the same phase, which leads to a heterogeneous system with a large interfacial area [1]. In this thesis, spherical solid particles dispersed in a fluid are used as a model system.

To belong to the class of colloids, the dispersed particles have to be of mesoscopic size, which ranges roughly from 1 nm to 1 µm [1–4]. The mesoscopic size regime implies that the dispersed colloidal particles are much larger than the molecules of the dispersion medium, which sets the the lower boundary [3]. Thus, the dispersion medium can be considered as a continuum, and the internal atomic structure of the particles can be neglected [4]. In the mesoscopic regime, the dispersed particles are so small that they move due to thermal energy, i.e. they undergo Brownian motion. If the particle radius is larger than about 1 µm, then gravity might not be negligible. This sets the upper limit of the mesoscopic size regime [3–5]. Due to their mesoscopic size, colloids can easily be observed with optical microscopy.

1.2 Structure in colloidal dispersions

The particles in colloidal dispersions can assume different spatial arrangements. At high concentrations, particles form ordered, crystalline arrangements, whereas at low concentrations they are in a disordered, fluid-like state [6]. A measure for the arrangement is the radial distribution function $g(r)$ [7, 8] which for a canonical ensemble reads [9]

$$g\left(\mathbf{r}\right) = \frac{1}{\rho_0^2} \left\langle \rho(\mathbf{r}')\rho(\mathbf{r}' + \mathbf{r}) \right\rangle_{\mathbf{r}'} \tag{1.1}$$

It represents the ensemble average of the radial density around a particle at distance r normalized by the average density ρ_0 of the system. For impenetrable hard spheres of diameter σ, $g(r{<}\sigma) = 0$. Moreover, for an ideal gas, $g(r{>}\sigma) = 1$. For a crystal, $g(r)$ shows distinct peaks reflecting the characteristic distances of its unit cell. In a fluid, the particles form loose shells around each other, which results in modulations of $g(r)$ (see Fig. 1.1). Typically, these oscillations are damped over short distances already. Liquids do not exhibit long-ranged order, i.e., $g(r{\to}\infty) = 1$ [7].

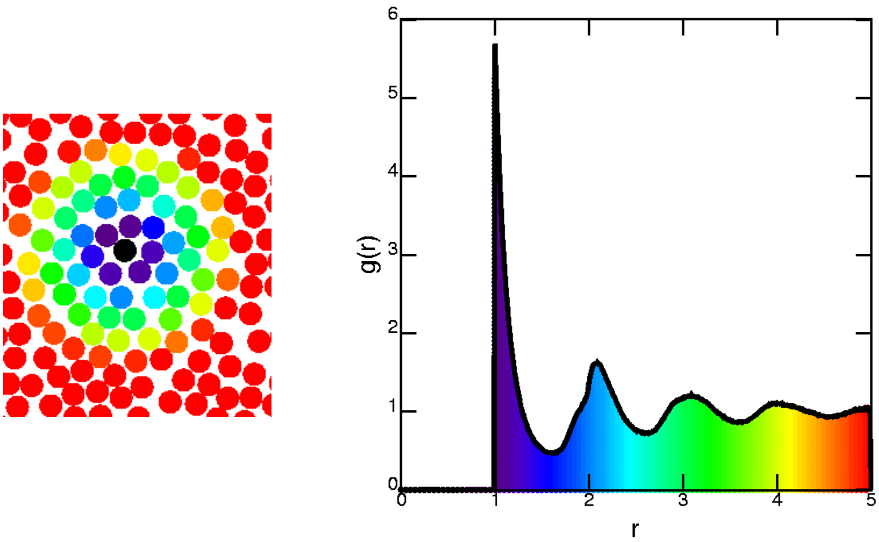

Figure 1.1 Left: Sketch of a colloidal fluid with particles coloured depending on their distance to the central black particle. Shell-formation is apparent. Right: Sketch of the radial distribution function $g(r)$ around the central black particle. Same colours are chosen as in the left sketch. The maxima in $g(r)$ correspond to the particle shells in left sketch. Reprinted from [8] with kind permission of Eric R. Weeks.

1.3 Dynamics in colloidal dispersions

In 1828, Robert Brown studied pollen in water with a microscope and, for the first time, described the random motion of colloidal particles [10]. This motion can be considered as a series of steps with uncorrelated step length and direction, a so-called random walk. It is caused by collisions of the solvent molecules with the dispersed particles, which move due to their thermal energy [11]. Nearly hundred years later, theoretical descriptions of Brownian motion were presented: Langevin described the colloidal dynamics due to a random force in 1908 [12]. Einstein and Smoluchowsky analysed the statistics of the random walk and the sedimentation-diffusion equilibrium few years before [13, 14]. In 1910, their findings were experimentally verified by Perrin [15].

To describe the Brownian motion of dilute colloidal suspensions, the displacement of one colloid, $\Delta\mathbf{r}(t) = \mathbf{r}(t + t_0) - \mathbf{r}(t_0)$, is considered, with the lag time t, the starting time t_0 and the d-dimensional vector $\mathbf{r}(t + t_0)$ containing the coordinates of one colloid at time $t + t_0$. As the motion is random, the ensemble average over the displacement vanishes, i.e. $\langle\Delta\mathbf{r}(t)\rangle = 0$. Therefore, the motion is quantified by the second moment, i.e., the mean-squared displacement (MSD), $\langle\Delta\mathbf{r}^2(t)\rangle$. Langevin showed that the MSD of a single colloid can be calculated as

$$\langle\Delta\mathbf{r}^2(t)\rangle = 2dD_0t, \tag{1.2}$$

with d giving the number of independent dimensions. D_0 is called the self-diffusion coefficient. For a sphere dispersed in a liquid, it is given by the Stokes-Einstein equation which reads

$$D_0 = \frac{k_\mathrm{B}T}{6\pi\eta_\mathrm{v}R} \tag{1.3}$$

with the solvent viscosity η_v and the particle radius R. For dilute solutions in equilibrium, the colloids are diffusing freely and thus the MSD is proportional to the time t [5]. For ergodic systems, statistics can be improved by taking a time-average over the starting time t_0 in the calculation of the MSD.

If the particles interact with each other or with an external potential, their motion is typically hindered and the MSD shows a power-law dependence on the lag time t with a diffusivity exponent $\mu(t)$ [16, 17]:

$$\langle\Delta\mathbf{r}^2(t)\rangle \propto t^{\mu(t)}. \tag{1.4}$$

Interactions typically lead to an exponent $\mu(t)$ which depends on the lag time t.

1.4 Colloid–colloid interactions

In this section, different types of colloidal interactions and phase behaviour are described. The interaction potential of experimental colloidal samples typically is a combination of different types of particle-particle interactions, e.g., van der Waals interaction, electrostatic and depletion interaction. Those interactions which are important for the scope of this thesis are explained in the following sections. However, under certain conditions, real systems effectively behave as colloidal hard spheres, as will be described below.

Hard-sphere interaction

The simplest kind of interaction between colloidal particles is the hard-sphere interaction. In this case, the colloidal particles interact like impenetrable, uncharged spheres: they feel an infinitely high potential barrier at contact, i.e. they cannot overlap and do not interact otherwise [18]. The interaction potential $U_{\mathrm{HS}}(r)$, which depends on the centre-to-centre distance r, reads as [1]:

$$U_{\mathrm{HS}}(r) = \begin{cases} \infty, & r \leq 2R \\ 0, & r > 2R \end{cases} . \tag{1.5}$$

The interaction potential is sketched in Figure 1.2a).

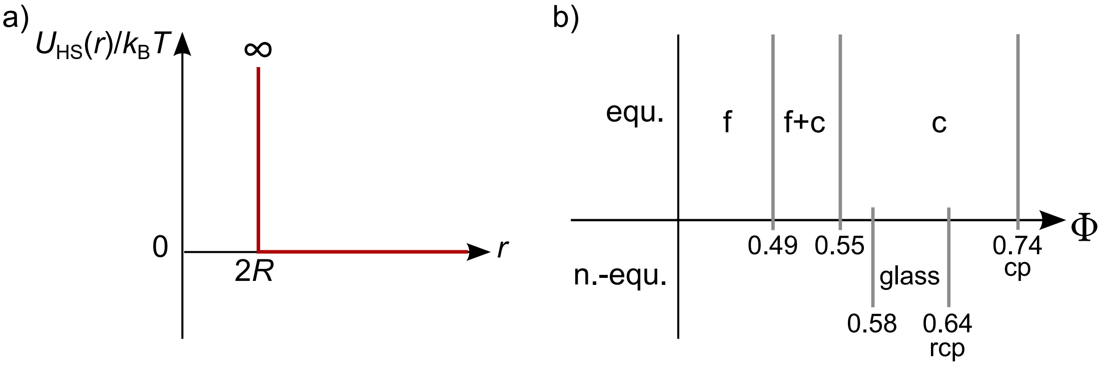

Figure 1.2 a) Sketch of the hard-sphere potential $U_{\mathrm{HS}}(r)$. b) Phase diagram of colloidal hard spheres: in equilibrium a fluid (f) phase up to colloid volume fraction $\Phi < 0.494$, a purely crystalline (c) phase for $0.545 < \Phi < \Phi_{\mathrm{cp}} = 0.74$ and a coexisting (f+c) phase in between are observed. A non-equilibrium glass phase can occur for $0.58 \lesssim \Phi < \Phi_{\mathrm{rcp}} = 0.64$.

Colloids exclusively interacting via a hard-sphere interaction show different equilibrium phases: a fluid, a crystal and a coexistence regime [3, 18, 19]. The equilibrium phase behaviour is controlled by only one parameter, namely the colloid concentration. It is independent of the temperature. The concentration can be expressed in terms of the colloid volume fraction, $\Phi = V_{\mathrm{colloid}}/V_{\mathrm{sample}}$, which is the volume of all colloids, V_{colloid}, divided by the total volume of the system, V_{sample}. Up to $\Phi = 0.494$, a fluid phase and, for $\Phi \geq 0.545$, a purely crystalline phase is observed which can reach a maximal volume fraction $\Phi_{\mathrm{cp}} = 0.74$. At Φ_{cp} the colloids are closed packed (cp) in a crystalline structure [5]. In between, i.e. for $0.494 < \Phi < 0.545$, a coexistence of fluid and crystalline phases is found [1, 6, 20]. If the system is brought out of equilibrium, e.g., by quenching it to a certain volume fraction, a non-equilibrium glass phase is observed for $\Phi \gtrsim 0.58$ [1, 21]. A colloidal glass is characterised by a random structure, in which the particles are caged by their neighbours. Thus, Brownian motion is hindered and the system prevented from reaching equilibrium [22]. The tightest non-crystalline packing is called random close packing (rcp), for which $\Phi_{\mathrm{rcp}} = 0.64$ in a monodisperse system. The value of Φ_{rcp} increases with polydispersity [23]. The equilibrium and non-equilibrium phase diagram for a three-dimensional colloidal hard-sphere system is sketched in Figure 1.2b).

Van der Waals interaction

Van der Waals interactions between colloids are always present. They are based on the attraction between the induced dipole moments of the colloids [5]. For identical, spherical colloids, the van der Waals potential $U_{\mathrm{vdW}}(r)$ forms a deep potential minimum and approximately reads

$$U_{\mathrm{vdW}}(r) = -\frac{A_{\mathrm{H}}}{6}\left[\frac{2R^2}{r^2 - 4R^2} + \frac{2R^2}{r^2} + \ln\left(1 - \frac{4R^2}{r^2}\right)\right] \tag{1.6}$$

with the Hamaker constant A_{H} which depends on the polarisabilities of the colloids and the dispersion medium [3]. If both materials have the same polarisability, e.g., if their refractive indices are matched, the van der Waals attraction is negligibly small. As the gain of potential energy at particle contact is much larger than the thermal energy, the colloids favour to coagulate and stabilisation is needed to prevent precipitation [3].

There are two widely used stabilisation methods: steric stabilisation and charge stabilisation. For steric stabilisation, the colloids are covered with polymer hairs and dispersed in a good solvent for the polymers. If the colloids come so close that the polymers are constrained, entropy decreases and the particles feel a repulsive force preventing coagulation [1, 3]. Charge stabilisation relies on electrostatic repulsion and will be explained in the next section. In the absence of further long-range interactions, well-stabilised particles can effectively be modelled as hard spheres [1].

Electrostatic interaction

If colloids are charged, e.g., by ionisation, electrostatic interactions are present. The counterions in the suspension medium form an electric double layer [1, 5]. The extent of the diffusive layer depends on the balance of the electric and thermal energy of the counterions [1]. The resulting interaction potential is derived based on the Poisson-Boltzmann equation and leads to a screened repulsive force between the colloids. The interaction potential can approximately be described by a Yukawa potential (or screened Coulomb potential) $U_{\mathrm{Y}}(r)$ for $r \geq 2R$ [3]:

$$U_{\mathrm{Y}}\left(r\right) = \frac{q_{\mathrm{e}}^{2}}{\varepsilon r}\,\mathrm{e}^{-\kappa r} \tag{1.7}$$

with the effective charge q_{e} of the particle, the dielectric constant ε of the solvent and the Debye screening parameter κ. The inverse, κ^{-1}, is the Debye screening length, at which the potential decreased to $1/e$ of the surface potential [1, 5]. The Debye length can be tuned by the ion concentration. In an organic system, κ^{-1} has been varied up to 12 µm [24]. In some colloidal systems far from equilibrium, long-range electrostatic interactions play a key role, especially in gel states [25]. In contrast, to achieve hard-sphere-like behaviour, the electrostatic contribution to the interaction potential has to be rather short-ranged, i.e. a short Debye screening length is needed. Deviations from the simple Yukawa model for screened electrostatic interactions might occur for charged spheres at high Φ [26].

If both electrostatic and van der Waals interactions are present, they are combined in the so-called Derjaguin-Landau-Verwey-Overbeek (DLVO) potential $U_{\mathrm{DLVO}}(r)$. Under the condition that $U_{\mathrm{DLVO}}(r)$ has just one minimum and a potential barrier much larger than $k_{\mathrm{B}}T$, the solution is stable (see Figure 1.3) [1].

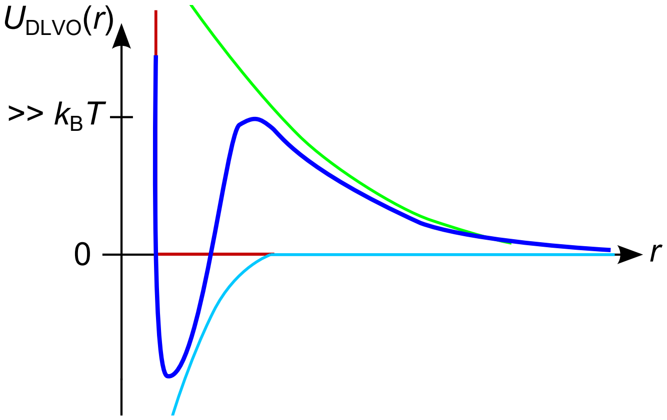

Figure 1.3 Sketch of the DLVO potential $U_{\mathrm{DLVO}}(r)$ (dark blue line). Shown are also sketches of the hard-sphere potential (red line), the van der Waals potential (light blue line) and the Yukawa potential (green line).

Depletion interaction

The addition of small colloids or non-adsorbing polymers to a colloidal hard sphere suspension offers a systematic way to tune attractive interactions. Due to the finite volume of the smaller species, a volume around each large colloid is depleted of the centres of the smaller species, i.e. the depletants. This depletion layer has an extension δ of the size of the smaller particles (see Fig. 1.4, left). If the depletion layers of two large colloids overlap, the osmotic pressure exerted by the depletants on the colloids is unbalanced. Thus, the large colloids feel an effective attraction, the so-called depletion interaction [27].

For small depletant concentrations, the depletion potential can be described by the Asakura-Oosawa-Vrij (AOV) potential U_{AOV}:

$$U_{\mathrm{AOV}}(r) = \begin{cases} \infty, & r \leq 2R \\ -PV_{\mathrm{overlap}}(r), & 2R < r \leq 2R + 2\delta \\ 0, & r > 2R + 2\delta \end{cases} \tag{1.8}$$

with the overlap volume of the depletion layers $V_{\mathrm{overlap}}(r) = (\pi/6)(2R + 2\delta - r)^2 (2R + 2\delta + r/2)$ [27]. If the depletion range is large, i.e. the ratio $q = \delta/R \gtrsim 0.15$, multiple overlap of depletion zones is possible and the effective interaction between the colloids is no longer pairwise additive. Small hard spheres used as depletants give rise to a slightly different potential, although the general form of the potential follows the AOV potential and can be tuned as explained below [27]. While Asakura and Oosawa

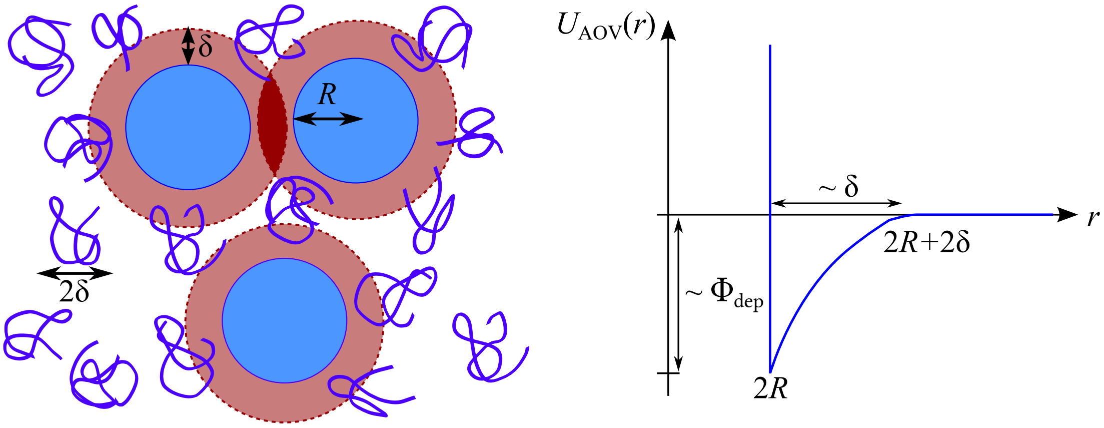

Figure 1.4 Left: Colloidal spheres with polymers as depletants. The dashed lines and red areas indicate the depletion layers which cannot be accessed by the centres of the polymers. Their overlap (dark red region) leads to an unbalanced osmotic pressure and an effective attraction between the colloids. Right: Asakura-Oosawa-Vrij potential $U_{\mathrm{AOV}}(r)$ versus particle distance r. Its range 2δ and its depth depend on the radius of depletants and the depletant concentration Φ_{dep}, respectively.

described the depletants as purely hard spheres [28], Vrij modelled them as penetrable hard spheres, but to act as hard spheres towards the large spheres [29]. The AOV potential is sketched in Figure 1.4, right. Its potential range and depth depends on the depletant size and concentration, respectively. In case of small hard spheres with radius R_{s} as depletants, the range is given by $2\delta = 2R_{\mathrm{s}}$, while it is $2\delta = 2R_{\mathrm{g}}$ for polymers with radius of gyration R_{g} at low polymer and colloid concentration. The potential depth is proportional to the volume fraction of the depletants $\Phi_{\mathrm{dep}} = V_{\mathrm{dep}}/V_{\mathrm{sample}}$ with the volume of all depletants, V_{dep}, of size R_{s} or R_{g}, respectively, as defined above.

A theory to describe the phase behaviour of systems with depletion interactions is the free volume theory (FVT). It is based on the osmotic equilibrium between the sample and a hypothetical depletant reservoir. The system always favours to maximize entropy, thus maximizing the free volume for the depletants. In FVT, the colloids and depletants are modelled as hard spheres and penetrable hard spheres, respectively [27, 30]. The model gives satisfactory results for colloid-polymer mixtures at low q or low Φ_{p} as well as for colloid-colloid mixtures with low q [27]. The phase behaviour of colloid-polymer mixtures at high q or high Φ_{p} can be obtained from the generalized free volume theory (GFVT) [31]. It incorporates that the depletion thickness δ (and thus the range of the potential) varies with Φ_{p}. At high polymer concentration, the polymers overlap, leading to significant polymer-polymer interactions and thus a strong deviation from ideality.

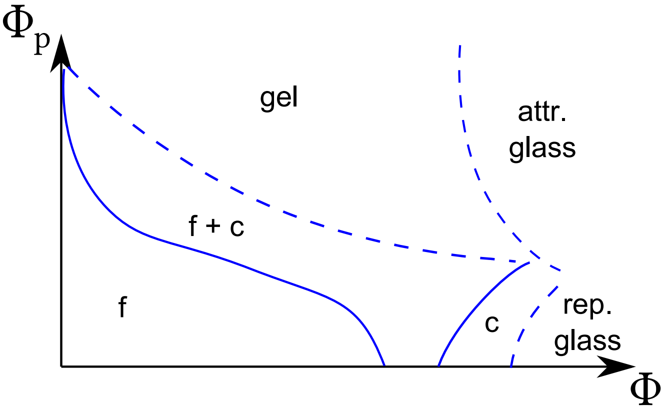

Figure 1.5 Sketch of the generic phase diagram of a colloid-polymer mixture with $q < 0.3$. In addition to the equilibrium phases (fluid (f), fluid+crystal (f+c), crystal (c)), several non-equilibrium phases are observed: gels, attractive and repulsive glasses.

A generic phase diagram of a colloid-polymer mixture with $q < 0.3$ is sketched in Figure 1.5. For very low polymer concentrations, the phase behaviour resembles the hard sphere case with the equilibrium phases of a fluid, a crystal as well as a fluid-crystalline coexistence. With increasing polymer concentration, the coexistence region widens up. In this coexistence region, a metastable gas-liquid phase separation is hidden. This causes a variety of non-equilibrium states [27]. Up to intermediate Φ and high Φ_p, gel states are observed [27, 32]. Furthermore, at high colloid concentrations Φ, two glassy states are found: the repulsive glass at low Φ_p and the attractive glass at high Φ_p [27, 33]. While in a repulsive glass, the particles are caged by their neighbours due to excluded volume effects, in attractive glasses, they are arrested due to the attractive depletion interaction [34–36].

One of the characteristics of a gel is a network-like structure spanning the whole sample volume. It has a high heterogeneity (see Fig. 1.6), which is most pronounced close to the gelation boundary [37]. The second main feature of gels is dynamical arrest, i.e. a slowing down of the particle dynamics [37]. To further the understanding of colloidal gels, it is desirable to explore the connection between the structural properties and the dynamical arrest.

The underlying mechanisms and pathways to gel formation are still heavily debated. Arrested phase separation has been suggested as one such mechanism [38, 39]. The hidden spinodal line in the fluid-crystal coexistence region can lead to density fluctuations

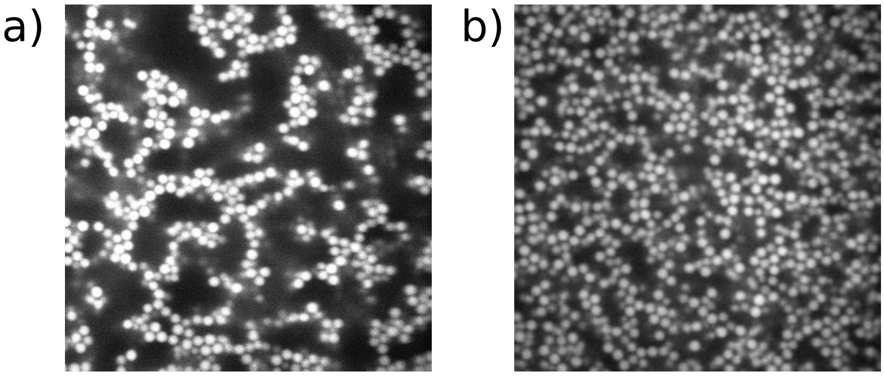

Figure 1.6 Typical 2D confocal microscopy image of a colloidal gel with volume fraction $\Phi \approx 0.2$ (a) and $\Phi \approx 0.4$ (b).

and phase separation in the sample, resulting in a dynamical arrest of the denser part. Other suggestions include a glass-like arrest of the dynamics [40], the formation of locally favoured structures [41] or the onset of rigidity percolation [42]. In colloidal systems with additional repulsive interaction, aggregation of clusters into a percolated network was reported [38].

1.5 Colloid–potential interactions

In this section, the creation of external potentials using optical forces is explained and the behaviour of colloids in potentials is described. Optical forces can be used to manipulate colloidal particles. Experiments of a colloidal particle trapped by two counter-propagating laser beams were first reported in 1970 [43]. Nowadays, optical tweezers are commonly used in biology, material science and medicine.

Optical generation of external potentials

Optical forces

Laser light exerts a forces on colloids, so-called optical forces [16, 17, 43–47]. We consider a colloid with radius R and refractive index n_c (larger than that of the surrounding solvent n_s) which is hit by a laser beam with wavelength λ. For $R \gg \lambda$, simple ray optics can be used to explain the optical forces, while for $R \ll \lambda$, the particle acts as a Rayleigh scatterer [16, 17, 44, 45, 47]. Both regimes will be explained in detail.

First, the case $R \gg \lambda$ is considered. The laser light that hits a transparent particle is scattered, reflected and refracted by the particle. Since photons carry a momentum

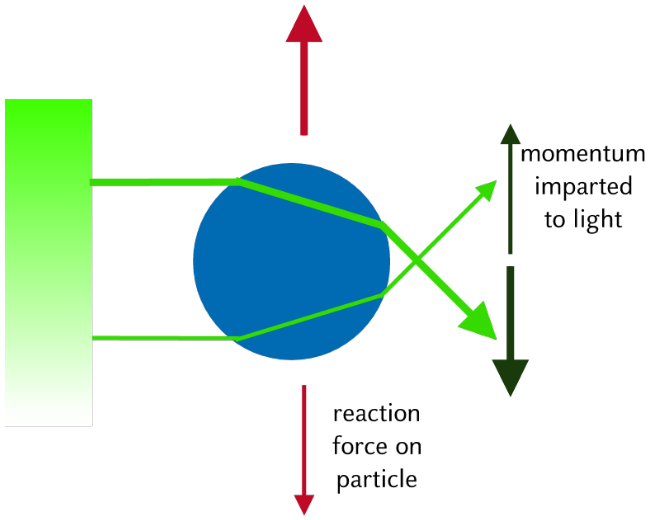

Figure 1.7 The incident laser light with an intensity gradient is refracted by a colloidal particle with $n_c > n_s$. During refraction, momentum is imparted to the light, which results in reaction forces on the particle. As a high intensity leads to a higher force, the resulting forces do not balance and the particle moves towards the region of higher intensity.

$p = h/\lambda$ with the Planck constant h and laser wavelength λ, the scattering and reflection lead to a momentum transfer to the particle and a force in the direction of the light propagation. This is called radiation pressure or scattering force. A momentum change is also imparted to the light during refraction. Due to the conservation of momentum, the transferred momentum results in a reaction force on the colloid [44]. As a higher light intensity results in a higher reaction force, the forces do not balance in the case of an intensity gradient [43–45]. Hence, in the present case the particle is pushed towards the intensity maximum (see Fig. 1.7) due to the gradient force. If the particle instead has a refractive index $n_c < n_s$, the light beams are refracted in the opposite directions and the gradient force is directed towards the intensity minimum instead. The resulting force, which the light exerts on the particle, is the sum of the reaction forces due to scattering, reflection and refraction [16, 17, 43–45, 47].

If the particle radius is much smaller than the wavelength, $R \ll \lambda$, ray optics do not apply. Due to its polarisability, an oscillating dipole is induced in the colloid by the electric field. It absorbs and re-emits the incident light, which is the reason for the scattering force acting on the particle. The force is given as follows [16, 17, 44, 45, 47]:

$$F_{\text{scat}} = \frac{128\pi^5 R^6 n_s}{3\lambda^4 c} \left(\frac{n^2-1}{n^2+2}\right)^2 I(\mathbf{r}). \tag{1.9}$$

The magnitude of the scattering force depends on the ratio of the refractive indices of the colloid and the solvent, $n = n_{\text{c}}/n_{\text{s}}$ and the intensity of the light, $I(\mathbf{r})$. Its direction is given by the propagation direction of the laser light. If the intensity of the incident light is spatially inhomogeneous, the particle additionally experiences the gradient force [17, 47, 48]:

$$F_{\text{grad}} = \frac{2\pi R^3 n_s}{c} \left(\frac{n^2-1}{n^2+2}\right) \nabla I(\mathbf{r}). \tag{1.10}$$

In this thesis, we use particles with $R \approx \lambda$, where Lorenz-Mie theory has to be used for exact calculations of the optical forces [17, 45, 49]. This case yields qualitatively similar but quantitatively different and much more complicated results. It will not be discussed here.

Sinusoidal potential

The interference of two Gaussian laser beams can be used to create a fringe pattern [46, 50–52]. (An experimental set-up is described in section 2.2.1.) The intensity profile across the fringes, $I\left(y\right)$, depends on the beam crossing angle θ [46, 50]:

$$I\left(y\right) = 2I_0\{1+\cos\left[2ky\sin\left(\theta/2\right)\right]\}\mathrm{e}^{-2y^2\cos^2(\theta/2)/a^2} \tag{1.11}$$

with the intensity of the incident laser beams I_0, their wavevector $k = 2\pi/\lambda$ and the beam waist radius a. The term in curly brackets forms the sinusoidal intensity pattern with a fringe spacing $d = \lambda/\left(2\sin\left(\theta/2\right)\right)$, while the Gaussian envelope is caused by the finite beam size. In a region, in which the influence of the Gaussian envelope is negligibly small, the intensity pattern converts into a sinusoidal potential of the form $V\left(y\right) = V_{\text{off}}\{1+\cos\left(qy\right)\}$ with potential wave vector $q_{\text{pot}} = 2\pi/d$ for a point-like particle. For particles with a finite size, the potential varies over the dimension of the particle size yielding the effective potential

$$V\left(y\right) = V_{\text{off}}\left\{1 + 3\frac{j_1\left(q_{\text{pot}}R\right)}{q_{\text{pot}}R}\cos\left(q_{\text{pot}}y\right)\right\} \tag{1.12}$$

with the first order spherical Bessel function j_1 [46]. Depending on the length scale ratio $q_{\mathrm{pot}}R$, the potential minima for the colloidal particles are formed by the regions of highest or lowest intensity, respectively. The potential offset is given by $V_{\mathrm{off}} = gP_{\mathrm{L}}\alpha$ with the set-up dependent parameter g, the laser power of the incident beams P_{L} and the particle polarisability $\alpha = R^3 n_s^2 \left(n^2 - 1\right) / \left(n^2 + 2\right)$ [53]. The potential amplitude is thus given by $V_0 = 3V_{\mathrm{off}}\, j_1 \left(q_{\mathrm{pot}}R\right) / (q_{\mathrm{pot}}R)$.

Colloids in a sinusoidal potential

Spatial arrangement

Colloidal particles in a sinusoidal potential prefer to stay in the potential minima. Additionally, due to the radiation pressure, they form a (quasi) two-dimensional layer, whose spatial arrangement has been studied extensively [46, 50, 51, 54–62]. It strongly depends on the commensurability ratio, $p = \sqrt{3}s/(2d)$, of the fringe spacing d and the mean interparticle distance s, which is set by the colloid concentration.

If the particles sitting in neighbouring fringes do not interact with each other, a high degree of order is induced perpendicular to the potential minima, but a disordered arrangement along the fringes. Such a structure is typically referred to as a modulated liquid [56]. It occurs, e.g., due to very short-ranged interactions, an incommensurate fringe spacing or a high potential amplitude. If the fringe spacing is chosen to be commensurate to the interparticle distance, i.e. $p = 1$, the formation of a two-dimensional hexagonal crystal is observed at increasing potential amplitude, if the particle concentration as well as the strength and the range of the particle-particle interactions are sufficient [50, 54–56]. This effect is called laser-induced freezing (LIF). By further increasing the potential amplitude, the particles are more strongly confined to the potential minima. This can lead to a reduced interaction between the particles on neighbouring fringes, depending on the interaction range, and to a laser-induced melting (LIM) of the crystalline structure to a modulated liquid [51, 57–59]. For a larger commensurability ratio $p = 2$, theory and Monte-Carlo simulations show an even more complex phase behaviour for colloids and hard discs, including a locked smectic phase [61, 62].

Typically, colloidal systems in nature and industry are much more complex, e.g. because of a higher degree of polydispersity. As a first step to investigate effects of polydispersity, another particle species is added to the system, which thus forms a binary mixture. Monolayers of binary colloidal mixtures form different spatial arrangements depending on three parameters: their size ratio $R_\mathrm{s}/R_\mathrm{l}$ between small and large colloids, their stoichiometric ratio $\xi = N_\mathrm{s}/N_\mathrm{l}$ with the particle numbers N_s and N_l for small and large particles, respectively, as well as the total packing fraction $\eta = (N_\mathrm{s}A_\mathrm{s} + N_\mathrm{l}A_\mathrm{l})/A$ with the investigated area A and the cross-sectional areas of small and large particles, A_s and A_l. Monolayers of binary hard-sphere and hard-disc mixtures have been studied in experiments [63, 64] and theoretically [65], respectively. Complexity can be increased by exposing a binary mixture to a sinusoidal potential. The potential modulates the arrangement of the colloids, which thus can be regarded to be in a non-equilibrium state caused by the external potential. In addition to the three particle-specific parameters, the resulting arrangement now also depends on the potential amplitude and the fringe spacing d. Monte-Carlo simulations of a binary hard-disc mixture in a sinusoidal potential reveal novel structural features, like the de-mixing of the particle species and the so-called fissuring phase, in which the small particles form fissures perpendicular to the potential minima in a crystal of large and small particles [66–70]. Experimentally, such a complex system is difficult to control. However, the simulation results indicate that the effort might pay off with a fascinating variety of tunable spatial arrangements.

Particle Dynamics

The dynamics of monodisperse colloids exposed to a sinusoidal potential already shows an interesting effect at low particle densities. While the particles can diffuse freely along the potential minima, their dynamics across the potential barriers is slowed down, leading to a plateau in the respective MSD at intermediate times [53]. Data for different particle sizes and fringe spacings can be scaled to dimensionless quantities. Hence, the depth and length of the plateau largely depend on the potential amplitude. The slowing-down in the dynamics resembles the MSD of a glass-forming colloidal suspension [53].

If the colloid packing fraction in the suspension is increased, particle-particle interactions become important as shown in Brownian Dynamics simulations [71]. In the simulations, a concentrated two-dimensional colloidal system was exposed to a commensurate sinusoidal potential with $p = 1$. While qualitative trends of the particle MSD across the potential barriers are similar to the dilute case, the dynamics along the potential minima is strongly influenced by the high particle concentration. With increasing potential amplitude, even the MSD along the minima shows the development of a plateau at intermediate times, up to a critical potential amplitude beyond which plateau height does not change anymore. Furthermore, in a one-dimensional channel, single-file diffusion was observed at increasing colloid concentration. It is characterised by a diffusivity exponent $\mu(t) \approx 0.5$ for intermediate and long t [72]. In a binary colloidal mixture exposed to a sinusoidal light field, the influence of the particle-particle interactions on the dynamics might be even more complex.

Bibliography

[1] Hamley, I. W. *Introduction to Soft Matter*; John Wiley & Sons, Ltd.: Chichester, 2007.

[2] Doi, M. *Soft Matter Physics*; University Press: Oxford, 2013.

[3] Pusey, P. N. In *Liquids, Freezing and Glass Transition*; Hansen, J. P., Levesque, D., Zinn-Justin, J., Eds.; Elsevier Science Publishers B.V.: Amsterdam, 1991; Chapter 10, pp 763–942.

[4] Frenkel, D. *Physica A* **2002**, *313*, 1–31.

[5] Jones, R. A. L. *Soft Condensed Matter*; University Press: Oxford, 2002.

[6] Pusey, P. N.; van Megen, W. *Nature* **1986**, *320*, 340–342.

[7] Demtröder, W. *Experimentalphysik 3*; Springer-Lehrbuch; Springer-Verlag: Heidelberg, 2010.

[8] Weeks, E. R. What is the pair correlation function g(r)? accessed at June 15th, 2017; `http://www.physics.emory.edu/faculty/weeks//idl/gofr.html`.

[9] Hansen, J.; Macdonald, I. *Theory of Simple Liquids*, 3rd ed.; Academic Press: London, 2006.

[10] Brown, R. *Philos. Mag. Ser. 2* **1828**, *4*, 161–173.

[11] Russel, W. B.; Saville, D. A.; Schowalter, W. R. *Colloidal Dispersions*; University Press: Cambridge, 1989.

[12] Langevin, P. *Comptes Rendues* **1908**, *146*, 530.

[13] Einstein, A. *Ann. Phys.* **1905**, *322*, 549–560.

[14] Smoluchowski, M. *Ann. Phys.* **1906**, *326*, 756–780.

[15] Perrin, J. *Ann. Chim. Phys.* **1909**, *8*, 5–114.

[16] Hanes, R. D. L. Colloids in controlled energy landscapes. Ph.D. thesis, Heinrich-Heine-Universität Düsseldorf, 2012.

[17] Bewerunge, J. Colloids in random potentials: Optical realization and characterization of rough laser light fields. Ph.D. thesis, Heinrich-Heine-Universität Düsseldorf, 2016.

[18] Poon, W. C. K.; Pusey, P. N.; Lekkerkerker, H. N. W. *Phys. World* **1996**, *9*, 27–32.

[19] Pusey, P. N.; Van Megen, W.; Underwood, S. M.; Bartlett, P.; Ottewill, R. H. *J. Phys.: Condens. Matter* **1990**, *2*, SA373–SA377.

[20] Hoover, W. G.; Ree, F. H. *J. Chem. Phys.* **1968**, *49*, 3609.

[21] Woodcock, L. V. *Ann. NY Acad. Sci.* **1981**, *37*, 274.

[22] Weeks, E. R.; Weitz, D. A. *Chem. Phys.* **2002**, *284*, 361–367.

[23] Schaertl, W.; Sillescu, H. *J. Stat. Phys.* **1994**, *77*, 1007–1025.

[24] Yethiraj, A.; Blaaderen, A. V. *Nature* **2003**, *421*, 513–517.

[25] Kohl, M.; Capellmann, R. F.; Laurati, M.; Egelhaaf, S. U.; Schmiedeberg, M. *Nat. Commun.* **2016**, *7*, 11817.

[26] Royall, C. P.; Leunissen, M. E.; Hynninen, A. P.; Dijkstra, M.; Van Blaaderen, A. *J. Chem. Phys.* **2006**, *124*, 244706.

[27] Lekkerkerker, H. N. W.; Tuinier, R. *Colloids and the Depletion Interaction*; Springer Science+Business Media B.V.: Heidelberg, 2011.

[28] Asakura, S.; Oosawa, F. *J. Pol. Sci.* **1958**, *33*, 183–192.

[29] Vrij, A. *Pure Appl. Chem.* **1976**, *48*, 471–483.

[30] Lekkerkerker, H. N. W.; Poon, W. C. K.; Pusey, P. N.; Stroobants, A.; Warren, P. B. *Europhys. Lett.* **1992**, *20*, 559–564.

[31] Fleer, G. J.; Tuinier, R. *Adv. Colloid Interface Sci.* **2008**, *143*, 1–47.

[32] Poon, W. C. K.; Pirie, A. D.; Pusey, P. N. *Faraday Discuss.* **1995**, *101*, 65–76.

[33] Bergenholtz, J.; Fuchs, M. *Phys. Rev. E* **1999**, *59*, 5706.

[34] Pham, K. N.; Puertas, A. M.; Bergenholtz, J.; Egelhaaf, S. U.; Moussaïd, A.; Pusey, P. N.; Schofield, A. B.; Cates, M. E.; Fuchs, M.; Poon, W. C. K. *Science* **2002**, *296*, 104–106.

[35] Pham, K.; Egelhaaf, S.; Pusey, P.; Poon, W. *Phys. Rev. E* **2004**, *69*, 011503.

[36] Eckert, T.; Bartsch, E. *Phys. Rev. Lett.* **2002**, *89*, 125701.

[37] Dibble, C. J.; Kogan, M.; Solomon, M. J. *Phys. Rev. E* **2006**, *74*, 041403.

[38] Zaccarelli, E. *J. Phys. Condens. Matter* **2007**, *19*, 323101.

[39] Lu, P. J.; Zaccarelli, E.; Ciulla, F.; Schofield, A. B.; Sciortino, F.; Weitz, D. A. *Nature* **2008**, *453*.

[40] Segrè, P. N.; Prasad, V.; Schofield, A. B.; Weitz, D. A. *Phys. Rev. Lett.* **2001**, *86*, 6042–6045.

[41] Royall, C. P.; Williams, S. R.; Ohtsuka, T.; Tanaka, H. *Nature Mater.* **2008**, *7*, 556–561.

[42] Valadez-Pérez, N. E.; Liu, Y.; Eberle, A. P. R.; Wagner, N. J.; Castañeda-Priego, R. *Phys. Rev. E* **2013**, *88*, 060302(R).

[43] Ashkin, A. *Phys. Rev. Lett.* **1970**, *24*, 156–159.

[44] Molloy, J. E.; Padgett, M. J. *Contemp. Phys.* **2002**, *43*, 241–258.

[45] Neuman, K. C.; Block, S. M. *Rev. Sci. Instrum.* **2004**, *75*, 2787–2809.

[46] Jenkins, M. C.; Egelhaaf, S. U. *J. Phys. Condens. Matter* **2008**, *20*, 404220.

[47] Evers, F.; Hanes, R. D. L.; Zunke, C.; Capellmann, R. F.; Bewerunge, J.; Dalle-Ferrier, C.; Jenkins, M. C.; Ladadwa, I.; Heuer, A.; Castañeda-Priego, R.; Egelhaaf, S. U. *Eur. Phys. J. Spec. Top.* **2013**, *222*, 2995–3009.

[48] Harada, Y.; Asakura, T. *Opt. Commun.* **1996**, *124*, 529–541.

[49] Bowman, R. W.; Padgett, M. J. *Reports Prog. Phys.* **2013**, *76*, 026401.

[50] Loudiyi, K.; Ackerson, B. J. *Physica A* **1992**, *184*, 1–25.

[51] Bechinger, C.; Brunner, M.; Leiderer, P. *Phys. Rev. Lett.* **2001**, *86*, 930–933.

[52] Capellmann, R. F.; Bewerunge, J.; Platten, F.; Egelhaaf, S. U. *Rev. Sci. Instrum.* **2017**, *88*, 056102.

[53] Dalle-Ferrier, C.; Krüger, M.; Hanes, R. D. L.; Walta, S.; Jenkins, M. C.; Egelhaaf, S. U. *Soft Matter* **2011**, *7*, 2064.

[54] Chowdhury, A.; Ackerson, B. J.; Clark, N. A. *Phys. Rev. Lett.* **1985**, *55*, 833.

[55] Loudiyi, K.; Ackerson, B. J. *Physica A* **1992**, *184*, 26–41.

[56] Wei, Q.; Bechinger, C.; Rudhardt, D.; Leiderer, P. *Prog. Colloid Polym. Sci.* **1998**, *110*, 46–49.

[57] Chakrabarti, J.; Krishnamurthy, H. R.; Sood, A. K.; Sengupta, S. *Phys. Rev. Lett.* **1995**, *75*, 2232–2235.

[58] Wei, Q.-H.; Bechinger, C.; Rudhardt, D.; Leiderer, P. *Phys. Rev. Lett.* **1998**, *81*, 2606–2609.

[59] Bechinger, C.; Wei, Q.-H.; Leiderer, P. *J. Phys. Condens. Matter* **2000**, *12*, A425–A430.

[60] Bechinger, C.; Frey, E. *J. Phys. Condens. Matter* **2001**, *13*, R321–R336.

[61] Radzihovsky, L.; Frey, E.; Nelson, D. R. *Phys. Rev. E* **2001**, *63*, 0315031.

[62] Bürzle, F.; Nielaba, P. *Phys. Rev. E* **2007**, *76*, 051112.

[63] Bonales, L. J.; Martínez-Pedrero, F.; Rubio, M. A.; Rubio, R. G.; Ortega, F. *Langmuir* **2012**, *28*, 16555–16566.

[64] Thorneywork, A. L.; Roth, R.; Aarts, D. G. A. L.; Dullens, R. P. A. *J. Chem. Phys.* **2014**, *140*, 161106.

[65] Likos, C. N.; Henley, C. L. *Philos. Mag. Part B* **1993**, *68*, 85–113.

[66] Franzrahe, K.; Nielaba, P. *Phys. Rev. E* **2007**, *76*, 061503.

[67] Franzrahe, K.; Nielaba, P.; Ricci, A.; Binder, K.; Sengupta, S.; Keim, P.; Maret, G. *J. Phys. Condens. Matter* **2008**, *20*, 404218.

[68] Franzrahe, K.; Nielaba, P. *Phys. Rev. E* **2009**, *79*, 051505.

[69] Wilms, D.; Deutschländer, S.; Siems, U.; Franzrahe, K.; Henseler, P.; Keim, P.; Schwierz, N.; Virnau, P.; Binder, K.; Maret, G.; Nielaba, P. *J. Phys. Condens. Matter* **2012**, *24*, 464119.

[70] Franzrahe, K. Theoretische Untersuchungen komplexer Modell-Kolloide: Computer-Simulationen struktureller und elastischer Eigenschaften. Ph.D. thesis, Universität Konstanz, 2008.

[71] Herrera-Velarde, S.; Castañeda-Priego, R. *Phys. Rev. E* **2009**, *79*, 041407.

[72] Lutz, C.; Kollmann, M.; Bechinger, C. *Phys. Rev. Lett.* **2004**, *93*, 026001.

This page has been left intentionally blank.

OVERVIEW 2

This thesis focusses on the spatial arrangement of colloidal mixtures in non-equilibrium. We consider two generic scenarios: non-equilibrium induced by intrinsic and extrinsic mechanisms. First, colloid-polymer and binary colloidal mixtures with large size asymmetry are investigated. In these mixtures, the polymers and the smaller colloids act as depletants. Given certain particle concentrations gels can form. These non-equilibrium structures arise from interparticle interactions and hence can be regarded as intrinsic non-equilibrium. In a second step, we study binary colloidal mixtures exposed to a sinusoidal potential. The particle-potential interactions modulate the spatial arrangement of the particles. Thus, they are considered to be in an extrinsic non-equilibrium caused by the external potential.

This chapter provides an overview of the studies on colloidal gels and concentrated binary colloidal mixtures. Each sub-section summarizes one of the publications. Figures and their captions are taken from the mentioned publication. The chapter concludes with an outlook about colloidal gels exposed to a sinusoidal potential.

2.1 Colloidal gels – intrinsic non-equilibrium

By comparing the experimental radial distribution functions of colloidal gels at intermediate volume fraction with the results of Monte Carlo simulations, an effective interaction potential consisting of a combination of a short-ranged attraction and a long-ranged repulsion can be obtained. With this effective interaction potential, other structural signatures, like the bond angle distribution and the bond number distribution, can be reproduced, although non-equilibrium effects are not explicitly included (cf. section 2.1.1). Applying a similar effective potential, experiments and Brownian dynamics simulations of colloidal gels at lower volume fraction were analysed and directed percolation as a pre-transition towards arrested gel states was observed (cf. section 2.1.2). Additionally, gel formation was found to be one of the mechanisms leading to dynamical arrest in binary colloidal mixtures with large size ratio (cf. section 2.1.3).

2.1.1 Competing interactions

Competing short-ranged attraction and long-ranged repulsion are found in many different systems, e.g., protein solutions [1], nanoparticle solutions [2] and colloidal gels [3]. At low volume fractions, the structure of colloidal gels could be successfully modelled with a combination of an AOV and a Yukawa potential [4]. Yet, at intermediate volume fraction, effects like crowding and compression of the polymers might complicate modelling. A former study comparing experiments to MCT-PRISM simulations only led to semi-quantitative agreement [5]. This sub-section summarizes a study (see Publication 1 in section 3.1, [6]) on this interplay of interactions in colloidal gels consisting of a colloid-polymer mixture with intermediate volume fraction.

The samples consisted of spherical colloids made out of polymethylmethacrylate (PMMA) of diameter $\sigma \approx 1.72$ µm and polystyrene (PS) polymers in a mixture of *cis*-decalin and cycloheptylbromide (CHB). This solvent matched the density and the refractive index of the colloids. Due to fluorescent labelling, the colloidal particles could be observed via confocal fluorescence microscopy. As the sterically stabilized PMMA colloids in CHB become charged, a salt (tetrabutylammonium chloride) was added to screen the charges. Two sets of samples (1 and 2) were prepared independently with $\Phi \approx 0.4$ and slightly different salt concentrations c_s, $4.5\mathrm{mM} < c_\mathrm{s} < 4.9\mathrm{mM}$ and $4.8\mathrm{mM} < c_\mathrm{s} < 5.3\mathrm{mM}$, respectively. In both sets, the polymer concentration was varied from $0c^*$ to $2c^*$ with the polymer overlap concentration $c^* = 3M_\mathrm{p}/4\pi R_\mathrm{g}^3 N_\mathrm{A}$, the molar mass M_p, the radius of gyration of the polymer R_g and the Avogadro constant N_A. The size ratio between polymers and colloids was $q \approx 0.08$ in a dilute suspension. Due to the high volume fraction and polymer concentration in our samples, the effective size ratio is expected to vary as $0.08 > q^* > 0.02$ according to GFVT. Although the sample compositions in both sets are similar, the structural arrangement can differ due to the different preparation history and solvent age. Whereas the solvent age might effect the effective particle charge and dissolved TBAC concentrations, the preparation history might induce differences especially in the non-equilibrium structures.

The structural signatures, e.g. the bond angle distribution, gained from experiments were compared to Monte Carlo (MC) simulations. In the simulations, the interparticle attractive and repulsive interactions were modelled with an effective potential. The effective potential for each sample was gained by fitting the radial distribution function, $g(r)$, as obtained from simulations, to the experimental $g(r)$. Samples without polymers were successfully fitted by a combination of a hard-sphere and a repulsive Yukawa potential. These fits provided approximate values for the effective particle charge Q_{eff} and Debye screening length κ^{-1}. In samples with a very low polymer concentration, $c_{\text{p}} = 0.1c^{*}$, the radial distribution function was dominated by the repulsive part of the potential. Thus, they could be fitted with the same combination of potentials. The parameters of the Yukawa potential were kept constant, while a slight change in Φ was included in the simulations. For the gel samples with $0.8c^{*} < c_{\text{p}} < 2.0c^{*}$, the effective potential consists of a combination of an attractive square-well and a repulsive Yukawa potential.

For these samples, the radial distribution functions $g(r)$ from experiments and simulations are presented in Figure 2.1. They are characterized by a sharp first and a broad second peak, which is typical for a heterogeneous gel structure [7, 8]. The shape of the first minimum at $r/\sigma \approx 1.1$ slightly varies between the two sets shown in a) and b). The fitting parameters of the Yukwawa potential were adjusted to $\kappa\sigma = 15$ and $Q_{\text{eff}} = 273$ and $\kappa\sigma = 30$ and $Q_{\text{eff}} = 514$ for the two sets, respectively. The different shapes of the first minimum might correlate with the different amount of charges and screening in the samples.

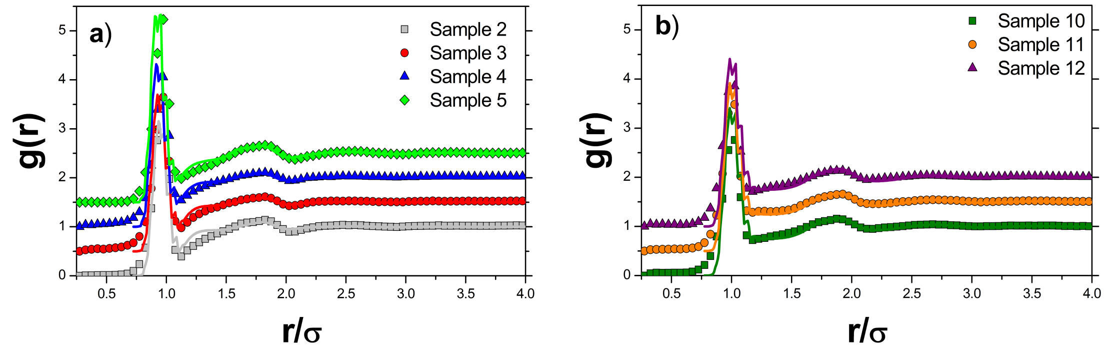

Figure 2.1 Radial distribution functions for gel samples with $c_{\text{p}} \geq 0.8c^{*}$ of two independent sets of experiments (a) and b)). Symbols denote experimental data, while lines represent simulation results. Shown are simulation results providing the effective interaction potential. Curves are vertically shifted for clarity. Figure reproduced and caption adapted from [6] by permission of The Royal Society of Chemistry.

Based on the experimental data and the effective potentials, respectively, the angular distribution function, $P(\varphi)$, and the distribution of the numbers of nearest neighbours, $P(n_\mathrm{b})$, were calculated. Two particles were identified as nearest neighbours if $r < 1.1\sigma$. Results for $P(\varphi)$ are shown in Figure 2.2 for both sets. A pronounced peak at 60° suggests that the particles primarily form triangular structures. The experimental curves are well reproduced by the simulations. Figure 2.3 presents the data of $P(n_\mathrm{b})$ for both sets. The experimental curves in each set are similar, while the mean value $\langle n_\mathrm{b} \rangle$ is slightly larger in set 2. These general trends are also found in the simulations. Hence, electrostatics strongly influences the structural arrangement of the gels, which is supported by the second virial coefficient B_2: for set 1, $B_2 > 0$, whereas for set 2, $B_2 < 0$, indicating net repulsions and attractions, respectively.

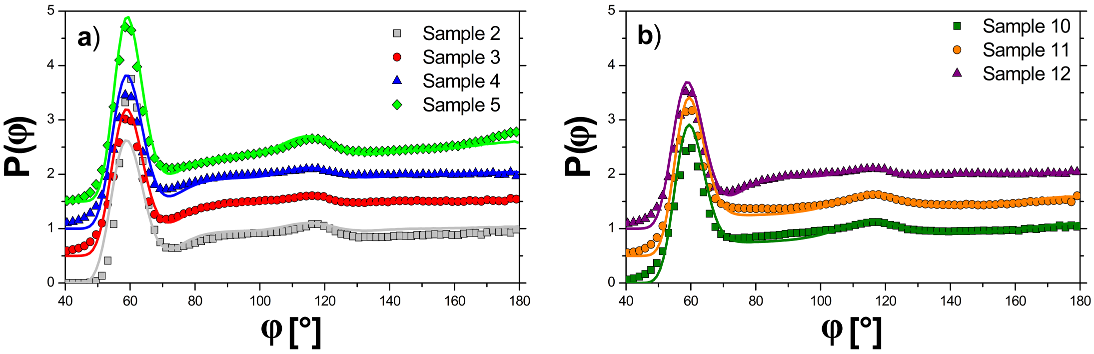

Figure 2.2 Bond angle distributions for gel samples with $c_\mathrm{p} \geq 0.8c^*$ of set 1 (a) and 2 (b). Experimental data (symbols) can be reproduced by simulations (lines) employing the effective interaction potential retrieved from fits to $g(r)$. Curves are vertically shifted for clarity. Figure and caption adapted from [6] by permission of The Royal Society of Chemistry.

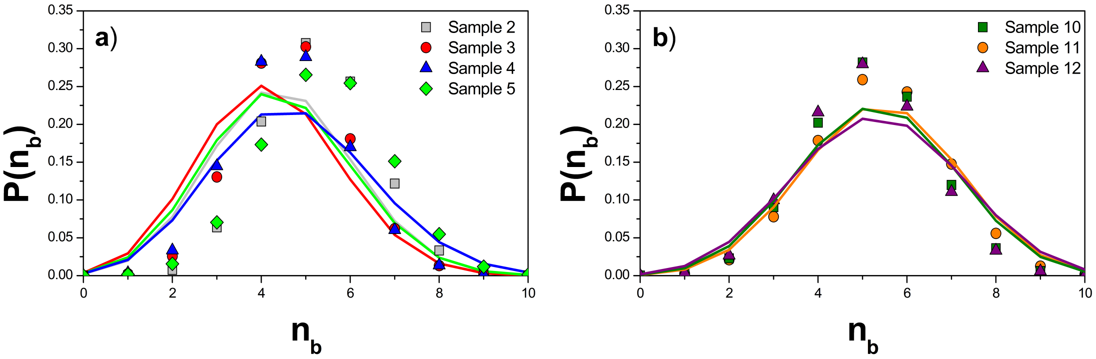

Figure 2.3 Distribution of the number of nearest-neighbours, $P(n_\mathrm{b})$, for samples of (a) set 1 and (b) set 2 as obtained by experiments (symbols) and MC simulations (solid lines). Figure and caption reproduced from [6] by permission of The Royal Society of Chemistry.

In conclusion, an effective interaction potential consisting of a combination of a square-well and a Yukawa potential can be used to reproduce structural characteristics of colloidal gels at intermediate volume fraction. However, due to the non-equilibrium, the effective potential depends on the sample composition and the preparation history. It can be determined by fitting the radial distribution functions of the gels.

2.1.2 Directed percolation in colloidal gels

We study the link between structure and dynamics in colloidal gels with lower volume fraction, exploiting effective interaction potentials. This sub-section summarizes Publication 2 (see section 3.2 and [9] for further details).

The experimental system is similar to that of the previous section: A colloid-polymer mixture of spherical PMMA colloids and polystyrene particles in a density-matched solvent mixture of *cis*-decalin and CHB. The effective size ratio between polymers and colloids was determined to be $q^* \approx 0.3$ according to GFVT. TBAC was added to screen the charges. The colloid volume fraction was $\Phi \approx 0.2$, while the polymer concentrations and salt concentrations were varied, tuning the strength of the attraction and the range of the repulsion, respectively. Experimental data obtained by confocal fluorescent microscopy was compared to Brownian Dynamics simulations of particles interacting via an attractive AOV plus repulsive Yukawa potential. The simulation parameters were chosen such that the average numbers of bonds calculated in the simulations match those of the experiments.

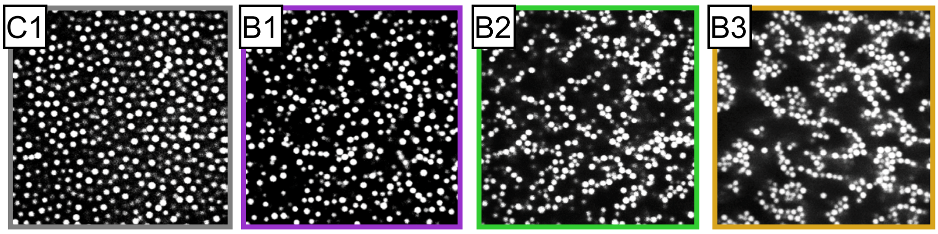

Figure 2.4 Two-dimensional confocal microscopy images of the four different states encountered: a fluid state (C1), a cluster fluid (B1), a continuous percolated gel (B2) and a directed percolated network (B3). Figure and caption adapted from [9] with permission of Springer Nature.

In experiments and simulations, four different structural states were observed: a fluid (sample C1), a cluster-fluid state (B1), a continuous percolated network (B2) and a directed percolated network (B3). In Figure 2.4, two-dimensional confocal microscopy images of the four different states are shown. The samples are characterized, e.g., by the average number of bonds per particle, $\langle n_\mathrm{b} \rangle$, and the bond number distribution. The dependence of $\langle n_\mathrm{b} \rangle$ on the strength of the AOV potential, $V_{\mathrm{D,min}}$, and the normalized inverse Debye length, $\kappa\sigma$, is presented in Figure 2.5. The coloured background and the filled dots indicate results of simulations and experiments, respectively. By increasing the strength of the AOV potential (path A) or by decreasing the range of the Yukawa potential (path B), $\langle n_\mathrm{b} \rangle$ increases continuously. A very sharp increase is found along path A at a total potential strength of $V_{\mathrm{min}} \approx -3.0 k_\mathrm{B}T$.

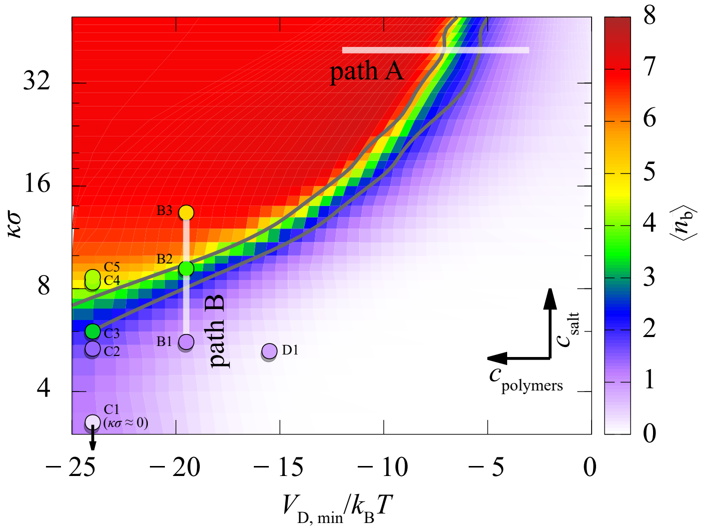

Figure 2.5 Average number of bonded particles, $\langle n_\mathrm{b} \rangle$, as a function of the potential depth $V_{\mathrm{D,min}}$ of the attractive AOV potential and the inverse screening length κ normalized by the inverse mean particle diameter σ^{-1}. The coloured background gives the values for the simulations, while the filled coloured circles represent the experiments. Paths A and B (white lines) with increasing polymer and salt concentration, respectively, are discussed in more detail. The lower and upper dark solid lines indicate the continuous and directed percolation transitions, respectively. Figure and caption adapted from [9] with permission of Springer Nature.

The bond angle distribution $P(\varphi)$ is examined for samples along paths A and B (see Figure 2.6). The first peak of $P(\varphi)$ at $\varphi \approx \pi/3$, which indicates triangular arrangements, grows continuously. At $V_{\mathrm{min}} \approx -3.0 k_\mathrm{B}T$, a second peak starts to develop at $\varphi \approx \pi/6$. For $V_{\mathrm{min}} < -3.0 k_\mathrm{B}T$, a pronounced peak at $\varphi \approx \pi$ is observed in experiments and simulations. This suggests a certain degree of directionality in the dense network filaments with large $\langle n_\mathrm{b} \rangle$. Thus, the system transverses from a continuous percolated network to a directed percolated network, consisting of connected directed clusters. In the former, pathways along the filaments might involve backward steps. In the latter, the system volume can be spanned by randomly directed pathways along gel filaments without any backward steps. Such pathways for a continuous and a directed percolated cluster are sketched in Figure 2.7a and complemented by typical microscopy images.

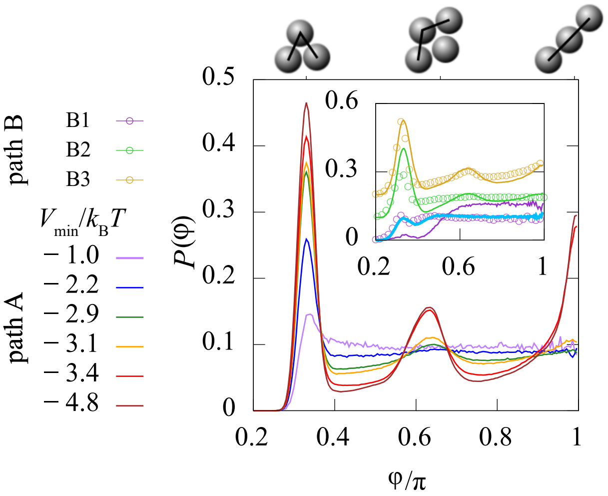

Figure 2.6 Bond angle distribution $P(\varphi)$ for the simulation data along path A with increasing depth $V_{\min}$ of the total interaction potential. Inset: $P(\varphi)$ along path B with decreasing Debye length. Circles and lines denote experimental and simulation data, respectively. The light blue line arises from simulations with parameters gained by an unconstrained fit. Above the plot, typical particle configurations for the certain bond angles are sketched. Figure and caption adapted from [9] with permission of Springer Nature.

For quantification, the probability $P(\Delta x)$ for a particle to be part of a directed path of projected length $l \geq \Delta x$ is calculated for simulations along path A (see lines in Figure 2.7b). For the experiments along path B, $P(\Delta x)$ (symbols in Figure 2.7 b)) is included, supporting the simulation results. It is shown that, for potential strengths $V_{\min} \lesssim -3.0 k_{\mathrm{B}}T$, the probability $P(\Delta x)$ does not decay, but forms a plateau. In contrast, the probability to be part of a continuous percolated path shows a plateau already at $V_{\min} \lesssim -2.2 k_{\mathrm{B}}T$ (see inset in Figure 2.7b). The values of $V_{\min}$ at the continuous and directed percolation transitions are defined to be the values at which $P(l_{\mathrm{box}}) = 0.2$ with the size of the simulation box l_{box}. The potential depths $V_P = -2.3 k_{\mathrm{B}}T$ and $V_P = -3.0 k_{\mathrm{B}}T$ for transitions to continuous and directed percolation, respectively, agree with the findings on the structural arrangement discussed above. Furthermore, for $V_{\min} = -3.1 k_{\mathrm{B}}T$, the slope of the decay of $P(\Delta x)$ is close to the critical exponent for directed percolation (see Figure 2.7) [10].

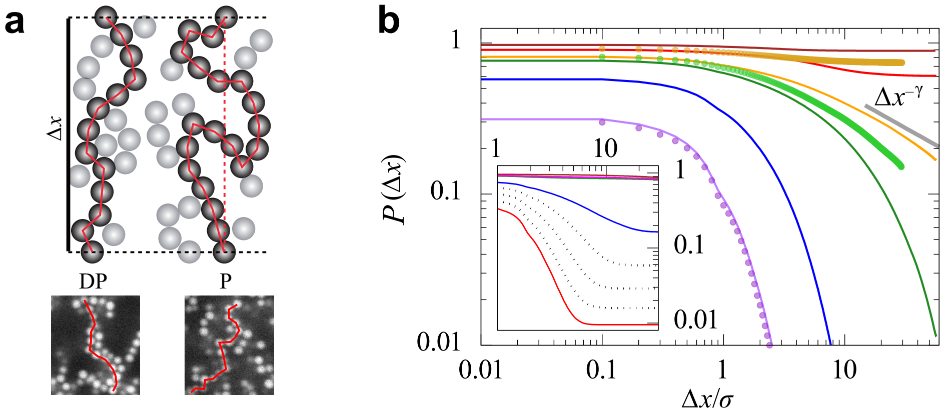

Figure 2.7 a) Two-dimensional sketch as well as images from experiments of (DP) a directed and (P) an undirected percolated cluster of length Δx. The path along a directed percolated cluster must not include backward steps in an arbitrarily chosen direction. b) Probability $P(\Delta x)$ for a particle to reside in a (main figure) directed and (inset) continuous cluster with a length larger than the minimum length Δx. Solid lines represent simulation data along path A and symbols experimental data along path B. Colours of the lines are defined in the legend of Figure 2.6. The grey solid line indicates the DP critical point, where the percolation probability is expected to be proportional to $\Delta x^{-\gamma}$ with $\gamma = 0.451$ [10]. Figure and caption adapted from [9] with permission of Springer Nature.

The directed percolation transition is connected to a slowing-down of the particle dynamics, as observed in the self-intermediate scattering functions. A dynamical arrest might occur deep in the region of directed percolation. Beyond the directed percolation transition, the system showed ageing effects in simulations, as shown by an increase of $\langle n_\mathrm{b} \rangle$ with waiting time after the initial quench. Furthermore, an effect similar to synaeresis was observed in directed percolation samples. Synaeresis appears in different systems, like gelatin [11] and protein gels [12], and indicates the contraction of a gel. In directed percolation samples, the detachment of the gel network from the bottom plate was observed in experiments and simulations. This finding and the connection to the directed percolation transition might be useful for industry, e.g., in food production and processing, and for measurement techniques, e.g., to explain wall slip in rheological measurements [9].

2.1.3 Dynamical arrest in binary mixtures

In the previous sub-section, it was shown that a connection between directed percolation and a slowing-down of the dynamics was found in colloid-polymer mixtures at intermediate Φ. Even in binary colloidal mixtures with a large size asymmetry, gelation can be one mechanism for dynamical arrest [13]. This sub-section contains a summary of Publication 3 (see section 3.3 and [13] for further details).

The colloid-colloid mixtures consist of two differently sized sterically stabilized PMMA spheres (radii $R_\mathrm{L} \approx 720 \pm 30$ nm and $R_\mathrm{S} \approx 65 \pm 10$ nm) with a size ratio $q \approx 0.09$. They are dispersed in a density-matched solvent mixture of *cis*-decalin and CHB and the added salt (TBAC) yields a a hard-sphere like particle interaction. The samples are prepared at a total volume fraction $\Phi_\mathrm{total} \approx 0.60$, while the fraction of the small particles, $x_\mathrm{s} = \Phi_\mathrm{s}/\Phi_\mathrm{total}$, is varied. Dynamics and structure of the large colloids is observed with confocal fluorescence microscopy.

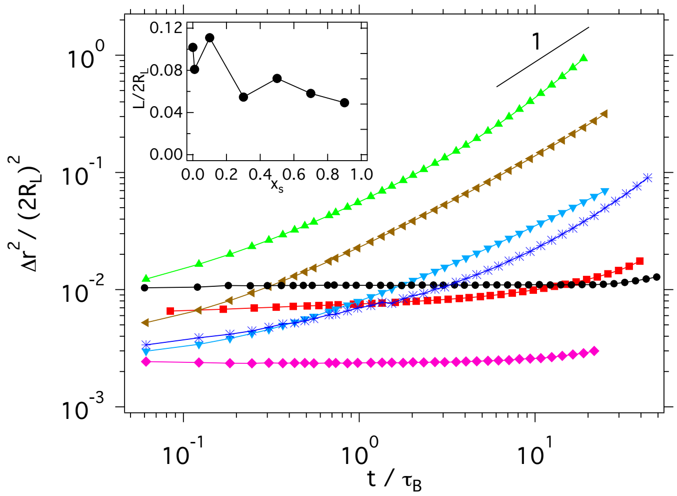

Figure 2.8 Mean squared displacements of the large spheres, $\Delta r^2/(2R_\mathrm{L})^2$, for samples with total volume fraction $\Phi \approx 0.60$, size ratio $q = 0.09$ and different compositions $x_\mathrm{s} = 0.0$ (●), 0.01 (■), 0.1 (▲), 0.3 (▼), 0.5 (◀), 0.7 ($*$), 0.9 (♦). Inset: Localization length $L/(2R_\mathrm{L})$ as a function of x_s. Reprinted figure and caption with permission from [13]. Copyright (2015) by the American Physical Society.

The MSD of the large colloids in a series of samples with increasing x_s is plotted in Figure 2.8. The degree of diffusivity for the different x_s follows a bimodal behaviour. For $x_\mathrm{s} < 0.1$, an extended plateau is formed in the MSD, while for $x_\mathrm{s} = 0.1$ the dynamics becomes diffusive. At $x_\mathrm{s} = 0.3$, again sub-diffusive behaviour occurs in the time window of the measurements. Further increasing the fraction of small particles, again increases the degree of diffusivity until dynamical arrest is found at $x_\mathrm{s} = 0.9$. This bimodal behaviour is also reflected in the localization length, $L/2R_\mathrm{L} = \sqrt{\Delta r^2(t_\mathrm{min})}/2R_\mathrm{L}$ (see inset of Figure 2.8).

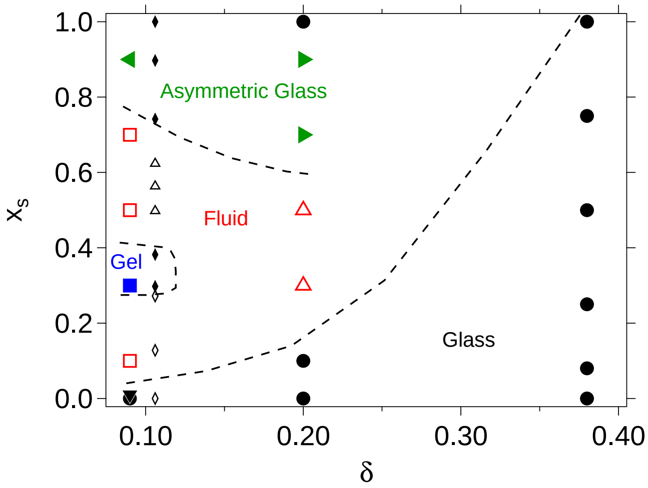

Figure 2.9 State diagram of samples with different compositions x_s and size ratios; $\delta = 0.09$ (present work), $\delta = 0.106$ [14], $\delta = 0.2$ and 0.38 [15–17]. Different arrested states are identified in the present work: repulsive glass (●), attractive glass (▼), asymmetric glass (◀) and gel (■). Open symbols indicate fluid states. In [14] fluids (△), fluid-crystal coexistence (◇), and amorphous solids (◆) were distinguished. Reprinted figure and caption with permission from [13]. Copyright (2015) by the American Physical Society.

The analysis of the distributions of displacements as well as the structural arrangement of the large colloids helped to identify the underlying mechanisms which lead to the dynamical arrest. The pair distribution function $g(r)$, the bond distribution, the cluster size distribution and the remoteness provide revealing information. The arrested states can be identified as a repulsive glass ($x_\mathrm{s} = 0.0$), an attractive glass ($x_\mathrm{s} = 0.01$), a gel ($x_\mathrm{s} = 0.3$) and an asymmetric glass ($x_\mathrm{s} = 0.9$). Especially in the attractive glass and the gel, the depletion interaction created by the small colloids is important. Yet, the mechanism of gel formation in binary colloidal mixtures is still debated. The results of this work are summarized in a state diagram and compared to other work at different size ratios (see Figure 2.9). All results agree and yield a more complete picture of the arrested states in colloidal binary mixtures at large size asymmetry.

2.2 Colloidal mixtures in a potential – extrinsic non-equilibrium

This section deals with concentrated binary mixtures in a sinusoidal potential, providing an extrinsic non-equilibrium. In the first sub-section, the experimental set-ups for the optical generation of the external potentials are described. In particular, an improved set-up with a Kösters prism was developed (cf. section 2.2.1). Then, the spatial arrangement of concentrated binary mixtures in a sinusoidal potential is analysed for different sample compositions and potential amplitudes (cf. section 2.2.2). Finally, results on the dynamics of concentrated binary mixtures in a sinusoidal potential are presented (cf. section 2.2.3).

2.2.1 Set-ups to create the external potential

A sinusoidal light field can be realized by an extended laser light field created by two interfering laser beams. Several designs for such an instrument have been reported (see [18] for an overview). In this sub-section, two experimental realisations are described. The first has been available for the major part of experiments, but has several disadvantages. Therefore, another improved set-up was designed and built up. Since it involves a Kösters prism as beam splitter, it is compact and thus more stable (see Publication 4 [19] and section 3.4 for further details).

The optical instrument used for the experiments in sub-sections 2.2.2 and 2.2.3 is described in detail in [20]. A laser beam (Coherent Verdi V5, wavelength λ= 532 nm) was directed onto a 50:50 beamsplitter providing two beams separated by an angle of 90°. Each of these beams was guided by a separate mirror onto a pair of movable mirrors, such that the two beams became parallel. They were focused by a lens and coupled into a self-built microscope by a dichroic mirror. They interfered in the sample plane under a crossing angle θ and formed a fringe pattern, i.e., a sinusoidal light field. By translating the movable pair of mirrors, the crossing angle θ and hence the fringe spacing $d = \lambda / (2 \sin(\theta/2))$ could be changed. The colloidal sample could be observed by the microscope which included a high numerical aperture microscope objective (Plan Apo VC 100, Nikon, numerical aperture 1.4) and a CMOS camera. As the two laser beams were separately guided by individual mirrors between splitting and recombining and the beam paths were rather long, the set-up was susceptible to changes in the ambient conditions and a high effort for alignment was needed.

Stability and operability could be improved by a design incorporating a Kösters prism as beam splitter and a commercial bright field microscope for observation. A Kösters prism is formed by two identical prisms which are glued together. As there is a semi-reflective silver coating applied between the prisms, the Kösters prism can be used as a beamsplitter. In several optical instruments, Kösters prisms are applied, e.g., in different types of interferometers [21–24] and particle velocimeters [25]. In our optical set-up, the Kösters prism leads to a reduction of the optical components which are necessary to split and recombine the laser beam, which improves stability, while the fringe spacing of the interference pattern is easily tunable. The optical set-up is sketched in Figure 2.10. The laser beam of a Verdi V-5 (Coherent, with wavelength $\lambda = 532$ nm and beam diameter 2.25 mm) is guided by 4 mirrors (M1-M4) to a 3× beam expander (BE). The expanded beam is directed by two further mirrors (M5, M6) to a Kösters prism (KP), which splits the beam in two parallel beams. A neutral density filter (ND) is introduced in the brighter beam to compensate for intensity differences. A lens (L1) recombines the beams with crossing angle θ and a dichroic mirror (D1) couples the beams in the light path of the microscope (Nikon Ti-E). In the sample plane, the laser beams interfere creating a sinusoidal light field. To protect the camera, the main part of the laser light is removed from the optical path behind the objective (Nikon, ELWD 40×, N.A. 0.60) by a dichroic mirror (D2) and a notch filter (NF).

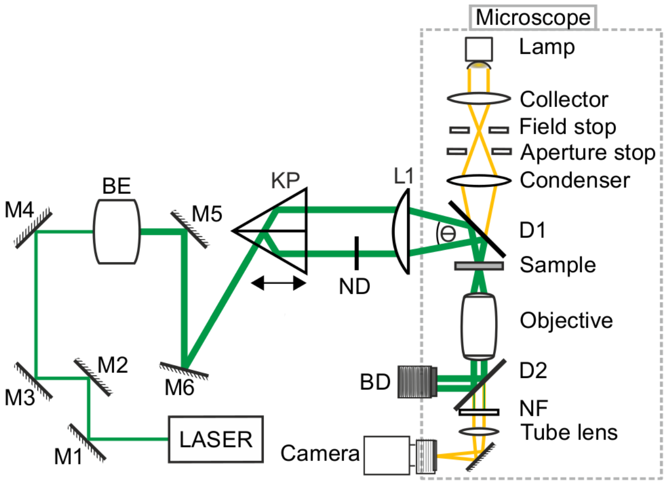

Figure 2.10 Schematic representation of the apparatus. Four mirrors (M1-M4) direct the beam to a beam expander (BE). Two further mirrors (M5, M6) guide the expanded beam to the Kösters prism (KP). The KP splits the beam into two parallel beams whose distance can be adjusted by translating the KP. A lens (L1) focuses the beams and, after being introduced into the light path of a microscope (grey dashed box) by a dichroic mirror (D1), combines them in the sample plane under an angle θ thus creating a fringe pattern. The beams are removed from the light path of the microscope by a dichroic mirror (D2) and collected by a beam dump (BD). A notch filter (NF) attenuates the remaining laser light. Reproduced from [19], with the permission of AIP Publishing.

By translating the Kösters prism along the propagation direction of the two parallel beams, the distance between the two beams and thus θ is varied. This is a simple and reliable method to tune the fringe spacing. This optical set-up creates a large interference pattern that fills the whole field of view of the microscope corresponding to about 212.1 × 169.3 $\mu\mathrm{m}^2$ for the magnification applied. The pattern is very stable. In particular, the fringe spacing $\langle d \rangle = (2.666 \pm 0.001)$ µm and the amplitude $\langle I_0 \rangle = (89.1 \pm 0.9)$ grey levels were found to have very small standard deviations over a period of 1.5 h. The high stability is due to the fact that the two laser beams are guided by the same components and have short path lengths. Thus, they are less sensitive to instabilities and changes of the ambient conditions. The instrument was successfully tested for the manipulation of colloidal particles with a sinusoidal potential [19].

2.2.2 Spatial arrangement of the particles

We studied the effect of a sinusoidal potential on the spatial arrangement of dense binary colloidal mixtures. The external potential induces order in the binary mixtures. Depending on the potential amplitude and the total area fraction, structural effects like homogenisation and partial demixing were observed [26]. They are caused by a competition between particle-particle and particle-potential interactions. This subsection summarizes the results of Publication 5 (see section 3.5 and [26] for further details).

The binary mixtures consist of Polystyrene particles with radii $R_\mathrm{s} = 1.05$ µm and $R_\mathrm{l} = 2.5$ µm dispersed in deionised water. The resulting size ratio $R_\mathrm{s}/R_\mathrm{l} = 0.42$ and the chosen stoichiometric ratio $1.1 \leq \xi \leq 1.4$ are close to the values for which a compact packing in a square lattice is predicted in the absence of an external potential [27]. The samples are exposed to a sinusoidal potential with an incommensurate fringe spacing $d \approx 4.1$ µm and different potential amplitudes. Due to their different sizes, the two particle species experience different potential amplitudes (see section 1.5).

We analysed measurements with increasing potential amplitude or total area fraction, keeping the other parameter approximately constant. Figure 2.11 shows snapshots of series C1, which correspond to the packing fraction $\eta \approx 0.73$ and increasing potential amplitudes $1.6\ k_\mathrm{B}T \leq V_{0,\mathrm{s}} \leq 8.0\ k_\mathrm{B}T$ and $3.5\ k_\mathrm{B}T \leq V_{0,\mathrm{l}} \leq 18\ k_\mathrm{B}T$ for the small and large particles, respectively. As both particle species prefer to occupy the potential minima, order perpendicular to the minima is induced. Along the potential minima instead, the samples remain fluid-like. Such a behaviour is typical for modulated liquids [28]. By increasing the potential amplitude, especially the large particles are more strongly confined to the potential minima, which reduces the available space in the minima for the small particles. Thus, more of them are found closer to the potential maxima. Furthermore, a partial demixing of the particle species can be found in the snapshots at increasing potential amplitude.

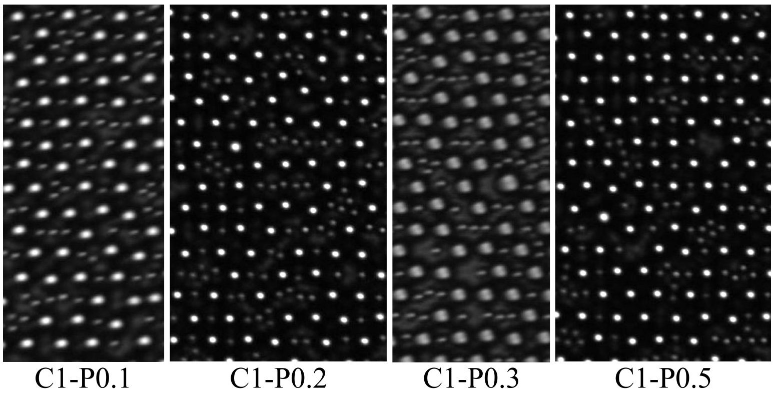
C1-P0.1 C1-P0.2 C1-P0.3 C1-P0.5

Figure 2.11 Images of samples with increasing amplitude of the external potential, V_0 (left to right), and constant area fraction $\eta \approx 0.73$ (series C1). The minima of the periodic potential are aligned horizontally. The small and large bright spots are the centres of the small and large particles, respectively. The images were adjusted in brightness and contrast for better visibility. Figure and caption taken from [26].

To characterize the spatial arrangement, we compute the pair distribution function parallel to the minima, $\hat{g}(r)$, separately for each particle species. $\hat{g}(r)$ accounts only for those surrounding particles found in a stripe parallel to the minima and of width d, which is centred around the particle under consideration. Results of $\hat{g}(r)$ for series C1 are shown in Figure 2.12. For the large particles, the first peak representing two neighbouring large particles, strongly increases with higher V_0, while the second peak only slightly increases, but shifts to smaller distances. Instead, the third peak at $r \approx 2R_\mathrm{s} + 2R_\mathrm{l}$ slightly decreases. A similar trend can be found for the small particles; the first and second peak at $r \approx 2R_\mathrm{s}$ and $r \approx 3R_\mathrm{s}$ rise, and the second peak is shifted to smaller r. This implies that particles of the same species prefer to be closer together and are prone to segregate.

The occupation probability $P(y)$ reveals information on the spatial arrangement perpendicular to the potential minima. It represents the probability of finding a particle at a certain distance away from the potential minima and, again, is calculated for each particle species separately (see Figure 2.13). Both particle species preferentially occupy the potential minima and become slightly more confined with increasing potential amplitude. Compared to the large particles, the small ones are more likely found close to the potential maximum, especially around $y \approx 0.3\,d$. This distance is

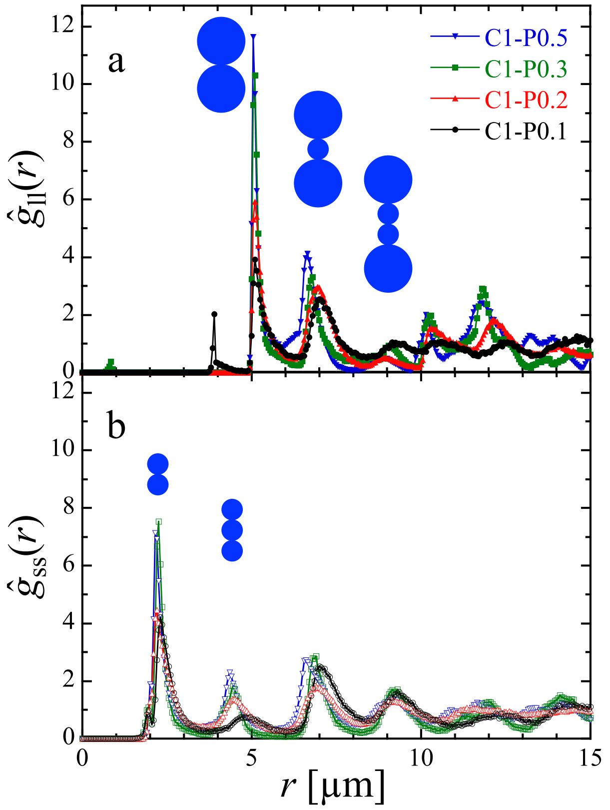

Figure 2.12 Pair distribution function parallel to the minima for (a) large, $\hat{g}_{\mathrm{ll}}(r)$, and (b) small particles, $\hat{g}_{\mathrm{ss}}(r)$. The amplitude of the potential, V_0, is varied (as indicated) while the area fraction is kept constant, $\eta \approx 0.73$ (series C1). Figure and caption taken from [26].

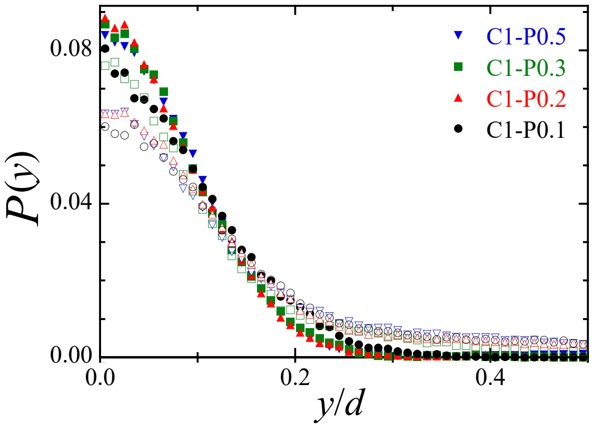

Figure 2.13 Occupation probability perpendicular to the minima, $P(y)$. The area fraction is kept constant at $\eta \approx 0.73$ (series C1) and the amplitude of the potential V_0 is varied (as indicated). The data referring to the large and small particles are indicated by closed and open symbols, respectively. Figure and caption adapted from [26].

consistent with the one found for doublets of small particles centred around the potential minima. The closer packing of the large particles and the formation of doublets of small particles were confirmed by the inspection of the angular bond distribution relative to the potential minima. Doublets of small particles are favoured due to the small size of the small particles compared to the fringe spacing.

If V_0 is kept constant and η is increased, another effect was observed. For low η, all particles fit into potential minima and rows of several particles of one species are formed. If the total area fraction is increased, the increased number of large particles reduces the space in the potential minima available for the small ones. Thus, the small particles tend to form doublets and triplets and are located closer to the potential maxima. This leads to a homogenization of the spatial arrangement. Moreover, we observed regions of kinetically arrested configurations, which are attributed to the restricted dynamics across the potential barriers. Furthermore, some of the observed configurations might be kinetically arrested, which is attributed to restricted dynamics across the potential barriers.

2.2.3 Dynamics of the particles

In addition to the spatial arrangement, we also studied the dynamics of binary mixtures in a sinusoidal potential in Publication 6 (see section 3.6 and [29] for details).

A binary colloidal mixture with a number ratio of about 1 of small ($R_s = 1.05$ µm) and large ($R_l = 2.5$ µm) particles and medium total area fraction $\eta \approx 0.57$ was exposed to periodic potentials with different amplitudes. The potential amplitudes $V_{0,\mathrm{l}}$ in the experiments ranged from $0\ k_\mathrm{B}T$ to $2\ k_\mathrm{B}T$ and the fringe spacing was held constant at $d = 5.2$ µm. The MSD of the large particles was extracted and compared to the dynamics of dilute monodisperse suspensions of large particles experiencing similar potentials. The results are normalized by the corresponding particle radius R and the Brownian time τ_B and presented in Figure 2.14. In x-direction, i.e., along the potential minima, normal diffusion was observed for all configurations (see inset of Figure 2.14). In y-direction, i.e., across the potential maxima, the shape of the MSD changes with potential amplitude and area fraction (Figure 2.14). For the particles in the dilute suspension (open symbols), a sub-diffusive regime at intermediate times is observed which becomes more pronounced with increasing potential amplitude. The MSD of the large particles in the binary mixture with $\eta \approx 0.57$, which are exposed to

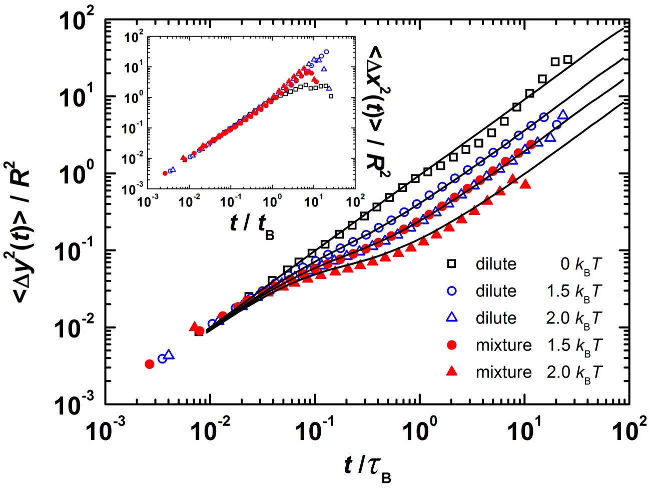

Figure 2.14 Particle dynamics, namely MSD across the barriers, i.e. in y direction (main figure), and along the valleys, i.e. in x direction (inset), of an individual dilute large particle ($R_l = 2.5$ µm, open symbols) and concentrated large particles in a binary mixture ($R_l = 2.5$ µm, $R_s = 1.05$ µm, total surface fraction $\eta \approx 0.57$ with an about equal number of large and small spheres, filled symbols), both in sinusoidally-varying periodic potentials with wavelength $d = 5.2$ µm and different amplitudes (as indicated). Lines represent Brownian Dynamics simulations of individual particles in a periodic potential with $V_{0,l}/k_BT = 0.0, 1.5, 2.0, 2.5$. Figure and caption adapted from [29] with kind permission of The European Physical Journal (EPJ).

a sinusoidal potential with potential amplitude $V'_{0,\mathrm{l}}$, is similar to the MSD of the dilute large particles experiencing a potential amplitude $V_{0,\mathrm{l}} \approx V'_{0,\mathrm{l}} + 0.5\ k_{\mathrm{B}}T$. The curves are consistent with Brownian Dynamics simulations of a single particle in a sinusoidal potential.

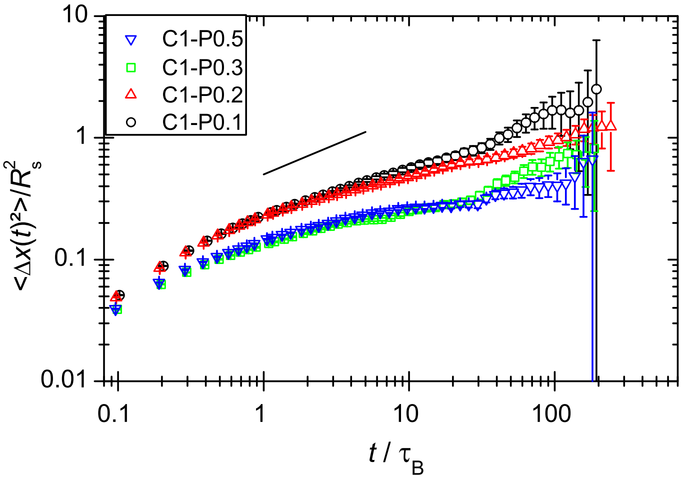

Figure 2.15 Normalized mean-squared displacement along the potential minima of small particles ($R_s = 1.05$ µm) in a binary mixture with total area fraction $\eta \approx 0.73$ and number ratio $1.1 \leq \xi \leq 1.4$. The mixture was exposed to sinusoidal potentials with fringe spacing $d \approx 4.1$µm and different potential amplitudes as indicated in the legend (series C1). The black line indicates the logarithmic slope of 0.5 characteristic for single line diffusion.

Instead, in a binary mixture with higher area fraction, $\xi \approx 0.73$, as the one in series C1 described in section 2.2.2, a slowing down of the dynamics is observed for both large and small particles even in the direction along the potential minima. Due to the higher area fraction and the incommensurable fringe spacing, the particles interact with each other more strongly. The normalized MSD is plotted in Figure 2.15. For low potential amplitudes and at intermediate times, the MSD shows a logarithmic slope close to 0.5 as expected for single file diffusion (black line in Figure 2.15). These experiments represent the first step to a systematic investigation of the interplay of particle-particle and particle-potential interactions on the dynamics in binary colloidal mixtures.

2.3 Outlook: Colloidal gels in potentials

This thesis focuses on non-equilibrium states: intrinsic non-equilibrium arising from particle-particle interactions and extrinsic non-equilibrium due to an external potential.

While the former leads to a disorder-disorder transition from a fluid to a gel, the latter induces order in the colloidal system at least along one dimension and thus can cause a disorder-order transition. Hence, the question emerges whether extrinsic non-equilibrium can lead to disorder-order transitions in intrinsic non-equilibrium states, e.g. a crystallisation of a gel by a sinusoidal potential. So far, ordering of gel structures could be achieved by applying oscillatory shear [8]. Simulations and theory predict another interesting phase, the so-called zebra-phase, for colloid-polymer mixtures with rather long-ranged attractions in sinusoidal potentials [30].

First qualitative tests reveal that the structure of a gel can be influenced by an external potential. One of the gel samples studied in Publication 2 [9] was exposed to a sinusoidal potential created by the set-up which exploits a Kösters prism (see section 2.2.1, [19]). In the beginning, a heterogeneous structure was observed (see Figure 2.16 left). After the light field was switched on, restructuring starts. Due to effects of fluorescence and scattering, the intensity of the laser had to be increased slowly in order to avoid a damage of the camera. The maximum laser power of the test, 800 mW, was achieved after about 30 minutes. It was observed that the particles in upper layers are pushed downwards, because of the radiation pressure, and out of the field of view. These dynamics resemble the the formation of two rollers in the upper and lower part of the field of view. It took about 6 hours until the bottom layer was clearly visible and started to rearrange into lines as shown in Figure 2.16, right. After switching off the external potential, the structure typically was frozen and no significant rearrangement was observed.

To understand the underlying mechanism in detail, quantitative experiments are needed. There are several challenges which one has to cope with. One important parameter is the fringe spacing d which has to be adjusted in a commensurable way. Furthermore, the strength of the potential has to be chosen such that it is strong enough to break or rearrange the gel, but so weak that it does not effect the sample chemically or thermally. This might lead to long run times of measurements. A third challenge is to find the balance between the degree of density matching for a stable gel and the degree of refractive index matching which affects the strength of the external potential. This thesis contributed to the understanding of the samples and tools for such kind of measurements and provides a basis for further investigations.

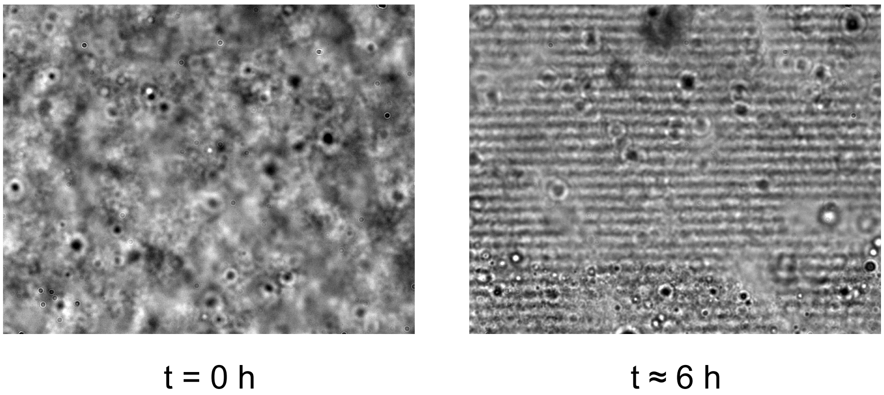

Figure 2.16 A colloidal gel consisting of PMMA colloids ($R \approx 860$ nm) with $\Phi \approx 0.2$, polystyrene ($R_\mathrm{g} \approx 65$ nm and concentration $c \approx 1c^*$) and TBAC in a mixture of *cis*-decalin and CHB was imaged with a bright-field microscope and exposed to a sinusoidal potential created with a laser power of up to 800 mW. In the beginning of the experiment (left), a heterogeneous structure was observed. After approximately 6 hours (right), the gel in the field of view is mainly reduced to few layers at the bottom which show a spatial arrangement similar to a fringe pattern.

Bibliography

[1] Stradner, A.; Sedgwick, H.; Cardinaux, F.; Poon, W. C. K.; Egelhaaf, S. U.; Schurtenberger, P. *Nature* **2004**, *432*, 492–495.

[2] Mani, E.; Sanz, E.; Bolhuis, P. G.; Kegel, W. K. *J. Phys. Chem. C* **2010**, *114*, 7780–7786.

[3] Zaccarelli, E. *J. Phys. Condens. Matter* **2007**, *19*, 323101.

[4] Royall, C. P.; Aarts, D. G. A. L.; Tanaka, H. *J. Phys. Condens. Matter* **2005**, *17*, S3401–S3408.

[5] Shah, S. A.; Chen, Y.-L.; Schweizer, K. S.; Zukoski, C. F. *J. Chem. Phys.* **2003**, *119*, 8747–8760.

[6] Capellmann, R. F.; Valadez-Pérez, N. E.; Simon, B.; Egelhaaf, S. U.; Laurati, M.; Castañeda-Priego, R. *Soft Matter* **2016**, *12*, 9303–9313.

[7] Smith, P. A. Colloidal Gels under Oscillatory Shear. Ph.D. thesis, University of Edinburgh, 2004.

[8] Smith, P. A.; Petekidis, G.; Egelhaaf, S. U.; Poon, W. C. K. *Phys. Rev. E* **2007**, *76*, 041402.

[9] Kohl, M.; Capellmann, R. F.; Laurati, M.; Egelhaaf, S. U.; Schmiedeberg, M. *Nat. Commun.* **2016**, *7*, 11817.

[10] Hinrichsen, H. *Adv. Phys.* **2000**, *49*, 815–958.

[11] Kunitz, M. *J. Gen. Physiol.* **1928**, *12*, 289–312.

[12] Mellema, M.; Walstra, P.; Van Opheusden, J. H. J.; Van Vliet, T. *Adv. Colloid Interface Sci.* **2002**, *98*, 25–50.

[13] Hendricks, J.; Capellmann, R.; Schofield, A. B.; Egelhaaf, S. U.; Laurati, M. *Phys. Rev. E* **2015**, *91*, 032308.

[14] Imhof, A.; Dhont, J. K. G. *Phys. Rev. Lett.* **1995**, *75*, 1662–1665.

[15] Sentjabrskaja, T.; Guu, D.; Lettinga, M. P.; Egelhaaf, S. U.; Laurati, M. *AIP Conf. Proc.* **2013**, *1518*, 206.

[16] Sentjabrskaja, T.; Babaliari, R.; Hendricks, J.; Laurati, M.; Petekidis, G.; Egelhaaf, S. U. *Soft Matter* **2013**, *9*, 4534.

[17] Sentjabrskaja, T.; Hermes, M.; Poon, W. C. K.; Estrada, C. D.; Castañeda-Priego, R.; Egelhaaf, S. U.; Laurati, M. *Soft Matter* **2014**, *10*, 6546.

[18] Durst, F.; Melling, A.; Whitelaw, J. H. *Principles and Practice of Laser-Doppler Anemometry*; Academic Press: London, 1976.

[19] Capellmann, R. F.; Bewerunge, J.; Platten, F.; Egelhaaf, S. U. *Rev. Sci. Instrum.* **2017**, *88*, 056102.

[20] Jenkins, M. C.; Egelhaaf, S. U. *J. Phys. Condens. Matter* **2008**, *20*, 404220.

[21] Darnedde, H. *Metrologia* **1992**, *29*, 349–359.

[22] Brown, M. S. *J. Phys. E: Sci. Instrum.* **1987**, *20*, 164 – 169.

[23] Ohtsuka, Y.; Nagaoka, F.; Tanaka, S. *Opt. Rev.* **1998**, *5*, 21–26.

[24] Láng, G. G.; Sas, N. S.; Vesztergom, S. *Chem. Biochem. Eng. Q.* **2009**, *23*, 1–9.

[25] Durst, F. *J. Fluids Eng.* **1982**, *104*, 284.

[26] Capellmann, R. F.; Khisameeva, A.; Platten, F.; Egelhaaf, S. U. *submitted to Phys. Rev. E* in June **2017**.

[27] Likos, C. N.; Henley, C. L. *Philos. Mag. Part B* **1993**, *68*, 85–113.

[28] Franzrahe, K.; Nielaba, P. *Phys. Rev. E* **2009**, *79*, 051505.

[29] Evers, F.; Hanes, R. D. L.; Zunke, C.; Capellmann, R. F.; Bewerunge, J.; Dalle-Ferrier, C.; Jenkins, M. C.; Ladadwa, I.; Heuer, A.; Castañeda-Priego, R.; Egelhaaf, S. U. *Eur. Phys. J. Spec. Top.* **2013**, *222*, 2995–3009.

[30] Vink, R. L. C.; Neuhaus, T.; Löwen, H. *J. Chem. Phys.* **2011**, *134*, 204907.

This page has been left intentionally blank.

PUBLICATIONS 3

3.1 Structure of colloidal gels at intermediate concentrations: the role of competing interactions

Journal: Soft Matter

Reference: *Soft Matter* **12**, 9303-9313 (2016)

Impact factor: 3.889

Authors: **Ronja F. Capellmann**, Néstor E. Valadez-Pérez, Benedikt Simon, Stefan U. Egelhaaf, Marco Laurati, and Ramón Castañeda-Priego

1st author

R. F. C. and B. S. conducted the experiments, N. E. V. P. performed the simulations, R. F. C., B. S. and N. E. V. P. analysed the data, M. L. and R. C. P. conceived and supervised the research and all authors contributed to the interpretation of the results, the comparison of the experimental and simulation results and the writing of the paper.

35% contribution of R. F. C. corresponding to 50% of the experimental effort.

Reproduced from [Capellmann, R. F.; Valadez-Pérez, N. E.; Simon, B.; Egelhaaf, S. U.; Laurati, M.; Castañeda-Priego, R.; *Soft Matter* **12**, 9303-9313 (2016)] by permission of The Royal Society of Chemistry.

This page has been left intentionally blank.

Soft Matter

PAPER

View Article Online
View Journal

Cite this: DOI: 10.1039/c6sm01822j

Structure of colloidal gels at intermediate concentrations: the role of competing interactions

Ronja F. Capellmann,[a] Néstor E. Valadez-Pérez,[b] Benedikt Simon,[a]
Stefan U. Egelhaaf,[a] Marco Laurati*[ab] and Ramón Castañeda-Priego*[b]

Received 6th August 2016,
Accepted 22nd October 2016

DOI: 10.1039/c6sm01822j

www.rsc.org/softmatter

Colloidal gels formed by colloid–polymer mixtures with an intermediate volume fraction ($\phi_c \approx 0.4$) are investigated by confocal microscopy. In addition, we have performed Monte Carlo simulations based on a simple effective pair potential that includes a short-range attractive contribution representing depletion interactions, and a longer-range repulsive contribution describing the electrostatic interactions due to the presence of residual charges. Despite neglecting non-equilibrium effects, experiments and simulations yield similar gel structures, characterised by, *e.g.*, the pair, angular and bond distribution functions. We find that the structure hardly depends on the strength of the attraction if the electrostatic contribution is fixed, but changes significantly if the electrostatic screening is changed. This delicate balance between attractions and repulsions, which we quantify by the second virial coefficient, also determines the location of the gelation boundary.

1 Introduction

Competing short-range attractive and long-range repulsive interactions between macromolecules are encountered in a vast number of systems in biology, medicine and materials science, namely protein solutions,[1–3] therapeutic monoclonal antibodies,[4–7] colloidal gels[8,9] and nanoparticle suspensions,[10] among others.

Mixtures of spherical colloids and non-adsorbing polymers dispersed in a solvent are often used as experimental models to investigate the behaviour of more complex systems with competing interactions. This is due to the fact that each contribution of the interaction potential can be tuned through the polymer concentration and size,[11] as well as the particle charge and salt concentration,[12] *i.e.* the degree of electrostatic screening. The short-range attractions arise due to entropy effects mediated by a second component,[13,14] *i.e.* the polymers, whereas long-range repulsions are caused by residual charges on the particle surface. In the presence of short-range attractions, fluid phases, fluid-crystal coexistence and crystalline phases can be observed in equilibrium,[15,16] while gels and glassy structures are found under non-equilibrium conditions.[8,11,16,17] In contrast, by reducing the degree of screening, additional states are observed, like fluids of clusters, gels and Wigner glasses.[18,19]

Gels are amorphous solids in which mechanical stability is achieved through the self-assembly of a load-bearing network structure. Since gels are non-equilibrium states, their properties depend on the preparation history. Different paths to the non-equilibrium gel states have been discussed. In the limit of purely attractive interactions, for example, arrested phase separation,[20] glass-like arrest,[21,22] rigidity percolation[23] and the formation of locally favoured structures[24] have been proposed. In the presence of electrostatic interactions, cluster aggregation into a percolating network[19,25–27] has been suggested, with recent results indicating the importance of directed rather than continuous percolation.[28]

A common feature of the gel state is structural heterogeneity with a characteristic length scale, which depends on the colloid volume fraction ϕ_c, the parameters controlling the interaction potential and, due to non-equilibrium conditions, the preparation procedure. Structures of cluster fluids and colloidal gels have been reported over a broad range of ϕ_c values and potential parameters, both in the moderately screened[19,25–27,29–31] and strongly screened[8,20,22,32–34] cases. For small ϕ_c, the structures observed in confocal microscopy experiments[20,28,35,36] were satisfactorily modelled using either an Asakura–Oosawa (AO) potential[13,14] in the strongly screened case[20] or a combination of the AO and Yukawa potentials in the moderately screened case.[28,35,36] Nevertheless, recent experimental results show that effects of anisotropic charge screening might lead to deviations from the behaviour predicted on the basis of this combination of potentials.[37] However, at intermediate and large $\phi_c > 0.2$, a direct comparison between simulations or theory and experiments has only been reported by Shah and coworkers,[38] where no

---

[a] *Condensed Matter Physics Laboratory, Heinrich Heine University, Universitätsstr. 1, 40225 Düsseldorf, Germany*
[b] *División de Ciencias e Ingenierías, Campus León, Universidad de Guanajuato, Loma del Bosque 103, Lomas del Campestre, 37150 León, Guanajuato, Mexico. E-mail: mlaurati@fisica.ugto.mx, ramoncp@fisica.ugto.mx*

satisfactory agreement between PRISM theory calculations and experimental structure factors could be obtained in the gel state. Hence, gelation in colloids with competing interactions has been studied extensively in the last few years,[28,35,36] but at intermediate and large concentrations several aspects can complicate a description of the structural properties of gel states in terms of the underlying interparticle potential that still are not fully understood. For instance, the possible importance of three-body interactions, the effects of crowding, as well as concentration effects on the polymer size have to be taken into account. Furthermore, the influence of the route leading to the final (non-equilibrium) gel structure might be important and hence, at the same sample composition, different gel structures might occur. In addition, typical experimental colloidal systems are polydisperse. Under these non-equilibrium conditions, only a description based on an *effective* interparticle interaction potential is possible and, furthermore, the potential is hard to accurately determine[39] through, for example, reverse Monte Carlo and integral equation techniques. In particular, these techniques have not been established yet for concentrated polydisperse colloidal systems.

In this contribution, we address the relationship between the effective interparticle interactions and the structure of the gel. As far as we are aware, here we provide for the first time a quantitative description of the effective interaction between particles that determines the local properties of the dispersion under non-equilibrium conditions. In particular, a combination of a short-range attraction and longer-range repulsion has been used to describe the effective interaction potential in intermediate volume fraction colloidal fluids and gels with $\phi_c \sim 0.40$. The parameters of the potential have been obtained by fitting only the simulated radial distribution function, $g(r)$, to the measured $g(r)$. Based on the determined potential, we have calculated further quantities describing the structure, such as the angular distribution function $P(\theta)$ and the nearest-neighbour distribution function $P(n_b)$, as well as the state diagram. As mentioned above, despite the difficulties in determining an effective interaction potential under non-equilibrium conditions, the structures of the colloidal fluids and gels appear to be accurately described based on the competing short-range attractive and longer-range repulsive interaction potential. We furthermore demonstrate that the short-range depletion attraction induced by the polymers can be reproduced by a short-range square-well potential, following the extended law of corresponding states.[40] Moreover, it is crucial to consider the electrostatic repulsion to properly reproduce the structure and the morphology of the gel structure although the investigated experimental systems were located in the regime between moderate and strong screening. The delicate balance between the attractive and repulsive contributions in the effective pair potential has a significant effect on the location of the gelation boundary.

2 Materials and methods

2.1 Experimental details

We have investigated mixtures of polymethylmethacrylate (PMMA) hard-sphere like particles fluorescently labelled with 7-nitrobenzo-2-oxa-1,3-diazole-methylmethacrylate (NBD-MMA) and linear polystyrene (PS, from Polymer Laboratories). The average diameter of the PMMA particles, $\sigma = 1720$ nm, and their polydispersity, which is about 7%, were determined by static and dynamic light scattering using very dilute samples. The radius of gyration of the PS (molecular weight $M_w = 3 \times 10^6$ g mol^{-1} with $M_w/M_n = 1.17$) in the solvent mixture used was estimated to be $r_g = 65.4$ nm.[41] In a dilute solution, this implies a polymer–colloid size ratio $\xi = 2r_g/\sigma = 0.076$. The effective polymer–colloid size ratio ξ^* (Table 1) was calculated according to the Generalised Free Volume Theory (GFVT),[42,43] taking into account the concentration dependence of the radius of gyration and the mesh size of the polymer in the semidilute regime.

Table 1 Colloid–polymer samples analysed in this work. ϕ_c^{exp} is the colloid volume fraction determined from the particle coordinates (*via* confocal microscopy) using the average diameter, c_s and c_p the concentrations of salt and polymer, respectively, c_p^{free} the polymer concentration in the volume not occupied by the colloids and ξ^* the resulting effective polymer–colloid size ratio, both estimated by Generalised Free Volume Theory.[42,43] Note that the two sets were prepared independently and might thus reflect different preparation paths

Sample	ϕ_c^{exp}	c_s [mM]	c_p [c^*]	c_p^{free} [c^*]	ξ^*
Set A					
1	0.39	4.9	0.0	0.0	—
2	0.41	4.5	0.8	1.5	0.04
3	0.39	4.5	1.0	1.8	0.03
4	0.39	4.5	1.0	1.8	0.03
5	0.40	4.5	2.0	3.4	0.02
Set B					
6	0.44	4.8	0.0	0.0	—
7	0.40	4.8	0.0	0.0	—
8	0.43	5.3	0.1	0.2	0.08
9	0.38	5.3	0.1	0.2	0.08
10	0.43	5.2	1.5	2.8	0.03
11	0.44	5.3	1.7	3.3	0.02
12	0.42	5.2	1.9	3.4	0.02

The particles and polymers were dispersed in a solvent mixture of *cis*-decalin and cycloheptylbromide, which closely matched the refractive index and the density of the colloidal particles. The density difference $\Delta\rho = \rho_c - \rho_s$ between the colloidal particles and the solvent mixture was estimated to be $\Delta\rho/\rho_c \lesssim 10^{-3}$, as no sedimentation was observed after centrifuging the sample for 24 h with 3500 rpm corresponding to an acceleration of about 1800g with g being the acceleration due to gravity. From this density difference, the gravitational Peclet number $\text{Pe} \equiv v_s\sigma/(2D)$, with v_s being the sedimentation velocity and D the free diffusion coefficient, was estimated to be $\text{Pe} \lesssim 7 \times 10^{-3}$ at 23 °C. In this solvent mixture, colloidal particles acquire a small charge, which is partially screened by the addition of tetrabutylammonium chloride (TBAC).[12,44] TBAC was added to the solvent mixture before preparing colloid and polymer stock solutions. Then, the solvent mixture was put on a flask shaker for at least 3 days to dissolve the salt.

The colloid stock solution was prepared by diluting a spun-down sediment, for which we initially assumed a volume fraction $\phi_c = 0.64$. Subsequently, the actual volume fraction of the samples was determined by confocal microscopy using the Voronoi construction to estimate the average volume fraction ϕ_c. Polymer stock solutions were prepared by adding the solvent mixture to a dry polymer and the polymer concentration c_p (mass/volume) of the solution was calculated from the weighed masses of the solvent and the polymer, and their corresponding densities. The polymer overlap concentration $c_p{}^*$ has been estimated by $c_p{}^* = 3M_w/4\pi N_A r_g{}^3$ with N_A being Avogadro's number. Colloid–polymer mixtures were prepared by mixing appropriate amounts of colloid stock with $\phi_c = 0.54$ and polymer stock solutions. Subsequently, samples were vigorously mixed using a vortex shaker and then homogenised in a flask shaker. The compositions of the samples are reported in Table 1. Note that the two sets A and B are prepared independently and hence the composition and the age of the solvent mixtures and in particular the particle charges and effective dissolved salt (TBAC) concentrations might actually be different as well as the details of the preparation path.

Microscopy measurements were performed within an hour after mixing to avoid effects due to ageing. Samples of set A were observed using a VT-Eye confocal unit (Visitech International) mounted on a Nikon Ti-U inverted microscope with a Nikon Plan Apo VC 100× (NA = 1.40) oil immersion objective. Samples of set B were imaged using a Nikon A1R-MP confocal unit on an inverted Nikon Ti-E microscope with a Nikon Plan Apo VC 60× (NA = 1.40) oil immersion objective. Between 25 and 30 stacks of 151 slices of 512 × 512 pixels each were recorded in z-steps of 200 nm corresponding to $54 \times 54 \times 30\ \mu m^3$ in the bulk of the sample. The stacks were acquired in less than 20 s per stack. Typically, the observation volume contained about 14 000 particles. Particle coordinates were obtained from images using standard routines,[45] including an algorithm to refine the particle coordinates.[46] Only particles whose centres were at least 4σ from the edges of the observation volume were considered in order to avoid boundary effects.

2.2 Effective interaction potentials and computer simulations

Attractive depletion interactions induced by non-adsorbing polymers were modelled using a short-range square-well (SW) potential.[47,48] This is simpler than the well-known Asakura–Oosawa (AO) potential.[13,14] Based on the extended law of corresponding states proposed by Noro and Frenkel,[40] we have shown that the phase diagrams obtained with the AO and SW potentials are similar[48] and can also be used to describe the phase behaviour of more complex systems, such as proteins.[49,50] The SW potential has the following form[47,48]

$$u_{ij}^{\mathrm{SW}}(r) = \begin{cases} \infty & r < \sigma_{ij} \\ -\varepsilon & \sigma_{ij} \le r \le \lambda\sigma_{ij}\,, \\ 0 & r > \lambda\sigma_{ij} \end{cases} \tag{1}$$

where r is the centre–centre distance between colloids of diameters σ_i and σ_j, with $\sigma_{ij} = (\sigma_i + \sigma_j)/2$, ε is the well depth given in units of the thermal energy k_BT and λ characterises the attraction range. The latter can be related to the effective polymer–colloid size ratio ξ^* of the experimental system, $\lambda \approx \sigma_{ij}/\sigma + \xi^*$ (Table 1).

The colloidal particles carried a net charge, which was screened by adding salt.[51–53] When the degrees of freedom of the small counterions are integrated out, the pure Coulombic interaction between colloids is replaced by a renormalised interaction potential of the Yukawa form[51–53]

$$u_{ij}^{\mathrm{sC}}(r) = Z_{ij}{}^2 \frac{\exp\left[-\kappa\left(r - \sigma_{ij}\right)\right]}{r/\sigma_{ij}}, \tag{2}$$

where κ is the inverse of the Debye length[51–53] and $Z_{ij}{}^2$ is the strength of the repulsion between the particles i and j in units of k_BT

$$Z_{ij}{}^2 = \frac{Q_i^{\mathrm{eff}} Q_j^{\mathrm{eff}}}{\left(1 + \kappa\sigma_{ij}/2\right)^2} \frac{\lambda_B}{\sigma_{ij}}, \tag{3}$$

with $Q_{i,j}^{\mathrm{eff}}$ being the net charge of species i or j in units of the electron charge and λ_B the Bjerrum length.[51–53] The definitions of the pair potentials, eqn (1) and (2), allowed us to include the size polydispersity.[54]

The total interaction between pairs of particles is described by a combination (not the sum) of the contributions in eqn (1) and (2). For separations larger than $\lambda\sigma_{ij}$, the interaction is purely repulsive and is given by eqn (2). At short distances, lower than $\lambda\sigma_{ij}$, we assume that the interaction is dominated by the attractive depletion interaction, which we model with a SW, eqn (1). Our choice of this simple effective model potential does not represent the true potential of the physical systems we are investigating. However, as will be shown, it is able to reproduce the experimental structures and allows us to separately study the contribution of the repulsion and of the attraction.

We have performed Monte Carlo (MC) computer simulations in the canonical ensemble (NVT) for systems with $N = 2916$ particles having 7% of polydispersity. The latter was taken into account by considering five populations of particles whose size and number fraction follow a discrete Schulz distribution,[54,55] see Fig. 1. The number fraction, $x_i = N_i/N$, is the relative population of particles with diameter σ_i; N_i and N are the number of particles of species i and the total number of particles in the system, respectively. The standard Metropolis algorithm was used to generate and accept new particle configurations.[56,57] We ran MC simulations for 5×10^8 MC steps to reach a steady-state and additional 5×10^8 MC steps to measure the structure. In both stages, new configurations were accepted with a probability of 30%. In all simulations, thermal equilibrium was reached after a few millions of MC steps.

3 Results

3.1 Structure of the fluids without polymers

The spatial arrangement of particles around a central one is characterised by the radial distribution function, $g(r)$. Fig. 2a shows the experimental $g(r)$ determined for samples without polymers (samples 1, 6 and 7, see Table 1). In all cases, it shows the structural characteristics of a fluid, *i.e.* a first peak roughly corresponding to the average particle distance $(\pi/6\phi_c)^{1/3}\sigma \approx 1.08\sigma$, and

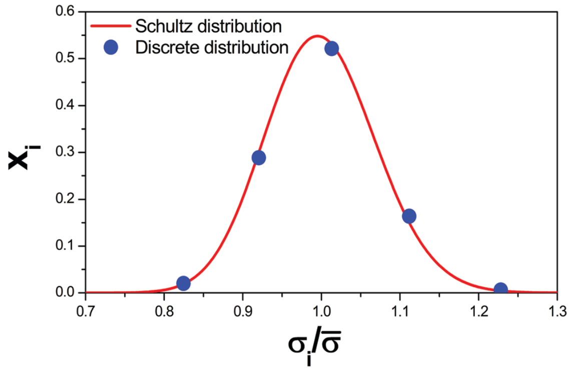

Fig. 1 Number fraction x_i of particles with diameter σ_i following a Schulz distribution (solid line) and discrete distribution with five populations used in the Monte Carlo simulations (symbols), respectively.

successive peaks that correspond to further shells of neighbours, until correlation is lost at larger distances where $g(r)$ tends to 1.

The experimental $g(r)$ is compared to MC simulations for hard-spheres with a polydispersity of about 7%. Simulating hard-sphere systems at high concentrations is difficult because non-overlapping initial configurations need to be generated. In a monodisperse system, one can initiate simulations with particles in a crystalline array, which melts during the simulation with no overlaps occurring between particles. In a polydisperse system, however, some big particles might be difficult to place in a non-overlapping configuration. To overcome this technical problem, the hard-sphere potential has been replaced by the potential $u_{ij}^{\mathrm{HS}}(r) = (r/\sigma_{ij})^{-10000}$, where the large exponent results in a hard-sphere-like interaction. Fig. 2a shows that the agreement between simulations and experiments is not satisfactory, especially at short separations, $r \approx \sigma$. The average distance, described by the position of the first peak in $g(r)$, is about σ in the simulations, while it is slightly larger in the experiments. This indicates that the effective size of the particles is larger than σ. This can result from residual charges. Therefore, we have also performed MC simulations including a repulsive Yukawa potential, see eqn (2). The parameters of the Yukawa potential were estimated using the Poisson–Boltzmann equation and assuming that all particles have the same diameter.[51] This led to a prefactor $Z_{ij}^{2} = 6.0$ and screening parameter $\kappa\sigma = 15$ and 30, corresponding to an effective charge $Q^{\mathrm{eff}} \approx 273$ and 514, for sets A and B, respectively, see Table 2. This effective charge is consistent with previous measurements.[36] The screening $\kappa\sigma$ differs by a factor of 2, although the salt concentration c_s in both sets is similar. This might be related to the fact that the dissolution of salt in the solvent mixture is limited and slow, and therefore different amounts of salt might actually be dissolved in the two sets, despite the added salt concentrations c_s being comparable. Furthermore, differences in the dissolution process imply different preparation paths which might affect the observed gel structure. Nevertheless, the excellent agreement between experiments and simulations (Fig. 2b) indicates that the amount of particle charge has an important effect on the structure of the dispersion due to the long range of the electrostatic interactions in organic solvents having small relative permittivities. The electrostatic interaction also affects the subsequent peaks, which are now well-reproduced. This indicates the need to include the electrostatic contribution (eqn (2)) together with the hard-sphere interaction to correctly represent the repulsive interactions between colloids.

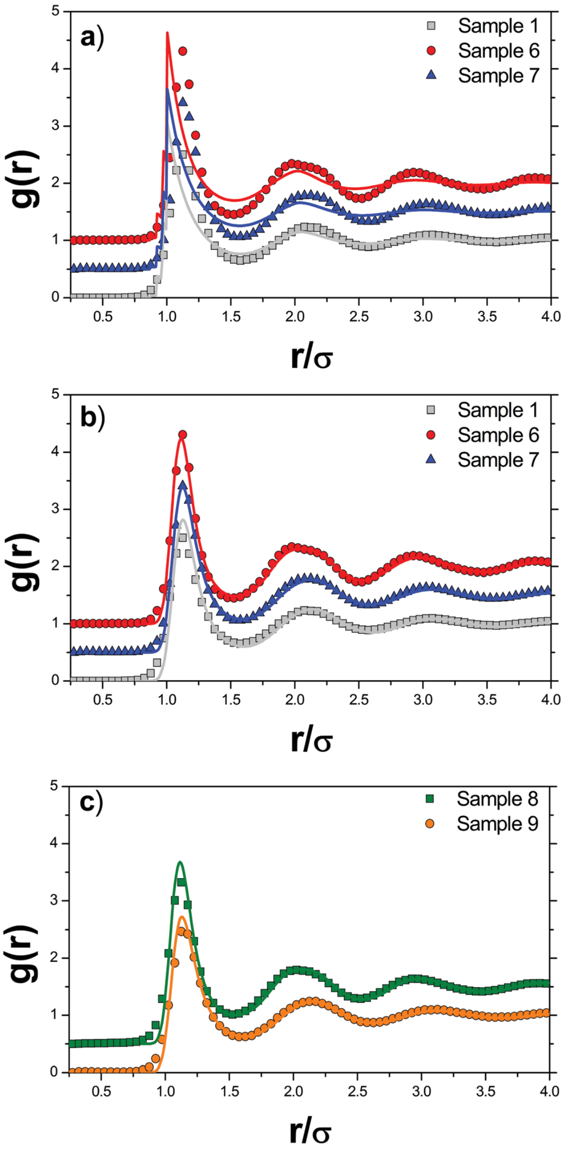

Fig. 2 (a) Radial distribution function $g(r)$ for polymer-free samples 1, 6 and 7 (symbols, Table 1) and MC simulation results for polydisperse hard-spheres (solid lines). (b) The same as in (a) but with simulation results for charged polydisperse particles interacting through a Yukawa pair potential (eqn (2)). (c) Samples 8 and 9 with low polymer concentration (symbols, Table 1) and simulation results for particles interacting through a SW (eqn (1)) and Yukawa pair potential (eqn (2)) (solid lines). Curves are vertically shifted for clarity.

Table 2 Values used in the MC simulations to describe the experimentally determined $g(r)$ for the samples given in Table 1. Average effective hard-sphere diameter σ_c, attraction strength ε, attraction range λ, effective charge Q^{eff} and inverse screening length κ. * indicates that the interaction between particles was modelled by a pure repulsive potential, resulting in B_2* values larger than 1

Sample	σ_c/σ	ε	λ	Q^{eff}	$\kappa\sigma$	B_2*
Set A						
1*	1.0	0.0	—	514	30	1.25
2	0.93	0.83	1.03	273	15	0.64
3	0.93	0.83	1.03	273	15	0.64
4	0.93	0.91	1.03	273	15	0.58
5	0.93	1.11	1.03	273	15	0.40
Set B						
6*	1.0	0.0	—	514	30	1.25
7*	1.0	0.0	—	514	30	1.25
8*	1.0	0.0	—	514	30	1.25
9*	1.0	0.0	—	514	30	1.25
10	0.97	1.33	1.07	514	30	−0.31
11	0.97	1.33	1.07	514	30	−0.31
12	0.97	1.43	1.07	514	30	−0.44

We assume that the parameters of the Yukawa potential remain constant upon addition of the polymer, although at larger polymer concentrations the high packing of particles in the gels might modify the charge distribution. However, the very good agreement obtained between experiments and simulations shown below supports the validity of this assumption.

3.2 Structure of the fluid at low polymer concentrations

The structure of samples containing a small amount of polymer, $c_p/c_p{}^* = 0.1$ (samples 8 and 9, Fig. 2c), was also experimentally determined. Due to the presence of the polymer, attractive interactions are present and result in a non-zero, although very small, ε. Nevertheless, $g(r)$ is very similar to that of the purely repulsive systems without the polymer. This suggests that repulsive interactions dominate at low polymer concentrations. In fact, $g(r)$ can be well reproduced in simulations using only the repulsive Yukawa potential with the same parameters as for the case without the polymer (except $\varepsilon = 0$; data not shown).

3.3 Structure of the gel at high polymer concentrations

3.3.1 Radial distribution function $g(r)$.

Fig. 3 shows $g(r)$ for samples with high polymer concentrations $c_p/c_p{}^* \geq 0.8$. The presence of significant attractions completely changes the shape of $g(r)$ compared to the samples without and with only a small amount of polymer (Fig. 2). The first peak becomes sharper. The position of the first minimum of $g(r)$, which appears at $r/\sigma \approx 1.1$, can be linked to the effective range of the attraction, characterised by $\lambda - 1$; the minimum is less pronounced for set B than for set A. The broad second peak is a typical feature of gels and is related to the broad distribution of distances to particles in the second shell caused by the heterogenous structure of the local clusters.[29,32] Beyond the second maximum, *i.e.* for distances beyond about 2.5σ, $g(r)$ quickly approaches unity, whereas the oscillations extend to much larger r for the samples without or with less polymer.

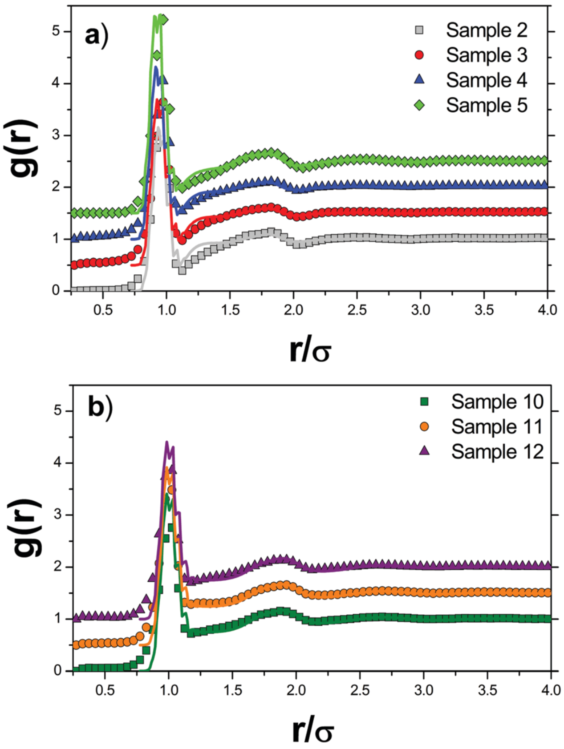

Fig. 3 Radial distribution function $g(r)$ for samples with high polymer concentrations (as indicated, Table 1), obtained in experiments (symbols) and MC simulations (solid lines). Curves are vertically shifted for clarity.

In MC simulations, the effective interparticle interactions were modelled through the attractive SW potential, eqn (1), and the repulsive Yukawa potential, eqn (2). The values of the parameters characterising the Yukawa contribution are taken from the samples without the polymer ($\kappa\sigma = 15$ and 30, $Q^{\text{eff}} \approx 273$ and 514 for sets A and B, respectively, see Table 2). For the range of the attractions, average values $\xi^* \leq \xi' \leq \xi$ are taken resulting in a constant $\lambda = \sigma_{ij}/\sigma + \xi'$ for each set (Table 2). Several simulations have been performed with different values of the depth of the square well ε to find the best fit to the experimental $g(r)$. Samples with high polymer concentrations cannot be accurately simulated using an average diameter $\sigma = 1720$ nm but, to match the experimental $g(r)$, a slightly smaller effective diameter σ_c was considered, which is within the uncertainties of the experimental value and the chosen size distribution. The reduction of the effective diameter in the gels seems to indicate a certain degree of softness of the particles. We have hence considered a soft-core potential represented by $(r/\sigma_c)^{-9}$ to model this degree of softness. The stronger reduction of the diameter in set A than B is associated with less screening of the electrostatic interaction, possibly indicating a relationship between the two quantities. The fitted values of σ_c and ε are reported in Table 2. With these values, the MC simulations agree well with the experimental results over the whole range of r values. This indicates that the effective potential reproduces the experimental structure at short and long interparticle separations. Table 2 also indicates that the well depth ε is a function of polymer, c_p, and, to some extent, colloid, ϕ_c, concentration.

3.3.2 Effective colloid–colloid interaction potential $u(r)$. The interactions in the colloid–polymer mixtures were approximated by a combination of a SW and Yukawa potential, given by eqn (1) and (2), respectively, where the hard-sphere infinite repulsion at contact in the SW potential has been slightly softened due to technical issues as discussed above. The parameters of the potentials have been determined by fitting the corresponding $g(r)$ to the experimental data (Fig. 2, 3 and Table 2). Note that these are effective interaction potentials. They depend on the sample compositions but, due to the non-equilibrium nature of gels, are also affected by the preparation histories. A different sample preparation procedure might lead to a different gel structure, here characterised by $g(r)$, and hence a different effective interaction potential, although the final sample composition might be identical. The dependence on the preparation path is, at least partially, responsible for the different fit parameters of sets A and B, although their compositions are not very different.

The combination of SW and Yukawa potential is compared to the potential of mean force, $w(r) = -k_BT\ln g(r)$ (Fig. 4a). This potential is an accurate representation of the effective potential between pairs of colloidal particles, $u(r)$, in a low concentration system.[58] At higher concentrations, $w(r)$ is a crude approximation of the effective potential $u(r)$ but gives some insights into its features. The main features of $w(r)$ are reproduced by the combination of a SW and Yukawa potential.

As an example, Fig. 4b displays the optimum effective potentials that describe the local structures of samples 5 (set A) and 12 (set B), respectively. The potential used for sample 5 shows a larger barrier and longer-range repulsion compared to sample 12. This illustrates the different amounts of residual charges and screening in the two sets as well as a possible effect of the preparation procedure (Table 2).

3.3.3 Angular distribution function $P(\theta)$. In addition to $g(r)$, it is interesting to determine the angular distribution function $P(\theta)$. This function considers the angle θ between the centre–centre lines of three nearest neighbours. Particles are considered nearest neighbours if their centre–centre distance is smaller than the distance to the first minimum of $g(r)$, which is $r = 1.1\sigma$. The experimentally obtained $P(\theta)$ values are shown in Fig. 5 together with the corresponding simulation results. The peak at $\theta \approx 60°$ indicates that particles tend to form structures with a triangular geometry. We have shown in previous work that in the presence of short-range attractions

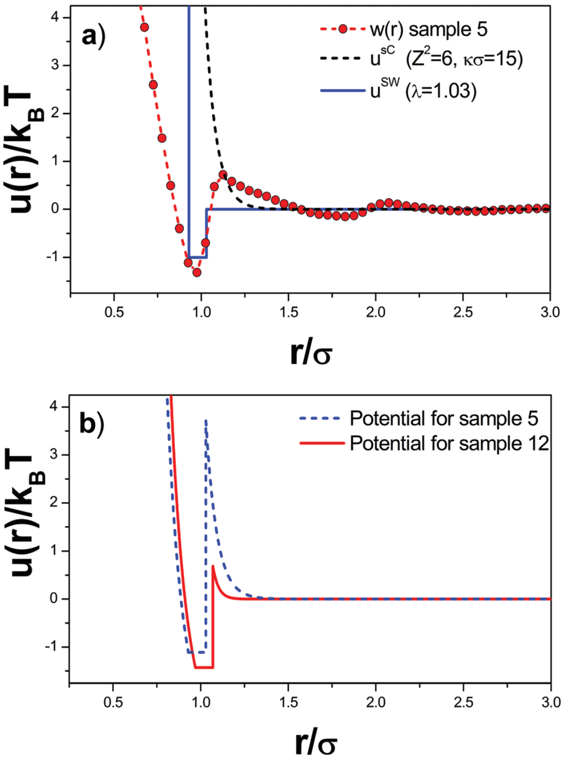

Fig. 4 (a) Square well $u^{SW}(r)$ (solid line), eqn (1), and Yukawa $u^{sC}(r)$ (dashed line), eqn (2), potentials and potential of mean-force $w(r) = -k_BT\ln g(r)$ (dashed-symbol) of sample 5. (b) Effective colloid–colloid interaction potentials $u(r)/k_BT$ in samples 5 (solid line) and 12 (dashed line), see Table 1.

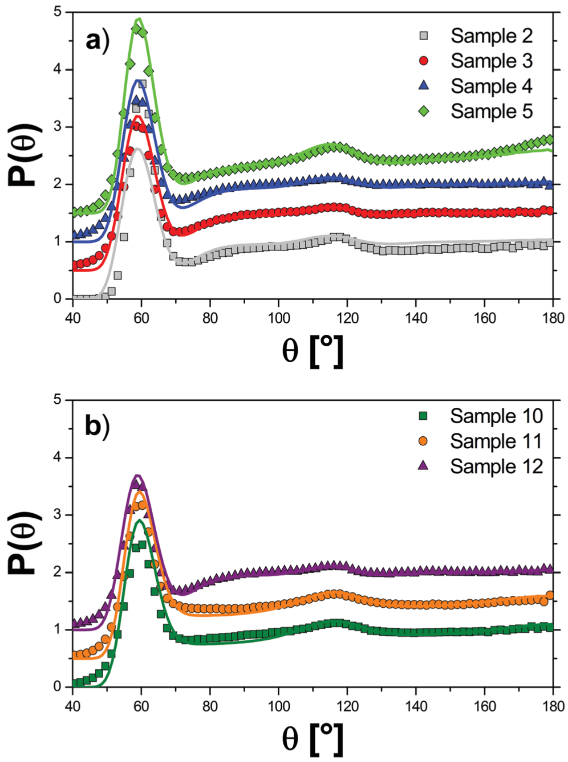

Fig. 5 Angular distribution function $P(\theta)$ for samples with high polymer concentrations (as indicated, Table 1) obtained in experiments (symbols) and MC simulations (solid lines). Curves are vertically shifted for clarity.

and long-range repulsions, these structures are energetically favoured over others.[59] A second smaller peak is located at $\theta \approx 120^\circ$, a value that corresponds to a structure where particles lie on two triangles that share an edge.

3.3.4 Nearest-neighbour distribution function $P(n_b)$. To gain more insight into the local structural features of the gel and its heterogeneity, we have also determined the nearest-neighbour distribution $P(n_b)$; it represents the probability for a particle to have n_b neighbours being closer than the cutoff distance $r = 1.1\sigma$. The average value $\langle n_b \rangle$ quantifies how crowded the local environment of a particle is. Previously, it was shown[23] that in a purely attractive system $\langle n_b \rangle = 2.4$ at the gel transition.

The nearest-neighbour distributions $P(n_b)$ are shown in Fig. 6a and b. One observes that for samples with a high polymer concentration, $c_p/c_p{}^* \geq 0.8$, the shape of the distribution is essentially identical and $\langle n_b \rangle \approx 5$, *i.e.* larger than the one found in purely attractive (sticky) particles.[23] This indicates local clusters with a highly compact shape. This also implies that the competing interaction potential plays a twofold role: first, the short-range attraction induces particle clustering and, second, the long-range repulsion stabilises the clusters towards network formation, *i.e.* limits their size, and avoids nucleation and subsequent crystallisation.[59] In contrast, in the presence of only a small amount of polymer, as in samples 8 and 9, the structure is characterised by a small number of neighbours, $\langle n_b \rangle \approx 2$ (data not shown). It is interesting to note that the neighbour distributions of sets A and B are comparable, despite the structural differences indicated by $g(r)$ and $P(\theta)$. The aforementioned trends can also be seen in snapshots of samples 1 (no polymer) and 5 (highest polymer concentration), displayed in Fig. 6c, with the number of neighbours indicated by the colour. Sample 5 contains a percolated network, *i.e.* a colloidal gel, whereas there is no network in sample 1. Fig. 6c also illustrates the heterogeneity of the particle distribution in the sample.

The structure of a system can also be visualised by the backbone or network formed by the nearest neighbours. In Fig. 7, slices with thickness 4σ of samples 1, 2 and 5 are considered and nearest neighbours are connected by a line. In sample 1, the connectivity is very low, as expected in the absence of attractions. In samples 2 and 5, particles form triangular structures that are connected into a sample spanning network, as previously reported.[25] Besides, applying the same criterion as the one proposed in ref. 28, we found evidence that the structures of samples 2 and 5 represent directed percolated networks, as recently proposed for gels with a lower colloid concentration[28] and a smaller $\langle n_b \rangle$. Samples 9 and 12 show similar results to samples 1 and 5: sample 9 presents a liquid-like structure, as indicated in Fig. 3, whereas a backbone is present in sample 12, which corresponds to a directed percolated network and presents components that form also triangular structures (data not shown).

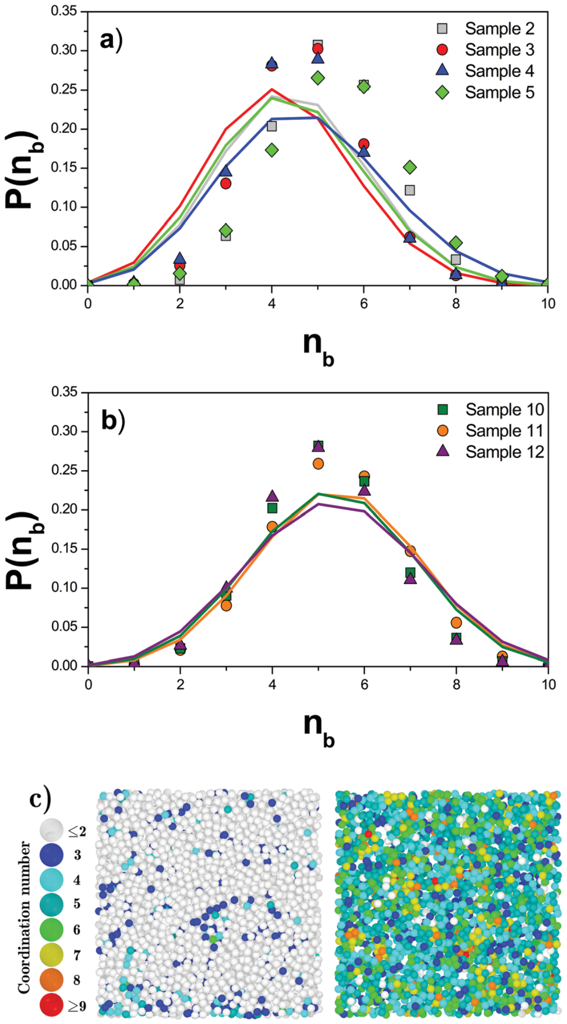

Fig. 6 Distribution of the number of nearest-neighbours, $P(n_b)$, for samples of (a) set 1 and (b) set 2 as obtained by experiments (symbols) and MC simulations (solid lines). (c) Snapshots of slices of samples 1 (left) and 5 (right) as obtained by simulations. The number of neighbours or the coordination number is indicated by the colour of the colloids.

3.4 State diagram

Since gels are out of equilibrium states, their structure also depends on the kinetic path followed to reach the gel state. It is therefore interesting to consider how the samples we studied can be located with respect to the equilibrium and the non-equilibrium state diagrams available from the literature, and obtained for the specific parameters of our system. Note, however, that care has to be taken when state diagrams based on parameters determined under equilibrium conditions are compared with state diagrams based on parameters of effective interaction potentials determined under non-equilibrium conditions, as in the present case.

We start considering the state diagram of colloid–polymer mixtures with purely attractive interactions.[11,16,48] The topology of the state diagram in the $c_p/c_p{}^*$ *vs.* ϕ_c plane depends on the polymer–colloid size ratio ξ; we only consider $\xi \sim 0.1$ (Fig. 8) and $\phi_c \leq 0.5$, which are the parameters relevant for our study. Previous studies showed that while at small polymer concentrations

3.1 Structure of colloidal gels at intermediate concentrations: the role of competing interactions

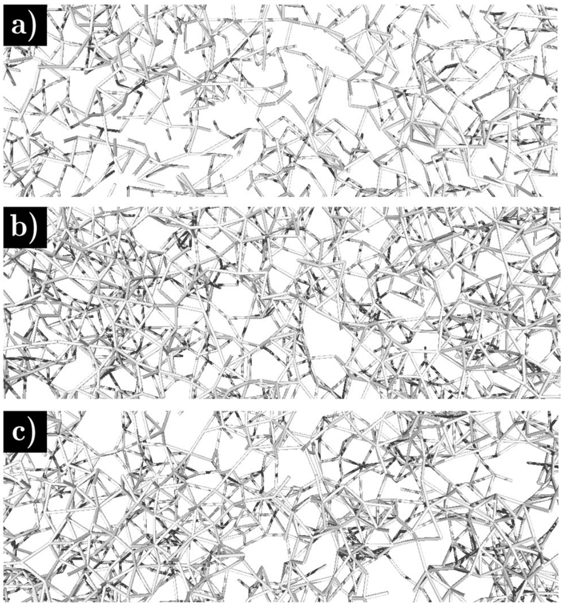

Fig. 7 Network of nearest neighbours as obtained by MC simulations. The centres of nearest neighbours are connected by lines. Samples (a) 1, (b) 2 and (c) 5 are shown.

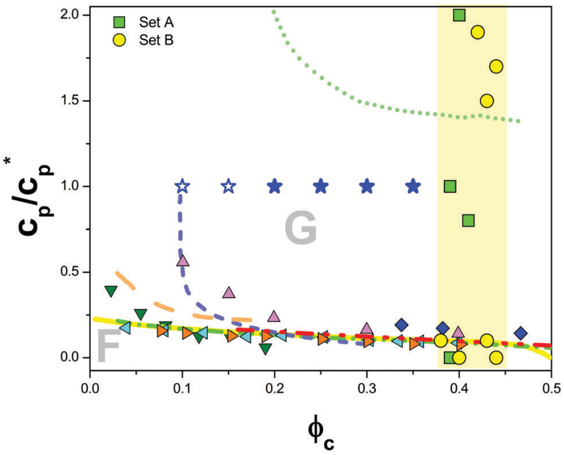

Fig. 8 State diagram of a colloid–polymer mixture with a size ratio $\xi \sim 0.1$ in the polymer concentration, $c_p/c_p{}^*$, *vs.* colloid volume fraction, ϕ_c, plane. Region covered by our samples (■: set 1, ●: set 2) is highlighted by a yellow background (Table 1), 'F' indicates fluid states and 'G' gel states, ☆ and ★: additional simulation results for $c_p/c_p{}^* = 1.0$ and different ϕ_c values where open (full) symbols indicate fluid (gel) states. Binodal line obtained using the Generalised Free Volume Theory[42,43] for $\xi = 0.076$ (–··–). For comparison, datasets from the literature are included: equilibrium fluid–solid coexistence for $\xi = 0.08$[16] (—), experimentally determined gelation points in purely attractive systems with $\xi = 0.061$[38] (◀), $\xi = 0.090$[38] (▶), $\xi = 0.06$[60] (▲), and $\xi = 0.059$[20] (– – –) and in systems with competing interactions with $\xi = 0.021$[18] (▼), $\xi = 0.13$[25] (– – –), and $\xi = 0.19$[19] (·····), experimentally observed attractive glasses with $\xi = 0.09$[61] (◆), mode-coupling predictions for the gelation boundaries for $\xi = 0.08$[21] (–·–·–).

the system is in a fluid state, with increasing polymer concentration a coexistence between fluid and crystals is observed (the solid line represents the fluid/solid coexistence boundary for $\xi = 0.08$[16]). Gas–liquid coexistence occurs within the fluid–solid coexistence region:[16] we report in Fig. 8 the binodal line (double-dotted-dashed line), calculated using the Generalised Free Volume Theory[42,43] for the size ratio of our samples, $\xi = 0.076$. We additionally report the boundaries to non-equilibrium gel states determined by different experiments and theories. For small volume fractions ($\phi_c < 0.2$), we show the gelation boundary obtained by Lu *et al.*[20] (large-dashed line, $\xi = 0.059$): in this work it is proposed that frustrated gas–liquid phase separation leads to the gel transition, and hence the gel states are expected inside the spinodal line. Furthermore, we show predictions of Mode-Coupling Theory from the study of Bergenholtz and coworkers for the gel boundary[21] extending over the whole ϕ_c range (dashed-dotted line, $\xi = 0.08$). The theory results are complemented by experimentally determined gel boundaries obtained by Shah and coworkers for $\xi = 0.061$ and 0.090,[38] and Poon and coworkers for $\xi \sim 0.06$.[60] Finally, we also plot the boundary between fluid and attractive glass determined by Pham and coworkers for $\xi = 0.09$.[61] As can be observed, the gel boundaries predicted by theory and observed in experiments are all lying close to or above the binodal line. This finding apparently supports the scenario in which arrested spinodal decomposition leads to gel formation.[20] However, recent studies indicate that this scenario is correct at low particle concentrations, while the role of rigidity percolation might be important at higher ϕ_c.[59,62] Moreover, we can observe that generally the transition from equilibrium fluid states to non-equilibrium solid states, either gel or glass, occurs at low polymer concentrations in systems where the interactions are purely attractive.

In comparison, systems with competing interactions exhibit a richer and more complex behaviour that also depends on the range and the strength of the repulsive interaction. If a repulsive barrier is present, the binodal tends to disappear and a cluster fluid phase is found instead.[3,25,63] In systems of highly charged colloids, at low concentrations $\phi_c < 0.17$ also other states are present, such as Wigner glasses and glassy cluster states,[19] while at moderate concentrations $0.15 < \phi_c < 0.30$ gel states are still being observed. In Fig. 8 we report the experimentally determined depletion boundaries for colloids with competing interactions from the study of Campbell and coworkers, for $\xi = 0.13$, $\kappa\sigma \approx 1.55$ and $Z^2 = 30$,[25] from the study of Klix and coworkers for $\xi = 0.19$, $\kappa\sigma \approx 1$ and $Z^2 = 15$,[19] and from Sedgwick and coworkers for $\xi = 0.021$[18] (values for the repulsive interaction could not be estimated in this case). In these and other studies[38,60] a cluster phase is observed in the same interval $0.03 \leq c_p/c_p{}^* \leq 2.0$, but at lower ϕ_c. We observe that the effect of the additional repulsive interaction is that of shifting the gel boundary to higher ϕ_c and larger c_p values when κ decreases and hence the range of electrostatic interactions increases.

The values of $\kappa\sigma$, ξ and Z^2 of our potential are even larger than those of the work of Campbell and coworkers.[25] We can therefore expect that the gel boundary lies at relatively low polymer concentrations and approaches that of purely attractive systems.

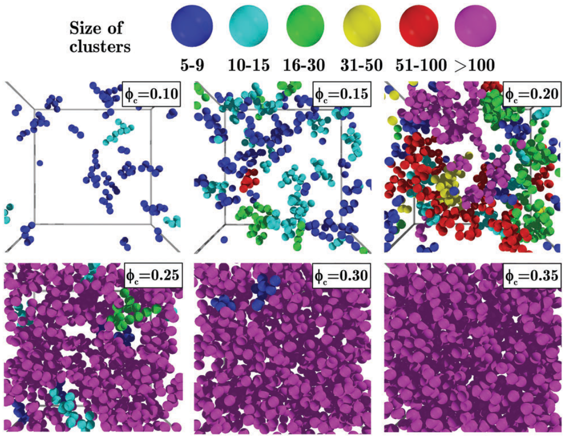

Fig. 9 Snapshots of systems at $c_p/c_p{}^* = 1$ for different colloidal volume fractions ϕ_c obtained from simulations with the size of the clusters in which the particle participates indicated by the colour of the particle. These systems are indicated by open (non-percolated states) and filled (percolated states) blue stars in Fig. 8.

This seems to be confirmed by the experimental data (Fig. 8), where, in the absence of the polymer and at small polymer concentration, we observe fluid states close to the gelation boundaries of the purely attractive systems and the data of ref. 25 if extrapolated to larger ϕ_c. At the same time, gel states are found well below the gelation boundary of ref. 19.

We have also performed simulations at constant $c_p/c_p{}^* = 1.0$ and different volume fractions, with the potential parameters describing sample 3. They indicate that the gelation boundary is slightly shifted compared to the data in ref. 25 (Fig. 8), and especially that gel states are not observed at small ϕ_c, in contrast to the purely attractive case. Snapshots of the simulations are shown in Fig. 9, where only particles participating in clusters with at least 5 particles are shown. At $\phi_c < 0.15$ small clusters are dispersed throughout the volume (these states are indicated as empty stars in Fig. 8). At $\phi_c = 0.20$ larger clusters are formed, probably percolated, which indicates that the system is close to the gelation boundary, and at higher concentrations, $\phi_c \geq 0.25$, large clusters dominate, consistent with the state diagram (these states are indicated as filled stars in Fig. 8).

We can therefore conclude that, even if our effective potential is strongly screened, the state diagram of our system does not seem to be fully compatible with that of a purely attractive system, but rather indicates the effects of competing attractive and repulsive interactions.

3.5 Second virial coefficient

The effective colloid–colloid interaction potential is characterised by a short-range attraction and a longer-range repulsion. This interplay determines the arrangement of the particles. However, due to the large volume fractions $0.38 \leq \phi_c \leq 0.44$ (Table 1) crowding also plays a significant role. To quantify the different contributions to the interactions, for all samples with $c_p/c_p{}^* > 0.1$ (Table 2) we have calculated the reduced second virial coefficient $B_2{}^* \equiv B_2/B_2^{\mathrm{HS}}$,[48,59] where B_2 is the second virial coefficient and B_2^{HS} the one of hard-spheres. For set A, $B_2{}^* > 0$, which indicates a strong effect of the repulsive component, while for set B, $B_2{}^* < 0$, which means that the attractive contribution dominates. Thus, the gel structure in our samples is determined by crowding combined with either dominantly repulsive (set A) or dominantly attractive (set B) interactions. A theoretical analysis of the binodal for $\xi = 0.076$ nevertheless suggests that all gel samples studied here are well inside the phase separation region (Fig. 8). However, none of the samples, particularly the ones in set A (where repulsion dominates), reach the value $B_2{}^* = -1.5$.[64] This value has been associated with the proximity of phase separation in systems with attractive pair potentials. This requires that the attractions are short-ranged, $\xi < 0.15$, and hence many-body effects are excluded,[65] which is the case in our samples. Thus, a more complex mechanism seems to be responsible for the gel transition at intermediate colloid volume fractions and especially in the presence of electrostatic repulsion.

4 Discussion and conclusions

The results presented in the previous section can be summarised to obtain a general picture of the system under investigation: in the absence of polymers ($c_p = 0.0$), the structure of the samples, namely homogeneously distributed particles in a colloidal fluid, can be described by a repulsive Yukawa potential, which is due to the residual charges (Fig. 2a and b). The addition of a small amount of polymers ($c_p/c_p{}^* = 0.1$) induces the formation of a few small clusters due to depletion attractions. However, the electrostatic repulsion dominates and the systems remain fluid and essentially homogeneous (Fig. 2c). Instead, with increasing amount of polymer ($0.8 \leq c_p/c_p{}^* \leq 2.0$), the attractions become more pronounced, as shown by the effective potentials obtained (Table 2) and clusters are formed which merge into a network gel structure. The radial distribution functions indicate for all gel samples a strong and short-range correlation between particles. However, even if the interaction potential is different, the $g(r)$ of the gels is relatively similar within each set of samples (Fig. 3, for sets A and B), but a flatter region around the minimum is observed for samples of set B. Similarly, the angular distribution functions also indicate comparable internal cluster structures within one set, with particles forming triangular and tetrahedral structures as indicated by peaks at 60° and 120°. The nearest-neighbour distributions are also similar within one set, but set B presents higher average numbers of neighbours. These results suggest that the structure of the gels is not particularly sensitive to variations in the strength of attractions at fixed screening (*i.e.* within a set), where the attraction strength ranges from $0.8k_BT$ to $1.4k_BT$, *i.e.* around the thermal energy. In contrast, the structural differences between the two sets A and B suggest a stronger influence of the electrostatic interactions, which also cover a larger range (Fig. 4b). These observations were complemented by calculations of the second virial coefficient for samples of the two sets (Table 2): we observed that, in addition to crowding, for set A gel formation is dominated by repulsion and for set B by attraction. These results indicate that the variation of the electrostatic contribution, which also induces variations in the effective attraction at short distances, is crucially affecting the gel structure.

By comparison with previous work on state diagrams of colloid–polymer systems, and our own calculations of the binodal line, we could additionally confirm that even if the repulsive electrostatic interactions are strongly screened, the structures that we observe are compatible with the state diagrams expected and observed for colloid–polymer mixtures with competing interactions.

In conclusion, we were able to describe the non-equilibrium structures of intermediate volume fraction gels observed in experiments by using a simple effective pair interaction potential although non-equilibrium effects are not explicitly considered. The effective interaction potential thus not only depends on the sample composition, but also the preparation history. Therefore, if the preparation path and hence maybe the gel structure are changed, also the effective interaction potential will change. Nevertheless, the effective interaction potentials and their parameters, which were determined by comparing the radial distribution function $g(r)$ obtained by experiments and simulations, respectively, were successfully used to predict other structural features, such as the angular distribution function $P(\theta)$ and the nearest-neighbour distribution function $P(n_b)$, as well as the state diagram. The effective interaction potential contains a short-range attraction modelled through a square-well and longer-range electrostatic repulsion modelled through a Yukawa form. Through the parameters of the potential we can assess the relative contribution of the attractive and the repulsive component to the gel structure. We found that the degree of screening of the electrostatics has an important influence on the structural organisation since it significantly affects the balance between repulsive and attractive interactions. Due to that, we observed different gel structures which are dominated by either repulsion or attraction.

Acknowledgements

We thank Andrew Schofield (The University of Edinburgh) for the PMMA particles. This work was supported by the International Helmholtz Research School of Biophysics and Soft Matter (IHRS BioSoft), by the Deutsche Forschungsgemeinschaft (DFG) and grant INST 208/617-1FUGG funding the confocal microscope, by CONACyT (grant no. 237425) and by the Universidad de Guanajuato (Convocatoria Institucional de Investigación Científica 2016–2017). R. C.-P. acknowledges the financial support provided by the Marcos Moshinsky fellowship 2013–2014 and the Alexander von Humboldt Foundation supporting his stay at the University of Düsseldorf during the summer 2016.

References

1 Y. Liu, L. Porcar, J. Chen, W.-R. Chen, P. Falus, A. Faraone, E. Fratini, K. Hong and P. Baglioni, *J. Phys. Chem. B*, 2011, **115**, 7238–7247.

2 Y. Liu, *Chem. Eng. Process Technol.*, 2013, **1**, 2–5.

3 A. Stradner, H. Sedgwick, F. Cardinaux, W. C. K. Poon, S. U. Egelhaaf and P. Schurtenberger, *Nature*, 2004, **432**, 492–495.

4 S. Yadav, T. M. Laue, D. S. Kalonia, S. N. Singh and S. J. Shire, *Mol. Pharmaceutics*, 2012, **9**, 791–802.

5 K. P. Johnston, J. A. Maynard, T. M. Truskett, A. U. Borwankar, M. A. Miller, B. K. Wilson, A. K. Dinin, T. A. Khan and K. J. Kaczorowski, *ACS Nano*, 2012, **6**, 1357–1369.

6 E. J. Yearley, I. E. Zarraga, S. J. Shire, T. M. Scherer, Y. Gokarn, N. J. Wagner and Y. Liu, *Biophys. J.*, 2013, **105**, 720–731.

7 E. J. Yearley, P. D. Godfrin, T. Perevozchikova, H. Zhang, P. Falus, L. Porcar, M. Nagao, J. E. Curtis, P. Gawande, R. Taing, I. E. Zarraga, N. J. Wagner and Y. Liu, *Biophys. J.*, 2014, **106**, 1763–1770.

8 E. Zaccarelli, *J. Phys.: Condens. Matter*, 2007, **19**, 323101.

9 T. Sentjabrskaja, E. Zaccarelli, C. De Michele, F. Sciortino, P. Tartaglia, T. Voigtmann, S. U. Egelhaaf and M. Laurati, *Nat. Commun.*, 2016, **7**, 11133.

10 E. Mani, E. Sanz, P. G. Bolhuis and W. K. Kegel, *J. Phys. Chem. B*, 2010, **114**, 7780–7786.

11 W. C. K. Poon, *J. Phys.: Condens. Matter*, 2002, **14**, R859–R880.

12 A. Yethiraj and A. van Blaaderen, *Nature*, 2003, **421**, 513–517.

13 S. Asakura and F. Oosawa, *J. Polym. Sci.*, 1958, **33**, 183.

14 F. Oosawa and S. Asakura, *J. Chem. Phys.*, 1954, **22**, 1255.

15 H. N. W. Lekkerkerker, W. Poon, P. Pusey, A. Stroobants and P. B. Warren, *Europhys. Lett.*, 1992, **20**, 559–564.

16 S. M. Ilett, A. Orrock, W. C. K. Poon and P. N. Pusey, *Phys. Rev. E: Stat. Phys., Plasmas, Fluids, Relat. Interdiscip. Top.*, 1995, **51**, 1344–1352.

17 S. Ramakrishnan, M. Fuchs, K. S. Schweizer and C. F. Zukoski, *J. Chem. Phys.*, 2002, **116**, 2201.

18 H. Sedgwick, S. U. Egelhaaf and W. C. K. Poon, *J. Phys.: Condens. Matter*, 2004, **16**, S4913.

19 C. L. Klix, C. P. Royall and H. Tanaka, *Phys. Rev. Lett.*, 2010, **104**, 165702.

20 P. J. Lu, E. Zaccarelli, F. Ciulla, A. B. Schofield, F. Sciortino and D. A. P. C. B. Weitz, *Nature*, 2008, **453**, 499–503.

21 J. Bergenholtz, W. C. K. Poon and M. Fuchs, *Langmuir*, 2003, **19**, 4493–4503.

22 S. Shah, Y. Chen, S. Ramakrishnan, K. Schweizer and C. F. Zukoski, *J. Phys.: Condens. Matter*, 2003, **15**, 4751–4778.

23 N. E. Valadez-Pérez, Y. Liu, A. P. R. Eberle, N. J. Wagner and R. Castañeda-Priego, *Phys. Rev. E: Stat., Nonlinear, Soft Matter Phys.*, 2013, **88**, 060302(R).

24 C. P. Royall, S. R. Williams, T. Ohtsuka and H. Tanaka, *Nat. Mater.*, 2008, **7**, 556–561.

25 A. I. Campbell, V. J. Anderson, J. S. van Duijneveldt and P. Bartlett, *Phys. Rev. Lett.*, 2005, **94**, 208301.

26 F. Sciortino, P. Tartaglia and E. Zaccarelli, *J. Phys. Chem. B*, 2005, **109**, 21942–21953.

27 E. Mani, W. Lechner, W. K. Kegel and P. G. Bolhuis, *Soft Matter*, 2014, **10**, 4479–4486.

28 M. Kohl, R. F. Capellmann, M. Laurati, S. U. Egelhaaf and M. Schmiedeberg, *Nat. Commun.*, 2016, **7**, 11817.

29 P. A. Smith, G. Petekidis, S. U. Egelhaaf and W. C. K. Poon, *Phys. Rev. E: Stat., Nonlinear, Soft Matter Phys.*, 2007, **76**, 041402.

30 J. C. F. Toledano, F. Sciortino and E. Zaccarelli, *Soft Matter*, 2009, **5**, 2390–2398.

31 I. Zhang, C. P. Royall, M. A. Faers and P. Bartlett, *Soft Matter*, 2013, **9**, 2076.

32 P. Varadan and M. J. Solomon, *Langmuir*, 2003, **19**, 509–512.

33 G. Foffi, C. De Michele, F. Sciortino and P. Tartaglia, *J. Chem. Phys.*, 2005, **122**, 224903.

34 M. Laurati, G. Petekidis, N. Noumakis, F. Cardinaux, A. Schofield, J. Brader, M. Fuchs and S. U. Egelhaaf, *J. Chem. Phys.*, 2009, **130**, 134907.

35 C. P. Royall, D. G. A. L. Aarts and H. Tanaka, *J. Phys.: Condens. Matter*, 2005, **17**, S3401.

36 C. P. Royall, M. E. Leunissen, A.-P. Hynninen, M. Dijkstra and A. van Blaaderen, *J. Chem. Phys.*, 2006, **124**, 244706.

37 C. L. Klix, K.-I. Murata, H. Tanaka, S. R. Williams, A. Malins and C. P. Royall, *Sci. Rep.*, 2013, **3**, 2072.

38 S. A. Shah, Y.-L. Chen, K. S. Schweizer and C. F. Zukoski, *J. Chem. Phys.*, 2003, **119**, 8747–8760.

39 C. P. Royall, A. A. Louis and H. Tanaka, *J. Chem. Phys.*, 2007, **127**, 044507.

40 M. G. Noro and D. Frenkel, *J. Chem. Phys.*, 2000, **113**, 2941–2944.

41 G. C. Berry, *J. Chem. Phys.*, 1966, **44**, 4550.

42 G. J. Fleer and R. Tuinier, *Phys. Rev. E: Stat., Nonlinear, Soft Matter Phys.*, 2007, **76**, 041802.

43 H. N. W. Lekkerkerker, W. C. K. Poon, P. N. Pusey, A. Stroobants and P. B. Warren, *Europhys. Lett.*, 1992, **20**, 559.

44 C. P. Royall, W. C. K. Poon and E. R. Weeks, *Soft Matter*, 2013, **9**, 17–27.

45 J. C. Crocker and D. G. Grier, *J. Colloid Interface Sci.*, 1996, **179**, 298–310.

46 M. Jenkins and S. U. Egelhaaf, *Adv. Colloid Interface Sci.*, 2008, **136**, 65–92.

47 E. Schöll-Paschinger, A. L. Benavides and R. Castañeda-Priego, *J. Chem. Phys.*, 2005, **123**, 234513.

48 N. E. Valadez-Pérez, A. L. Benavides, E. Schöll-Paschinger and R. Castañeda-Priego, *J. Chem. Phys.*, 2012, **137**, 084905.

49 F. Platten, N. E. Valadez-Pérez, R. Castañeda-Priego and S. U. Egelhaaf, *J. Chem. Phys.*, 2015, **142**, 174905.

50 S. Bucciarelli, N. Mahmoudi, L. Casal-Dujat, M. Jehannin, C. Jud and A. Stradner, *J. Phys. Chem. Lett.*, 2016, **7**, 1610–1615.

51 J. Dobnikar, R. Castañeda-Priego, H. H. von Grünberg and E. Trizac, *New J. Phys.*, 2006, **8**, 277.

52 L. F. Rojas-Ochoa, R. Castañeda-Priego, V. Lobaskin, A. Stradner, F. Scheffold and P. Schurtenberger, *Phys. Rev. Lett.*, 2008, **100**, 178304.

53 E. Trizac, L. Belloni, J. Dobnikar, H. H. von Grünberg and R. Castañeda-Priego, *Phys. Rev. E: Stat., Nonlinear, Soft Matter Phys.*, 2007, **75**, 011401.

54 B. D'Aguanno and R. Klein, *J. Chem. Soc., Faraday Trans.*, 1991, **87**, 379–390.

55 G. V. Schulz, *Z. Phys. Chem.*, 1939, **B43**, 25.

56 M. P. Allen and D. J. Tildesley, *Computer Simulations of Liquids*, Oxford Science Publications, 1989.

57 D. Frenkel and B. Smith, *Understanding Molecular Simulation, From Algorithms to Applications (Computational Science)*, Academic Press, 2nd edn, 2001.

58 E. López-Sánchez, C. D. Estrada-Alvarez, G. Pérez-Angel, J. M. Méndez-Alcaraz, P. González-Mozuelos and R. Castañeda-Priego, *J. Chem. Phys.*, 2013, **139**, 104908.

59 N. E. Valadez-Pérez, R. Castañeda-Priego and Y. Liu, *RSC Adv.*, 2013, **3**, 25110–25119.

60 W. C. K. Poon, L. Starrs, S. P. Meeker, A. Moussaid, R. M. L. Evans, P. N. Pusey and M. M. Robins, *Faraday Discuss.*, 1999, **112**, 143–154.

61 K. N. Pham, S. U. Egelhaaf, P. N. Pusey and W. C. K. Poon, *Phys. Rev. E: Stat., Nonlinear, Soft Matter Phys.*, 2004, **69**, 011503.

62 A. P. R. Eberle, N. J. Wagner and R. Castañeda-Priego, *Phys. Rev. Lett.*, 2011, **106**, 105704.

63 P. D. Godfrin, N. E. Valadez-Pérez, R. Castañeda-Priego, N. J. Wagner and Y. Liu, *Soft Matter*, 2014, **10**, 5061–5071.

64 G. A. Vliegenthart and H. N. W. Lekkerkerker, *J. Chem. Phys.*, 2000, **112**, 5364–5369.

65 R. Tuinier and M. S. Feenstra, *Langmuir*, 2014, **30**, 13121–13124.

This page has been left intentionally blank.

3.2 Directed percolation identified as equilibrium pre-transition towards non-equilibrium arrested gel states

Journal: Nature Communications

Reference: *Nat. Commun.* **7**, 11817 (2016)

Impact factor: 12.124

Authors: Matthias Kohl*, **Ronja F. Capellmann***, Marco Laurati, Stefan U. Egelhaaf, and Michael Schmiedeberg

* joint 1st author

M. K. performed the simulations, R. F. C. conducted the experiments, M. K. and R. F. C. analysed the data and all authors contributed to the design of the research, the interpretation of the results and the writing of the paper.

45% contribution of R. F. C. corresponding to the major part of the experimental effort.

Reprinted with permission of Springer Nature.

nature COMMUNICATIONS

ARTICLE

Received 18 Sep 2015 | Accepted 3 May 2016 | Published 9 Jun 2016

DOI: 10.1038/ncomms11817

OPEN

Directed percolation identified as equilibrium pre-transition towards non-equilibrium arrested gel states

M. Kohl[1,*], R.F. Capellmann[2,*], M. Laurati[2], S.U. Egelhaaf[2] & M. Schmiedeberg[1,3]

The macroscopic properties of gels arise from their slow dynamics and load-bearing network structure, which are exploited by nature and in numerous industrial products. However, a link between these structural and dynamical properties has remained elusive. Here we present confocal microscopy experiments and simulations of gel-forming colloid–polymer mixtures. They reveal that gel formation is preceded by continuous and directed percolation. Both transitions lead to system-spanning networks, but only directed percolation results in extremely slow dynamics, ageing and a shrinking of the gel that resembles synaeresis. Therefore, dynamical arrest in gels is found to be linked to a structural transition, namely directed percolation, which is quantitatively associated with the mean number of bonded neighbours. Directed percolation denotes a universality class of transitions. Our study hence connects gel formation to a well-developed theoretical framework, which now can be exploited to achieve a detailed understanding of arrested gels.

---

[1] Institute for Theoretical Physics II: Soft Matter, Heinrich Heine University, Universitätsstraße 1, 40225 Düsseldorf, Germany. [2] Condensed Matter Physics Laboratory, Heinrich Heine University, Universitätsstraße 1, 40225 Düsseldorf, Germany. [3] Institute of Theoretical Physics 1, Friedrich-Alexander University Erlangen-Nürnberg, Staudtstr. 7, 91058 Erlangen, Germany. * These authors contributed equally to this work. Correspondence and requests for materials should be addressed to M.S. (email: michael.schmiedeberg@fau.de).

Amorphous solids are ubiquitous in natural and engineered materials: sand piles, window glass, ceramics, plastics, nanocomposites, gelatin and living cells are just a few examples of solid materials with an amorphous structure. Glassy systems are amorphous solids in which the solid-like mechanical properties are linked to a dramatic slowdown of the microscopic dynamics when decreasing the temperature or increasing the particle density[1–7]. Gels also show arrested dynamics[8–17], but their structure is different. They exhibit a heterogeneous load-bearing network structure that is formed by cross-linking (chemical gels) or attraction-induced aggregation (physical gels)[18–31]. Dynamical arrest was associated with different mechanisms, for example, arrested phase separation[21], cluster aggregation[21], the occurrence and spatial organization of locally favoured structures[18] and the onset of rigidity percolation[32]. Furthermore, a progressive slowdown of the dynamics after sample preparation, that is, ageing, is observed. However, the relation between the slowdown and arrest of the dynamics, and the structural properties of these systems are still under debate[8,9].

Model systems of physical gels have been established, for example, dispersions of spherical colloidal particles, in which attractive forces are induced by a temperature variation or depletion effects due to the addition of linear non-adsorbing polymer chains[30,31]. Nevertheless, there are only few studies on the relation between the slowdown of the dynamics and the microscopic structure.

Here we show that the slowdown of the particle dynamics and the onset of ageing can be related to the microscopic structure of colloidal gels, namely a directed percolation (DP) transition. This is demonstrated in experiments on charged colloid–polymer mixtures[30,33] and in Brownian dynamics simulations of particles interacting through a combination of coulombic repulsion and depletion-induced attraction modelled by the Asakura–Oosawa potential[34]. The onset of DP is investigated along different paths in which either the attractive or the repulsive parts of the interactions are varied. We find that in any case continuous percolation precedes DP and that both can be associated with characteristic values of the mean number of bonds per particle. Furthermore, DP is found to be linked to the onset of ageing effects.

Results

States of the system. In charged colloid–polymer mixtures, two particle–particle interactions compete on different length scales: First, screened electrostatic interactions, which are long ranged for low salt concentrations and become shorter ranged on addition of salt; second, depletion interactions, which are short ranged, typically at most one tenth of the colloidal particle diameter, and controlled through the radius of gyration of the polymers. We experimentally investigated charged colloidal polymethylmethacrylate (PMMA) spheres with volume fraction $\Phi \approx 0.2$ and diameter $\sigma = 1.72\,\mu\mathrm{m}$ in the presence of non-adsorbing linear polystyrene with radius of gyration $r_g = 65\,\mathrm{nm}$, where the effective polymer-colloid size ratio $\xi^{\mathrm{eff}} \approx 0.03$ (Supplementary Table 1).

In experiments and simulations, we consistently observe four states that differ in the structural arrangements of the colloidal particles (Fig. 1, left). Which state occurs depends on the salt concentration c_{salt}, and therefore the screening length κ^{-1} characterizing the range of the repulsion and the polymer concentration c_{p}, that is, attraction strength. We consider fixed c_{p} and vary c_{salt}, which will be referred to as 'path B'. In the absence of salt, mainly individual particles but also very few clusters are distributed homogeneously throughout the sample (sample C1; note that c_{p} of this sample is higher than the one of the other samples, Supplementary Table 1). Adding salt, particles aggregate into isolated small clusters (sample B1). At large salt concentrations, larger clusters are observed which form a network in three dimensions (sample B2). Furthermore, a heterogeneous network structure with thick strands consisting of even larger, dense clusters are formed at the largest salt concentration studied (sample B3).

These states show different pair correlation functions $g(r)$ (Fig. 1, right). Without salt (C1), $g(r)$ is dominated by a peak located at the mean particle distance $\rho^{-1/3}$. Furthermore, a small peak at particle contact reflects the presence of a small number of aggregated particles. For small amounts of added salt (B1), the increase in the contact peak and a corresponding decrease of the second peak of $g(r)$ is consistent with the presence of doublets, triplets or small string-like clusters (visible in Fig. 1a). The size of the clusters is limited by the repulsive contribution to the potential[22,35,36]. For sample B2, the large peak at contact reflects the large fraction of particles forming clusters. Its $g(r)$ is reminiscent of a percolated gel-like network structure[32,37,38]. Finally, the radial distribution function of sample B3 with its very high first peak at contact reflects the presence of a large number of bonded particles. Furthermore, its deep first minimum and pronounced split second peak can arise from triplet structures and local close packed arrangements. These features of the $g(r)$ are observed in the experiments as well as in the simulations. While there is qualitative agreement between experimental and simulation results, small quantitative differences indicate that the potential and its parameter values used in the simulations are not perfectly describing the interactions present in the samples. (The mapping of the simulation and experimental parameters is described in Supplementary Note 1.) Nevertheless, both, experiments and simulations, reveal different states on the path towards a gel; homogeneously distributed individual particles, small clusters, networks with thin and thicker strands consisting of larger, more compact and denser clusters, respectively.

Characterization of the different states by number of bonds. The different structures are distinguished by the degree of particle aggregation. This can be linked to the mean number of bonds per particle, $\langle N \rangle$. Individual particle–particle bonds cannot be determined unambiguously because the first peak in $g(r)$ is broadened due to polydispersity (about 7%). Hence, two particles are defined to be bonded if they are closer than the position of the first minimum in $g(r)$, which is located between 1.10 and 1.22σ (Fig. 1, right).

The mean number of bonds per particle, $\langle N \rangle$, is determined as a function of the interactions, which depend on the salt concentration c_{salt}, determining the screening length κ^{-1}, and the polymer concentration c_{p}, controlling the depletion part of the potential $V_{\mathrm{D,min}} = V_{\mathrm{D}}(\sigma^{\mathrm{eff}})$ evaluated at the overall potential minimum $V_{\mathrm{min}} = V(\sigma^{\mathrm{eff}})$ (Fig. 2). At low polymer, c_{p}, and/or salt, c_{salt}, concentrations, only very few bonds are found (white to purple), whereas high c_{p} and/or c_{salt} result in a bonded state (red). In contrast to previous results[23], $\langle N \rangle$ monotonically grows without a re-entrant transition. Even for large screening and strong attraction, $\langle N \rangle$ hardly exceeds seven and hence the highly bonded state appears not to be in equilibrium. For a purely repulsive interaction[39,40] or in spring lattice models[41] such a change is expected once the system becomes isostatic, that is, globally stable with six bonds per particle.

The structures along two paths are analysed in more detail (Fig. 3). Along path A, the salt concentration c_{salt} and hence the screening length κ^{-1} is kept constant while the polymer concentration c_{p} is increased and hence the value $V_{\mathrm{D,min}}$ of the potential at its minimum is decreased, that is, the attraction

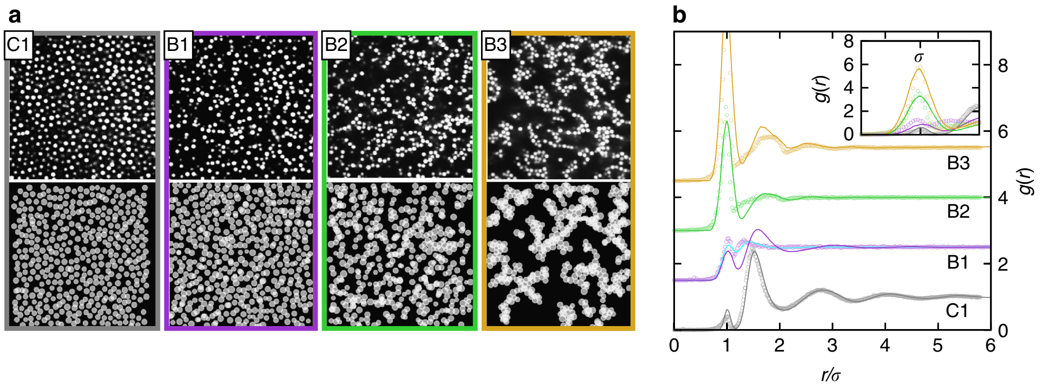

Figure 1 | On the path towards a gel four different states are found. (**a**) Two-dimensional slices of the three-dimensional systems in the following states: (C1) Fluid state with mainly individual particles and only very few small aggregates, (B1) isolated small chain-like clusters of particles, (B2) larger clusters forming a continuously percolated network in three dimensions and (B3) directed percolated network. The upper row shows confocal microscopy data, where the polymer concentrations are $3c^*$ (C1) and $2c^*$ (B1–B3) with the overlap concentration c^*. The salt concentration increases from left to right (Supplementary Table 1). The lower row represents the corresponding states as observed in the simulations. (**b**) Corresponding pair correlation functions $g(r)$ determined from the three-dimensional data as a function of the particle-particle distance r in units of the particle diameter σ, which, for the simulation data, is taken to be the effective particle diameter, that is, $\sigma = \sigma^{\mathrm{eff}}$. Symbols represent experimental data, solid lines simulation data and (only for B1) the light blue solid line simulation data with parameters obtained by an unconstrained fit (for details see Supplementary Note 1). Data have been shifted for clarity. The inset shows the (unshifted) first peaks.

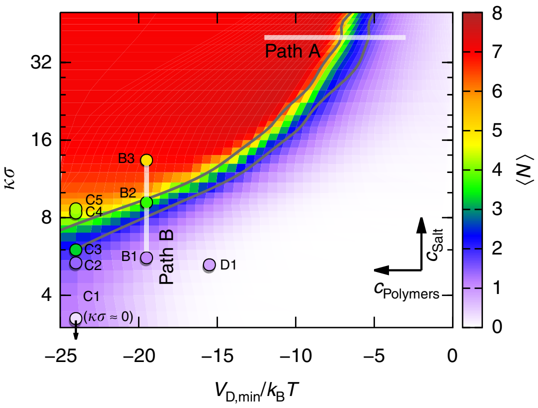

Figure 2 | The mean number of bonds characterizes the different stages towards a gel. Mean number of bonds per particle, $\langle N \rangle$, as a function of the minimum of the attractive part of the potential, evaluated at the global minimum, $V_{\mathrm{D,min}}$ in units of the thermal energy $k_{\mathrm{B}}T$, and the inverse screening length κ normalized by the inverse particle diameter σ^{-1}, which, for the simulation data, is taken to be the mean particle diameter, that is, $\sigma = \sigma_0$, in a semi-logarithmic representation. The background colour represents $\langle N \rangle$ as obtained by simulations, while the positions and colours of the circles indicate the compositions and $\langle N \rangle$, respectively, of the experimental samples, which are labelled. The two white lines indicate two paths, during which either only the polymer concentration ('path A') or only the salt concentration ('path B') are changed. The lower and upper dark solid lines indicate the continuous and directed percolation transitions, respectively, which are taken to occur when the corresponding $p(l_{\mathrm{box}}) = 0.2$ (Fig. 4c).

strength is increased. (Note that path A implies a high salt concentration, which cannot be achieved in the organic solvent mixture used in the experiments.) Instead, along path B, the screening length κ^{-1} is reduced at constant attraction strength. On increasing attraction on path A, $\langle N \rangle$ increases and the distribution of the number of bonds per particle, $p(N)$, first broadens, indicating a more heterogeneous structure, but then narrows again indicating that the probability to find monomers is reduced to zero, consistent with the observed network structure (Figs 1a,3a). Along path B, that is, increasing c_{salt} (inset), the distributions also shift to larger N and broaden, again indicating the coarsening of the structure. Compared with path A, the $p(N)$ are sharper, indicating that monomers are suppressed at low salt concentrations. Under these conditions, repulsions are long ranged and still substantial at the mean monomer separation. The system avoids this unfavourable situation by forming clusters. Although the repulsion between the clustered monomers is even larger, cluster formation is favoured by the short-ranged attractions and the larger mean cluster separation that reduces cluster–cluster repulsion.

We characterize $p(N)$ by its mean $\langle N \rangle$, variance $\langle \Delta N^2 \rangle$ and maximum $N_{\max}$. With increasing attraction, that is, $|V_{\mathrm{D,min}}|$, they all sharply increase at $V_{\min} \approx -3.0\ k_{\mathrm{B}}T$, where $k_{\mathrm{B}}T$ is the thermal energy (Fig. 3b). Furthermore, we consider the distribution $p(\varphi)$ of angles between two successive bonds, φ. The distribution is normalized by the solid angle covered by the angle φ, that is, such that $2\pi \int p(\varphi) \sin\varphi \, \mathrm{d}\varphi = 1$. It reveals a qualitative change that also occurs at $V_{\min} \approx -3.0\ k_{\mathrm{B}}T$ (Fig. 3c). While the peak at $\varphi = \pi/3$, which is related to locally dense tetrahedral packings, grows monotonically with $|V_{\min}|$, a second peak at $\varphi = 2\pi/3$ develops and becomes pronounced for $|V_{\min}| > 3.0\, k_{\mathrm{B}}T$. Furthermore, for these large potential depths, a peak at $\varphi = \pi$ emerges, which indicates the formation of straight strings of connected particles. Therefore, based on the mean number of bonds per particle $\langle N \rangle$, the different structures on the path towards a gel can be distinguished and quantitatively characterized.

Continuous and DP transitions. We will now show that the particle networks undergo two percolation transitions, a continuous percolation transition and a DP transition. In both cases, percolated networks span the whole system. In continuous percolation, a path along a percolating cluster may contain steps in all directions, including backward steps (Fig. 4a, P). Instead, in the case of DP, only paths along an arbitrarily chosen direction

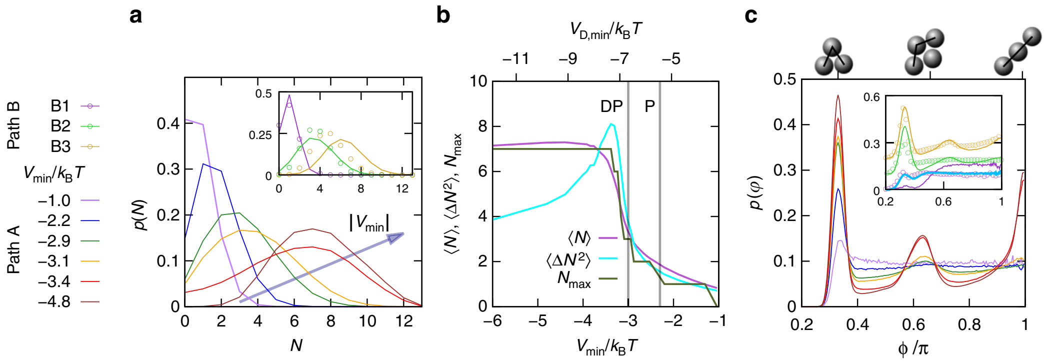

Figure 3 | Quantitative analysis of structures along paths from fluid to gel. (**a**) Distribution of the number of bonds per particle, $p(N)$, as obtained by simulations for constant screening length $\kappa\sigma = 40$ and varying attraction (as indicated on the left), that is, path A in Fig. 2. In the inset simulation (lines) and experimental (circles) results for varying $\kappa\sigma$ and constant attraction, that is, path B, are compared. Along the paths, $p(N)$ first broadens, revealing a coarsening of the structure, before narrowing again (along path A). This indicates rather homogeneous structures for high attractions. (**b**) Mean $\langle N\rangle$, variance $\langle \Delta N^2\rangle$ and the most probable value N_{max} of $p(N)$ as a function of attraction strength, V_{min}, along path A as obtained by simulations. All three functions show an increase at $V_{min} \approx -3.0\ k_BT$. The grey vertical lines denote the percolation (P) and the directed percolation (DP) transition as determined through the condition $p(l_{box}) = 0.2$ (Fig. 4c). (**c**) Distribution of the angle between two successive bonds, $p(\varphi)$, along path A as obtained by simulations. The inset shows $p(\varphi)$ along path B as obtained by simulations (lines) and experiments (circles). Also $p(\varphi)$ reveals a qualitative change at $V_{min} \approx -3.0\ k_BT$, as the peaks at $\varphi = 2\pi/3$ and $\varphi = \pi$ become pronounced. This reflects the occurrence of straight thick string-like particle formations. The light blue line in the inset represents simulation data with parameters obtained by an unconstrained fit (for details see Supplementary Notes 1). Colours of the other lines as in **a** and indicated on the left.

are considered whereas possible backward steps in this direction are not considered (Fig. 4a, DP). In the limit of an infinite system size, percolating clusters occur in all directions in the sample. Therefore, on a macroscopic scale no preferred direction exists in a directed percolated network.

The (cumulative) probabilities $p(\Delta x)$ that a particle participates in paths with a projected length of at least Δx and in directed paths with a length of at least Δx along any arbitrarily chosen direction are shown in the inset and main part of Fig. 4b, respectively, where the solid lines represent simulation data along path A and symbols indicate results from experiments along path B. For both percolation conditions, the probabilities decay to zero in the case of weak attractions (small $|V_{min}|$). In contrast, for strong attractions plateaus develop, indicating large clusters that span the whole system. The height of the plateaus correspond to the fractions $p(l_{box})$ of particles that are part of clusters with the maximum possible length, that is, the box size l_{box} (Fig. 4c). The system size determines l_{box} and also affects the simulations. Nevertheless, within the investigated system sizes only a weak dependence on system size, quantified by the total number of particles M, is observed. In particular, the occurrence of the sharp increases of $p(l_{box})$ and their positions are not significantly affected. These sharp increases indicate the continuous and DP transitions.

We determine the continuous and DP transitions in simulations for the complete parameter space of Fig. 2. The locations are chosen to coincide with the percolation probability $p(l_{box}) = 0.2$ for systems with 9,856 particles (Fig. 4c). Using this condition, along path A, the continuous percolation transition occurs at $V_P = -2.3\ k_BT$ and the DP transition is found at $V_{DP} = -3.0\ k_BT$. The latter coincides with the significant changes observed in other parameters; $\langle N\rangle$ (Fig. 2, dark solid lines) as well as $p(N)$, $\langle \Delta N^2\rangle$, N_{max} and $p(\varphi)$ (Fig. 3). Furthermore, this indicates that the continuous percolation transition occurs at $\langle N\rangle \approx 2$ and the DP transition at $\langle N\rangle \approx 3$ (Fig. 3b). This suggests a connection between the percolation transitions and $\langle N\rangle$. Previous work[32,37] on particles with attractive square-well interactions also observed continuous percolation for $\langle N\rangle \approx 2$. This work moreover suggested that rigidity percolation is associated with gelation, which was found to occur at $\langle N\rangle \approx 2.4$, that is, just in between our estimates for the onsets of continuous and DP. The possible link between rigidity and DP deserves further investigation.

Furthermore, close to the transitions the values of $p(l_{box})$ obey critical power law scaling with $V_P - V_{min}$ and $V_{DP} - V_{min}$, respectively (Fig. 4c,d). Note that up to leading order the probability for a bond between neighbours is proportional to V_{min} and therefore scaling laws for $p(l_{box})$ as a function of this probability also hold for $p(l_{box})$ as a function of V_{min}. Our data are consistent with theoretical predictions for the critical exponents of the power law scalings, that is, $\beta_P = 0.42$ for continuous percolation[42,43] and $\beta_{DP} = 0.58$ for directed percolation[44] (black lines in Fig. 4c,d; only the intercepts are fitted and the data with almost constant $p(l_{box})$ at large $V_P - V_{min}$ and $V_{DP} - V_{min}$, respectively, are not included in the fits). These findings strongly suggest that, on the path towards a gel, continuous and DP networks occur with well-defined transitions to other states as well as between them. Furthermore, this links the formation of gels to a universality class of transitions, namely DP, and hence a well-developed theoretical framework.

Onset of slowdown and ageing in directed percolated systems. The dynamics of the different structures are quantified by the self-intermediate scattering function F and mean squared displacement $\langle \Delta r^2\rangle$ (Fig. 5). Diffusive dynamics is observed for individual particles and small clusters, characteristic for fluids. In continuous percolated samples, open network structures are formed (Fig. 1, B2) that are rearranged by local motions requiring only slightly more time of the order of the Brownian time τ_B (Fig. 5). In contrast, a marked slowdown of the dynamics is observed beyond the directed percolation (DP) transition. DP is characterized by dense clusters with thick strands (Fig. 1, B3) and thus rearrangements are expected to involve long-range, global motions and the breaking of several bonds. Correspondingly, they require long times. The dynamics of the different states hence are

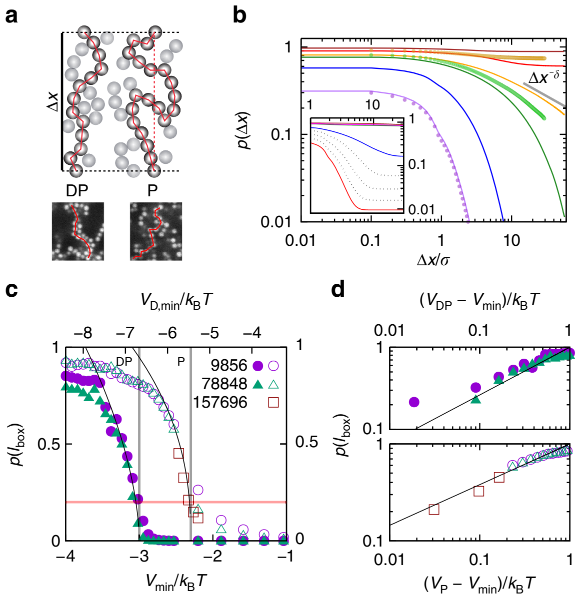

Figure 4 | Continuous and directed percolation and their transitions. (**a**) Two-dimensional sketch as well as images from experiments of (DP) a directed and (P) an undirected percolated cluster of length Δx. The path along a directed percolated cluster must not include backward steps in an arbitrarily chosen direction. (**b**) Probability $p(\Delta x)$ for a particle to reside in a (main figure) directed and (inset) continuous cluster with a length larger than the minimum length Δx. Solid lines represent simulation data along path A and symbols experimental data along path B. Colours of the lines are defined in the legend of Fig. 3. The grey solid line indicates the DP critical point, where the percolation probability is expected to be proportional to $\Delta x^{-\delta}$ with $\delta = 0.451$ (ref. 44). (**c**) Probability $p(l_{box})$ for a particle to reside in a (solid symbols) directed and (open symbols) continuous cluster with the maximum possible length, that is, box size l_{box}, and hence system-spanning, for different system sizes, quantified by the number of particles M (as indicated). Vertical lines indicate the (left) directed and (right) continuous percolation transitions defined by $p(l_{box}) = 0.2$ (horizontal red line) occurring at $V_{DP} = -3.0\ k_BT$ and $V_P = -2.3\ k_BT$, respectively. Solid black lines represent critical power law fits with (left) $p(l_{box}) \sim (V_{DP} - V_{min})^{0.58}$ and (right) $p(l_{box}) \sim (V_P - V_{min})^{0.42}$. (**d**) Same data as in **c**, but in double-logarithmic representations and relative to the (top) directed and (bottom) continuous percolation transitions.

consistent with our structural observations. They suggest that the slowdown associated with gelation sets in at the DP transition and the dynamics eventually arrests deeper in the gel region.

The simulation data presented so far have been determined for a fixed waiting time of 300 τ_B after the initial quench. The effect of the waiting time is illustrated for the dependence of the mean number of bonds per particle, $\langle N \rangle$, on the potential depth V_{min} (Fig. 6), which has been linked to the continuous and DP transitions (Fig. 3b). For small attraction strengths, $|V_{min}| \leq 3.0\, k_BT$, $\langle N \rangle$ is independent of the waiting time within the examined time range. However, for $|V_{min}| > 3.0\, k_BT$ and thus for DP, $\langle N \rangle$ is found to increase with waiting time. This indicates that ageing effects are important in directed percolated systems and equilibrium is reached only very slowly. In continuous percolation, in contrast, equilibrium is attained quickly. These findings also indicate the importance of the above-mentioned local and global rearrangement processes in continuous and directed percolated systems, respectively. In addition, it also

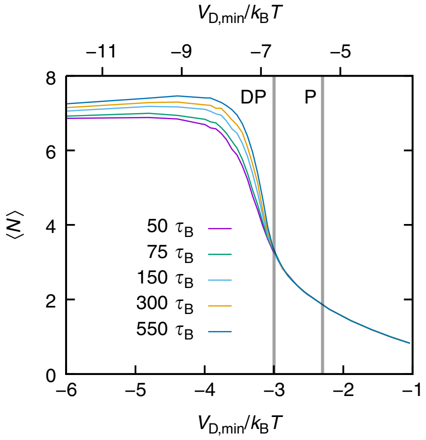

Figure 6 | In directed percolated systems ageing occurs. Mean number of bonds per particle, ⟨N⟩, as a function of the attraction strength, V_{min}, for different waiting times after the initial quench (as indicated, in units of the Brownian time τ_B) as obtained by simulations. Vertical lines indicate the (DP) directed and (P) continuous percolation transitions as determined through the condition $p(l_{box}) = 0.2$ (Fig. 4c). For systems beyond the directed percolation transition, ⟨N⟩ increases with the waiting time indicating ageing effects.

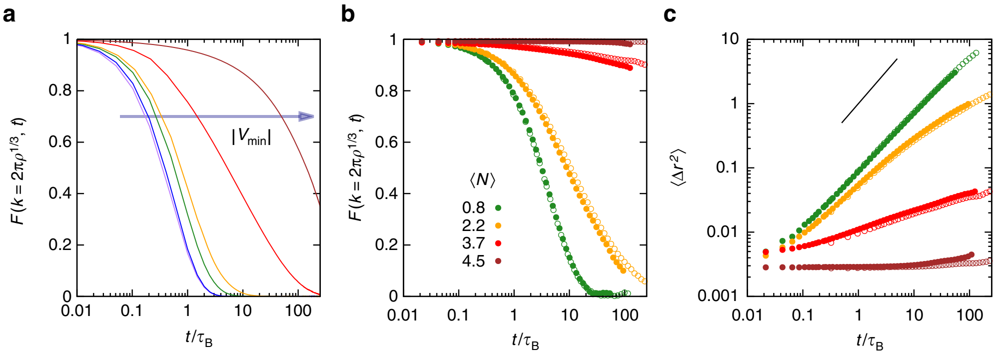

Figure 5 | In directed percolated systems the dynamics slow down. Self intermediate scattering function F at the scattering vector $k = 2\pi\rho^{-1/3}$ as a function of delay time t, normalized by the Brownian time τ_B, (**a**) along path A as obtained by simulations (with the colours of the lines defined in the legend of Fig. 3) and (**b**) for different mean numbers of bonds ⟨N⟩ (as indicated) as obtained by experiments and (**c**) corresponding mean squared displacements $\langle \Delta r^2 \rangle$ as obtained by experiments. The line indicates a slope of one.

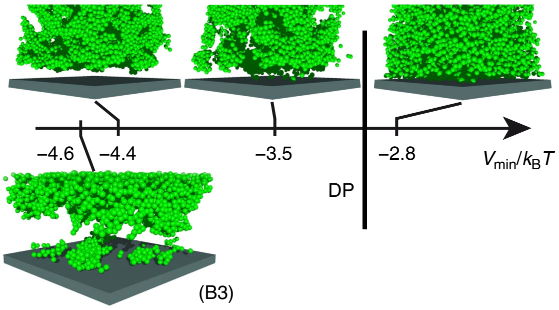

Figure 7 | Particle depletion close to walls in directed percolated systems. Rendered snapshots of samples in the vicinity of a wall obtained in (top) simulations with systems along path A and (bottom) an experiment with sample B3. Beyond the directed percolation transition, that is, for $V_{\mathrm{min}}/k_{\mathrm{B}}T < -3.0$, the vicinity of the walls starts to be depleted of particles.

supports the above conclusion that the DP transition is an equilibrium transition just before the onset of dynamical arrest.

Synaeresis in directed percolated systems. We also investigate the vicinity of walls (Fig. 7). Initially, the particles fill the whole volume, also close to the wall. In fluids and continuously percolated samples this remains like this at least for several weeks (about $10^6\ \tau_{\mathrm{B}}$). In contrast, in directed percolated systems, the vicinity of the walls becomes depleted of particles in less than a day (about $3 \times 10^4\ \tau_{\mathrm{B}}$), except for very few clusters which remain attached to the cover slip in the experiments, likely due to depletion and van der Waals attractions[45]. The depletion close to the walls indicates that directed connections between particles tend to compact the network. This resembles synaeresis, that is, the macroscopic expulsion of fluid from a gel due to the shrinking of the network. This has been observed in a variety of materials, like gelatin[46], polysaccharide gels[47,48], protein gels[49], organogels[50], microgels[51] and also weakly attractive colloidal gels[52]. The link between network shrinkage and DP might provide new aspects for the understanding of synaeresis.

Discussion

We investigate gel formation in a system with competing attractive and repulsive interactions. Confocal microscopy experiments on charged colloid–polymer mixtures are combined with Brownian dynamics simulations of particles interacting via the Asakura–Oosawa and Coulomb potentials. Depending on the overall potential minimum V_{min}, which can be varied through the attractive and/or repulsive component of the interactions, different states are identified; fluids of individual particles or clusters as well as continuous and directed percolated networks. The transitions between these states are associated with changes in structural and dynamical parameters, in particular, the number of bonds per particle with significant increases in the mean, variance and most probable value of the distribution of the number of bonds.

The effect of continuous percolation on the dynamics is small. However, DP leads to a significant slowdown of the dynamics. This is attributed to the large number of bonds and concomitant strong confinement of the particles in the attractive potentials of their neighbours, which is also reflected in significant ageing observed in directed percolated systems. It suggests that equilibration is very slow in directed percolated systems, but occurs quickly in continuous percolated systems. Hence, our findings suggest that the slowdown associated with gelation already sets in at the DP transition. Deeper in the gel region, the dynamics then becomes arrested without any additional structural transition occurring.

Our finding that DP precedes the formation of arrested gels, establishes a relation between structural and dynamic features of gels. While previous studies linked gelation in adhesive hard spheres to continuous percolation[28,29,31], we argue that in colloid–polymer mixtures with competing attractive and repulsive interactions directed rather than continuous percolation indicates the transition to gel states. Moreover, DP is a universality class of transitions. Thus gel formation can be linked to critical behaviour and the corresponding theoretical formalism[53], which can be exploited to obtain a deeper understanding of gel formation. Moreover, maybe gel collapse under gravity[30] is also initiated by percolation transitions. Our results hence contribute to an improved understanding of the relation between structural and dynamic features of gel-forming systems and hint at their importance for gel collapse and rheological properties.

Furthermore, in directed percolated systems the dense and directed networks appear to lead to a contraction. This results in a detachment from the walls and hence a layer that is depleted of particles appears. This phenomenon resembles synaeresis and might have important implications for applications and industrial products but also, for example, gel collapse and rheological measurements, in particular concerning wall slip[45,54–56].

Methods

Experiments. The samples consist of spherical PMMA particles, sterically stabilized with poly(12-hydroxystearic acid) polymers and fluorescently labelled with 7-nitrobenzo-2-oxa-1, 3-diazole-methyl-methacrylate, as well as linear polystyrene. The particles have a diameter $\sigma = 1.72\,\mu\mathrm{m}$ and a polydispersity of 7%, which are determined by static and dynamic light scattering of a very dilute suspension (volume fraction $\Phi = 0.005$). They are dispersed in a mixture of cis-decalin and cycloheptylbromide, which matches the density and almost matches the refractive index of the particles. We do not observe any indication of anisotropy, sedimentation or creaming of the samples during the observation time (days), indicating a high degree of density matching between solvent and particles. In some samples, creaming is observed after several weeks. In this solvent mixture, PMMA particles acquire a charge[33,57].

To prepare the colloid stock solution, the particles are sedimented using a centrifuge. The sediment is assumed to be random close packed with a volume fraction $\Phi_{\mathrm{RCP}} = 0.64$ and used to prepare a colloid stock solution with $\Phi \approx 0.40$. The polystyrene has a molar mass $M_{\mathrm{w}} = 3 \times 10^6\,\mathrm{kg\,mol^{-1}}$ resulting in a radius of gyration $r_{\mathrm{g}} = 65\,\mathrm{nm}$ (ref. 58) and polydispersity characterized by $M_{\mathrm{w}}/M_{\mathrm{n}} = 1.17$. For a dilute mixture, the polymer-colloid size ration $2r_{\mathrm{g}}/\sigma = 0.076$. Since r_{g} depends on concentration, an effective polymer-colloid size ratio $\xi^{\mathrm{eff}} \approx 0.03$ is estimated based on the Generalized Free Volume Theory[59–61] (Supplementary Table 1). Different polymer stock solutions are prepared by dispersing dry polymer in the solvent mixture to yield concentrations $4.3\,\mathrm{mg\,ml^{-1}} \leq c_{\mathrm{p}} = m_{\mathrm{p}}\rho_{\mathrm{s}}/m_{\mathrm{s}} \leq 18.9\,\mathrm{mg\,ml^{-1}}$ with m_{p} the mass of the dry polymer, ρ_{s} the density and m_{s} the mass of the solvent mixture, respectively. Furthermore, the overlap concentration is calculated using $c_{\mathrm{p}}^{*} = 3M_{\mathrm{w}}/4\pi N_{\mathrm{A}} r_{\mathrm{g}}^3$ with N_{A} Avogadro's constant. To obtain colloid–polymer mixtures with $\Phi \approx 0.2$, colloid and polymer stock solutions are mixed with a volume ratio of 50:50 for samples B1–B3, C1, C3 and D1, while dry polymer is added to the diluted colloid stock solution in the case of samples C2, C4 and C5. (The exact composition of each sample is reported in Supplementary Table 1.) To homogenize the samples, the mixtures are left on a vortex mixer for some minutes and then on a flask shaker for at least one day. To vary the screening length κ^{-1}, different amounts of salt (tetrabutylammoniumchloride, Supplementary Table 1)[33] are added and the mixture gently moved on the flask shaker for three days to help the dissolution of the salt in the organic solvent mixture, which is slow and only very limited. Therefore, unfortunately, the exact amount of dissolved salt is unknown. For a quantitative comparison with the simulations, hence a fitting procedure is applied (Supplementary Note 1).

Within 3 h after mixing, the samples are transferred to a home-built sample cell[62] and imaged with a confocal unit (Visitech VT-Eye and Nikon A1R-MP for the structural and dynamic measurements, respectively) that is mounted on an inverted microscope (Nikon Ti-U and Nikon Ti-E, respectively) equipped with an oil immersion objective (Nikon Plan Apo VC × 100). In the structural measurements, for each sample, 25–32 image stacks are recorded, each consisting of 151 frames (512 × 512 pixels) with z steps of 200 nm, corresponding to a volume of $54 \times 54 \times 30\,\mu\mathrm{m}^3$, which contains about 7,000 particles. With a rate of 30 slices per second and averaging of 3 slices to obtain 1 frame, a sampling time smaller than 20 s per stack is achieved. For the determination of the dynamics, two-dimensional slices (512 × 512 pixels) corresponding to an area $63.5 \times 63.5\,\mu\mathrm{m}^2$

are recorded. For each sample, at least two series with 10,000 slices at a rate of 15 slices per second and 4,000 slices at 1 slice per second are taken.

The particle coordinates are extracted using standard methods[63] and, where necessary, are refined[62]. The mean squared displacement is calculated from the particle coordinates according to $\langle \Delta r^2(t)\rangle_{i,t_0}=\langle [r_i(t_0+t)-r_i(t_0)]^2\rangle_{i,t_0}$ where the average is taken over particles i and starting times t_0. For the intermediate scattering function $F(k,t)=\langle \exp[i\vec{k}\cdot\vec{\Delta} r_i(t)]\rangle_{i,t_0}=\langle \exp[ik\cdot(\Delta x_i+\Delta y_i+\Delta z_i)]\rangle_{i,t_0}$ the magnitude of the scattering vector is chosen as $k=2\pi\rho^{1/3}\approx 2.37\,\mu\mathrm{m}^{-1}$. The delay time is scaled with the Brownian time $\tau_\mathrm{B}=\sigma^2/(3\pi D_0)\approx 3.1$ s for our system with the short-time self-diffusion coefficient $D_0=k_\mathrm{B}T/\gamma$ and the friction coefficient of a particle, γ. Note that we correct for possible drift in the set-up by subtracting the centre-of-mass motion of all particles in the observation volume.

Computer simulations. We simulate a system consisting of M particles with mean diameter σ_0 and a polydispersity of about 7%. The polydispersity is realized by shifting the interaction potentials multiple times corresponding to 17 different particle diameters σ_i, whose numbers M_i are normally distributed with a standard deviation of the diameter of 0.07σ and $M=\sum_i M_i$. If not stated otherwise, $M=9{,}856$.

Particles interact with a potential $V(r_{ij})=V_\mathrm{C}(r_{ij})+V_\mathrm{D}(r_{ij})$ that is composed of a repulsive screened Coulomb part[64]

$$V_\mathrm{C}(r_{ij}) = C_0\left(\frac{2}{2+\kappa\sigma_{ij}}\right)^2\frac{\sigma_{ij}}{r_{ij}}\exp\left[-\kappa(r_{ij}-\sigma_{ij})\right], \tag{1}$$

where $\sigma_{ij}=(\sigma_i+\sigma_j)/2$, and a short-ranged depletion potential according to the continuous Asakura–Oosawa potential[34,65] plus a steep power law potential

$$V_\mathrm{D}(r_{ij}) = -\frac{W_0}{2}\left[2-3\frac{r_{ij}/\sigma_{ij}}{(1+\xi^\mathrm{eff})}+\frac{(r_{ij}/\sigma_{ij})^3}{(1+\xi^\mathrm{eff})^3}\right]+V_\mathrm{H}(r_{ij}). \tag{2}$$

Motivated by the experiments, $\xi^\mathrm{eff}=0.03$ is fixed although in our model this does not necessarily imply that the position of the potential minimum is fixed. The hard interaction of particles at contact is approximated by $V_\mathrm{H}(r_{ij})=H_0(r_{ij}/\sigma_{ij})^{-32}$ (ref. 66). The prefactor W_0 defines the energy scale of the attractive part and the prefactor H_0 the energy scale of the hard-sphere-like potential and is kept constant at $H_0=0.25\,k_\mathrm{B}T$. We cut the potential and the corresponding force at 4σ and shift them to zero at the cut-off distance. In our model, the range of the attractive part in the potential may vary while other parameters are changed. The interaction potential exhibits a minimum $V_\mathrm{min}=V(\sigma_{ij}^\mathrm{eff})$ with the effective diameter σ_{ij}^eff slightly smaller than σ_{ij}. The effective packing fraction $\Phi^\mathrm{eff}=(\pi/6V)\sum_i M_i(\sigma_i^\mathrm{eff})^3=0.2$, with V the volume of the system, is kept constant. For bulk simulations we employ periodic boundary conditions to the cubic simulation boxes. For simulations with parallel flat walls, particles are exposed to an external force, which is defined for the bottom wall as

$$\mathbf{F}_i^\mathrm{ext}(z) = \mathbf{e}_\mathrm{z}\begin{cases} F^\mathrm{wall}\,\mathrm{atan}\left(-\frac{(z-\sigma_i/2)}{10\sigma}\right) & , \quad z<\sigma_i/2 \\ 0 & , \quad \text{else}\end{cases}, \tag{3}$$

where we fix $F^\mathrm{wall}\sigma=10^4 k_\mathrm{B}T$. An analogous force is introduced for the top wall. These forces imply interactions close to hard wall interactions but with a small soft contribution to be suitable for simulations. In our Brownian dynamics simulations particle trajectories are governed by their individual Langevin equations[67]

$$\gamma_i\dot{\mathbf{r}}_i(t) = \mathbf{F}_i(\mathbf{r}_1,\ldots,\mathbf{r}_N)+\mathbf{f}_i(t), \tag{4}$$

with the friction coefficient γ_i and $\langle \mathbf{f}_i(t)\mathbf{f}_j^\mathrm{T}(t')\rangle=2\gamma_i k_\mathrm{B}T\delta_{ij}\delta(t-t')\mathbf{I}_3$, where $\mathbf{f}_j^\mathrm{T}$ is the transpose of $\mathbf{f}_j$, $\mathbf{I}_3$ the three-dimensional unity matrix, γ_i the friction coefficient of a particle with diameter σ_i, and $\delta(t-t')$ and δ_{ij} the Dirac delta and the Kronecker delta, respectively.

As in the experiments, the Brownian time $\tau_\mathrm{B}=\sigma^2/(3\pi D_0)$, with the short-time self-diffusion coefficient $D_0=k_\mathrm{B}T/\gamma$ and the friction coefficient of a particle with average diameter, γ, is used as time scale. The time steps are $10^{-4}\tau_\mathrm{B}$ or less. Starting from an initially randomly distributed ensemble, the systems are equilibrated for 300 τ_B before statistics are gathered, unless stated otherwise.

Data availability. The data from experiments as well as the data of the simulations are available from the corresponding author.

References

1. Angell, C. A. Formation of glasses from liquids and biopolymers. *Science* **267,** 1924–1935 (1995).
2. Liu, A. J. & Nagel, S. R. Nonlinear dynamics: Jamming is not just cool any more. *Nature* **396,** 21–22 (1998).
3. Debenedetti, P. G. & Stillinger, F. H. Supercooled liquids and the glass transition. *Nature* **410,** 259–267 (2001).
4. McKenna, G. B. Glass dynamics: diverging views on glass transition. *Nat. Phys.* **4,** 673–673 (2008).
5. Hunter, G. L. & Weeks, E. R. The physics of the colloidal glass transition. *Rep. Prog. Phys.* **75,** 066501 (2012).
6. Hendricks, J., Capellmann, R. F., Schofield, A. B., Egelhaaf, S. U. & Laurati, M. Different mechanisms for dynamical arrest in largely asymmetric binary mixtures. *Phys. Rev. E* **91,** 032308 (2015).
7. Mattsson, J. *et al.* Soft colloids make strong glasses. *Nature* **462,** 83–86 (2009).
8. Götze, W. & Sjögren, L. Relaxation processes in supercooled liquids. *Rep. Prog. Phys.* **55,** 241 (1992).
9. Santen, L. & Krauth, W. Absence of thermodynamic phase transition in a model glass former. *Nature* **405,** 550–551 (2000).
10. Lin, M. Y. *et al.* Universality in colloid aggregation. *Nature* **339,** 360–362 (1989).
11. Tanaka, H., Meunier, J. & Bonn, D. Nonergodic states of charged colloidal suspensions: repulsive and attractive glasses and gels. *Phys. Rev. E* **69,** 031404 (2004).
12. Sedgwick, H., Egelhaaf, S. U. & Poon, W. C. K. Clusters and gels in systems of sticky particles. *J. Phys. Condens. Matter* **16,** S4913 (2004).
13. Khalil, N., de Candia, A., Fierro, A., Ciamarra, M. P. & Coniglio, A. Dynamical arrest: interplay of glass and gel transitions. *Soft Matter* **10,** 4800–4805 (2014).
14. Royall, C. P. & Williams, S. R. The role of local structure in dynamical arrest. *Phys. Rep.* **560,** 1–75 (2015).
15. Segré, P. N., Prasad, V., Schofield, A. B. & Weitz, D. A. Glass-like kinetic arrest at the colloidal gelation transition. *Phys. Rev. Lett.* **86,** 6042–6045 (2001).
16. Sedgwick, H. *et al.* Non-equilibrium behavior of sticky colloidal particles: Beads, clusters and gels. *Eur. Phys. J. E* **16,** 77–80 (2005).
17. Bergenholtz, J., Poon, W. & Fuchs, M. Gelation in model colloid-polymer mixtures. *Langmuir* **19,** 4493–4503 (2003).
18. Royall, P. C., Williams, S. R., Ohtsuka, T. & Tanaka, H. Direct observation of a local structural mechanism for dynamic arrest. *Nat. Mater.* **7,** 556–561 (2008).
19. de Candia, A., Del Gado, E., Fierro, A., Sator, N. & Coniglio, A. Colloidal gelation, percolation and structural arrest. *Physica A* **358,** 239–248 (2005).
20. Trappe, V. & Sandkühler, P. Colloidal gels—low-density disordered solid-like states. *Curr. Opin. Colloid Interface Sci.* **8,** 494–500 (2004).
21. Zaccarelli, E. Colloidal gels: equilibrium and non-equilibrium routes. *J. Phys. Condens. Matter* **19,** 323101 (2007).
22. Zhang, T. H., Klok, J., Tromp, H. R., Groenewold, J. & Kegel, W. K. Non-equilibrium cluster states in colloids with competing interactions. *Soft Matter* **8,** 667–672 (2012).
23. Dibble, C. J., Kogan, M. & Solomon, M. J. Structure and dynamics of colloidal depletion gels: coincidence of transitions and heterogeneity. *Phys. Rev. E* **74,** 041403 (2006).
24. Dibble, C. J., Kogan, M. & Solomon, M. J. Structural origins of dynamical heterogeneity in colloidal gels. *Phys. Rev. E* **77,** 050401 (2008).
25. Pham, K. N. *et al.* Multiple glassy states in a simple model system. *Science* **296,** 104–106 (2002).
26. Eckert, T. & Bartsch, E. Re-entrant glass transition in a colloid-polymer mixture with depletion attractions. *Phys. Rev. Lett.* **89,** 125701 (2002).
27. Lu, P. J. *et al.* Gelation of particles with short-range attraction. *Nature* **453,** 499–503 (2008).
28. Verduin, H. & Dhont, J. K. G. Phase-diagram of a model adhesive hard-sphere dispersion. *J. Colloid Interface Sci.* **172,** 425–437 (1995).
29. Grant, M. C. & Russel, W. B. Volume-fraction dependence of elastic moduli and transition temperature for colloidal silica gels. *Phys. Rev. E* **47,** 2606–2614 (1993).
30. Poon, W. C. K. The physics of a model colloid-polymer mixture. *J. Phys. Condens. Matter* **14,** R859–R880 (2002).
31. Eberle, A. P. R., Wagner, N. J. & Castañeda Priego, R. Dynamical arrest transition in nanoparticle dispersions with short-range interactions. *Phys. Rev. Lett.* **106,** 105704 (2011).
32. Valadez-Pérez, N. E., Liu, Y., Eberle, A. P. R., Wagner, N. J. & Castañeda Priego, R. Dynamical arrest in adhesive hard-sphere dispersions driven by rigidity percolation. *Phys. Rev. E* **88,** 060302 (R) (2013).
33. Yethiraj, A. & van Blaaderen, A. A colloidal model system with an interaction tunable from hard sphere to soft and dipolar. *Nature* **421,** 513–517 (2003).
34. Asakura, S. & Oosawa, F. Interaction between particles suspended in solutions of macromolecules. *J. Polym. Sci.* **33,** 183–192 (1958).
35. Stradner, A. *et al.* Equilibrium cluster formation in concentrated protein solutions and colloids. *Nature* **432,** 492–495 (2004).
36. Stradner, A., Cardinaux, F., Egelhaaf, S. U. & Schurtenberger, P. Do equilibrium clusters exist in concentrated lysozyme solutions? *Proc. Natl Acad. Sci. USA* **105,** E75 (2008).
37. Godfrin, P. D., Valadez-Pérez, N. E., Castañeda-Priego, R., Wagner, N. J. & Liu, Y. Generalized phase behavior of cluster formation in colloidal dispersions with competing interactions. *Soft Matter* **10,** 5061–5071 (2014).
38. Valadez-Pérez, N. E., Castañeda-Priego, R. & Liu, Y. Percolation in colloidal systems with competing interactions: the role of long-range repulsion. *RSC Adv.* **3,** 25110 (2013).
39. O'Hern, C. S., Langer, S. A., Liu, A. J. & Nagel, S. R. Random packings of frictionless particles. *Phys. Rev. Lett.* **88,** 075507 (2002).

40. O'Hern, C. S., Silbert, L. E., Liu, A. J. & Nagel, S. R. Jamming at zero temperature and zero applied stress: The epitome of disorder. *Phys. Rev. E* **68,** 011306 (2003).
41. Souslov, A., Liu, A. J. & Lubensky, T. C. Elasticity and response in nearly isostatic periodic lattices. *Phys. Rev. Lett.* **103,** 205503 (2009).
42. Stanley, H. E. Cluster shapes at the percolation threshold: An effective cluster dimensionality and its connection with critical-point exponents. *J. Phys. A Math. Gen* **10,** L211 (1977).
43. Bunde, A. & Havlin, S. *Fractals and Disordered Systems* (Springer-Verlag, 1991).
44. Hinrichsen, H. Non-equilibrium critical phenomena and phase transitions into absorbing states. *Adv. Phys.* **49,** 815–958 (2000).
45. Ballesta, P., Petekidis, G., Isa, L., Poon, W. C. K. & Besseling, R. Wall slip and flow of concentrated hard-sphere colloidal suspensions. *J. Rheol.* **56,** 1005–1037 (2012).
46. Kunitz, M. Syneresis and swelling of gelatin. *J. Gen. Physiol.* **12,** 289–312 (1928).
47. Matsuhashi, T. A. & In Harris, P. (ed.). *Food Gels* chap. 1**,** 1–51 (Elsevier Science Publishers LTD, 1990).
48. Divoux, T., Mao, B. & Snabre, P. Synaeresis and delayed detachment in agar plates. *Soft Matter* **11,** 3677–3685 (2015).
49. Mellema, M., Walstra, P., van Opheusden, J. H. J. & van Vliet, T. Effects of structural rearrangements on the rheology of rennet-induced casein particle gels. *Adv. Colloid Interface Sci.* **98,** 25–50 (2002).
50. Wu, J. *et al.* Gelation induced reversible synaeresis via structural evolution. *J. Mater. Chem.* **19,** 3971 (2009).
51. Gan, T., Guan, Y. & Zhang, Y. Thermogelable PNIPAM microgel dispersion as 3D cell scaffold: effect of syneresis. *J. Mater. Chem.* **20,** 5937 (2010).
52. Cipelletti, L., Manley, S., Ball, R. C. & Weitz, D. A. Universal aging features in the restructuring of fractal colloidal gels. *Phys. Rev. Lett.* **84,** 2275–2278 (2000).
53. Hinrichsen, H. Non-equilibrium phase transitions. *Physica A* **369,** 1–28 (2006).
54. Ballesta, P., Koumakis, N., Besseling, R., Poon, W. C. K. & Petekidis, G. Slip of gels in colloid-polymer mixtures under shear. *Soft Matter* **9,** 3237–3245 (2013).
55. Laurati, M., Egelhaaf, S. U. & Petekidis, G. Nonlinear rheology of colloidal gels with intermediate volume fraction. *J. Rheol.* **55,** 673–706 (2011).
56. Walls, H. J., Caines, S. B., Sanchez, A. M. & Khan, S. A. Yield stress and wall slip phenomena in colloidal silica gels. *J. Rheol.* **47,** 847–868 (2003).
57. Leunissen, M. E. *Manipulating Colloids with Charges and Electric Fields* (PhD thesis, Utrecht Univ., 2007).
58. Berry, G. C. Thermodynamic and conformational properties of polystyrene. I. Light-scattering studies on dilute solutions of linear polystyrenes. *J. Chem. Phys.* **44,** 4550 (1966).
59. Fleer, G. J. & Tuinier, R. Analytical phase diagram for colloid-polymer mixtures. *Phys. Rev. E* **76,** 041802 (2007).
60. Lekkerkerker, H. N. W., Poon, W. C. K., Pusey, P. N., Stroobants, A. & Warren, P. B. Phase behaviour of colloid-polymer mixtures. *Europhys. Lett.* **20,** 559–564 (1992).
61. Aarts, D. G. A. L., Tuinier, R. & Lekkerkerker, H. N. W. Phase behaviour of mixtures of colloidal spheres and excluded-volume polymer chains. *J. Phys. Condens. Matter* **14,** 7551–7561 (2002).
62. Jenkins, M. C. & Egelhaaf, S. U. Confocal microscopy of colloidal particles: towards reliable, optimum coordinates. *Adv. Colloid Interface Sci.* **136,** 65–92 (2008).
63. Crocker, J. C. & Grier, D. G. Methods of digital video microscopy for colloidal studies. *J. Colloid Interface Sci.* **179,** 298–310 (1996).
64. Lindsay, H. M. & Chaikin, P. M. Elasticity of colloidal crystals and glasses. *J. Chem. Phys.* **76,** 3774 (1982).
65. Royall, C. P., Aarts, D. G. A. L. & Tanaka, H. Fluid structure in colloid-polymer mixtures: the competition between electrostatics and depletion. *J. Phys. Condens. Matter* **17,** S3401 (2005).
66. Puertas, A. M., Fuchs, M. & Cates, M. E. Simulation study of nonergodicity transitions: Gelation in colloidal systems with short-range attractions. *Phys. Rev. E* **67,** 031406 (2003).
67. Allen, M. & Tildesley, D. *Computer Simulation of Liquids* (Clarendon Press, 1999).

Acknowledgements

We thank Andrew Schofield (University of Edinburgh) for providing the PMMA particles. This work was supported by the International Helmholtz Research School of Biophysics and Soft Matter (IHRS BioSoft) and by the DFG within the Emmy-Noether programme (Schm 2657/2) and grant INST 208/617-1 FUGG funding the confocal microscope.

Author contributions

M.K. performed the simulations, R.F.C. conducted the experiments, M.K. and R.F.C. analysed the data and all authors contributed to the design of the research, the interpretation of the results and the writing of the paper.

Additional information

Supplementary Information accompanies this paper at http://www.nature.com/naturecommunications

Competing financial interests: The authors declare no competing financial interests.

Reprints and permission information is available online at http://npg.nature.com/reprintsandpermissions/

How to cite this article: Kohl, M. *et al.* Directed percolation identified as equilibrium pre-transition towards non-equilibrium arrested gel states. *Nat. Commun.* 7:11817 doi: 10.1038/ncomms11817 (2016).

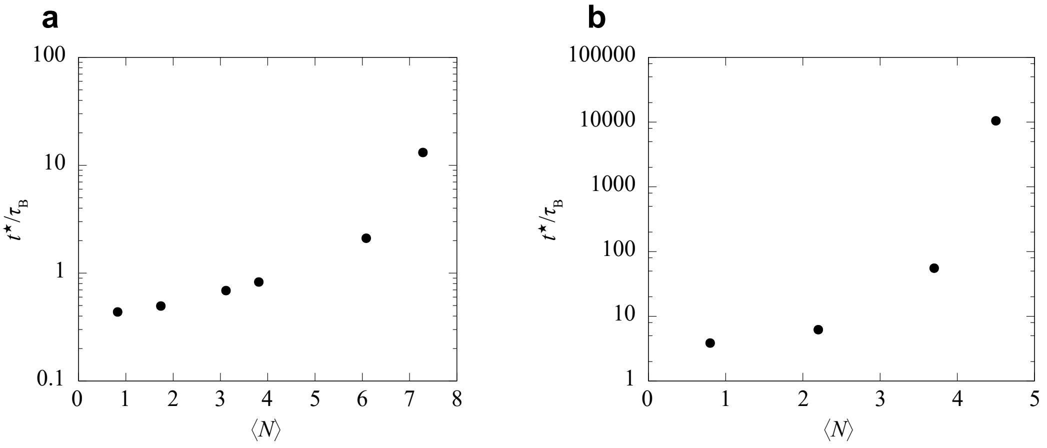

Supplementary Figure 1: Characteristic decay time of the self intermediate scattering function. Characteristic decay time $t^\star$ at which the self intermediate scattering function $F(k,t)$ reaches 0.4, normalized by the Brownian time τ_B, as a function of the mean number of bonds per particle $\langle N \rangle$ as obtained by (a) simulations and (b) experiments. The times $t^\star$ have been determined by fitting a single exponential decay to $F(k,t)$ at short times (Fig. 5).

Sample	$\mathit{\Phi}$	c_p/c_p^*	c_p^{free}/c_p^*	ξ^{eff}	c_{salt} [mM]
B1	0.19	1.46 ± 0.01	1.95 ± 0.01	0.031 ± 0.001	3.5 ± 0.5
B2	0.23	1.54 ± 0.01	2.06 ± 0.01	0.030 ± 0.001	9.4 ± 0.5
B3	0.21	1.55 ± 0.01	2.01 ± 0.01	0.030 ± 0.001	20.1 ± 0.5
C1	0.20	2.25 ± 0.01	2.87 ± 0.01	0.025 ± 0.001	0.0 ± 0.5
C2	0.23	2.24 ± 0.01	2.98 ± 0.01	0.024 ± 0.001	3.2 ± 0.5
C3	0.20	2.25 ± 0.01	2.87 ± 0.01	0.025 ± 0.001	4.0 ± 0.5
C4	0.20	2.24 ± 0.01	2.86 ± 0.01	0.025 ± 0.001	7.8 ± 0.5
C5	0.24	2.24 ± 0.01	3.02 ± 0.01	0.024 ± 0.001	8.4 ± 0.5
D1	0.19	0.76 ± 0.01	0.97 ± 0.01	0.045 ± 0.001	2.8 ± 0.5

Supplementary Table 1: Experimental samples and their compositions. Colloid volume fraction $\mathit{\Phi}$; bulk polymer concentration normalized by the overlap concentration, c_p/c_p^*; free polymer concentration, i.e. in the volume not occupied by the colloids[1–3], normalized by the overlap concentration, c_p^{free}/c_p^*; effective polymer-colloid size ratio ξ^{eff}; salt concentration c_{salt}.

Supplementary Notes

Supplementary Note 1:
Mapping of simulation and experimental parameters

Two aspects are impeding a direct calculation of the interaction potential (Eqs. 1, 2) from the experimental values of the polymer, c_{p}, and salt, c_{salt}, concentrations. The Asakura-Oosawa potential is not quantitatively accurate at the large polymer concentrations and, furthermore, although c_{salt} is well-known experimentally, the amount of salt that is effectively dissolved and/or the conductivity, and hence the ionic strength, cannot be determined accurately enough[4]. The low dielectric constant of the organic solvent mixture also precludes an exact measurement of the zeta potential of the particles[5,6]. Due to these uncertainties, a fitting procedure has been applied to determine the best parameter values of the potential (Eqs. 1, 2), which is guided by the experimentally determined pair correlation functions $g(r)$ (Fig. 1b). This is done following two procedures. First, all parameters are fitted, which provides very good fits to $g(r)$ (Fig. 1b, light blue line) but unreasonable values for C_0, κ and W_0, as explained and discussed in the last paragraph of this Supplementary Note 1. Hence this procedure is not used to obtain the diagram in Fig. 2 but the results are reported for comparison (Figs. 1b, 3c inset). Second, the parameters of the depletion (electrostatic) potential are kept constant along path B (path A) and the knowledge on the sequence of increasing strength and range of the electrostatic (depletion) potential is exploited. (Details are explained in the following.) This yields reasonable values for C_0, κ and W_0, but compromises the quality of the fits somehow. Nevertheless, this procedure is applied to obtain Fig. 2.

Calibration of $\mathbf{C_0}$. The experiments have been carried out with charged particles. The charge of the particles is contained in the interaction parameter C_0 in the electrostatic part of the interaction potential (Eq. 1). Using simulations, C_0 is fitted. The fit is based on the pair correlation function $g(r)$ of a sample without added salt (C1, see Supplementary Table 1) and thus interactions that are dominated by the electrostatic interaction. In the fit, only the parameter C_0 (Eq. 1) is varied and, as suggested by the low salt concentration, $\kappa\sigma = 0.25$ is fixed. Best agreement with the data was obtained for $C_0 = 200\,k_{\mathrm{B}}T$. Consequently, this value was used for all samples. With C_0 fixed, the attraction strength W_0 (Eq. 2) was successively increased.

Fitting based on the mean number of bonds $\langle \mathrm{N} \rangle$. In order to map the experimental samples onto the $V_{\mathrm{D,min}}$– $\kappa\sigma$ plane (Fig. 2), the positions of all samples have been fitted simultaneously based on their mean number of bonds $\langle N \rangle$ and taking into account the following two constraints: First, their relative distances along the $\kappa\sigma$ axis is given by their relative rather than their absolute screening lengths according to Supplementary Table 1. Second, the attraction strengths W_0 corresponding to the three polymer concentrations $c_{\mathrm{p}}^{\mathrm{free}} = [c_{\mathrm{p}}^*, 2c_{\mathrm{p}}^*, 3c_{\mathrm{p}}^*]$ are assumed to differ by at least $4\,k_{\mathrm{B}}T$. Thus, only affine transformations of the sample positions in the $V_{\mathrm{D,min}}$– $\kappa\sigma$ plane are considered in a simultaneous fit of all sample positions. The absolute positions were determined by minimizing the difference between $\langle N \rangle_{\mathrm{sim}}$ and $\langle N \rangle_{\mathrm{exp}}$ as determined in simulations and experiments, respectively, i.e. the minimum Min$\{\sum_{\mathrm{B}_i,\mathrm{C}_i,\mathrm{D}_i} |\langle N_j \rangle_{\mathrm{sim}} - \langle N_j \rangle_{\mathrm{exp}}|\}$, where the individual $\langle N_j \rangle_{\mathrm{sim}}$ are constrained by the allowed affine transformation, as explained above. This fit determines the relative positions of all samples, such that the overall agreement between the mean number of bonds from experiments and simulations are optimized. While this fitting procedure is appropriate for our purposes, there might be small deviations to the precise absolute positions of the experimental samples.

Unconstrained fit. In order to further optimize the individual sample positions within the $V_{\text{D,min}}$– $\kappa\sigma$ plane, we additionally performed a free fit where the parameters are not constrained to any path. This fit is based on the minimization of the absolute error vector $\Delta g(r) = |g_{\text{sim}}(r) - g_{\text{exp}}(r)|$ between the pair correlations in simulations and experiments, respectively, over the interval $[\sigma, 3\sigma]$. Thus, the pair correlation functions, $g(r)$ (Fig. 1b), and the distributions of the angle between two successive bonds, $p(\varphi)$ (Fig. 3c, inset), agree better, but the fitted positions , i.e. $V_{\text{D,min}}$ and κ, are not fully consistent with the compositions of the samples.

Supplementary Note 2:
Characteristic decay time $t^\star$ of the self intermediate scattering function $F(k,t)$ in directed percolated systems

In directed percolated systems the dynamics of the system slows down significantly, which is quantified by the self intermediate scattering function $F(k,t)$ (Fig. 5). The characteristic decay time $t^\star$ of $F(k,t)$ is defined as the time required to reach $F(k,t^\star) = 0.4$. Not all $F(k,t)$ decay to 0.4 in the time windows of the experiments. Thus, a single exponential decay was fitted to $F(k,t)$ at short times with $F(k,0)$ set to the value of the first data point and $F(k,\infty)$ set to 0. This leaves only the characteristic decay time $t^\star$ as free parameter. For consistency, this fitting procedures was applied to simulation and experimental data sets and both data sets are represented as a function of the mean number of bonds per particle $\langle N \rangle$.

The dependencies of $t^\star$ on $\langle N \rangle$ are presented in Supplementary Fig. 1. In simulations as well as in experiments, $t^\star$ increases moderately for small $\langle N \rangle$, but increases by several orders of magnitude for large $\langle N \rangle$ that correspond to directed percolation. This trend is consistently observed in simulations and experiments. Note that the experimental and simulation results cannot be compared directly, because they are determined along different paths.

Supplementary References

[1] Fleer, G. J. & Tuinier, R. Analytical phase diagram for colloid-polymer mixtures. *Phys. Rev. E* **76**, 041802 (2007).

[2] Lekkerkerker, H. N. W., Poon, W. C. K., Pusey, P. N., Stroobants, A. & Warren, P. B. Phase behaviour of colloid-polymer mixtures. *Europhys. Lett.* **20**, 559–564 (1992).

[3] Aarts, D. G. A. L., Tuinier, R. & Lekkerkerker, H. N. W. Phase behaviour of mixtures of colloidal spheres and excluded-volume polymer chains. *J. Phys.: Condens. Mat.* **14**, 7551–7561 (2002).

[4] Dukhin, A. & Parlia, S. Ions, ion pairs and inverse micelles in non-polar media. *Curr. Opin. Coll. Interf. Sci.* **18**, 93–115 (2013).

[5] Miller, J. F., Schätzel, K. & Vincent, B. The determination of very small electrophoretic mobilities in polar and nonpolar colloidal dispersions using phase analysis light scattering. *J. Coll. Interf. Sci.* **143**, 532–554 (1991).

[6] McNeil-Watson, F., Tscharnuter, W. & Miller, J. A new instrument for the measurement of very small electrophoretic mobilities using phase analysis light scattering (PALS). *Colloids Surf. A Physicochem. Eng. Asp.* **140**, 53–57 (1998).

3.3 Different mechanisms for dynamical arrest in largely asymmetric binary mixtures

Journal: Physical Review E

Reference: *Phys. Rev. E* **91**, 032308 (2015)

Impact factor: 2.366

Authors: Jan Hendricks, **Ronja Capellmann**, Andrew B. Schofield, Stefan U. Egelhaaf, and Marco Laurati

2nd author

J. H. performed the experiments, J. H. and R. F. C. contributed to the analysis of the data, A. B. S. synthesized colloidal particles, J. H., M. L. and S. U. E. conceived the research and interpreted the results and all authors contributed to the writing of the paper.

10% contribution of R. F. C.

This page has been left intentionally blank.

PHYSICAL REVIEW E **91**, 032308 (2015)

Different mechanisms for dynamical arrest in largely asymmetric binary mixtures

J. Hendricks,[1] R. Capellmann,[1] A. B. Schofield,[2] S. U. Egelhaaf,[1] and M. Laurati[1,*]
[1]*Condensed Matter Physics Laboratory, Heinrich-Heine University, Universitätsstr. 1, 40225 Düsseldorf, Germany*
[2]*SUPA, School of Physics & Astronomy, University of Edinburgh, Peter Guthrie Tait Road, Edinburgh EH9 3FD, United Kingdom*

(Received 6 November 2014; revised manuscript received 30 January 2015; published 16 March 2015)

Using confocal microscopy we investigate binary colloidal mixtures with large size asymmetry, in particular the formation of dynamically arrested states of the large spheres. The volume fraction of the system is kept constant, and as the concentration of small spheres is increased we observe a series of transitions of the large spheres to different arrested states: an attractive glass, a gel, and an asymmetric glass. These states are distinguished by the degree of dynamical arrest and the amount of structural and dynamical heterogeneity. The transitions between two different arrested states occur through melting and the formation of a fluid state. While a space-spanning network of bonded particles is found in both arrested and fluid states, only arrested states are characterized by the presence of a space-spanning network of dynamically arrested particles.

DOI: 10.1103/PhysRevE.91.032308 PACS number(s): 64.70.pv, 61.43.−j, 63.50.Lm, 83.80.Kn

I. INTRODUCTION

The glass transition in model one-component hard-sphere colloidal dispersions has been the subject of many studies [1–7]. The formation of a glass state for volume fractions $\phi > 0.58$ is due to the dynamical arrest of particles in cages formed by their neighbors. Only activated processes can release the constraints that limit the motion of the particles to the in-cage space and then lead to diffusion [6].

Addition of a second component with a different size affects the glass transition [8–23]. For moderate size disparities, $\delta = R_s/R_L \gtrsim 0.35$, mixing particles with different radii R_s and R_L, respectively, results in a shift of the glass transition to larger total volume fractions ϕ, similar to the effect of polydispersity [8–10]. On the other hand if the size disparity is larger, $\delta \lesssim 0.35$, depending on the mixing ratio $x_s = \phi_s/\phi$, with ϕ_s the volume fraction of small spheres, different glass states have been predicted by mode-coupling theory (MCT) and the self-consistent generalized Langevin equation theory (SCGLE) [10–12,16].

The different glass states are distinguished by the arrest mechanism of the large spheres and the mobility of the small spheres. At small x_s, a double glass is expected, in which both species are arrested through caging of spheres of the same species, and in addition the large particles might be bonded. At intermediate x_s a single glass occurs, in which only the large particles are arrested while the small particles are still mobile; for $\delta \gtrsim 0.2$ the large particles are expected to always form an attractive glass, while for smaller δ a repulsive glass is also predicted. At large x_s, an asymmetric or *torroncino* glass forms, in which the large particles are localized in a glass of small spheres. Furthermore, it has been proposed that equilibrium gel states of the large spheres form at intermediate x_s due to the oscillatory form of the effective potential [16].

The existence of some of these states has been verified in experiments and simulations. A transition from a double glass to an asymmetric glass was recently observed in experiments for $\delta = 0.2$ [18,19], showing similarities with simulations on soft spheres [14,15] and asymmetric mixtures of star polymers [24,25]. This change in caging mechanism is responsible for glass softening, facilitated yielding and acceleration of the dynamics of the large particles under shear at intermediate x_s [18,19]. Dynamically arrested states of the large spheres in which the smallest component remains mobile have been observed experimentally at $\delta \approx 0.1$ [13] and in simulations [14,15].

Despite these findings, a systematic investigation of dynamically arrested states in largely asymmetric hard-sphere mixtures with $\delta \lesssim 0.2$ is still missing. In particular an experimental characterization of the theoretically predicted different arrested states of the large spheres as a function of the composition x_s and the total volume fraction ϕ and a discussion of the role of depletion interactions and bonding at these large size disparities are still missing.

Here we investigate, using confocal microscopy and particle tracking, the occurrence of dynamically arrested states in binary mixtures of hard-sphere colloids with size ratio $\delta \approx 0.09$ and fixed total volume fraction $\phi \approx 0.60$ [26]. We analyze the average dynamics of the large particles in the mixtures through the mean squared displacements to reveal dynamically arrested states, and we determine the presence and spatial distribution of dynamical heterogeneities. We complement this dynamical information with information on the arrangement of the large particles, namely, their pair distribution function, the distribution of the number of bonds, and the organization of bonded particles into clusters and eventually into a network, as well as the degree of structural heterogeneity. Combining the dynamical and structural information we reveal the existence of repulsive and attractive glasses at small x_s, a gel state at intermediate x_s, and an asymmetric glass of clusters at large x_s. The transition between the glass states involves the melting of the glasses and the occurrence of fluid states.

II. MATERIALS AND METHODS

A. Samples

The samples are mixtures of polymethylmethacrylate (PMMA) colloids with radii of the large spheres $R_L = 720 \pm 30$ nm (labeled with NBD), as determined by static light scattering, and radii of the small spheres $R_s = 65 \pm 10$ nm

---

[*] marco.laurati@uni-duesseldorf.de

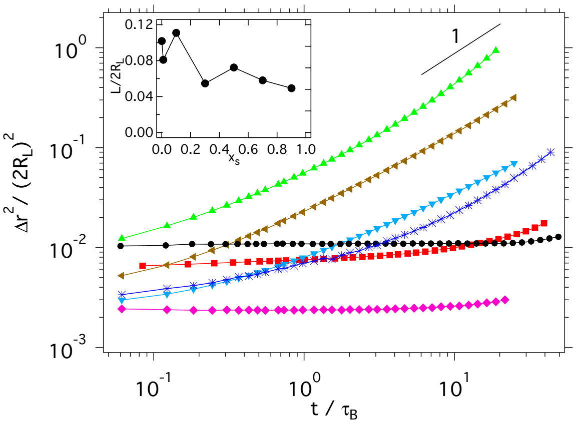

FIG. 1. (Color online) Mean squared displacements of the large spheres, $\Delta r^2/(2R_\mathrm{L})^2$, for samples with total volume fraction $\phi \approx 0.60$, size ratio $\delta = 0.09$, and different compositions $x_\mathrm{s} = 0.0$ (●), 0.01 (■), 0.1 (▲), 0.3 (▼), 0.5 (◀), 0.7 (∗), 0.9 (♦). Inset: Localization length $L/(2R_\mathrm{L})$ as a function of x_s.

(labeled with DiIC$_{18}$), as determined by dynamic light scattering, corresponding to a size ratio $\delta = R_\mathrm{L}/R_\mathrm{s} = 0.09$. The polydispersity of the large spheres, $\sigma_\mathrm{L} \approx 13\%$, was also estimated by static light scattering. For the small spheres, the absence of crystallization in the quiescent and sheared state suggests $\sigma_\mathrm{s} > 12\%$ [27]. Particles are dispersed in a mixture of cis-decalin and cyclohexylbromide (CHB), which closely matches their density and refractive index. In this solvent mixture the particles acquire a charge, which is screened by adding 4 mM tetrabutylammoniumchloride (TBAC) [28]. Under these conditions the particle interactions are hard-spherelike [26].

A sediment of the large particles with $\phi = 0.66$, as estimated from comparison with numerical simulations [29], is diluted to yield a one-component dispersion of large spheres with $\phi \approx 0.60$, where, following a recent study [30], the uncertainty $\Delta\phi$ can be as large or above 3%. Nevertheless the arrested dynamics of this dispersion (Fig. 1) indicate $\phi > 0.58$. The sample of large spheres with $\phi \approx 0.60$ is used as a reference. The volume fraction of a glass sample containing only small particles is adjusted in order to obtain comparable linear viscoelastic moduli after normalization of the viscoelastic moduli with the energy density $3k_\mathrm{B}T/4\pi R^3$, where $k_\mathrm{B}T$ is the thermal energy, and the frequency by the inverse free-diffusion Brownian time $\tau_0^{-1} = D_0/R^2 = k_\mathrm{B}T/6\pi\eta R^3$, where $\eta = 2.2$ mPa s is the solvent viscosity. For our system the ϕ-dependent short-time Brownian time of the large spheres was estimated as $\tau_\mathrm{B} = R_\mathrm{L}^2/D_\mathrm{L}(\phi) \approx 56$ s, with $D_\mathrm{L}(\phi) = f(\phi)D_0^L$ the ϕ-dependent long-time diffusion coefficient. The factor $f(\phi)$ was estimated by extrapolating the data in Fig. 8 of Ref. [3] to $\phi = 0.60$, yielding $f \approx 1/30$. The viscoelatic moduli of the two one-component glass samples were measured using a stress controlled AR2000ex rheometer and a cone-plate geometry (see Ref. [18] for additional details). In this way we obtain samples with comparable rheological properties and, according to the generalized Stokes-Einstein relation [31], also dynamics and hence a similar location with respect to the glass transition. The comparable dynamics but different polydispersities of the one-component samples imply slightly different ϕ.

Samples with constant total volume fraction $\phi \approx 0.60$ and different compositions, namely, fractions of small particles $x_\mathrm{s} = \phi_\mathrm{s}/\phi$, where ϕ_s is the volume fraction of small particles, are prepared by mixing the one-component samples. Despite the relatively large uncertainty in ϕ, the important control parameter of our study, x_s, has a small uncertainty, less than 1%. This is achieved by weighting the one-component samples before mixing. The mixture was successively homogenized in a vortex mixer for a few minutes and in a roller mixer for at least 12 hours.

B. Confocal microscopy

Confocal microscopy measurements were performed using a Nikon A1R-MP confocal scanning unit mounted on a Nikon Ti-U inverted microscope, with a 60× Nikon Plan Apo oil immersion objective (NA = 1.40). Each stack consists of 100 frames of 512×512 pixels acquired at a rate of 30 fps, except for $x_\mathrm{s} = 0$ and 0.01, for which each stack consists of 150 frames of 512×512 pixels. One stack corresponds to a volume of approximately $72 \times 72 \times 30\ \mu\mathrm{m}^3$ ($x_\mathrm{s} = 0.0$ and 0.01) or $72 \times 72 \times 20\ \mu\mathrm{m}^3$ ($0.1 \leqslant x_\mathrm{s} \leqslant 0.9$). Time series of 500 stacks were acquired for five different volumes for each sample, except for $x_\mathrm{s} = 0.0$ for which 1000 stacks were acquired. The total measurement time of a time series is $t_\mathrm{meas} \approx 30\tau_B$ ($0.1 \leqslant x_\mathrm{s} \leqslant 0.9$), $60\tau_B$ ($x_\mathrm{s} = 0.0$), and $44\tau_B$ ($x_\mathrm{s} = 0.01$), respectively. Coordinates and trajectories of the large particles were extracted from the time series using standard particle tracking routines [32].

III. RESULTS AND DISCUSSION

A. Dynamics

1. *Mean squared displacement and distribution of displacements*

Based on the time series of three-dimensional confocal microscopy stacks of images, particle trajectories were determined and used to calculate mean squared displacements (MSDs) $\Delta r^2(t)$ of the large spheres in mixtures with different compositions (Fig. 1):

$$\Delta r^2(t) = \left\langle r_i^2(t,t_0) - r_i^2(t_0)\right\rangle_{i,t_0}, \qquad (1)$$

where t is the delay time, t_0 a time during the trajectory of a particle i, and $\langle\ \rangle_{i,t_0}$ indicates the average over all particles i in the observation volume and all times t_0.

The one-component system of large spheres ($x_\mathrm{s} = 0.0$) presents arrested dynamics, as indicated by the plateau of the MSD extending to long delay times, with particles localized on a length scale $L/2R_\mathrm{L} = \sqrt{\Delta r^2(t_\mathrm{min})}/2R_\mathrm{L} \approx 0.1$, with t_min the minimum delay time at which the MSD was measured. (Note that in samples with a less well established plateau at t_min, the value of the localization length L is only indicative.) The value $L/2R_\mathrm{L} \approx 0.1$ is characteristic of a colloidal hard-sphere glass, in which particles are caged by nearest neighbors. Consistent with this observation, the distributions of particle displacements in x direction, $P(\Delta x)$, calculated for different

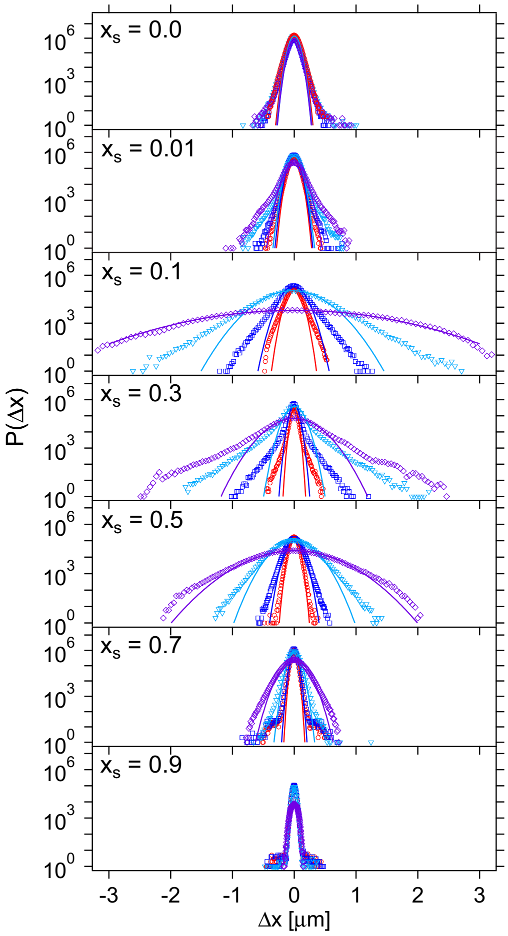

FIG. 2. (Color online) Distributions of displacements of the large spheres in x direction, $P(\Delta x)$, over delay times $\Delta t/\tau_B = 0.06$ (○), 0.3 (□), 3.0 (▽), 18.0 (◇) for samples with $\phi \approx 0.60$, $\delta = 0.09$, and different compositions x_s, as indicated. Lines represent Gaussian fits.

delay times t (Fig. 2) show hardly any evolution of the dynamics and the presence of small non-Gaussian tails, characteristic of glassy systems [5,33]. The distributions in y and z directions show similar results. For $x_s = 0.01$, the dynamics are still arrested, again indicating a glass state, with an even smaller localization length, $L/2R_L \approx 0.08$. A smaller localization length indicates a tightening of the cage. Since the volume fraction of large spheres is slightly smaller than for $x_s = 0.0$, the tightening of the cage is expected to result from the intercalation of small spheres in between large spheres and/or the exclusion of small spheres from depletion zones between large spheres, thus inducing an effective attraction (bonds) between the large spheres (see below). At long times the dynamics appear to be slightly faster than for $x_s = 0.0$. Furthermore, the distribution of displacements $P(\Delta x)$ shows comparable Gaussian contributions as the sample with $x_s = 0.0$, but more pronounced non-Gaussian tails, which indicate that the dynamics is significantly more heterogeneous (Fig. 2).

The dynamics of the mixture with $x_s = 0.1$ are not arrested (Fig. 1). Diffusive behavior is encountered at long times, while a localization plateau might exist at very short times. Due to the absence of a clear plateau, only an upper bound can be estimated for the localization length, $L/2R_L \lesssim 0.1$, which, if it exists, is smaller than that of the one-component glass. The displacement distributions $P(\Delta x)$ indicate fast dynamics, but, at short and intermediate times, also the presence of pronounced non-Gaussian tails, which again indicate significant dynamic heterogeneities. At longer times, when particles begin to diffuse, the non-Gaussian tails disappear (Fig. 2).

Increasing the amount of small spheres to $x_s = 0.3$ induces a reentrant behavior. The dynamics considerably slow down and show a subdiffusive behavior (Fig. 1). The subdiffusive dynamics suggest the presence of a broad distribution of particle mobilities, and possibly dynamical heterogeneities. This is confirmed by $P(\Delta x)$, which shows a relatively narrow, Gaussian central peak, and very long, almost exponential tails reflecting large displacements of some particles (Fig. 2). The concave shape of the tails at long times is qualitatively different from all other samples. Moreover, the localization length, $L/2R_L \lesssim 0.055$, becomes significantly smaller than that of samples with $x_s = 0.0$ and 0.01. The small localization length indicates a pronounced tightening of the cage, which again might be associated with particle-particle bonding or intercalation of small particles in between large particles (see below).

For $x_s = 0.5$ the dynamics become faster and, while still slightly subdiffusive, approach diffusion at long times. The localization length, $L/2R_L \approx 0.07$, is also significantly larger compared to $x_s = 0.3$. The non-Gaussian tails in $P(\Delta x)$ are considerably less pronounced and have a different shape than for $x_s = 0.3$, suggesting less heterogeneous dynamics. Further increasing the amount of small spheres to $x_s = 0.7$ the dynamics slow down but are still almost diffusive. Furthermore, the non-Gaussian contributions in $P(\Delta x)$ are much smaller than for $x_s = 0.5$, indicating a decreasing dynamical heterogeneity. At the same time, the localization length, $L/2R_L \approx 0.056$ is smaller than for $x_s = 0.5$ and rather comparable to $x_s = 0.3$. For $x_s = 0.9$ the dynamics are again arrested and the localization length becomes even smaller, $L/2R_L \approx 0.05$, about a factor 2 smaller than in the one-component glass of large particles (Fig. 1). Also $P(\Delta x)$ is very narrow with hardly any evolution of the dynamics and very small non-Gaussian tails (Fig. 2). In summary, both the localization length L and the degree of diffusivity of the long-time dynamics indicate a bimodal shape as a function of x_s, which reflects the transition between different arrested states, characterized by melting and the formation of fluid states.

2. *Spatial distribution of mobile particles*

Beyond the average dynamics of the large particles, quantified by $\Delta r^2(t)$ and $P(\Delta x)$, we investigated the spatial distribution of single particle mobilities, in particular whether they show spatial heterogeneities [34], and whether they are related to the spatial distribution of the small spheres. The particles which, in a given sample, perform the 20% largest displacements over a time interval of about $\tau_B/4$ are identified and highlighted in Fig. 3 [35]. Qualitatively similar results are obtained for longer time intervals; time intervals up to $5\tau_B$ are

3.3 Different mechanisms for dynamical arrest in largely asymmetric binary mixtures

examined. In the fluid samples the dynamical heterogeneities reduce once the diffusive regime is reached.

In the one-component glass of large spheres, $x_s = 0.0$, the particles with a large mobility appear to be grouped in small clusters, which are randomly distributed in the sample. For $x_s = 0.01$, the 20% fastest particles are still distributed throughout the sample, but seem to coincide with regions with only few large spheres and a clear majority of small particles (which are not visible and therefore appear as voids in the images). This correlation becomes particularly evident in mixtures with $x_s = 0.1$, 0.3, and 0.5. This suggests that contact with the more mobile small spheres enhances the dynamics of the large spheres, as already observed in mixtures with smaller size asymmetry [36,37]. Further increasing x_s, the large particles become more dilute and hence the voids expand. Concomitantly, the most mobile particles again become more homogeneously distributed in the sample.

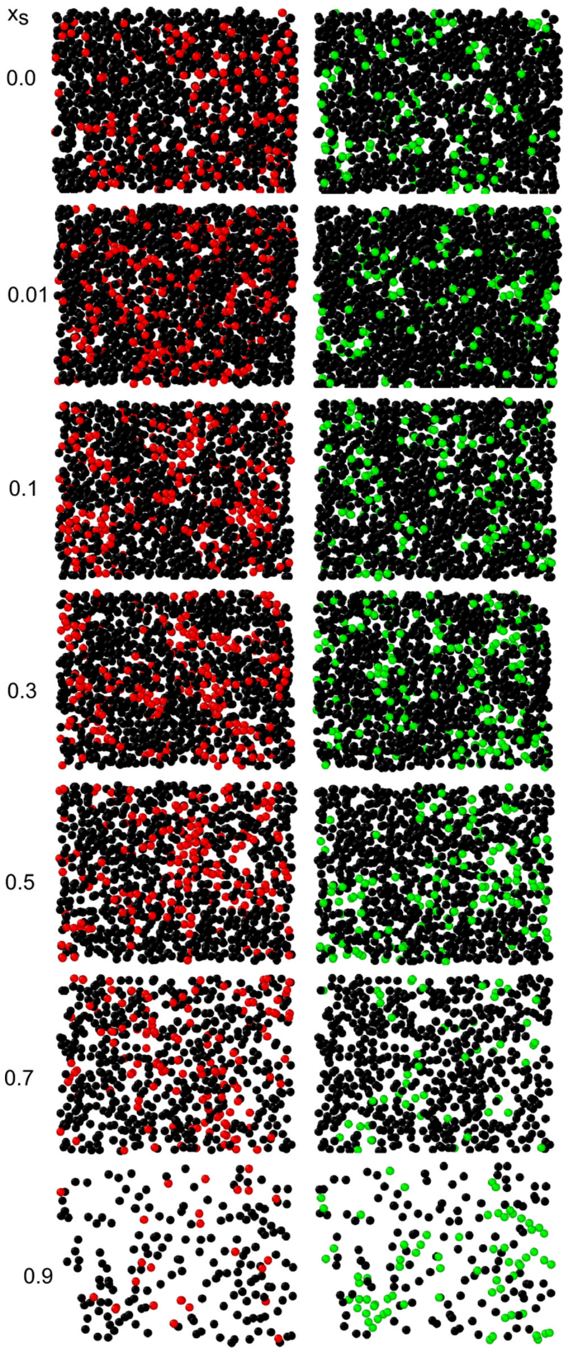

FIG. 3. (Color online) Rendering of 3 μm thick slices of a central region of 44×33 μm^2, in the bulk of samples with $\phi \approx 0.60$, $\delta = 0.09$ and different compositions x_s (as indicated) as obtained from coordinates extracted from confocal microscopy images. Left: Large particles with the 20% largest displacements over a time interval of about $\tau_B/4$ are shown in red (light gray). Right: Large particles with the 20%–30% smallest number of bonds per particle are shown in green (light gray). The small particles are not shown.

B. Structure

1. Pair distribution function

The particle positions calculated using the confocal micrographs allow us to determine the pair distribution function $g(r) = N(r)/4\pi\rho r^2\,dr$, with $N(r)$ the number of particles in a shell of thickness dr at distance r from a selected particle and $\rho = 3\phi/(4\pi R_L^3)\{1 - x_s(1 - 1/\delta^3)\}$ the average bulk number density of colloids (Fig. 4). For all x_s the $g(r)$ indicate an amorphous ordering, with the first peak representing the first shell of nearest neighbors and the following peaks the successive shells. The increasing dilution of the large spheres with increasing x_s is evident in the snapshots in Fig. 3 and also in the $g(r)$ for small and large x_s; the first peak decreases and shifts to larger interparticle distances, and the fluctuations at longer distances become less pronounced. However, at intermediate x_s, additional effects like bonding and structural heterogeneity, also visible in Fig. 3, lead to nonmonotonic and nontrivial variations of the heights, areas, and positions of the peaks and minima as a function of x_s (Fig. 5).

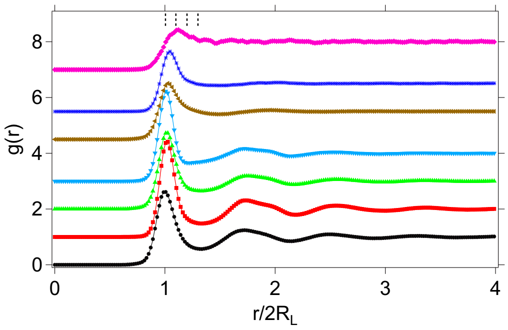

FIG. 4. (Color online) Pair distribution function $g(r)$ of large particles with radius R_L in mixtures with $\phi \approx 0.60$, $\delta = 0.09$ and different compositions $x_s = 0.0$ (•), 0.01 (■), 0.1 (▲), 0.3 (▼), 0.5 (◀), 0.7 (*), 0.9 (♦). Data for $x_s > 0$ are shifted vertically for clarity. Dashed lines indicate particle-particle distances $r = 2R_L$, $r = 2(R_L + R_s)$, $r = 2(R_L + 2R_s)$, and $r = 2(R_L + 3R_s)$.

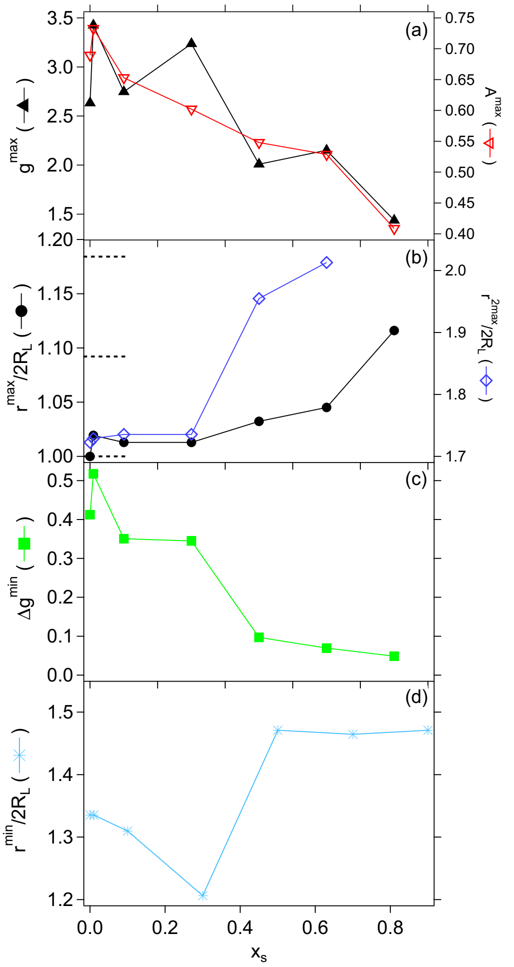

FIG. 5. (Color online) (a) Value of the pair distribution function $g(r)$, shown in Fig. 4, at the first peak, $g^{\max}$ (left y axis) and peak area $A^{\max}$(right y axis), (b) position of the first peak $r^{\max}/2R_{\mathrm{L}}$ (left y axis) and second peak $r^{2\max}/2R_{\mathrm{L}}$ (right y axis), dashed lines indicate particle-particle distances $r = 2R_{\mathrm{L}}$, $r = 2(R_{\mathrm{L}}+R_{\mathrm{s}})$, $r = 2(R_{\mathrm{L}}+2R_{\mathrm{s}})$, (c) depth of the first minimum $\Delta g^{\min} = 1 - g(r^{\min})$, and (d) position of the first minimum $r^{\min}/2R_{\mathrm{L}}$, as a function of x_{s}.

Upon addition of a tiny fraction of small spheres, i.e., from $x_{\mathrm{s}} = 0.0$ to $x_{\mathrm{s}} = 0.01$, the height $g^{\max}$ and area $A^{\max}$ of the first peak increase, while its position $r^{\max}$ shifts to slightly larger values [Figs. 5(a) and 5(b)]. Thus, while the large spheres are slightly diluted and hence the peak is shifted, their contacts are more pronounced, suggesting the formation of particle-particle bonds. Hence the reduction of the localization length in the MSD of this sample (Fig. 1) seems to be associated to bond formation rather than to the intercalation of small particles between the large spheres, which is supported by the fact that $r^{\max} < 2(R_{\mathrm{L}}+R_{\mathrm{s}})$.

With the addition of a larger fraction of small spheres, $x_{\mathrm{s}} = 0.1$, the first peak remains at approximately the same position, but its height $g^{\max}$ and area $A^{\max}$ decrease, and it becomes broader [Figs. 4, 5(a), and 5(b)], indicating a smaller number of particles in the first shell of neighbors. In contrast, the first minimum shifts to smaller distances and becomes less pronounced [Figs. 4, 5(c), and 5(d)]. A less pronounced first peak could be related to the increasing dilution of the large spheres, but, together with its broadening and the shifted and flatter first minimum, might also indicate a more heterogeneous structure, possibly associated with cluster formation. An increase of the structural heterogeneity is also evidenced by the snapshots shown in Fig. 3 and will be discussed in more detail below.

For $x_{\mathrm{s}} = 0.3$ the first peak increases in height but decreases in area with respect to $x_{\mathrm{s}} = 0.1$ while it remains at the same position [Figs. 4, 5(a), and 5(b)]. This suggests that on average there are less particles in the first shell, which, however, tend to be in closer contact. The first minimum shifts to considerably smaller distances [Figs. 4 and 5(d)]. Its depth is comparable to that of $x_{\mathrm{s}} = 0.1$ [Figs. 4 and 5(c)], but it is much more extended with the second maximum becoming less pronounced (Fig. 4). This indicates a further increase of structural heterogeneity, which is also evident in the snapshots of Fig. 3 and might reflect the dynamical heterogeneities described above (Sec. III A).

Further increasing x_{s} to 0.5 the height $g^{\max}$ and area $A^{\max}$ of the first peak decrease significantly and the first peak moves to larger values of r [Figs. 4, 5(a), and 5(b)]. At the same time the peak broadens and an extended shoulder is observed in between the main peak and the first minimum at $r/2R_{\mathrm{L}} \approx 1.5$, which is also more pronounced [Figs. 4 and 5(c)]. The relatively weak second maximum is now located at $r/2R_{\mathrm{L}} \approx 2.0$, i.e., at a distance corresponding to a second spherical shell of neighbors. The shift of the peaks and minimum to larger distances, and the decrease of the first peak height $g^{\max}$ and area $A^{\max}$, are consistent with the progressive dilution of the large spheres, their looser structural organization and the reduction of the number of particle contacts. At the same time, the reduction of the peak and its broadening with an extended shoulder between the first peak and first minimum also indicate the presence of structural heterogeneity, also visible in Fig. 3.

If the fraction of small spheres is further increased to $x_{\mathrm{s}} = 0.7$ and 0.9, the first and second peaks again shift to larger distances, and the first peak height $g^{\max}$ and area $A^{\max}$ are reduced [Figs. 4, 5(a), and 5(b)]. The first minimum, while staying at the same location, becomes increasingly more shallow [Figs. 4, 5(c), and 5(d)]. Furthermore, the shoulder in between the main peak and first minimum is less pronounced at $x_{\mathrm{s}} = 0.7$ and disappears at $x_{\mathrm{s}} = 0.9$ (Fig. 4). This suggests that the structural organization of the large spheres tends to that of a fluid of isolated large particles and the large particles appear as homogeneously distributed impurities in the dense structure of small spheres (Fig. 3). For $x_{\mathrm{s}} = 0.9$, however, $g(r)$ is significantly different from that of a one-component dispersion of large spheres with volume fraction $\phi(1 - x_{\mathrm{s}}) = 0.06$. The first peak is observed at $r \approx 2R_{\mathrm{L}}+2R_{\mathrm{s}}$, corresponding to a configuration in which two large particles are separated by a small particle, an “extended dimer configuration.” The existence of such dimers is attributed to the depletion interactions at this large size disparity.

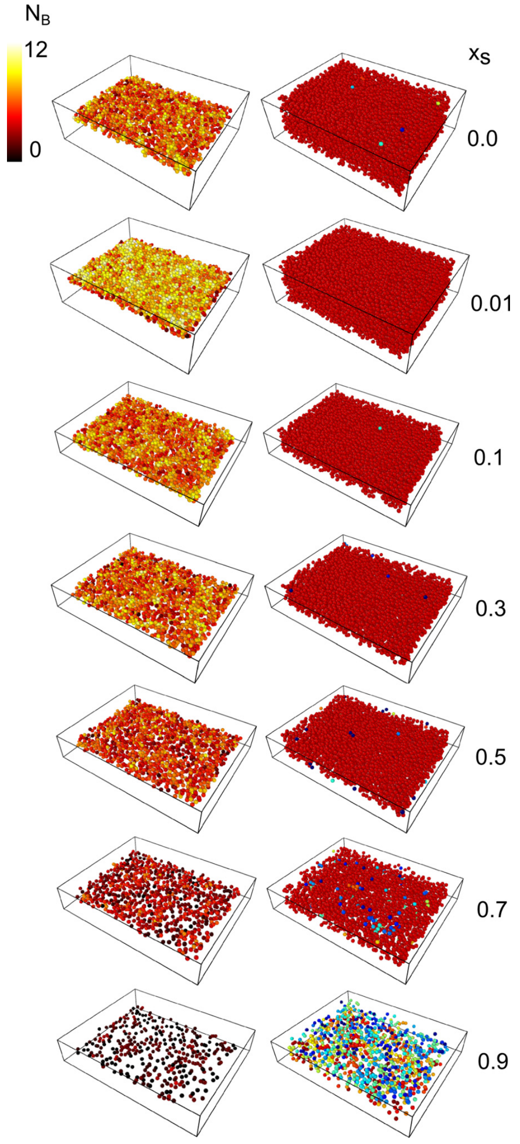

FIG. 6. (Color online) Left: Rendering of $4\,\mu$m thick slices of area $58 \times 42\,\mu\mathrm{m}^2$ in the bulk of samples with $\phi \approx 0.60, \delta = 0.09$ and different compositions x_s (as indicated) as obtained from coordinates extracted from confocal microscopy images. (Left) Large particles have different color (gray-scale value) according to their number of bonds N_B (as indicated). (Right) Large particles pertaining to the same cluster are indicated with the same color (gray-scale value). The small particles are not shown.

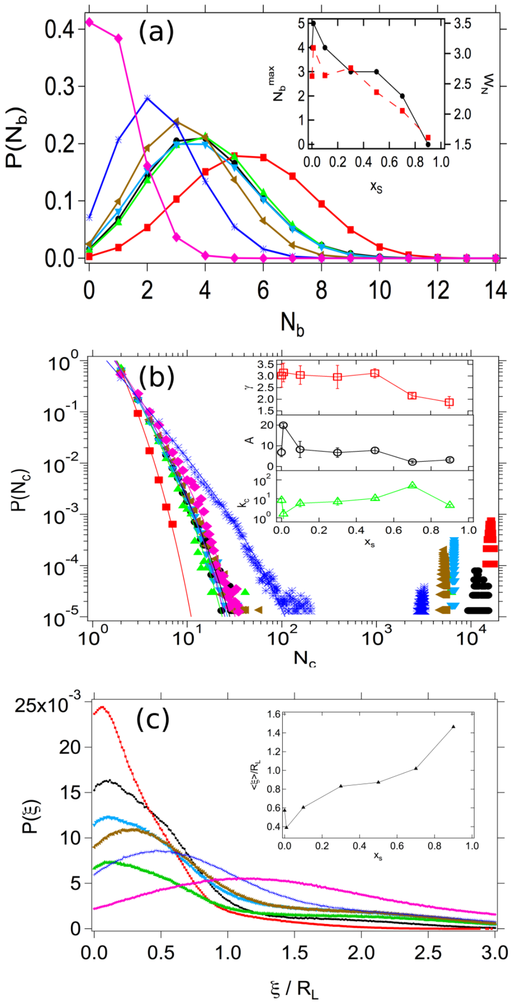

FIG. 7. (Color online) (a) Distribution of the number of bonds N_b per large particle, $P(N_b)$. Inset: Most likely number of bonds $N_b^{\max}$ (●, left axis) and width W_N of $P(N_b)$ (🟥, right) as a function of composition x_s. (b) Cluster size distribution $P(N_c)$, with N_c the number of particles forming the cluster. Lines are fits of a power-law dependence $f(N_c) = A N_c^{-\gamma} \exp(-N_c/k_c)$. Inset: Fit parameters A, γ, and k_c as a function of x_s (c) Remoteness distribution, $P(\xi)$, Inset: Average remoteness $\langle \xi \rangle$ as a function of x_s. The mixtures had $\phi \approx 0.60, \delta = 0.09$ and different compositions $x_s = 0.0$ (●), 0.01 (🟥), 0.1 (▲), 0.3 (▼), 0.5 (◀), 0.7 (*), 0.9 (♦).

2. Particle bonds and cluster sizes

We analyzed in more detail the formation and rearrangement of network structures by determining the number of bonds per particle, N_b, as well as its distribution, $P(N_b)$. Two particles are considered bonded if their centers are closer than the first minimum of $g(r)$ of the sample with $x_s = 0.0$, i.e., if $r \leqslant 2.85 R_L$. We verified that slightly different definitions of the bond length do not qualitatively affect the results. The samples are then rendered with the particles colored according to their number of bonds (Fig. 6, left) [35] and the corresponding distribution of the number of bonds $P(N_b)$ is calculated taking into account and averaging all stacks of a time series [Fig. 7(a)]. For the one-component purely repulsive hard-sphere glass also particle-particle bonds are identified due to the definition of the bond length (Fig. 6, left). The distribution of bonds per particle presents a maximum for $N_b^{\max} = 4$ [Fig. 7(a)]. For $x_s = 0.01$, there is a significant increase in N_b (Fig. 6) and, accordingly, the distribution shifts to larger values of N_b, with the maximum occurring at $N_\mathrm{b}^\mathrm{max} = 5$, and becomes broader [Fig. 7(a)]. The number of bonds decreases again for $x_\mathrm{s} = 0.1$ (Fig. 6), and the distribution is almost identical to that of $x_\mathrm{s} = 0.0$, suggesting that small particles start to intercalate between large particles breaking part of the bonds present for $x_\mathrm{s} = 0.01$. Upon a dilution of the large spheres to $x_\mathrm{s} = 0.3$, N_b remains almost unchanged (Fig. 6) with only a slight shift of the distribution $P(N_\mathrm{b})$ to smaller values. This can be attributed to the formation of clusters within which large particles maintain their average number of bonds due to the increased local concentration of large particles. This implies that the sample becomes heterogeneous on a mesoscopic length scale, as also suggested by the increased width of $P(N_\mathrm{b})$ [Fig. 7(a)]. Upon further increasing x_s, however, N_b considerably decreases (Fig. 6) and the distribution shifts to progressively smaller values of N_b and becomes narrower, suggesting a decreasing structural heterogeneity. Nevertheless, bonds are present in all samples, including $x_\mathrm{s} = 0.9$, where a significant number of dimers is found, consistent with our other findings. The x_s dependence of N_b closely resembles that of A^max, as expected from the criterion chosen to define a bond. Furthermore, the width of the distributions, W_N, presents a bimodal shape as a function of x_s, similar to that of the localization length L and the maximum of $g(r)$. Bonded large particles organize into clusters of different sizes, i.e., different numbers of large particles N_c belonging to the same cluster, that eventually connect to form a network. This is illustrated in Fig. 6, which shows rendered sample volumes, with particles pertaining to the same cluster having the same color. It is evident that for $x_\mathrm{s} \leqslant 0.7$ a percolating network of bonded particles spans the whole system. This is confirmed by the distribution of cluster sizes, $P(N_\mathrm{c})$ [Fig. 7(b)]. Most of the particles organize into one big cluster representing the space spanning network [the data points at the far right in Fig. 7(b)], while also a few small clusters, composed of at most 100 particles, are present in these samples. [Note that $P(N_\mathrm{c})$ is the probability for a cluster, not for a particle to be located in a cluster, of size N_c.] Whereas the distributions are very similar for samples with $x_\mathrm{s} = 0.0$, 0.1, 0.3, and 0.5, the mixture with $x_\mathrm{s} = 0.01$ shows very few small clusters, suggesting a more homogeneous structure in comparison to the samples with higher x_s. For the sample with $x_\mathrm{s} = 0.7$ a network is still present [Figs. 6 and 7(b)], but $P(N_\mathrm{c})$ is significantly broader for the smaller clusters, extending to sizes beyond 50 particles per cluster. This indicates a transition from a network structure of large particles to isolated clusters of large particles immersed in a "sea" of small particles. This transition is completed for $x_\mathrm{s} = 0.9$, where no large clusters are observed.

The function $f(N_\mathrm{c}) = AN_\mathrm{c}^{-\gamma}\exp(-N_\mathrm{c}/k_\mathrm{c})$ fits the experimental distributions $P(N_\mathrm{c})$, where the fit parameters A, γ, and k_c are not completely uncorrelated and thus their values have to be treated with care. The fit function is expected to describe the cluster distribution of irreversible physical gels [38]. An exponent $\gamma < 3$ indicates the presence of a space spanning network of clusters. Initially ($x_\mathrm{s} \leqslant 0.5$) the exponent is approximately constant, $\gamma \approx 3 \pm 0.5$, and then decreases with a minimum at $x_\mathrm{s} = 0.7$. These values of γ are consistent with the presence of a space-spannning network. The exponential cutoff k_c quantifies the limiting cluster size. It is almost constant except a minimum for $x_\mathrm{s} = 0.01$ and a maximum for $x_\mathrm{s} = 0.7$. The intercept A, which is related to the fraction of particles not pertaining to any cluster, shows a slight decrease except for a peak at $x_\mathrm{s} = 0.01$ and a minimum for $x_\mathrm{s} = 0.7$. The trends of the fit parameters are consistent with the more homogeneous structure of sample $x_\mathrm{s} = 0.01$ and confirm the broad distribution of cluster sizes of sample $x_\mathrm{s} = 0.7$.

3. Remoteness

In order to investigate the degree of structural heterogeneity, we determined the distribution of particle remoteness $P(\xi)$ [39,40] [Fig. 7(c)]. Particle remoteness ξ measures the distance of a point from the surface of the closest particle. A large value of the remoteness ξ is therefore an indication of large voids or open arrangements and a broad distribution of ξ of heterogeneous structures. Although our samples are densely packed with $\phi = 0.60$, we are interested in the arrangement of the large spheres only and hence consider as "void" any volume which is not occupied by large spheres. A large fraction of the voids is thus occupied by small (invisible) particles.

The one-component glass of large spheres shows a $P(\xi)$ which is peaked at a small value, $\xi \approx 0.2R_\mathrm{L}$ and shows only a very small probability for $\xi > R_\mathrm{L}$. This reflects the small interstitial voids between densely packed large spheres. For $x_\mathrm{s} = 0.01$, the $P(\xi)$ is shifted to smaller ξ and the probability of large voids is further suppressed. This is also indicated by the smaller average remoteness $\langle\xi\rangle$ [Fig. 7(c), inset]. In contrast, for $x_\mathrm{s} = 0.1$, while the main peak remains at about the same position, the distribution considerably broadens and $\xi > R_\mathrm{L}$ becomes more probable, with a second very weak maximum at $\xi \approx 2.25R_\mathrm{L}$ and $\langle\xi\rangle$ is increased. Thus larger unoccupied regions exist. The probability of larger ξ, including the weak maximum and $\langle\xi\rangle$, increase further for $x_\mathrm{s} = 0.3$ while the main peak remains at $\xi \approx 0.2R_\mathrm{L}$. This suggests the presence of a backbone of bonded particles in close contact, i.e., a network of large particles. For $x_\mathrm{s} = 0.5$ and 0.7 the probability of large $\xi/R_\mathrm{L} > 2$ remains almost unchanged, but the main peak shifts to larger ξ and $\langle\xi\rangle$ slightly increases while the distribution broadens. For $x_\mathrm{s} = 0.9$ the whole distribution is significantly shifted to large values of ξ. This is an indication that the gel network starts to melt due to the increasing dilution of large spheres (increase of $\langle\xi\rangle$) and for $x_\mathrm{s} = 0.9$ disappears, and isolated particles or "extended dimer configurations" are prevailing. The presence of a few, homogeneously distributed isolated particles or extended dimers is consistent with a more homogeneous distribution of remoteness.

C. Comparison of dynamics and structure: Glass, gel, and fluid states

1. Different arrested states

The information on the dynamics and structure is now combined to provide a comprehensive characterization of the different states as a function of the sample composition x_s.

The dynamics indicate that the one-component system of large spheres, $x_s = 0.0$, and the mixtures with a majority of one species, i.e., $x_s = 0.01$ and 0.9, as well as an intermediate composition, $x_s = 0.3$, present very slow, arrested dynamics, characteristic of glasses and gels. These samples show, however, significantly different degrees of arrest, subdiffusion and localization lengths of the large spheres. In the following we discuss these differences, and later compare the dynamically arrested states with the fluid states which occur at intermediate compositions $x_s = 0.1$ as well as $x_s = 0.5$ and 0.7.

Considering the arrested states, the localization length of the large spheres decreases continuously from $x_s = 0.0$ to 0.01, 0.3, and 0.9. In the fluid states that characterize the transitions between two arrested states, instead the localization lengths are larger. Dynamical arrest is particularly pronounced for $x_s = 0.0$ and 0.9, and less so for $x_s = 0.3$. The extended plateau in the MSD with a small localization length of sample $x_s = 0.01$ implies a tight cage and is attributed to the formation of interparticle bonds, which are characteristic for an attractive glass state. This is supported by the structural analysis; the arrangement of the large particles is amorphous although in a space spanning network with an increased average number of bonds per particle. Nevertheless, on a mesoscopic scale the large particles are homogeneously distributed with the distribution of remoteness indicating the absence of large voids unoccupied by large particles (but by small particles). Again, this is typical for an attractive glass rather than a gel. As proposed recently, caging is possibly still the origin of dynamical arrest in attractive glasses [41].

For $x_s = 0.3$ the localization length is even smaller, but the plateau and subdiffusion are less pronounced. The structure of this sample indicates that the tight localization in the dynamics is caused by a high probability for particle contacts due to depletion attraction induced by the small particles. Furthermore, the presence of significant structural heterogeneity seems responsible for the broad distribution of relaxation times leading to the subdiffusive MSD. These observations suggest a gellike state of this mixture, which is supported by the presence of a large cluster.

The mixture with $x_s = 0.9$ exhibits the smallest localization length with an extended plateau and the most pronounced dynamical arrest. There is no network in this sample, but many small clusters and a few slightly larger clusters. Furthermore, due to the large dilution, large particles are not caged by other large particles and the pair correlation function shows fluidlike particle organization. The dynamical arrest of the large particles therefore must be caused by the small particles. This suggests an asymmetric glass state, in which individual large particles or small clusters of a few large particles are caged by small particles. Due to the ability of small particles to tightly pack around large particles, these cages are smaller than cages formed by large spheres, even by attractive large spheres. Therefore, we observe four different arrested states: a repulsive glass ($x_s = 0.0$), an attractive glass ($x_s = 0.01$), a gel ($x_s = 0.3$), and an asymmetric glass ($x_s = 0.9$).

The transitions between these arrested states (except between the repulsive and attractive glasses) involve the melting of the glasses and the formation of fluids. We observe diffusive dynamics for samples with $x_s = 0.1$, separating the attractive glass and gel state, as well as $x_s = 0.5$ and 0.7, separating the gel and the asymmetric glass states. Despite the diffusive dynamics, these fluids are characterized by particle-particle bonds and dynamic networks. It is conceivable that, for $x_s = 0.1$, the volume fraction of large spheres is too small for a glass state, as it exists for $x_s = 0.01$, and the volume fraction of small spheres too small for depletion attraction to induce gelation, like for $x_s = 0.3$. For $x_s = 0.5$ and 0.7 melting can be associated with the dilution of the gel structure and thus a breakdown of the system-spanning network on one hand (from $x_s = 0.3$ to 0.5) and dilution of the glass matrix of small spheres on the other hand (from $x_s = 0.9$ to 0.7).

The comparison between arrested and fluid states indicates that the presence of a space-spanning network, defined on the basis of a structural criterion (particle distances) is not sufficient to distinguish between the two states. We thus combine structural and dynamical information. For each composition x_s, we identify the particles that, over the whole observation time $t_{\mathrm{meas}} \approx 45\tau_{\mathrm{B}}$, perform displacements which are smaller than the typical cage size of the one-component glass ($x_s = 0.0$), quantified by its localization length L (Fig. 1). We call these particles "arrested." The fraction of arrested particles as a function of x_s (Fig. 8) shows that the glass states ($x_s = 0.0$, 0.01 and 0.9) are characterized by the largest fractions of arrested particles, while the gel state ($x_s = 0.3$) presents a lower fraction, which is still larger than that of the neighbor fluid states. Then clusters of arrested particles are determined by applying the same criterion used previously to define bonded particles and are shown in Fig. 9. In the repulsive and attractive glasses ($x_s = 0.0$ and 0.01, respectively), the arrested particles form a dense space-spanning network. In contrast, for $x_s = 0.1$ there is only a small fraction of arrested particles, which in addition do not form a space-spanning network. For $x_s = 0.3$, instead, a dense space-spanning network of arrested particles is again observed. Subsequently, for $x_s = 0.5$, the arrested particles are organized in smaller clusters which are not space spanning. Again, a space-spanning but open network is observed for $x_s = 0.7$. Finally, for $x_s = 0.9$ there are only isolated arrested particles or individual small clusters of arrested particles. This suggests that the glass ($x_s = 0.0$, 0.01) and gel ($x_s = 0.3$) states are characterized by the presence of a dense space-spanning network of arrested large particles, while

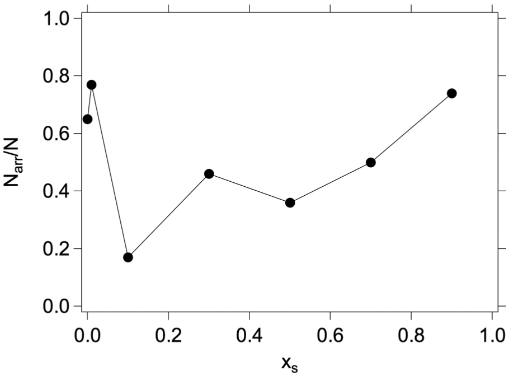

FIG. 8. Fraction of arrested particles N_{arr}/N as a function of composition x_s.

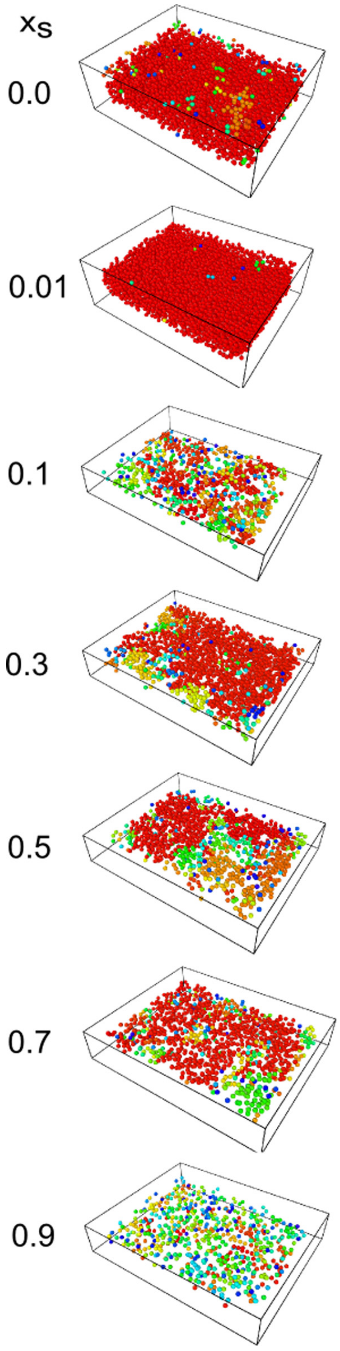

FIG. 9. (Color online) Rendering of the arrested large particles in samples with $\phi \approx 0.60$, $\delta = 0.09$, and different compositions x_s (as indicated) as obtained from trajectories extracted from confocal microscopy images. Only arrested large particles are shown with particles pertaining to the same cluster indicated with the same color (gray-scale value). Particles within two diameters of the surface of the observation volumes are not shown.

this network is not present in the fluid states ($x_s = 0.1, 0.5$) and in the asymmetric glass ($x_s = 0.9$). The sample with $x_s = 0.7$ shows an intermediate behavior.

Furthermore, we observed that in samples with a heterogeneous network structure, $0.1 \leqslant x_s \leqslant 0.7$, the fastest large particles are located in regions sparse of large particles (Fig. 3, left), and thus one might expect them to have also a smaller number of bonds with other large particles than an average particle. This, however, is true only for very few cases (Fig. 3, right). Therefore, despite their lower local volume fraction they typically maintain their number of bonds. This suggests that the fast particles form anisotropic clusters with other large particles, which allows them to keep their average coordination with other large particles while increasing the number of contacts with small particles. This could increase their mobility due to the vicinity of the more mobile small particles. Moreover, the mobility of the particles also depends on the strength (or rather weakness) of the bonds, which is experimentally not accessible to us.

2. *Dependence on size disparity*

We compare these findings with results obtained in previous work for $\delta = 0.38$ and 0.2 [17–19] as well as previous experiments for $\delta = 0.1$ [13] and theory predictions [11,12]. They are summarized in a state diagram as a function of composition x_s and size ratio δ (Fig. 10). In binary mixtures with $\delta = 0.38$ only a repulsive glass state is observed, while in mixtures with $\delta = 0.2$ two glass states of the large spheres are observed, namely, for small x_s a glass in which the large spheres are caged by large spheres and for large x_s an asymmetric glass. No evidence for a gel state was found. Very small values of x_s, like $x_s = 0.01$, were not investigated for $\delta = 0.2$ and therefore the existence of an attractive glass cannot be excluded. The asymmetric glass state observed for

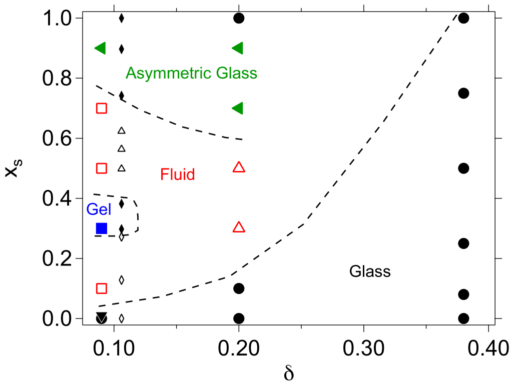

FIG. 10. (Color online) State diagram of samples with different composition x_s and size ratios; $\delta = 0.09$ (present work), $\delta = 0.106$ [13], $\delta = 0.2$ and 0.38 [17–19]. Different arrested states are identified in the present work: repulsive glass (●), attractive glass (▼), asymmetric glass (◀), and gel (■). Open symbols indicate fluid states. In [13] fluids (△), fluid-crystal coexistence (◇), and amorphous solids (♦) were distinguished.

$\delta = 0.2$ is different from the one in this work: only individual large particles but no dimers or other small clusters were found. Since small particles can pack less effectively around dimers and small clusters than around single particles, particles forming dimers and small clusters are possibly less localized. This is consistent with the fact that for $\delta = 0.2$ the reduction of the localization length in the asymmetric glass with respect to the one-component glass, $L(x_s = 0.9)/L(x_s = 0.0) \approx 0.2 = \delta$ is considerably larger than in the case $\delta = 0.09$, namely, $L(x_s = 0.9)/L(x_s = 0.0) \approx 0.5 > \delta$.

Previous experiments on binary mixtures of silica particles with $\delta \approx 0.1$ [13] revealed an arrested state in which both components are arrested at large x_s (Fig. 10, ♦), and an arrested state in which only the large spheres are arrested at intermediate x_s (Fig. 10, ♦), while fluid-crystal coexistence was observed at small x_s (Fig. 10, ♢) and metastable fluid states at large intermediate x_s (Fig. 10, △). The arrested states of the large spheres were not further characterized in that work. Our findings suggest that the glass they observed at large x_s [13] is an asymmetric glass. Moreover, the arrested state at intermediate x_s might correspond to the gel state observed in the present work. At small x_s we find amorphous glass states or fluids, but no evidence of crystallization, which we attribute to the considerably larger polydispersity of our system, in particular of the small spheres.

Size disparities as large as $\delta = 0.1$ were not investigated by MCT or SCGLE theories [11,12]. Nevertheless, the attractive glass state observed for $x_s = 0.01$ might be related to the depletion-driven glass state predicted by MCT in this region of the phase diagram for $\delta \leqslant 0.2$ (minimum value investigated $\delta = 0.18$). Moreover, an asymmetric glass state at large x_s is predicted by MCT and SCGLE for $\delta \leqslant 0.35$. The asymmetric glass of single particles observed for $\delta = 0.2$ and $x_s = 0.9$, and predicted by theory, might be observed for $\delta = 0.09$ for values of $x_s > 0.9$. Asymmetric glass states were also reported for binary mixtures of size asymmetric star polymers [24,25], possibly indicating that in general this state is induced by a dynamical asymmetry irrespective of the details of the interaction potential.

To our knowledge, gels formed by binary mixtures have only been reported by Dinsmore and coworkers [42]. Their gels collapsed under gravity and thus represent transient states. Furthermore, gel formation in binary mixtures was observed under confinement with the addition of polymers as depletants [43]. In contrast, the gel state we observe is long lived and forms without addition of polymers but shows structural and dynamical analogies with gels formed by colloid-polymer mixtures at intermediate colloid volume fraction [44–51]; for example a large structural heterogeneity and a broad distribution of particle dynamics. The mechanism responsible for gel formation in our binary mixtures is not clear at present. Different mechanisms have been proposed for colloid-polymer mixtures, among them arrested phase separation [45,52–54], glasslike arrest [55] and rigidity percolation [56]. Moreover, equilibrium gelation in binary mixtures has been predicted as a result of the specific form of the interaction potential in these systems [16]. In order to investigate the route leading to gelation and the subsequent aging, time-resolved structural measurements are needed and will be the subject of future work.

IV. CONCLUSIONS

Different arrested states are observed for large spheres in binary mixtures with size disparity $\delta = 0.09$ and total volume fraction $\phi \approx 0.60$. While the one-component system of large spheres forms a repulsive glass, all arrested states in the mixtures are characterized by bonding, as a result of the strong depletion interaction induced by the small spheres at this size ratio. The arrested states in the mixtures significantly differ in terms of the arrest mechanism as well as structure and dynamics. If a small amount of small spheres is added to the repulsive glass of large spheres, depletion-induced attractions induce bonding and formation of an attractive glass ($x_s = 0.01$). This state is melted by further addition of small spheres ($x_s = 0.1$), possibly due to the dilution of the large spheres and a concomitant melting of the cage. Only if the amount of small spheres is increased ($x_s = 0.3$) the attraction becomes strong enough to cause dynamical arrest in the form of gelation, i.e., the formation of a network of bonded and arrested particles. This gel state shows a structural organization of the large spheres analogous to that observed in colloid-polymer mixtures. Also the gel state is melted by further dilution of the large spheres. Nevertheless, clusters of particles and a space spanning network persist ($x_s = 0.5$, 0.7) which are not arrested but fluid like. At large values of x_s an additional arrest mechanism is observed; isolated small clusters of large spheres are arrested by the highly concentrated small spheres, which possibly form a glass ($x_s = 0.9$). While asymmetric glass states were already observed for a smaller size asymmetry $\delta = 0.2$ [18,19] and for mixtures of star polymers [24,45], this asymmetric glass state is special in that depletion-induced bonding between the dilute large spheres leads to the formation of clusters, in particular "extended clusters."

Size asymmetric binary mixtures therefore represent a tunable model system to investigate transitions between different arrested states, which can be obtained by only changing the composition of the mixture. Thus the properties and behavior of different arrested states can be investigated in a consistent way using a single model system.

ACKNOWLEDGMENTS

We thank R. Castañeda-Priego, P. Chaudhuri, C. De Michele, J. Horbach, G. Petekidis, T. Sentjabrskaja, T. Voigtmann, E. Zaccarelli, and A. Zaccone for illuminating discussions. This work was funded by the Deutsche Forschungsgemeinschaft (DFG) through the research unit FOR1394, project P2. We also acknowledge funding of the confocal microscope through grant INST 208/617-1 FUGG. A.B.S. is partially funded by the UK Engineering and Physical Sciences Research Council (Grant EP/J007404/1).

---

[1] P. N. Pusey and W. van Megen, Nature (London) **320**, 340 (1986).

[2] P. N. Pusey, W. V. Megen, S. M. Underwood, P. Bartlett, and R. H. Ottewill, Physica A **176**, 16 (1991).

[3] W. van Megen, T. C. Mortensen, S. R. Williams, and J. Müller, Phys. Rev. E **58**, 6073 (1998).
[4] J. L. Barrat, W. Götze, and A. Latz, J. Phys.: Condens. Matter **1**, 7163 (1989).
[5] E. R. Weeks, J. C. Crocker, A. C. Levitt, A. Schofield, and D. A. Weitz, Science **287**, 627 (2000).
[6] G. Brambilla, D. El Masri, M. Pierno, L. Berthier, L. Cipelletti, G. Petekidis, and A. B. Schofield, Phys. Rev. Lett. **102**, 085703 (2009).
[7] G. L. Hunter and E. R. Weeks, Rep. Prog. Phys. **75**, 066501 (2012).
[8] S. R. Williams and W. van Megen, Phys. Rev. E **64**, 041502 (2001).
[9] G. Foffi, W. Götze, F. Sciortino, P. Tartaglia, and T. Voigtmann, Phys. Rev. Lett. **91**, 085701 (2003).
[10] W. Götze and T. Voigtmann, Phys. Rev. E **67**, 021502 (2003).
[11] T. Voigtmann, Europhys. Lett. **96**, 36006 (2011).
[12] R. Juárez-Maldonado and M. Medina-Noyola, Phys. Rev. E **77**, 051503 (2008).
[13] A. Imhof and J. K. G. Dhont, Phys. Rev. Lett. **75**, 1662 (1995).
[14] A. Moreno and J. Colmenero, J. Chem. Phys. **125**, 164507 (2006).
[15] A. J. Moreno and J. Colmenero, Phys. Rev. E **74**, 021409 (2006).
[16] P. Germain and S. Amokrane, Phys. Rev. Lett. **102**, 058301 (2009).
[17] T. Sentjabrskaja, D. Guu, M. P. Lettinga, S. U. Egelhaaf, and M. Laurati, AIP Conf. Proc. **1518**, 206 (2013).
[18] T. Sentjabrskaja, R. Babaliari, J. Hendricks, M. Laurati, G. Petekidis, and S. U. Egelhaaf, Soft Matter **9**, 4524 (2013).
[19] T. Sentjabrskaja, M. Hermes, W. C. K. Poon, C. D. Estrada, R. Castañeda-Priego, S. U. Egelhaaf, and M. Laurati, Soft Matter **10**, 6546 (2014).
[20] P. Yunker, Z. Zhang, and A. G. Yodh, Phys. Rev. Lett. **104**, 015701 (2010).
[21] S. Sanyal and A. K. Sood, Phys. Rev. E **57**, 908 (1998).
[22] T. Hamanaka and A. Onuki, Phys. Rev. E **75**, 041503 (2007).
[23] F. Ebert, P. Keim, and G. Maret, Eur. Phys. J. E **26**, 161 (2008).
[24] C. Mayer, E. Zaccarelli, E. Stiakakis, C. N. Likos, F. Sciortino, A. Munam, M. Gauthier, N. Hadjichristidis, H. Iatrou, P. Tartaglia, H. Löwen, and D. Vlassopoulos, Nat. Mater. **7**, 780 (2008).
[25] C. Mayer, F. Sciortino, C. N. Likos, P. Tartaglia, H. Löwen, and E. Zaccarelli, Macromolecules **42**, 423 (2009).
[26] C. P. Royall, W. C. K. Poon, and E. R. Weeks, Soft Matter **9**, 17 (2013).
[27] P. N. Pusey, J. Phys. France **48**, 709 (1987).
[28] A. Yethiraj and A. van Blaaderen, Nature (London) **421**, 513 (2003).
[29] W. Schaertl and H. Silescu, J. Stat. Phys. **77**, 1007 (1994).
[30] W. C. K. Poon, E. R. Weeks, and C. P. Royall, Soft Matter **8**, 21 (2012).
[31] T. G. Mason, Rheol. Acta **39**, 371 (2000).
[32] J. C. Crocker and D. G. Grier, J. Colloid Interface Sci. **179**, 298 (1996).
[33] W. K. Kegel and A. van Blaaderen, Science **287**, 290 (2000).
[34] L. Berthier, G. Biroli, J.-P. Bouchaud, L. Cipelletti, and W. van Saarloos, *Dynamical Heterogeneities in Glasses, Colloids, and Granular Media (International Series of Monographs on Physics)* (Oxford University Press, New York, 2011).
[35] A. Stukowski, Modelling Simul. Mater. Sci. Eng. **18**, 015012 (2010).
[36] J. M. Lynch, G. C. Cianci, and E. R. Weeks, Phys. Rev. E **78**, 031410 (2008).
[37] T. Narumi, S. V. Franklin, K. W. Desmond, M. Tokuyama, and E. R. Weeks, Soft Matter **7**, 1472 (2011).
[38] A. Zaccone, H. H. Winter, M. Siebenbürger, and M. Ballauff, J. Rheol. **58**, 1219 (2014).
[39] R. M. L. Evans and M. D. Haw, Europhys. Lett. **60**, 404 (2002).
[40] M. D. Haw, Soft Matter **2**, 950 (2006).
[41] E. Zaccarelli and W. C. K. Poon, Proc. Natl. Acad. Sci. USA **106**, 15203 (2009).
[42] A. D. Dinsmore, A. G. Yodh, and D. J. Pine, Phys. Rev. E **52**, 4045 (1995).
[43] R. Pandey and J. C. Conrad, Soft Matter **9**, 10617 (2013).
[44] W. C. K. Poon, J. Phys.: Condens. Matter **14**, R859 (2002).
[45] E. Zaccarelli, J. Phys.: Condens. Matter **19**, 323101 (2007).
[46] M. Laurati, G. Petekidis, N. Koumakis, F. Cardinaux, A. B. Schofield, J. M. Brader, M. Fuchs, and S. U. Egelhaaf, J. Chem. Phys. **130**, 134907 (2009).
[47] N. Koumakis and G. Petekidis, Soft Matter **7**, 2456 (2011).
[48] M. Laurati, S. U. Egelhaaf, and G. Petekidis, J. Rheol. **55**, 673 (2011).
[49] S. A. Shah, Y. L. Chen, S. Ramakrishnan, K. S. Schweizer, and C. F. Zukoski, J. Phys.: Condens. Matter **15**, 4751 (2003).
[50] P. Varadan and M. J. Solomon, Langmuir **19**, 509 (2003).
[51] C. J. Dibble, M. Kogan, and M. J. Solomon, Phys. Rev. E **74**, 041403 (2006).
[52] S. Manley, H. M. Wyss, K. Miyazaki, J. C. Conrad, V. Trappe, L. J. Kaufman, D. R. Reichman, and D. A. Weitz, Phys. Rev. Lett. **95**, 238302 (2005).
[53] P. J. Lu, E. Zaccarelli, A. B. Schofield, F. Sciortino, and D. A. Weitz, Nature (London) **453**, 499 (2008).
[54] M. E. Helgeson, Y. Gao, S. E. Moran, J. Lee, M. Godfrin, A. Tripathi, A. Bose, and P. S. Doyle, Soft Matter **10**, 3122 (2014).
[55] K. Kroy, M. E. Cates, and W. C. K. Poon, Phys. Rev. Lett. **92**, 148302 (2004).
[56] A. P. R. Eberle, N. J. Wagner, and R. Castañeda-Priego, Phys. Rev. Lett. **106**, 105704 (2011).

This page has been left intentionally blank.

3.4 Using a Kösters prism to create a fringe pattern

Journal: Review of Scientific Instruments

Reference: *Rev. Sci. Instrum.* **88**, 056102 (2017)

Impact factor: 1.515

Authors: **Ronja F. Capellmann**, Jörg Bewerunge, Florian Platten, and Stefan U. Egelhaaf

1st author

R. F. C. and J. B. designed the set-up and performed preliminary experiments, R. F. C. built the instrument, conducted and analysed the experiments, R. F. C., F. P. and S. U. E. conceived the research and interpreted the results and all authors contributed to the writing of the paper.

80% contribution of R. F. C.

Reproduced from [Capellmann, R. F.; Bewerunge, J.; Platten, F.; Egelhaaf, S. U.; *Rev. Sci. Instrum.* **88**, 056102 (2017)], with the permission of AIP Publishing.

This page has been left intentionally blank.

Note: Using a Kösters prism to create a fringe pattern

R. F. Capellmann,[1] J. Bewerunge,[1] F. Platten,[1] and S. U. Egelhaaf[1]

Condensed Matter Physics Laboratory, Heinrich Heine University, D-40225 Düsseldorf

(Dated: 6 April 2017)

The interference of two crossed laser beams results in a standing wave. Such fringe patterns are exploited in different instruments such as interferometers or laser-Doppler anemometers. We create a fringe pattern in the sample plane of a microscope using a compact apparatus based on a Kösters prism. The fringe pattern is shown to be spatially and temporally very stable, covers a large area and its spacing is easily tunable. In addition, we exploit it to impose a sinusoidal potential on colloidal particles.

Sinusoidal fringe or standing wave patterns are exploited to, e.g., measure the velocity of particles with laser-Doppler anemometers,[1–4] study thermal diffusion[5,6] or manipulate colloids.[7–15] They are created by the interference of two laser beams. This requires to split a laser beam and recombine the two beams under an angle. Several layouts to achieve this have been proposed.[2,3] Fringe patterns have been created using a beam splitter, a special double prism or two plane-parallel coated blocks to split the beam as well as several mirrors to guide the two beams, with the number of movable optical components significantly increasing if a variation of the fringe spacing, fringe area or other parameters is desired.[1–3] The challenge is to achieve a high stability while still allowing for some variability of the pattern, which typically are conflicting; they require a small and large number of components, respectively.

By using a Kösters prism to split the beam[16,17] (and a lens), we reduce the number of essential components to two without compromising flexibility.[3] Kösters prisms have been used in, e.g., compact interferometers,[18–21] white-light frequency-domain interferometers,[22] electrochemical interferometers,[23] light scattering and particle velocimetry instruments,[3,4,24–26] and for testing of optical components.[27,28] We realize an apparatus based on a Kösters prism with a simple and compact layout, in particular short and symmetric beam paths, resulting in very good stability. It is also versatile since a translation of the prism changes the fringe spacing easily and reliably. In addition, this apparatus can create a large fringe pattern in the sample plane of a microscope.

Our apparatus (Fig. 1) includes a laser (Coherent Verdi V5, wavelength $\lambda = 532$ nm, beam diameter 2.25 mm), four mirrors (M1-M4) to direct the beam through a 3× beam expander (BE) and two further mirrors (M5, M6) to guide the beam to the Kösters prism (KP, sides 8 cm, height 4 cm, Bernhard Halle Nachfl.). The Kösters prism consists of two identical prisms that are attached to each other with a semi-reflective silver coating at the prism–prism interface.[16,17] The prism splits the beam into two parallel beams of about the same intensity, with the coating absorbing about 10 % of the intensity. The ratio of the two intensities is adjusted with a neutral density filter (ND, optical density OD = 0.15). Both beams are focused with a plano-convex lens (L1, diameter 75 mm, focal length 150 mm) on the sample plane of an inverted microscope (Nikon Ti-E) where they interfere, thus creating a standing wave pattern (Fig. 2). The beams are coupled into the light path of the microscope using a dichroic mirror (D1, Chroma, ZT543rdc, wavelengths up to ∼550 nm are reflected) and removed by another dichroic mirror (D2, Chroma, Z532rdc, wavelengths between ∼500 nm and 540 nm are reflected) and a notch filter (NF, Edmund Optics, OD = 4, center wavelength 532 nm, FWHM (26.6 ± 2.7) nm) to prevent the CMOS camera (Pixelink, PL-B741F) from damage. Nevertheless, the fringe pattern can be observed if D2 and NF are removed and the camera is replaced by a laser beam profiler (Coherent LaserCam-HR). To aid the alignment,

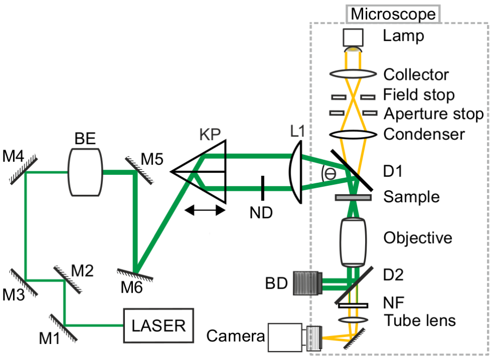

FIG. 1. **Schematic representation of the apparatus.** Four mirrors (M1-M4) direct the beam to a beam expander (BE). Two further mirrors (M5, M6) guide the expanded beam to the Kösters prism (KP). The KP splits the beam into two parallel beams whose distance can be adjusted by translating the KP. A lens (L1) focuses the beams and, after being introduced into the light path of a microscope (grey dashed box) by a dicroic mirror (D1), combines them in the sample plane under an angle Θ thus creating a fringe pattern. The beams are removed from the light path of the microscope by a dichroic mirror (D2) and collected by a beam dump (BD). A notch filter (NF) attenuates the remaining laser light.

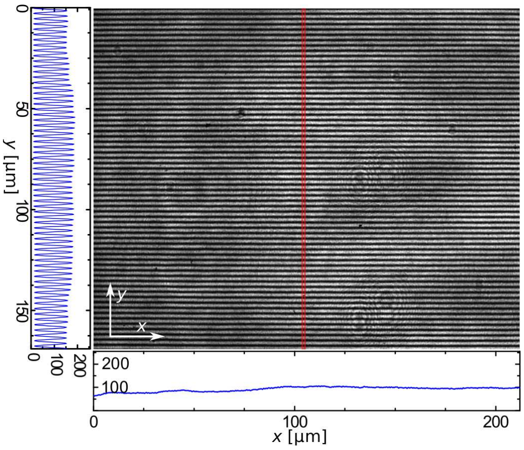

FIG. 2. **Image of the fringe pattern $I(x, y)$.** The mean intensities $\langle I(x, y)\rangle_y$ and $\langle I(x, y)\rangle_x$ are shown below and on the left, respectively. The black spots are caused by dust on the camera chip. The red box indicates the slice that was used to characterize the temporal stability.

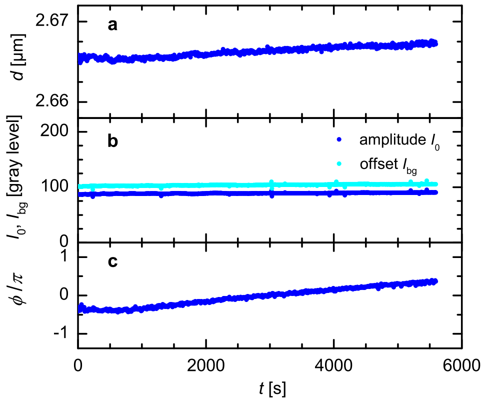

FIG. 3. **Temporal stability of the fringe pattern.** Time evolution of the parameters describing the sinusoidal pattern (Eq. 1). (a) Fringe spacing d, (b) amplitude $I_0(x)$ and offset $I_{\mathrm{bg}}(x)$, and (c) phase ϕ.

a Helium-Neon-laser beam is used to define the optical axis. It is fed into the microscope running against the main laser beam (see Supplementary Material).

The crossing-angle Θ determines the fringe spacing $d = \lambda/(2\sin(\Theta/2))$. Moving the prism along the direction of the two parallel beams changes their distance and hence Θ, which provides a simple way to vary d. A large range of fringe spacings d can be obtained with the minimum d, i.e. largest Θ, defined by the size of the dichroic mirror D1 and its holder, and the maximum d, i.e. smallest Θ, given by the beam radius because this determines the minimum distance of the beam centers to the apex of the prism. Hence a compromise has to be found between the maximum achievable d and the size of the pattern, which also depends on the beam radius.

The intensity distribution $I(x, y)$ is imaged using the laser beam profiler (Fig. 2) while a water-filled sample cell[29] is in place to ensure that the sample plane is in focus. The fringe pattern appears homogeneous and fills the whole field of view, in the present configuration about $212.1 \times 169.3\,\mu\mathrm{m}^2$ (1270×1014 pixels). Beams with large diameters and/or separations use the lens close to its edge. This causes image distortions and requires to shift the sample plane out of the nominal focal plane. This has been confirmed by ray tracing using the program OSLO.

For a quantitative characterization, the image is divided into slices of width $\Delta x = 1.67\,\mu\mathrm{m}$, i.e. 10 pixels (e.g. red box in Fig. 2). For each slice, the intensity is averaged in x direction yielding $\langle I(x, y)\rangle_{\Delta x}$, which resembles $\langle I(x, y)\rangle_x$ (Fig. 2, left) and, in y direction, is expected to show a sine squared or, equivalently, a sine dependence with a fixed background $I_{\mathrm{bg}}(x) = \langle\langle I(x, y)\rangle_{\Delta x}\rangle_y \approx \langle I(x, y)\rangle_y$:

$$\langle I(x, y)\rangle_{\Delta x} = I_0(x) \sin\left(\frac{2\pi}{d(x)}\, y + \phi(x)\right) + I_{\mathrm{bg}}(x). \quad (1)$$

Fits yield a spacing $d(x)$ with no significant x dependence and mean value $\langle d\rangle \approx (2.663 \pm 0.005)\ \mu\mathrm{m}$, as well as an amplitude $I_0(x)$ that closely follows the trend of $\langle I(x, y)\rangle_y$, but is smaller than $\langle I(x, y)\rangle_y$ due to variations in the background intensity along y which is positive by definition. The phase $\phi(x)$ changes by $\sim 0.35\pi$, i.e. $0.45\,\mu\mathrm{m}$, which could be due to distortions or a shift of the fringes or of their image and is mainly attributed to the non-ideality of the lens.

The temporal stability is characterized by the evolution of the mean intensity in one slice, $\langle I(106\,\mu\mathrm{m}, y, t)\rangle_{\Delta x}$, over 1.5 h (Fig. 2, red box), while the room temperature is kept at $T = (18.0 \pm 0.2)°\mathrm{C}$. A fit using Eq. 1 yields the temporal fluctuations of the parameters (Fig. 3). The spacing $d(t)$ is very stable with a difference between the maximum and minimum values of less than $0.003\,\mu\mathrm{m}$ and mean $\langle d\rangle = (2.666 \pm 0.001)\ \mu\mathrm{m}$ whose standard deviation corresponds to a change of the distance of the two beams leaving the prism of only $\sim 10\,\mu\mathrm{m}$. Furthermore, $I_0(t)$ and $I_{\mathrm{bg}}(t)$ are essentially constant except for very few outliers that are up to 6 gray levels from the mean values $\langle I_0\rangle = (89.1 \pm 0.9)$ gray levels and $\langle I_{\mathrm{bg}}\rangle = (104.0 \pm 1.17)$ gray levels, respectively. The variation of the phase $\phi(t)$ is larger, $\sim 0.66\pi$, that is $0.59\,\mu\mathrm{m/h}$, which is the largest variation of the phase observed; typically the variation is $\sim 0.25\pi/\mathrm{h}$. It might arise from instabilities in the apparatus, e.g. a drift of the Kösters prism or dichroic mirror, but also from small drifts of the microscope, e.g. the objective, which cannot be distinguished easily. Even this largest observed phase shift is much smaller than the displacements of the colloidal particles exposed to the fringe pattern. On the other hand, the parameters significantly affecting the particles, d and I_0, are very stable. This is achieved by using the same components (KP, L1, D1) for both beams and hence both are affected in the same way

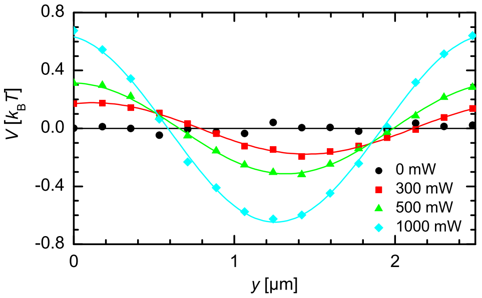

FIG. 4. **Potential $V(y)$ imposed on the colloids.** It is shown in units of the thermal energy $k_\mathrm{B}T$ as a function of position y and different laser powers (as indicated) as determined based on Eq. 2 (symbols). The statistical error of the data is comparable to the symbol size or smaller. The solid lines represent sinusoidal fits with fixed wavelength $d = 2.664$ µm.

by instabilities, which is not the case if beams are, e.g, guided by individual mirrors.

The fringe pattern is imposed onto a dilute aqueous suspension of polystyrene spheres with radius $R = 1.4$ µm which is imaged with the microscope simultaneously. The particles have different dielectric properties than water and hence experience a force. First, the particles are pushed in beam direction due to radiation pressure.[9,30,31] Thus, any asymmetry of the interfering beams causes a drift of the particles. This can be exploited to refine the alignment (see Supplementary Material). Moreover, the fringe pattern translates into a sinusoidal potential imposed on the colloidal particles.[9–11,30,31]

We quantitatively characterize the potential. The particle number density $n(x, y, i)$ is determined for each frame i of a time series and the average $\langle n(x, y, i)\rangle$ calculated by averaging over all frames i and positions x as well as collapsing the y dependence onto one fringe. The suspension is dilute enough to neglect particle interactions and hence $\langle n(x, y, i)\rangle$ follows a Boltzmann distribution:

$$\langle n(x, y, i)\rangle = C\, \mathrm{e}^{-V(y)/k_\mathrm{B}T} \qquad (2)$$

with $V(y)$ the potential experienced by the particles and the constant C such that $\int_0^d V(y)\ \mathrm{d}y = 0$. For a fixed fringe spacing $\langle d\rangle \approx (2.664 \pm 0.007)$ µm (determined from the intensity as described above) and different laser powers P, we have determined the potential $V(y)$ (Fig. 4). A fit is performed based on a sinusoidal dependence; $V(y) = V_0 \sin(2\pi y/\langle d\rangle + \varphi) + V_\mathrm{bg}$. This describes the data well indicating that the particles indeed experience a sinusoidal potential with the same period as the fringe pattern. The amplitude V_0 is found to increase linearly with P; namely $V_0 = (0.63 \pm 0.01)\, k_\mathrm{B}T\, (P/\mathrm{W})$. The phase φ does not significantly vary between measurements and the offset $V_\mathrm{bg} \approx 0$.

To summarize, we have realized a compact apparatus that creates a sinusoidal light pattern, i.e. fringe pattern, in the sample plane of a microscope through the interference of two crossed laser beams. It is based on a Kösters prism and here used to expose colloidal particles to a sinusoidal potential. The apparatus offers several advantages: it is very stable, the fringe spacing can easily be tuned by translating the prism, and the pattern covers a large area. Due to these characteristics and its simple layout with only very few optical components, we expect this apparatus to be useful for several applications.[1–9]

Supplementary material

See supplementary material for detailed instructions on the alignment of the apparatus.

We thank the International Helmholtz Research School of Biophysics and Soft Matter for support.

[1] D. B. Brayton and W. H. Goethert, ISA Trans. **10**, 40 (1971).
[2] F. Durst and J. H. Whitelaw, Proc. R. Soc. Lond. A **324**, 157 (1971).
[3] F. Durst, A. Melling, and J. H. Whitelaw, *Principles and Practice of Laser-Doppler Anemometry* (Academic Press, London, 1976).
[4] A. Stümke and H. Umhauer, in *Proceedings of the Dynamic Flow Conference 1978*, 2, edited by B. W. Hansen (1978) pp. 417–423.
[5] W. Köhler and R. Schäfer, Adv. Polym. Sci. **151**, 1 (2000).
[6] S. Wiegand, J. Phys. Condens. Matter **16**, R357 (2004).
[7] Q. H. Wei, C. Bechinger, D. Rudhardt, and P. Leiderer, Phys. Rev. Lett. **81**, 2606 (1998).
[8] C. Bechinger and E. Frey, J. Phys. Condens. Matter **13**, R321 (2001).
[9] F. Evers, R. D. L. Hanes, C. Zunke, R. F. Capellmann, J. Bewerunge, C. Dalle-Ferrier, M. C. Jenkins, I. Ladadwa, A. Heuer, R. Castañeda Priego, and S. U. Egelhaaf, Eur. Phys. J.: Spec. Top. **222**, 2995 (2013).
[10] K. Loudiyi and B. J. Ackerson, Physica A **184**, 1 (1992).
[11] M. C. Jenkins and S. U. Egelhaaf, J. Phys. Condens. Matter **20**, 404220 (2008).
[12] C. Dalle-Ferrier, M. Krüger, R. D. L. Hanes, S. Walta, M. C. Jenkins, and S. U. Egelhaaf, Soft Matter **7**, 2064 (2011).
[13] M. K. Mazumder and D. L. Wankum, IEEE J. Quantum Electron. **QE 5**, 316 (1969).
[14] A. E. Chiou, W. Wang, G. J. Sonek, J. Hong, and M. W. Berns, Opt. Commun. **133**, 7 (1997).
[15] W. Mu, Z. Li, L. Luan, G. C. Spalding, G. Wang, and J. B. Ketterson, J. Opt. Soc. Am. B **25**, 763 (2008).
[16] W. Kösters, German patent 595211 (12 April 1934).
[17] J. B. Saunders, J. Res. Natl. Bur. Stand. **58**, 21 (1957).
[18] H. Darnedde, Metrologia **29**, 349 (1992).
[19] C. F. Bruce, J. Sci. Instrum. **33**, 478 (1956).
[20] J. E. Decker, R. Schodel, and G. Bonsch, Proc. SPIE **5190**, 14 (2003).
[21] M. S. Brown, J. Phys. E: Sci. Instrum. **20**, 164 (1987).
[22] Y. Ohtsuka, F. Nagaoka, and S. Tanaka, Opt. Rev. **5**, 21 (1998).
[23] G. G. Láng, N. S. Sas, and S. Vesztergom, Chem. Biochem. Eng. Q. **23**, 1 (2009).
[24] K. Schätzel, M. Drewel, and J. Ahrens, J. Phys. Condens. Matter **2**, SA393 (1990).
[25] F. Durst, J. Fluids Eng. Transact. ASME **104**, 284 (1982).
[26] F. Durst and M. Zaré, Appl. Opt. **13**, 2562 (1974).
[27] J. B. Saunders, J. Res. Natl. Bur. Stand. **58**, 27 (1957).
[28] J. W. Gates, Proc. Phys. Soc. **68**, 1065 (1955).
[29] M. C. Jenkins and S. U. Egelhaaf, Adv. Colloid Interface Sci. **136**, 65 (2008).
[30] A. Ashkin, Phys. Rev. Lett. **24**, 156 (1970).
[31] K. C. Neuman and S. M. Block, Rev. Sci. Instrum. **75**, 2787 (2004).

Supplementary Material
Note: Using a Kösters prism to create a fringe pattern

R. F. Capellmann, J. Bewerunge, F. Platten, and S. U. Egelhaaf

Condensed Matter Physics Laboratory, Heinrich Heine University, D-40225 Düsseldorf

Supplementary Note 1: Alignment of the optical apparatus

To aid the alignment of the apparatus, a Helium Neon laser (JDS uniphase, wavelength 633 nm, output power 15 mW) is used to define the optical axis. The alignment beam enters the microscope through a camera port and thus runs against the laser beam creating the fringe pattern. Using two mirrors the alignment beam is adjusted such that it enters the microscope through the center of the camera port and leaves it through the center of the objective back aperture. The first is accomplished using the cover disc for the camera port provided by Nikon, which has a small spine exactly at its center which scatters light, while the cover otherwise is reflective. The latter is achieved using an alignment disc (Thorlabs) consisting of frosted glass with a pinhole at the center, which is put onto the objective thread of the microscope. These two measures ensure that the beam runs along the optical axis of the microscope.

Subsequently, the alignment disc is screwed onto the top of the empty filter cube, which will later hold the dichroic mirror D1. This aids the alignment of the filter cube with respect to the beam. Then, the dichroic mirror D1 is inserted and aligned. For this reason, two irises are mounted on the prism stage along a line parallel to its translation direction, and the alignment disc moved from the top of the filter cube to its side pointing towards the Kösters prism. The mirror D1 is tilted and the prism stage moved sidewards until the beam runs through both pinholes. Furthermore, the mirror is moved such that the beam hits the mirror at the center, which is checked using the alignment disc. Typically, several iterations are required until the alignment beam hits the dichroic mirror D1 at the center and runs through both pinholes and hence parallel to the translation direction of the prism stage.

In the next step the Kösters prism is put on the stage. The horizontal rotation of the prism and hence its orientation relative to the optical axis and the translation direction of the stage is aligned using the back reflection of the alignment beam. The fine adjustment of the vertical tilt of the dichroic mirror D1 is also performed by aligning the back reflection of the alignment beam from the Kösters prism. After D1 is tilted, the position of D1 might need to be re-adjusted such that the beam again hits the center of the alignment disc.

After this procedure, two horizontal slit diaphragms are placed between the Kösters prism and the dichroic mirror D1 to define the height of the optical axis. Then, the main laser beam is aligned using the two mirrors M5 and M6 (Fig. 1) to hit the surface of the Kösters prism perpendicularly to reduce the loss during transmission. Furthermore, the beam position and direction with respect to the Kösters prism is aligned such that the two parallel beams run in the direction of the optical axis and in the predefined height (also when the stage is translated). Now the two slit diaphragms are removed. Before the focusing lens L1 is added, an iris diaphragm is inserted close to the Kösters prism, which is aligned with respect to the alignment beam. The tilt of the lens is adjusted using the back reflection of the alignment beam and the lens position refined such that the alignment beam runs through the iris diaphragm. The alignment of the lens typically requires several iterations. Once the alignment of the lens is completed, the iris diaphragm is removed. Very small changes of the tilt of the dichroic mirror D1 might be necessary to center the fringe pattern in the field of view of the microscope.

To ensure that the two beams hit the sample plane at exactly the same angle, further alignment might be needed. This can be done using colloidal particles. Here we use an aqueous suspension of polystyrene spheres with radius $R = 1.4$ µm. The suspension is filled into home-made sample cells[1], which are built of three cover glasses attached to a microscope slide to form a capillary and sealed with UV glue (Norland Products, NOA 61). When the sample is put into the sample plane of the microscope, the colloids are exposed to the fringe pattern, i.e. a sinusoidal light field, and can be observed with the microscope at the same time. The suspension is very dilute with a mean surface fraction below 1%.

If the two beams creating the fringe pattern are symmetrically aligned with respect to the sample plane and have the same intensity, the resulting radiation pressure pushes the particles towards the cover slip, but does not induce any drift in the sample plane. In contrast, a tilt of the beams with respect to the sample plane results in a drift of the particles whose magnitude depends on the tilt and the laser intensity. Therefore, the motion of the particles is followed and quantitatively analyzed. After switching on the fringe pattern, the colloidal particles are equilibrated for 250 s and then imaged with 2 frames per second. The positions of the particles were extracted and linked to yield trajectories. From the trajectories, the particles' displacements $\Delta x(t)$ and $\Delta y(t)$ in x- and y-direction, respectively, are determined and their ensemble-averages, $\langle \Delta x(t) \rangle_i$ and $\langle \Delta y(t) \rangle_i$, calculated taking the different durations of the individual trajectories into account (Supplementary Figure 1). For all applied laser intensities, the average displacements fluctuate around zero, suggesting that there is no significant drift of the particles. This indicates a good alignment of the apparatus. The increase of the fluctuations with time is caused by the Brownian motion of the colloids. In contrast, drift would result in a directed motion and hence a linear increase of the displacements $|\Delta x|$ and $|\Delta y|$. This can serve as an aid to (iteratively) improve the alignment, especially the tilt and position of mirror D1 as well as the intensities of the two beams.

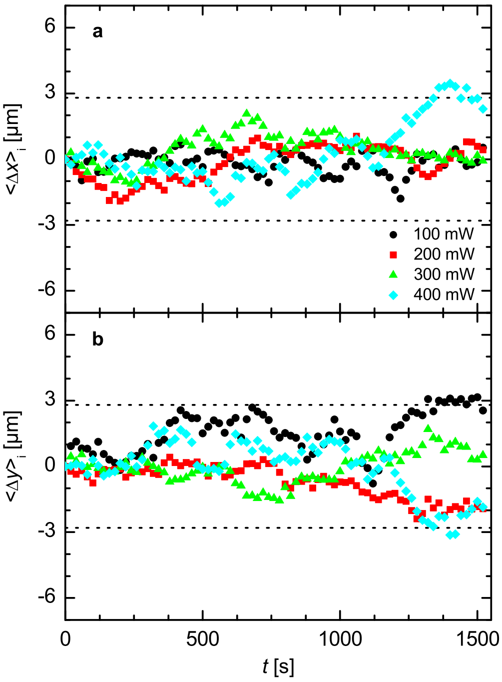

Supplementary Figure 1: Displacement of colloids exposed to the fringe pattern. Mean distance traveled by the particles (a) along the potential minima, $\langle \Delta x \rangle$, and (b) across the potential maxima, $\langle \Delta y \rangle$, during time t for different laser powers (as indicated). The black dotted lines indicate the particle diameter. The fringe spacing $\langle d \rangle \approx 2.66$ µm was similar to the particle diameter $2R = 2.8$ µm. For clarity, only every 40th data point is plotted.

Supplementary References

[1] M. C. Jenkins and S. U. Egelhaaf, Adv. Colloid Interface Sci. **136**, 65 (2008).

This page has been left intentionally blank.

3.5 Dense colloidal mixtures in a sinusoidal potential

Journal: submitted to Physical Review E, June 2017

Impact factor: 2.366

Authors: **Ronja F. Capellmann**, Alina Khisameeva, Florian Platten, and Stefan U. Egelhaaf

1st author

R. F. C. and A. K. conducted the experiments, R. F. C. analysed all the data, R. F. C., F. P. and S. U. E. conceived the research and interpreted the results and all authors contributed to the writing of the draft.

80% contribution of R. F. C.

This page has been left intentionally blank.

Dense colloidal mixtures in a sinusoidal potential

R. F. Capellmann[1], A. Khisameeva[1], F. Platten[1], S. U. Egelhaaf[1]
[1] *Condensed Matter Physics Laboratory, Heinrich Heine University, Universitätsstr. 1, 40225 Düsseldorf, Germany.*

(Dated: June 19, 2017)

Concentrated binary colloidal mixtures were exposed to a periodic potential that was realized using a light field, namely two crossed laser beams creating a fringe pattern. The particle arrangement was recorded using optical microscopy and characterized in terms of the pair distribution function along the minima, the occupation probability perpendicular to the minima, the angular bond distribution and the average potential energy per particle. The competition between particle-particle and particle-potential interactions determines the arrangement of the particles. An increase in the potential amplitude induces a local demixing of the two particle species, whereas an increase in the total packing fraction favors a more homogeneous and partially ordered arrangement.

I. INTRODUCTION

Colloids are widely used as model systems to investigate questions in statistical physics, such as disorder-order transitions and phase behavior. In these studies, colloidal particles typically are considered as ‘big atoms’ [1–3]. They are not only larger but, due to their size, also slower than atoms or molecules. Thus, they can be investigated with optical methods, in particular light scattering and optical microscopy [3–5]. Using microscopy, they even can be followed on an individual-particle level [6, 7]. In colloidal systems, furthermore, the particle-particle interactions can be tuned in a broad range and hence the effects of particle interactions on, e.g., the phase behavior can be studied [2, 3, 8, 9]. In addition to bulk systems, also quasi-two-dimensional samples can be prepared either by confinement or at a surface or interface [9–15].

Moreover, colloids are susceptible to external potentials [16, 17]. This can be utilized in experiments, for example to manipulate colloids [18–20]. Colloids exposed to light are typically drawn towards areas of high intensity and pushed in the propagation direction of the beam. Focused laser beams are exploited in optical tweezers to manipulate individual colloids [18–22], whereas extended light patterns can be used to impose potential landscapes onto colloidal particles [23–25]. Advanced optical components can be used to create a broad range of light fields and hence a large variety of external potentials [26–30]. This allows for a systematic investigation of particle-potential interactions as well as their interplay with particle-particle interactions.

The susceptibility to external potentials also has important consequences for the arrangement and dynamics of colloids. Two-dimensional colloidal suspensions of particles in a periodic (sinusoidal) potential have previously been studied [24, 31–33]. The periodic potential can induce a disorder-order transition which is known as light-induced freezing [34–37]. If the amplitude of the external potential is increased further, the particle fluctuations become more localized. This reduces the interactions between particles in neighboring minima and hence destabilizes the crystal and laser-induced melting to a modulated liquid is observed [34–41]. This relies on the balance between particle-particle and particle-potential interactions. In particular, this behavior results from an intricate interplay between length scales, namely the wavelength of the external potential, the range of the potential explored by the particles, the range of the particle-particle interactions, and the mean interparticle distance.

A further length scale can be introduced by using binary colloidal suspensions. Even without an external potential, binary mixtures show a variety of arrangements and dynamics that depend on the size and mixing ratios as well as the total concentration [10, 11, 42–53] and also three-dimensional binary systems have attracted considerable attention [54–61]. In the presence of a sinusoidal potential, computer simulations reveal new arrangements, such as segregated particle species or the so-called fissuring phase, in which the small particles form fissures in a crystal of large and small particles [62–65]. Moreover, in similar situations the particle dynamics have been studied [66].

In this work, we experimentally investigated the effects of sinusoidal potentials on concentrated binary mixtures in quasi-two dimensions. The particle radii were chosen such that both particle species undergo significant Brownian motion and can easily be tracked using optical microscopy; $R_\mathrm{s} = 1.05$ µm and $R_\mathrm{l} = 2.5$ µm yielding $R_\mathrm{s}/R_\mathrm{l} = 0.42$. Furthermore, to enhance mixing effects, the number densities of large and small particles were chosen to be roughly similar. These ratios in size and density allow for a compact packing in a square lattice which occurs at $R_\mathrm{s}/R_\mathrm{l} = 0.414$ and equal numbers of large and small particles [42, 45]. We expect the most interesting phase behavior to occur if the large particles in neighboring fringes are coupled, i.e. cannot pass each other, while the small particles are free to move. This requires a spacing of the minima d between the two diameters; we have chosen $d = 4.1$ µm. This spacing is not commensurate with the square lattice. It hence leads to an interplay between ideal packing and external potential. To investigate this competition between particle-particle and particle-potential interactions, we focussed on dense samples, i.e. area fractions $\eta > 0.55$.

The remainder of the article is structured as follows: In the next section, section II, we describe the samples and the observation method, digital video microscopy, as well as the creation of the sinusoidal potential and the parameters used to quantify the particle arrangement, namely the pair distribution function parallel to the fringes, $\hat{g}(x)$, the occupation probability perpendicular to the fringes, $p(y)$, the angular bond distribution $N_{\mathrm{b}}(\theta)$, and the average potential energy per particle, E_{V}. In section III, we analyze the effects of the particle-potential and particle-particle interactions by varying the amplitude of the potential, V_0, and the area fraction, η, keeping the other parameters approximately constant. The article concludes with a brief summary of the results in section IV.

II. MATERIALS AND METHODS

II.1. Preparation and observation of the colloidal suspensions

The samples contained two species of spheres of polystyrene with sulfonated chain ends (both from Invitrogen): small particles with radius $R_{\mathrm{s}} = 1.05$ µm and polydispersity 2.5 % as well as large particles with radius $R_{\mathrm{l}} = 2.5$ µm and polydispersity 1.2 %. Appropriate amounts of the stock suspensions were mixed and diluted with deionised water (ELGA purelab flex, electrical resistivity 18.2 MΩcm). The refractive indices of the particles and water were $n_{\mathrm{p}} = 1.59$ and $n_{\mathrm{s}} = 1.33$, respectively, resulting in a ratio of the refractive indices $n = n_{\mathrm{p}}/n_{\mathrm{s}} = 1.20$. The samples were filled in home-built sample cells consisting of three cover-glasses (No. 1.5, 22 mm × 22 mm, VWR) glued on a microscope slide (76 mm × 26 mm × 1 mm, VWR) to form a capillary [7]. Before the cells were assembled, the glassware was cleaned with a mixture of deionised water and 1% alkaline liquid concentrate (Hellmanex II, Hellma Analytics) in an ultrasound bath and thoroughly rinsed with deionised water afterwards. Then the samples were filled in the capillaries, which were sealed with UV glue (NOA 61, Norland). The filled sample cells were stored under ambient conditions.

The samples were imaged using a home-built upright microscope based on a high numerical aperture microscope objective (Plan Apo VC 100×, Nikon, numerical aperture 1.4) and equipped with a CMOS camera (PL-A741, PixeLink, 1280 × 1024 pixels) [27]. In each measurement, 10,800 images were recorded with 2 fps. The pixel pitch was 0.143 µm/px or 0.133 µm/px in two independent sets of experiments. The particle positions were extracted using standard routines [6] where the positions of the large and small particles were determined in separate analysis runs.

II.2. Experimental realization of the sinusoidal potential

A sinusoidal light field, i.e. a fringe pattern, was created by the interference of two laser beams (Verdi V5, Coherent, wavelength $\lambda = 532$ nm) with a crossing angle δ, as described previously [27]. This pushed the particles to the lower cover slip, where they formed a two-dimensional layer, and imposed a sinusoidal potential on the particles that had a period $d = \lambda/(2\sin(\delta/2))$ or wave vector $q = 2\pi/d$ [27, 36]:

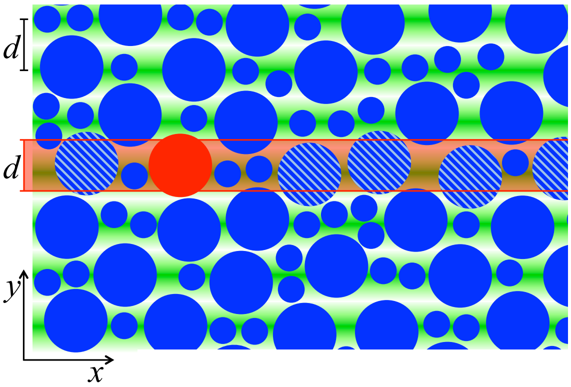

FIG. 1. Schematic representation of a binary colloidal mixture in a sinusoidal potential with period d. For the calculation of the pair distribution functions $\hat{g}_{\mathrm{ii}}(r)$ a particle of species i (red particle) is considered with all distances to other particles of the same species i (striped) whose centers are within a strip that is parallel to the fringes and has width $d/2$ either side of the particle under consideration (indicated by the red area).

$$V(x,y) = gP_{\mathrm{L}}\alpha\left[1 - 3\frac{j_1(qR_{\mathrm{i}})}{qR_{\mathrm{i}}}\cos(qy)\right] \times \exp\left\{-\frac{2\left[x^2 + y^2\cos^2(\theta/2)\right]}{a^2}\right\}, \quad (1)$$

where the x and y directions are chosen along and across the fringes, respectively (Fig. 1), and j_1 denotes the first order spherical Bessel function. The sinusoidal potential was superimposed by a Gaussian envelope, which depends on the radius of the laser beams, a, and their crossing angle δ. The region of interest (ROI) was restricted such that the Gaussian envelope did not decrease by more than 30 %. This decrease is assumed to have a negligible effect on the particle arrangement. Within the ROI, thus,

$$V(y) \approx V_0\,(1 - \cos(qy)) + V_{\mathrm{c}} \quad (2)$$

which is independent of x. The amplitude of the potential, $V_0 = 3gP_{\mathrm{L}}\alpha\, j_1(qR_{\mathrm{i}})/(qR_{\mathrm{i}})$, depends on a set-up dependent parameter g, the laser power P_{L}, the polarizability of the particles $\alpha = R_i^3 n_{\mathrm{s}}^2(n^2-1)/(n^2+2)$, the wave vector q, and the particle radius R_i. The constant offset reads $V_{\mathrm{c}} = V_0\,\{qR_i/[3j_1(qR_i)] - 1\}$. Thus, large and small particles experience different potential amplitudes and offsets. To determine the amplitude of the potential experienced by the small particles, $V_{0,\mathrm{s}}$, a sequence of images (with 4 fps for 30 min) of a dilute suspension of small particles at different laser powers, 0.1 W $\leq P_{\mathrm{L}} \leq$ 0.5 W, was taken. After correcting for slight drifts, the distribution of particles across the fringes was determined, from which the amplitude of the potential experienced by the small particles, $V_{0,\mathrm{s}}(P_{\mathrm{L}})$, was

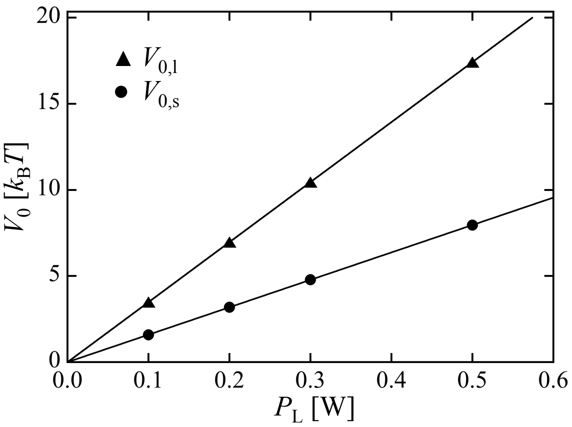

FIG. 2. Amplitude of the potential experienced by the large and small particles, $V_{0,\mathrm{l}}$ and $V_{0,\mathrm{s}}$, respectively, as function of the applied laser power P_L. The amplitude $V_{0,\mathrm{s}}$ was determined experimentally as described in the text, based on which $V_{0,\mathrm{l}}$ was calculated. The lines indicate linear fits.

inferred (Fig. 2), as described previously [28]. A linear fit yielded $V_{0,\mathrm{s}} = 15.9\,(P_\mathrm{L}/\mathrm{W})\,k_\mathrm{B}T$ with the thermal energy $k_\mathrm{B}T$. Since g is independent of the particle size [32], the amplitude for the large particles can be calculated, $V_{0,\mathrm{l}} = R_\mathrm{l}^2 j_1(qR_\mathrm{l})/[R_\mathrm{s}^2 j_1(qR_\mathrm{s})]\,V_{0,\mathrm{s}} = 34.8\,(P_\mathrm{L}/\mathrm{W})\,k_\mathrm{B}T$ (Fig. 2). Thus the potential experienced by the large particles has about double the amplitude of the potential experienced by the small particles.

Before each group of measurements, the optical setup was readjusted to reduce differences in the intensities and incident angles of the two interfering beams to avoid light-induced particle drifts and to produce a fringe spacing $d \approx 4.1$ µm. The actual fringe spacings, 4.04 µm $\leq d \leq$ 4.16 µm, were determined by imaging the light field. The light field was imaged before and after each group of measurements, which did not reveal any changes of d during the measurements. These images were also used to determine the area and position of the ROI. Its area A varied between 30.2 µm × 68.6 µm = 2072 µm^2 and 53.3 µm × 73.7 µm = 3928 µm^2.

Each colloidal mixture was exposed to the light field for 90 min. Before recording images, the particles were allowed to equilibrate in the potential for at least 4 min.

II.3. Data analysis

The composition of the samples is characterized by the total area fraction η and the number ratio of small to large particles, ξ. They were determined for each image based on the numbers of small and large particles in the ROI, N_s and N_l, respectively, according to

$$\eta = \frac{N_\mathrm{s}\pi R_\mathrm{s}^2 + N_\mathrm{l}\pi R_\mathrm{l}^2}{A} \tag{3}$$

and

$$\xi = \frac{N_\mathrm{s}}{N_\mathrm{l}}\ . \tag{4}$$

Subsequently, each measurement was divided into subsets with about constant η and ξ. This is necessary because particles tend to enter an illuminated area and hence the number of particles slightly increased during the measurements. The η and ξ were considered about constant if their absolute standard deviations were smaller than 0.016 and 0.059, respectively. These subsets contained between 1385 and 4001 images and are also considered (individual) ‘measurements’ in the following.

The structure of the colloidal suspensions along the minima, i.e. in x direction (Fig. 1), is characterized by the pair distribution functions parallel to the minima, $\hat{g}_\mathrm{ss}(r)$ and $\hat{g}_\mathrm{ll}(r)$, that consider the small and large particles, respectively. For each particle of species i, the distances to particles of the same species i are considered if their centers are located within a strip that is parallel to the minima, centered around the particle under consideration, and has width d (Fig. 1). All particles of species i in an image and all images of a measurement were taken into account.

To characterize the structure perpendicular to the minima, i.e. in y direction, the occupation probability, $p_i(y)$, was calculated for the small and large particles separately. First the number of small or large particles at position y (and any position x), $N_\mathrm{f,i}(y)$, was determined and then all M periods collapsed onto half a period and normalized by the total number of small or large particles N_i, respectively; $p_i(y) = (1/N_i)\sum_{m=1}^{M}[N_\mathrm{f,i}((m-1)d+y) + N_\mathrm{f,i}(md-y)]$ with $0 \leq y < d/2$. The probability $p_i(y)$ was averaged over three blocks of 200 images in the beginning, the middle and the end of each measurement, during which the position $y = 0$ was chosen to coincide with the maximum probability to find a large particle and was found to be constant for these 200 images.

The local arrangement of particles is quantified by the angular distribution of center-to-center lines (‘bonds’) of neighboring particles of the same species, $N_\mathrm{b,i}(\theta)$, where the angle θ describes the direction of the bond relative to the direction of the minima, i.e. the x direction. Thus the angle covers the range $0° \leq \theta < 90°$. The $N_\mathrm{b,i}(\theta)$ of the small and large particles were determined separately. A particle is considered a neighbor if its center is closer than the distance r_m at which the first minimum of $\hat{g}_\mathrm{ii}(r_\mathrm{m})$ is observed, here $r_\mathrm{m,s} = 3.4\,$µm and $r_\mathrm{m,l} = 6.0\,$µm for the small and large particles, respectively. Since $r_\mathrm{m,l} > d$, large particles in neighboring minima can be neighbors, whereas this is not possible for small particles. The angular bond distribution was averaged over all particles of species i and all images of a measurement, where, to avoid edge effects, only particles at least r_m from the edges were considered whereas their bonded neighbors can be any particle in the ROI. The average number of bonds per particle is obtained through $\sum_j N_\mathrm{b,i}(\theta_j)$.

The average potential energy per particle, E_V, was cal-

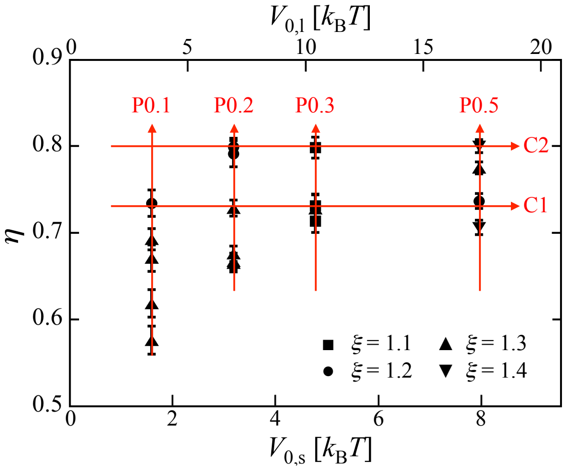

FIG. 3. In the experiments, the total area fraction η and laser power P_L was varied, while the number ratio of small and large particles ξ was about constant (symbols, as indicated). The laser power P_L controls the amplitude of the potential imposed on the small and large particles, $V_{0,\mathrm{s}}$ and $V_{0,\mathrm{l}}$, respectively. The measurements were arranged in series with constant P_L = 0.1 W, 0.2 W, 0.3 W and 0.5 W and varying η (series P0.1 to P0.5) and constant η = 0.73 and 0.80 and varying P_L (C1, C2). Variations (typically increases) in η during the experiments are shown as error bars.

culated according to

$$E_\mathrm{V} = \sum_j p(y_j)\,[V(y_j) - V_\mathrm{c}] \tag{5}$$

which only takes into account the modulated part of the potential but not the constant offset V_c. It was separately determined for small and large particles.

III. RESULTS AND DISCUSSION

In the experiments, we varied the total area fraction η as well as the laser power P_L and hence the amplitude of the external potential, V_0 (Fig. 3). Through the area fraction η the effect of the particle-particle interactions is varied while the particle-potential interactions are controlled through V_0, where the effect of the potential on the large particles is about twice as strong as on the small particles (Fig. 2). The size ratio $R_\mathrm{s}/R_\mathrm{l} = 0.42$ was kept constant and the fringe spacing $d \approx 4.1\,\mu\mathrm{m}$ as well as the number ratio of small and large particles $1.1 \le \xi \le 1.4$ were about constant. In the following we discuss the dependence on the amplitude of the external potential, V_0, for two area fractions $\eta \approx 0.73$ and 0.80 (series C1, C2) as well as the dependence on the area fraction η for four laser powers P_L = 0.1 W, 0.2 W, 0.3 W, and 0.5 W (series P0.1, P0.2, P0.3 and P0.5, Fig. 3) corresponding to amplitudes of the external potential, $1.6\,k_\mathrm{B}T \le V_{0,\mathrm{s}} \le 8.0\,k_\mathrm{B}T$ and $3.5\,k_\mathrm{B}T \le V_{0,\mathrm{l}} \le 18\,k_\mathrm{B}T$, for the small and large particles, respectively (Fig. 3).

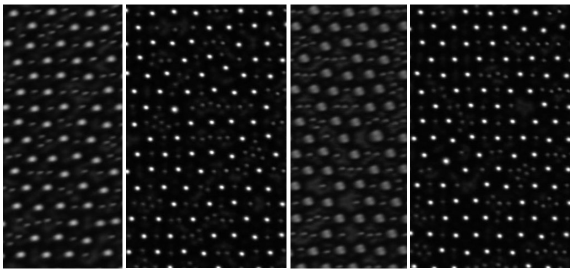
C1-P0.1 C1-P0.2 C1-P0.3 C1-P0.5

FIG. 4. Images of samples with increasing amplitude of the external potential, V_0 (left to right), and constant area fraction $\eta \approx 0.73$ (series C1). The minima of the periodic potential are aligned horizontally. The small and large bright spots are the centers of the small and large particles, respectively. The images were adjusted in brightness and contrast for better visibility.

III.1. Dependence on the amplitude of the potential, V_0

We examined the effect of increasing amplitude V_0 for two different, about constant area fractions $\eta \approx 0.73$ and 0.80 (series C1 and C2, respectively; Fig. 3). For all amplitudes V_0, the particles tend to occupy the potential minima (Fig. 4). This implies order perpendicular to the minima, i.e. in y direction, whereas the particles appear randomly located along the minima, i.e. in x direction. This is characteristic for a modulated liquid [64]. With increasing V_0, in particular the large particles are located closer to the potential minima. Hence they are increasingly confined to a smaller part of the potential resulting in a denser packing of the large particles along the minima. This leads to an increasingly ordered, almost crystalline arrangement of the large particles although with many 'vacancies' that are occupied by small particles. The stronger confinement of the large particles to the minima leaves less space for the small particles in the minima. As a consequence, with increasing V_0 we observe more small particles further from the minima as well as a segregation of small and large particles, especially along the minima.

These qualitative observations are quantified using the pair distribution functions parallel to the minima, i.e. in x direction, of the large and small particles, $\hat{g}_\mathrm{ll}(r)$ and $\hat{g}_\mathrm{ss}(r)$, respectively. First, we consider the arrangement of the large particles (Fig. 5a). With increasing V_0, the first peak of $\hat{g}_\mathrm{ll}(r)$ at $r \approx 5\,\mu\mathrm{m} = 2R_\mathrm{l}$ rises from about 4 to about 12, indicating the increased probability to find two large particles next to each other. The second peak at $r \approx 7\,\mu\mathrm{m} \approx 2(R_\mathrm{l}+R_\mathrm{s})$, corresponding to two large particles separated by one small particle, becomes skewed towards smaller r and increases only slightly while the third peak at $r \approx 9\,\mu\mathrm{m} \approx 2(R_\mathrm{l}+2R_\mathrm{s})$, corresponding to

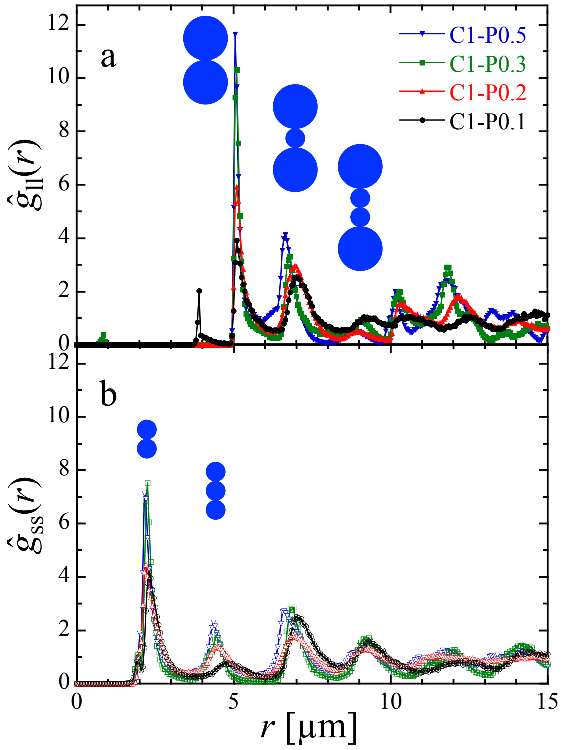

FIG. 5. Pair distribution function parallel to the minima for (a) large, $\hat{g}_{ll}(r)$, and (b) small particles, $\hat{g}_{ss}(r)$. The amplitude of the potential, V_0, is varied (as indicated) while the area fraction is kept constant, $\eta \approx 0.73$ (series C1).

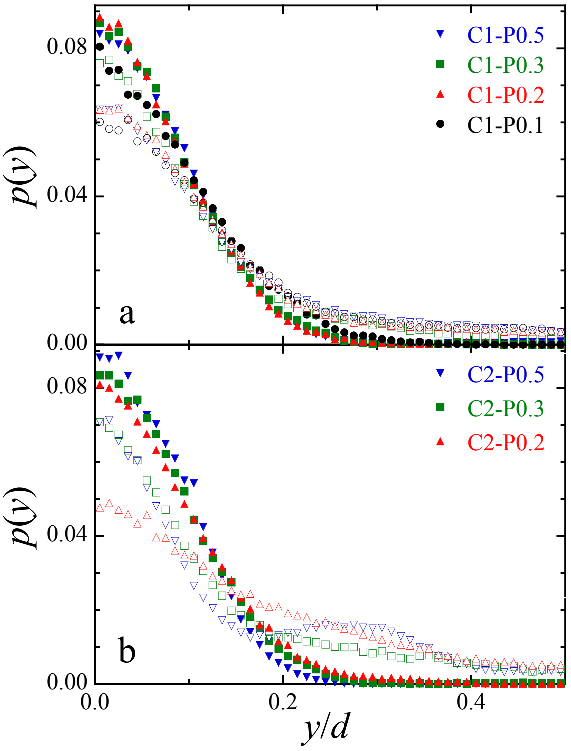

FIG. 6. Occupation probability perpendicular to the minima, $p(y)$. The area fraction is kept constant at (a) $\eta \approx 0.73$ (series C1) and (b) $\eta \approx 0.80$ (series C2) and the amplitude of the potential V_0 is varied (as indicated). The data referring to the large and small particles are indicated by closed and open symbols, respectively.

two large particles separated by two small particles, even tends to decrease. This indicates an increasing trend for the particles to move closer and for the large particles to stay close to each other along the minima of the potential. The corresponding behavior of the small particles is indicated by $\hat{g}_{ss}(r)$ (Fig. 5b). The first two maxima of $\hat{g}_{ss}(r)$ at $r \approx 2.2\,\mu\mathrm{m} \approx 2R_\mathrm{s}$ and $r \approx 4.5\,\mu\mathrm{m} \approx 4R_\mathrm{s}$ increase and also become skewed towards small r with increasing V_0. Thus, the probability to find two or three small particles next to each other along a minimum increases. In the direction of the minima, hence, with increasing V_0 the particles move closer to particles of the same species while the two species tend to segregate.

The arrangement of the particles perpendicular to the minima, i.e. in y direction, is characterized by the occupation probability $p(y)$ which was determined for the large and small particles separately (Fig. 6). Both, the large and small particles are most likely located in the potential minima, i.e. at $y = 0$. Upon increasing V_0, the large and small particles are more localized in the potential minima. However, the small particles can also be found some distance from the minima. The $p_\mathrm{s}(y)$ indicate that some small particles are even located around the maximum ($y \approx d/2$), essentially independent of V_0. In the denser sample with $\eta \approx 0.80$, at low V_0 the $p_\mathrm{s}(y)$ indicates a relatively low probability to find particles in the minima which, however, significantly increases if V_0 is increased. Nevertheless, with increasing V_0 small particles are also located especially around $y \approx 0.3d$. The location $y \approx 0.3d$ corresponds to about R_s and indicates that pairs of small particles are orientated perpendicular to the minima. This is attributed to the stronger confinement of the large particles to the minima, which decreases the available space in the minima for the small particles. Thus, the $p(y)$ indicate that the large particles are almost exclusively located in the minima and the more so as V_0 is increased. As a consequence, the small particles, although they as well tend to stay in the minima, are also found further away from the minima.

The angular distribution of center-to-center lines ('bonds') $N_\mathrm{b}(\theta)$ provides information on the local arrangement of small and large particles beyond the two directions discussed so far (Fig. 7). The $N_{\mathrm{b,l}}(\theta)$ of the large particles show peaks at 0°, indicating pairs aligned along the minima, and around 50°, which involves two particles located in neighboring minima. All peaks become slightly more pronounced with increasing V_0. For the low area fraction $\eta \approx 0.73$, furthermore, with increasing V_0

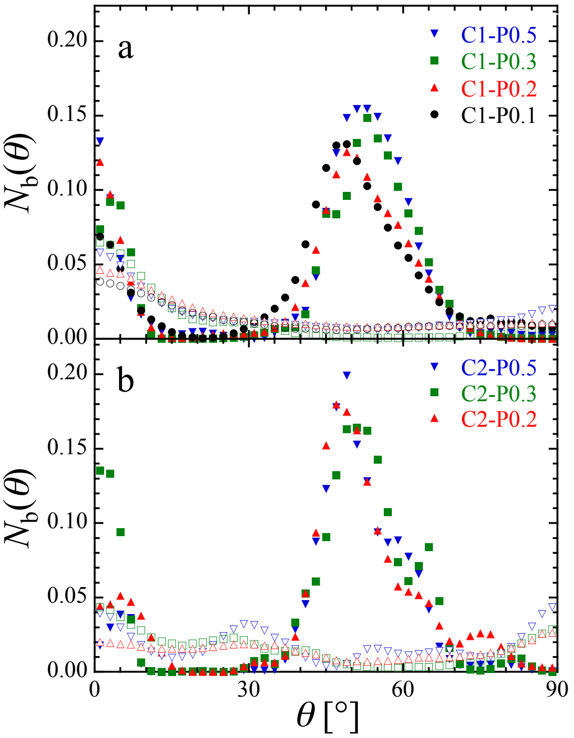

FIG. 7. Angular bond distribution $N_{\mathrm{b}}(\theta)$. The area fraction is kept constant at (a) $\eta \approx 0.73$ (series C1) and (b) $\eta \approx 0.80$ (series C2) and the amplitude of the potential V_0 is varied (as indicated). The data referring to the large and small particles are indicated by closed and open symbols, respectively.

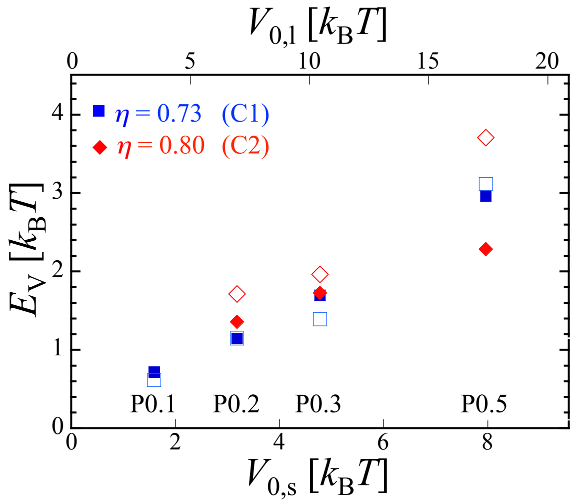

FIG. 8. Average potential energy E_{V} per large particle (closed symbols) and per small particle (open symbols), respectively, for area fractions $\eta \approx 0.73$ (series C1) and 0.80 (series C2, as indicated) and varying amplitude of the potential, V_0.

the second peak shifts from 49° to 53°, indicating a closer packing. In contrast, for the high area fraction $\eta \approx 0.80$, the peak essentially remains at $\theta \approx 49°$. Also the small particles are preferentially aligned along the minima as indicated by peaks of $N_{\mathrm{b,s}}(\theta)$ at 0°. With increasing V_0, a further, small peak at 90° develops, indicating an alignment perpendicular to the minima and hence consistent with the arrangement suggested by $p_{\mathrm{s}}(y)$. For the higher area fraction $\eta \approx 0.80$, even at low V_0 the $N_{\mathrm{b,s}}(\theta)$ shows more pronounced peaks at 90° and additional peaks at about 30°, which correspond to a triangular arrangement.

Based on the positions of the particles, characterized by the occupation probability $p(y)$ (Fig. 6), the average potential energy per particle, E_{V}, was calculated. For the low area fraction $\eta \approx 0.73$ and a specific condition, i.e. laser power P_{L}, the average potential energies E_{V} are very similar for the large and small particles (Fig. 8). This is consistent with expectations for low enough particle concentrations. At the higher area fraction $\eta \approx 0.80$, accordingly, the constraints imposed by crowding lead to differences in the average energies of the large and small particles, which become more pronounced as the amplitude of the external potential, V_0, increases. The average potential energy of the small particles is found to be larger than the one of the large particles, consistent with the observation that the small particles are more frequently located further from the minima. This could be attributed to the fact that the small particles are less susceptible to the external potential by a factor of about two which, however, is counterbalanced by the smaller stretch of a minimum required to place a small particle, also by about a factor of two. This suggests that this behavior is rather due to their smaller size which implies that their spatial requirements are smaller and thus they can more flexibly be placed achieving a better packing. Small particles placed in minima, furthermore, use space inefficiently since they are much smaller than the distance between minima. Nevertheless, the average potential energy per particle (irrespective of their size) does not significantly depend on the area fraction but increases about linearly with the amplitude of the potential, V_0.

In summary, an increase of the amplitude of the potential, V_0, confines the particles more strongly to the minima, in particular the large particles. This forces the particles to move closer together. The small particles can also be found further from the minima, including pairs oriented perpendicular to the minima and triangular configurations. This is attributed to the limited space and their smaller susceptibility to the external potential but in particular to their smaller size. In addition, the large and small particles show some segregation.

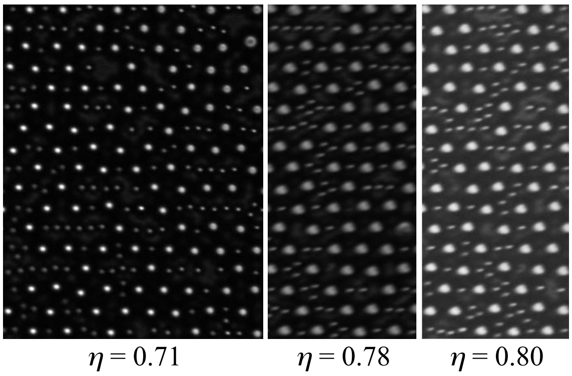
$\eta = 0.71$ $\eta = 0.78$ $\eta = 0.80$

FIG. 9. Images of samples with increasing area fraction η (as indicated) and constant external potential corresponding to a laser power $P_{\mathrm{L}} = 0.5$ W (series P0.5). The minima of the periodic potential are aligned horizontally. The small and large bright spots are the centers of the small and large particles, respectively. The images were adjusted in brightness and contrast for better visibility.

III.2. Dependence on the total area fraction η

The effects of the area fraction η on the arrangement of the particles are investigated in measurement series with constant amplitudes of the external potential, V_0, but increasing area fraction η (series P0.1 to P0.5, Fig. 3). The particles are observed to mainly occupy the minima and hence appear ordered perpendicular to the minima, i.e. in y direction (Fig. 9). They, however, are rather disordered along the minima, i.e. in x direction. At low packing fraction, along the minima several particles of the same species are observed next to each other whereas they are more mixed at higher area fractions. Thus, the increase in area fraction η leads to a more homogeneous arrangement which also is increasingly ordered perpendicular to the minima and hence appears more crystalline. However, some of the positions of the large particles are taken by small particles, either by individual small particles as well as pairs or triplets of small particles. Nevertheless, in contrast to samples with lower area fractions, the large and small particles are much more mixed.

This behavior is reflected in the pair distribution functions parallel to the minima of the large and small particles, $\hat{g}_{\mathrm{ll}}(r)$ and $\hat{g}_{\mathrm{ss}}(r)$, respectively. For the large particles, the first peak at $r \approx 5$ µm $= 2R_{\mathrm{l}}$ decreases with increasing η, while the second and the third peaks increase (Fig. 10a). Thus, it becomes less likely that two large particles are neighbors but more likely for one or two small particles to be located in between two large particles. The $\hat{g}_{\mathrm{ss}}(r)$ of the small particles is consistent with the behavior of the large particles (Figure 10b). Both, the first peak at $r \approx 2.2$µm $\approx 2R_{\mathrm{s}}$ and the second peak at $r \approx 4.4$ µm $\approx 4R_{\mathrm{s}}$, decrease corresponding to a lower probability to find two or three small particles next to each other. Instead, the third peak at $r \approx 6.8$ µm increases. This distance roughly corresponds to four small particles next to each other, $6R_{\mathrm{s}} = 6.3$ µm, or a large particle between two small particles, $2R_{\mathrm{s}} + 2R_{\mathrm{l}} = 7.1$ µm, where the decreasing first two peaks and the images suggest that a large particle between two small particles is more likely. Hence $\hat{g}_{\mathrm{ll}}(r)$ as well as $\hat{g}_{\mathrm{ss}}(r)$ suggest that, upon increasing η, the distribution of large and small particles along the minima becomes more homogeneous.

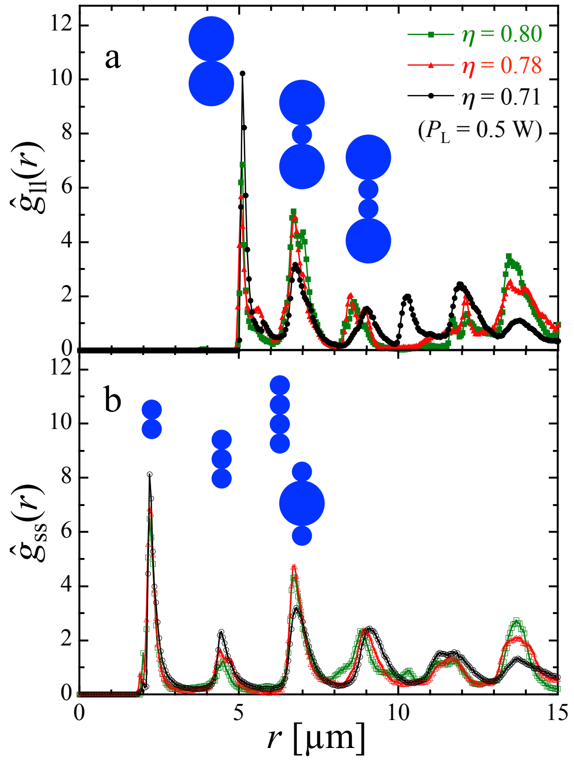

FIG. 10. Pair distribution function parallel to the minima for (a) large, $\hat{g}_{\mathrm{ll}}(r)$, and (b) small particles $\hat{g}_{\mathrm{ss}}(r)$. The area fraction is varied from $\eta = 0.71$ to 0.80 (as indicated) while the amplitude of the potential, V_0, is kept constant (series P0.5).

The occupation probability of the large particles, $p_{\mathrm{l}}(y)$, shows only a weak dependence on the area fraction η for all investigated amplitudes of the potential V_0 (Fig. 11). In contrast, it indicates a progressive localization in the minima with increasing V_0, as already described above (Fig. 6). In contrast, the $p_{\mathrm{s}}(y)$ suggest a different behavior of the small particles. The small particles are slightly less localized in and close to the minima ($y \lesssim 0.1d$) but, correspondingly, occur with a higher probability at and close to the maxima ($y \gtrsim 0.2d$). This becomes more pronounced as the area fraction η increases; for larger η the $p_{\mathrm{s}}(y{\approx}0)$ decrease and $p_{\mathrm{s}}(y{\gtrsim}0.2d)$ increase. For the largest V_0 even a peak at $y \approx 0.3d$ appears. A peak at $y \approx 0.3d$ suggests the existence of pairs of small particles orientated perpendicular to the minima. These features become more pronounced as V_0 increases, as already de-

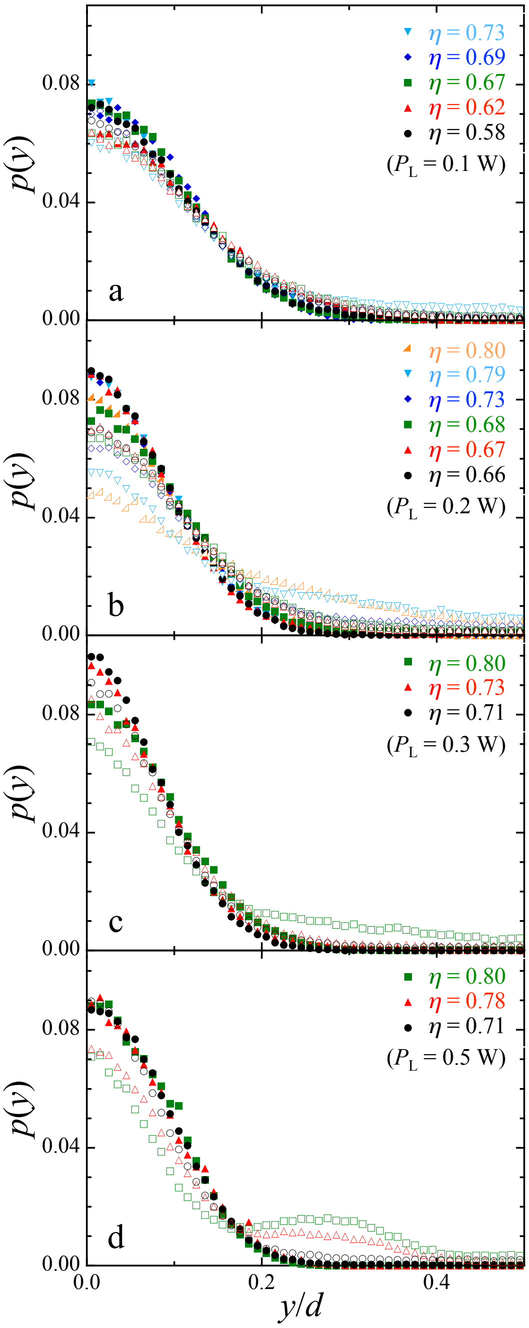

FIG. 11. Occupation probability perpendicular to the minima, $p(y)$. The laser power P_L and hence the amplitude of the potential, V_0, is kept constant at (a) $P_L = 0.1$ W (series P0.1), (b) 0.2 W (P0.2), (c) 0.3 W (P0.3), and (d) 0.5 W (P0.5) and the area fraction η is varied (as indicated). The data referring to the large and small particles are indicated by closed and open symbols, respectively.

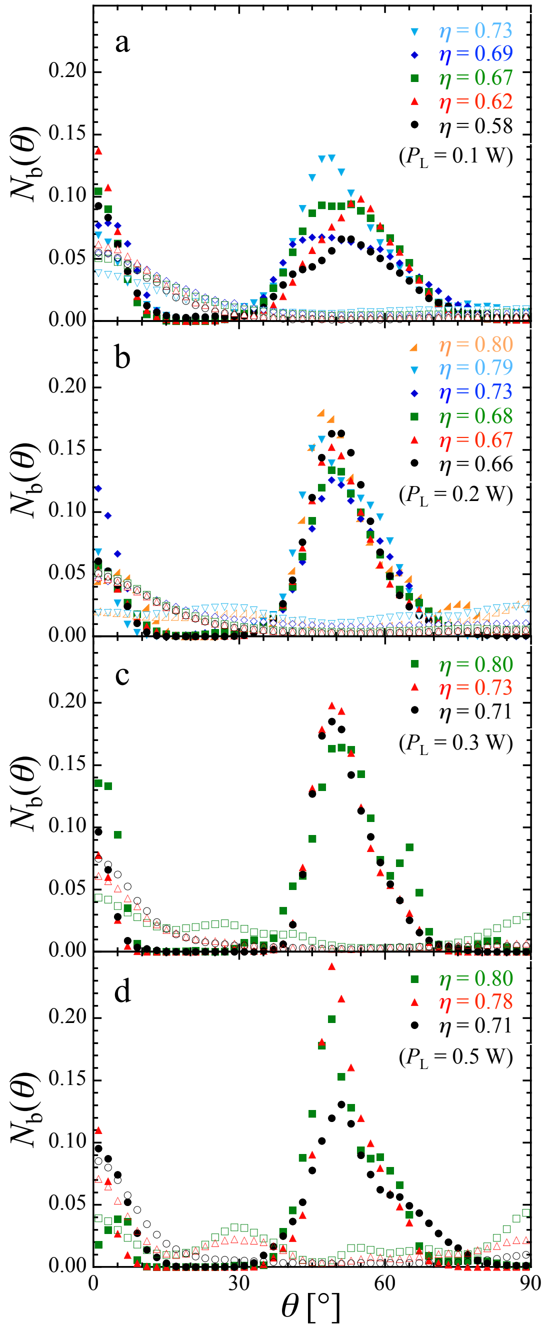

FIG. 12. Angular bond distribution $N_b(\theta)$. The laser power P_L and hence the amplitude of the potential, V_0, is kept constant at (a) $P_L = 0.1$ W (series P0.1), (b) 0.2 W (P0.2), (c) 0.3 W (P0.3), and (d) 0.5 W (P0.5) and the area fraction η is varied (as indicated). The data referring to the large and small particles are indicated by closed and open symbols, respectively.

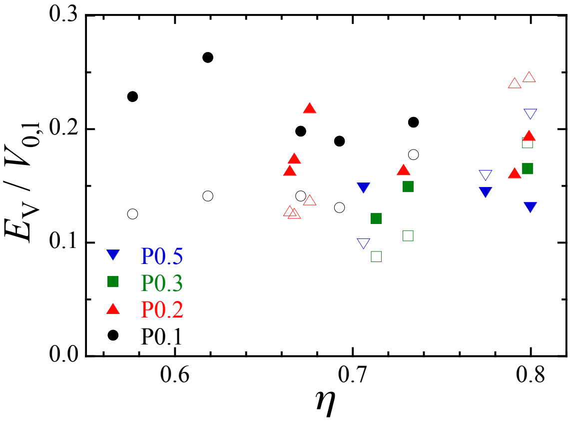

FIG. 13. Average potential energy per particle normalized by the amplitude of the potential experienced by the large particles, $E_\mathrm{V}/V_{0,\mathrm{l}}$, for large (closed symbols) and small particles (open symbols), respectively, as a function of area fraction η. The different laser powers P_L are distinguished by symbols.

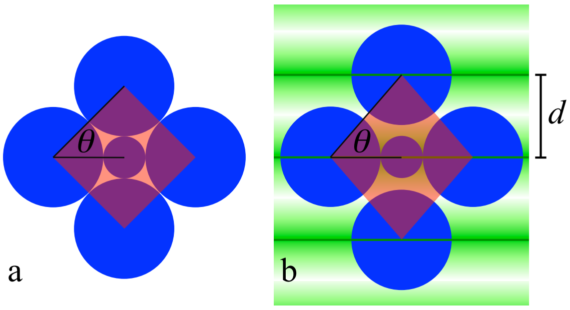

FIG. 14. Schematic representation of (a) a unit cell of a square lattice of large particles with small particles in their interstices and (b) a unit cell of an oblique lattice of large particles with small particles in their interstices in the presence of the external potential. The unit cell is indicated by the red area and the bond angle θ is labeled. Sizes are to scale.

scribed in the previous section.

The angular bond distribution of the large particles, $N_{\mathrm{b,l}}(\theta)$, shows two peaks independent of η and also V_0; at 0°, indicating alignment with the minima, and at about 50°, involving two large particles in neighboring minima (Fig. 12). These peaks tend to become narrower and higher with increasing η and, as discussed above, with increasing V_0. Their position does not significantly depend on η but shifts to slightly larger θ with increasing V_0, as also discussed above. For the small particles the peaks evolve differently. With increasing η, the peak at 0° slightly decreases and hence it becomes less likely to find two (or more) small particles next to each other along a minimum. Hence the arrangement along the minima becomes more homogeneous. A further peak at 90° develops, which reflects the arrangements of pairs of small particles orientated perpendicular to the minima. It becomes more pronounced as η is increased. With increasing η, moreover, a third peak emerges at about 30° indicating the formation of triangular configurations with one particle in a minimum and the other two besides the minimum. All these trends are more pronounced for larger V_0, as described above.

The average potential energy per particle, E_V, was found to depend about linearly on the amplitude of the potential, V_0 (Fig. 8). When discussing the dependence on the area fraction η, this is taken into account by considering the average potential energy per particle normalized by the amplitude of the potential experienced by the large particles, $E_\mathrm{V}/V_{0,\mathrm{l}}$. This normalization was arbitrarily chosen; a normalization by the amplitude of the potential experienced by the small particles results in exactly the same trends since $E_\mathrm{V}/V_{0,\mathrm{l}} = 0.458\,E_\mathrm{V}/V_{0,\mathrm{s}}$. Indeed, $E_\mathrm{V}/V_{0,\mathrm{l}}$ is found to be virtually independent of the area fraction η (Fig. 13). The normalized average potential energy per large particle, $E_{\mathrm{V,l}}/V_{0,\mathrm{l}}$, tends to decrease and the normalized average potential energy per small particle, $E_{\mathrm{V,s}}/V_{0,\mathrm{l}}$, tends to increase with area fraction η, but this is a rather weak dependence and not significant within the fluctuations and uncertainties. These fluctuations might be related to the slightly different number ratios of small to large particles ξ (Fig. 3) but are mainly attributed to kinetic effects combined with the large effect of particles located close to the potential maxima, where, due to their small number, even small variations in their number have relatively large effects on $E_{\mathrm{V,s}}/V_{0,\mathrm{l}}$.

The size ratio $R_\mathrm{s}/R_\mathrm{l} = 0.42$ and number ratio $1.1 \leq \xi \leq 1.4$ in our experiments are close to the parameters of a compact packing, $R_\mathrm{s}/R_\mathrm{l} = 0.414$ and $\xi = 1$ [42, 45]. Without an external potential, a square lattice of the large particles with the small particles in the interstices between the large particles is predicted to form (Fig. 14a). Due to the size ratio $\xi > 1$, this should coexist with a one-component triangular lattice of small particles [42]. In the presence of the external potential, the unit cell is expected to be stretched to accommodate the particle positions to the potential minima (Fig. 14b). This significantly reduces the maximum area fraction, to $\eta = 0.793$, which still is compatible with the explored range of area fractions $\eta \lesssim 0.80$. It also changes the lattice symmetry to oblique and hence increases the angle θ. Upon increasing the amplitude of the potential V_0, indeed an increase of the angle θ has been observed (Fig. 7a). At low area fractions η, along the minima the samples are disordered and the two particle species are partially segregated, while the large particles avoid each other in neighboring minima. The samples resemble modulated liquids [64]. At higher area fractions η, particle-particle interaction become more important and ordered structures appear (Fig. 9). The expected oblique symmetry dominates, although with many defects. Moreover, a coexisting triangular structure of small particles was not observed, rather pairs, triplets or small groups of small particles within the lattice of large particles. These difference between observed and expected structures might be due to several reasons. The perturbative argument might not be valid at the present strengths of the external potential. Furthermore, the crystal structure was predicted for a temperature $T = 0$, while the experiments are performed at finite temperature. This might affect the thermodynamically favored structure [48, 49]. In another binary system, the large particles were observed to remain essentially ordered whereas the lattice of small particles became disordered upon increasing the temperature [48]. In addition, the contribution of the configurational entropy is ignored in the geometric packing argument that only considers the free volume entropy. A significant contribution of the configurational entropy is expected in a binary system where not only spatial order but also compositional order must be maintained. Furthermore, two-dimensional binary systems have been suggested to possess a rough energy landscape [48, 53] and observed to form glasses [11, 67, 68]. Thus, the system might not reach the minimum energy configuration favored by thermodynamics but become trapped in a metastable state. The particle motion, in addition, is constrained by the external potential. This renders rearrangements, especially across the maxima, less likely, which is similar to the situation of tethered disks [69]. It hence is likely that some of the observed structures represent kinetically arrested states and, to some extent, depend on the sample history. This is consistent with the observed (modest) fluctuations in $E_{\mathrm{V}}/V_{0,\mathrm{l}}$ as a function of η (Fig. 13).

IV. CONCLUSIONS

We studied dense binary colloidal mixtures in a sinusoidal potential. The potential induces a high degree of order perpendicular to the minima and a varying degree of order along the minima, depending on the amplitude of the potential V_0. An increase of V_0 leads to a stronger confinement of the particles to the minima. Especially the large particles are tightly confined to the minima whereas the small particles can also be found further from the minima, even close to the maxima. Hence the average potential energy per particle tends to be larger for the small particles than the large particles. This behavior of the small particles is attributed to the larger number of possibilities to place a small particle and the better match of the period with the size of the large particles. The different behaviors of the two particle species result in a local demixing of small and large particles along the minima. A more homogeneous arrangement of the particles and also a higher degree of order is observed upon increasing the total area fraction η. Due to the incommensurability of the period of the sinusoidal potential, d, with the square lattice, the particles are arranged in an oblique lattice, in which the small particles occupy the interstices of the large particles. However, many defects exist and the small particles do not only occur individually but also in pairs and triplets. This is attributed to kinetic effects which are expected to play an important role in this system.

V. ACKNOWLEDGEMENTS

We thank Hartmut Löwen and Jörg Bewerunge (University Düsseldorf), Peter Nielaba (University Konstanz) and Ramón Castañeda-Priego (University of Guanajuato, León) for stimulating and very helpful discussions. We acknowledge support by the International Helmholtz Research School of Biophysics and Soft Matter (BioSoft) and funding by the Deutsche Forschungsgemeinschaft (DFG, project EG 269/6-1).

[1] W. C. K. Poon, Science **304**, 830 (2004).
[2] W. C. K. Poon, P. Pusey, and H. Lekkerkerker, Physics World **9**, 27 (April 1996).
[3] P. N. Pusey, "Colloidal suspensions," in *Liquids, Freezing and Glass Transition*, edited by J. P. Hansen, D. Levesque, and J. Zinn-Justin (Elsevier Science Publishers, 1991) pp. 763–942.
[4] B. J. Berne and R. Pecora, *Dynamic Light Scattering* (Wiley, 1976).
[5] V. Prasad, D. Semwogerere, and E. R. Weeks, J. Phys.: Condens. Matter **19**, 113102 (2007).
[6] J. C. Crocker and D. G. Grier, J. Coll. Interf. Sci. **179**, 298 (1996).
[7] M. C. Jenkins and S. U. Egelhaaf, Adv. Coll. Interf. Sci. **136**, 65 (2008).
[8] P. N. Pusey and W. van Megen, Nature **320**, 340 (1986).
[9] L. J. Bonales, J. E. F. Rubio, H. Ritacco, C. Vega, R. G. Rubio, and F. Ortega, Langmuir **27**, 3391 (2011).
[10] L. J. Bonales, F. Martínez-Pedrero, M. A. Rubio, R. G. Rubio, and F. Ortega, Langmuir **28**, 16555 (2012).
[11] F. Ebert, P. Keim, and G. Maret, Europ. Phys. J. E **26**, 161 (2008).
[12] F. Ebert, P. Dillmann, G. Maret, and P. Keim, Rev. Sci. Instrum. **80**, 083902 (2009).
[13] U. Gasser, C. Eisenmann, G. Maret, and P. Keim, Chem. Phys. Chem. **11**, 963 (2010).
[14] T. O. E. Skinner, S. K. Schnyder, D. G. A. L. Aarts, J. Horbach, and R. P. A. Dullens, Phys. Rev. Lett. **111**, 128301 (2013).
[15] X. Ma, W. Chen, Z. Wang, Y. Peng, Y. Han, and P. Tong, Phys. Rev. Lett. **110**, 078302 (2013).
[16] H. Löwen, J. Phys.: Condens. Matter **13**, R415 (2001).
[17] H. Löwen, J. Phys.: Condens. Matter **20**, 404201 (2008).
[18] K. C. Neuman and S. M. Block, Rev. Sci. Instrum. **75**, 2787 (2004).
[19] D. G. Grier, Nature **424**, 810 (2003).
[20] K. Dholakia, P. Reece, and M. Gu, Chem. Soc. Rev. **37**, 42 (2008).
[21] A. Ashkin, Phys. Rev. Lett. **24**, 156 (1970).
[22] K. Dholakia, G. Spalding, and M. MacDonald, Physics World **15**, 31 (October 2002).
[23] M. P. N. Juniper, R. Besseling, D. G. A. L. Aarts, and R. P. A. Dullens, Opt. Express **20**, 28707 (2012).

[24] F. Evers, R. D. L. Hanes, C. Zunke, R. F. Capellmann, J. Bewerunge, C. Dalle-Ferrier, M. C. Jenkins, I. Ladadwa, A. Heuer, R. Castañeda-Priego, and S. U. Egelhaaf, Eur. Phys. J.: Spec. Top. **222**, 2995 (2013).

[25] J. Bewerunge, A. Sengupta, R. F. Capellmann, F. Platten, S. Sengupta, and S. U. Egelhaaf, J. Chem. Phys. **145**, 044905 (2016).

[26] A. E. Chiou, W. Wang, G. J. Sonek, J. Hong, and M. W. Berns, Opt. Commun. **133**, 7 (1997).

[27] M. C. Jenkins and S. U. Egelhaaf, J. Phys.: Condens. Matter **20**, 404220 (2008).

[28] R. F. Capellmann, J. Bewerunge, F. Platten, and S. U. Egelhaaf, Rev. Sci. Instrum. **88**, 056102 (2017).

[29] R. D. L. Hanes, M. C. Jenkins, and S. U. Egelhaaf, Rev. Sci. Instrum. **80**, 083703 (2009).

[30] J. Bewerunge and S. U. Egelhaaf, Phys. Rev. A **93**, 013806 (2016).

[31] S. Herrera-Velarde and R. Castañeda-Priego, J. Phys.: Condens. Matter **19**, 226215 (2007).

[32] C. Dalle-Ferrier, M. Krüger, R. D. L. Hanes, S. Walta, M. C. Jenkins, and S. U. Egelhaaf, Soft Matter **7**, 2064 (2011).

[33] X.-G. Ma, P.-Y. Lai, and P. Tong, Soft Matter **9**, 8826 (2013).

[34] C. Bechinger, M. Brunner, and P. Leiderer, Phys. Rev. Lett. **86**, 930 (2001).

[35] A. Chowdhury, B. J. Ackerson, and N. A. Clark, Phys. Rev. Lett. **55**, 833 (1985).

[36] K. Loudiyi and B. J. Ackerson, Physica A **184**, 1 (1992).

[37] Q. H. Wei, C. Bechinger, D. Rudhardt, and P. Leiderer, Phys. Rev. Lett. **81**, 2606 (1998).

[38] J. Chakrabarti, H. R. Krishnamurthy, A. K. Sood, and S. Sengupta, Phys. Rev. Lett. **75**, 2232 (1995).

[39] W. Strepp, S. Sengupta, and P. Nielaba, Phys. Rev. E **63**, 046106 (2002).

[40] W. Strepp, S. Sengupta, and P. Nielaba, Phys. Rev. E **66**, 056109 (2002).

[41] W. Strepp, S. Sengupta, M. Lohrer, and P. Nielaba, Comp. Phys. Comm. **147**, 370 (2002).

[42] C. N. Likos and C. L. Henley, Phil. Mag. B **68**, 85 (1993).

[43] C. J. Kiely, J. Fink, M. Brust, D. Bethell, and D. J. Schiffrin, Nature **396**, 444 (1998).

[44] C. J. Kiely, J. Fink, J. G. Zheng, M. Brust, D. Bethell, and D. J. Schiffrin, Adv. Mater. **12**, 640 (2000).

[45] T. Kennedy, Discrete Comput. Geom. **35**, 255 (2006).

[46] T. Stirner and J. Sun, Langmuir **21**, 6636 (2005).

[47] H. Ma and L. L. Dai, Langmuir **25**, 11210 (2009).

[48] A. D. Law, D. M. A. Buzza, and T. S. Horozov, Phys. Rev. Lett. **106**, 128302 (2011).

[49] A. D. Law, T. S. Horozov, and D. M. A. Buzza, Soft Matter **7**, 8923 (2011).

[50] A. L. Thorneywork, R. Roth, D. G. A. L. Aarts, and R. P. A. Dullens, J. Chem. Phys. **140**, 161106 (2014).

[51] L. Assoud, R. Messina, and H. Löwen, Europhys. Lett. **80**, 48001 (2007).

[52] J. Fornleitner, F. Lo Verso, G. Kahl, and C. N. Likos, Soft Matter **4**, 480 (2008).

[53] J. Fornleitner, F. Lo Verso, G. Kahl, and C. N. Likos, Langmuir **25**, 7836 (2009).

[54] M. D. Eldridge, P. A. Madden, and D. Frenkel, Nature **365**, 35 (1993).

[55] P. Bartlett, R. H. Ottewill, and P. N. Pusey, Phys. Rev. Lett. **68**, 3801 (1992).

[56] M. E. Leunissen, C. G. Christova, A. P. Hynninen, C. P. Royall, A. I. Campbell, A. Imhof, M. Dijkstra, R. van Roij, and A. van Blaaderen, Nature **437**, 235 (2005).

[57] P. Bartlett and A. I. Campbell, Phys. Rev. Lett. **95**, 128302 (2005).

[58] E. V. Shevchenko, D. V. Talapin, N. A. Kotov, S. O'Brian, and C. B. Murray, Nature **439**, 55 (2006).

[59] A. P. Hynninen, C. G. Christova, R. van Roij, A. van Blaaderen, and D. Dijkstra, Phys. Rev. Lett. **96**, 138308 (2006).

[60] T. Sentjabrskaja, E. Zaccarelli, C. De Michele, F. Sciortino, P. Tartaglia, T. Voigtmann, S. U. Egelhaaf, and M. Laurati, Nat. Comm. **7**, 11133 (2016).

[61] J. Hendricks, R. Capellmann, A. B. Schofield, S. U. Egelhaaf, and M. Laurati, Phys. Rev. E **91**, 032308 (2015).

[62] K. Franzrahe and P. Nielaba, Phys. Rev. E **76**, 061503 (2007).

[63] K. Franzrahe, P. Nielaba, A. Ricci, K. Binder, S. Sengupta, P. Keim, and G. Maret, J. Phys.: Condens. Matter **20**, 404218 (2008).

[64] K. Franzrahe and P. Nielaba, Phys. Rev. E **79**, 051505 (2009).

[65] D. Wilms, S. Deutschländer, U. Siems, K. Franzrahe, P. Henseler, P. Keim, N. Schwierz, P. Virnau, K. Binder, G. Maret, and P. Nielaba, J. Phys.: Condens. Matter **24**, 464119 (2012).

[66] P. Tierno and A. V. Straube, Eur. Phys. J. E **39**, 54 (2016).

[67] S. Mazoyer, F. Ebert, G. Maret, and P. Keim, Europhys. Lett. **88**, 66004 (2009).

[68] P. Richard, L. Oger, J.-P. Troadec, and A. Gervois, Phys. Rev. E **60**, 4551 (1999).

[69] R. C. Doty, R. T. Bonnecaze, and B. A. Korgel, Phys. Rev. E **65**, 061503 (2002).

This page has been left intentionally blank.

3.6 Colloids in light fields: Particle dynamics in random and periodic energy landscapes

Journal: European Physical Journal: Special Topics

Reference: *Eur. Phys. J.: Spec. Top.* **222**, 2995 (2013)

Impact factor: 1.399

Authors: Florian Evers, Richard D. L. Hanes, Christoph Zunke, **Ronja F. Capellmann**, Jörg Bewerunge, Cecile Dalle-Ferrier, Matthew C. Jenkins, Imad Ladadwa, Andreas Heuer, Ramón Castañeda-Priego, and Stefan U. Egelhaaf

4th author

In this review article, R. F. C. contributed new unpublished results of a binary colloidal mixture in a sinusoidal potential (Figure 6) for which she conducted the experiments, analysed the data and contributed to their interpretation. She also contributed to the writing of the article.

10% contribution of R. F. C.

Reprinted with kind permission of The European Physical Journal (EPJ).

This page has been left intentionally blank.

Eur. Phys. J. Special Topics **222**, 2995–3009 (2013)
© EDP Sciences, Springer-Verlag 2013
DOI: 10.1140/epjst/e2013-02071-2

THE EUROPEAN
PHYSICAL JOURNAL
SPECIAL TOPICS

Review

Colloids in light fields: Particle dynamics in random and periodic energy landscapes

F. Evers[1,a], R.D.L. Hanes[1], C. Zunke[1], R.F. Capellmann[1], J. Bewerunge[1],
C. Dalle-Ferrier[1], M.C. Jenkins[1], I. Ladadwa[2,3], A. Heuer[2], R. Castañeda-Priego[4],
and S.U. Egelhaaf[1,b]

[1] Condensed Matter Physics Laboratory, Heinrich Heine University, 40225 Düsseldorf, Germany
[2] Institute of Physical Chemistry, University Münster, 48149 Münster, Germany
[3] Fahad Bin Sultan University, 71454 Tabuk, Saudi-Arabia
[4] Division of Sciences and Engineering, University of Guanajuato, 37150 León, Mexico

Received 6 September 2013 / Received in final form 17 September 2013

Abstract. The dynamics of colloidal particles in potential energy landscapes have mainly been investigated theoretically. In contrast, here we discuss the experimental realization of potential energy landscapes with the help of laser light fields and the observation of the particle dynamics by video microscopy. The experimentally observed dynamics in periodic and random potentials are compared to simulation and theoretical results in terms of, e.g. the mean-squared displacement, the time-dependent diffusion coefficient or the non-Gaussian parameter. The dynamics are initially diffusive followed by intermediate subdiffusive behaviour which again becomes diffusive at long times. How pronounced and extended the different regimes are, depends on the specific conditions, in particular the shape of the potential as well as its roughness or amplitude but also the particle concentration. Here we focus on dilute systems, but the dynamics of interacting systems in external potentials, and thus the interplay between particle-particle and particle-potential interactions, are also mentioned briefly. Furthermore, the observed dynamics of dilute systems resemble the dynamics of concentrated systems close to their glass transition, with which it is compared. The effect of certain potential energy landscapes on the dynamics of individual particles appears similar to the effect of interparticle interactions in the absence of an external potential.

1 Introduction

The motion of colloidal particles in potential energy landscapes is a central process in statistical physics which is relevant for a variety of scientific and applied fields such as hard and soft condensed matter, nanotechnology, geophysics and biology [1–3].

---

[a] e-mail: `Florian.Evers@hhu.de`
[b] e-mail: `Stefan.Egelhaaf@hhu.de`

3.6 Colloids in light fields: Particle dynamics in random and periodic energy landscapes

Particle diffusion in periodic and random external fields is encountered in many situations [4–7], such as atoms, molecules, clusters or particles moving on a surface with a spatially varying topology or interaction [8], or moving through inhomogeneous bulk materials, e.g. porous media or gels [9], rocks [2], living cells or biological membranes [10–15]. It also includes the diffusion of charge carriers in a conductor with impurities [16,17], particle diffusion on garnet films [18–20] or diffusion in optical lattices [21,22], superdiffusion in active media [23], and vortex dynamics in superconductors [24]. Moreover, some processes are modelled by diffusion in the configuration space of the system, e.g. the glass transition [25–30] and protein folding [31–33].

Thermal energy drives the Brownian motion of colloidal particles [34,35]. In free diffusion, their mean-squared displacement $\langle \Delta x^2(t) \rangle$ increases linearly with time t; $\langle \Delta x^2(t) \rangle \propto t^{\mu}$ with $\mu = 1$. Particle-potential (as well as particle-particle) interactions can modify the dynamics significantly leading to $\mu \neq 1$ [14,36–42]. Often the dynamics slow down; on an intermediate time scale subdiffusion ($\mu < 1$) is observed, while at long times diffusion is reestablished with a reduced (long-time) diffusion coefficient D_{∞}. Different theoretical models have been developed to describe particle dynamics in external potentials, including the random barrier model [43], the random trap model [38,44], the continuous time random walk [45], diffusion in rough and regular potentials [7,46–48], the Lorentz gas model [49], and diffusion in quenched-annealed binary mixtures [50]. Typically, theories focus on the asymptotic long-time limit, which is often difficult to reach in experiments. In contrast, less is known about the behaviour at intermediate times, where the transitions between the different regimes occur. Furthermore, theoretical calculations have mainly been exploited to extract information from experimental data, while only recently have theoretical predictions been compared systematically with experiments [18–20,51–58].

Here we thus focus on recent experimental results on the dynamics of colloidal particles in potential energy landscapes and their comparison to simulations and theoretical predictions. A prerequisite for systematic experiments is the controlled creation of external potential energy landscapes. This, for example, is possible due to the interaction of colloidal particles with light [59–66]. The effect of light on particles with a refractive index different (typically larger) from the one of the surrounding liquid is usually described by two forces: a scattering force or “radiation pressure”, which pushes the particles along the light beam, and a gradient force, which pulls particles toward regions of high light intensity. A classical application of this effect is optical tweezers which are used to trap and manipulate individual particles or ensembles of particles by a tightly focused laser beam or several laser beams, respectively [65–68]. Extended light fields rather than light beams can be used to create potential energy landscapes. Arbitrary light fields can be generated using a spatial light modulator [61,68] or an acousto-optic deflector [63,64,69], while crossed laser beams [60], diffusors [70] and other optical devices can be used to create particular high-quality light fields (Sect. 2).

Light fields can affect the arrangement and dynamics of colloidal particles within distinct phases but can also induce phase transitions. For example, upon increasing the amplitude of a periodic light field applied to a colloidal fluid, a disorder-order transition is induced in a two-dimensional charged colloidal system, known as light-induced freezing [41,71–73]. A further increase of the amplitude results in the melting of the crystal into a modulated liquid; this process is called light-induced melting. Extended light fields can also be applied to direct heterogeneous crystallization and hence the structure and unit cell dimensions of the formed bulk crystals or quasi-crystals [74–78]. Using light fields, the effect of periodic as well as random potentials on the particle dynamics has been experimentally investigated [52–54] and compared to simulations and theoretical predictions [7,38–40,46,54–56,79,80]. Most of the theoretical predictions only concern the asymptotic long-time behaviour. Possible links between the long-time behaviour and the intermediate dynamics, as observed in the experiments, are discussed [53,56,81]. Furthermore, the dynamics of individual particles in sinusoidal potentials show similarities with the dynamics in glasses [54,82]. Inspired by this idea, in this review the dynamics of individual particles in different external potentials are compared to the dynamics of concentrated hard spheres [29,83,84]. Energy landscapes are not only considered in the context of glasses, but random energy landscapes with a Gaussian distribution of energy levels of width $\varepsilon \approx \mathcal{O}(k_\mathrm{B}T)$, where $k_\mathrm{B}T$ is the thermal energy, seem to be relevant for proteins, RNA and transmembrane helices [85,86]. Moreover, the diffusion (or "permeation") of rodlike viruses through smectic layers can be described by the diffusion in a sinusoidal potential of amplitude $\varepsilon \approx k_\mathrm{B}T$ [87,88].

2 Colloids in light fields: Creation of potential energy landscapes

The optical force on a colloidal particle has been investigated extensively, in particular in the context of optical tweezers [62–67,89–95]. We consider a transparent colloidal particle with a refractive index n_c suspended in a medium with a smaller refractive index n_m, that is $n_\mathrm{c} > n_\mathrm{m}$, and begin with the case of a particle much larger than the wavelength of light. In this case, the simple picture of ray optics applies. If light is incident on a particle, it will be scattered and reflected. While light arrives from only one direction, the scattered and reflected light travels in different directions. Hence the direction of the light and accordingly the momenta of the photons are changed. Due to conservation of momentum, an equal but opposite momentum change will be imparted on the particle. The rate of momentum change determines the force on the particle, which acts in the direction of light propagation and might, e.g. due to the astigmatism of the objective, also have effects outside the main beam [96]. This is the so-called scattering force or, considering the photon "bombardment", the radiation pressure.

When hitting the particle, the light beam will also be refracted, that is the particle acts as a (microscopic) lens. This, again, changes the direction of the beam and hence the momentum of the photons. The resulting force pushes the particle toward higher light intensities, mainly into the centre of the beam. This is the gradient force, which acts in lateral direction and gradients typically also exist in axial direction, e.g. toward a focus. This decomposition of the optical force into two components, the scattering and gradient forces, is done traditionally although both originate from the same physics.

If the particle with radius R is much smaller than the wavelength of light, λ, that is in the so-called Rayleigh regime, the particle's polarizability is considered. The electric field of the light induces an oscillating dipole in the dielectric particle, which re-radiates light. This leads to the scattering force [91–94]

$$F_\mathrm{scatt} = \frac{\sigma n_\mathrm{m}}{c} I_0 \quad \text{with} \quad \sigma = \frac{128\pi^5 R^6}{3\lambda^4} \left(\frac{m^2-1}{m^2+2}\right)^2 , \tag{1}$$

where I_0 is the incident light intensity, σ the scattering cross section of a spherical particle, c the speed of light and $m = n_\mathrm{c}/n_\mathrm{m}$.

The incident light intensity is typically inhomogeneous, $I_0(\mathbf{r})$, which leads to a further (component of the) force acting on the particle. An induced dipole in an inhomogeneous electric field experiences a force in the direction of the field gradient, the gradient force [93,94]

$$F_\mathrm{grad} = \frac{2\pi\alpha}{c n_\mathrm{m}} \nabla I_0(\mathbf{r}) \quad \text{with} \quad \alpha = n_\mathrm{m}^2 R^3 \left(\frac{m^2-1}{m^2+2}\right) , \tag{2}$$

where α characterises the polarizability of a sphere. The gradient force pushes particles with $n_c > n_m$ towards regions of higher intensity.

In the experiments described in the following, the particles are of comparable size to the wavelength of light. However, this case is much more difficult to model [63,64,97,98] and will thus not be described here.

In optical tweezers, tightly focused laser light is used to trap particles. In contrast, exploiting the gradient force, here, extended spatially modulated light fields are applied to create potential energy landscapes [60]. The modulations in the potential are relatively weak such that typically particles are not trapped for long times, but only remain for some time in certain areas. Since the light field acts on the whole volume of the particle, its volume has to be convoluted with the light intensity to obtain the potential felt by the particle. Depending on the size of the particle and the modulation of the light field, the centre of the particle might thus be attracted to bright or dark regions [60]. Furthermore, it is difficult to impose potentials with features smaller than the particle size.

Extended space- and also time-dependent light fields can be created using various optical devices, e.g. holographic instruments based on a spatial light modulator (SLM) [61,67,68] or an acousto-optic deflector (AOD) [69]. Spatial light modulators use arrays of liquid-crystal pixels. Each pixel imposes a modulation of the phase, amplitude or polarization, which can be externally controlled. This allows the creation of almost any light field, within the limits of the finite size, pixelation and modulation resolution of the SLM. The latter result in a noise component in the light field. This can be exploited to create random potentials. It can also be avoided by cycling different realizations of the same light field but with different phases, with a refresh rate beyond the structural relaxation rate of the sample [52,53,99]. Furthermore, the dynamic possibilities of a holographic instrument can be improved by combining it with galvanometer-driven mirrors [68].

A conceptually simple but more specialized set-up is based on a crossed-beam geometry, which yields a standing wave pattern, i.e. a sinusoidally-varying periodic light field, within an overlying Gaussian envelope due to the finite size of the beams [60,72,73,100–102]. Moreover, optical devices, such as diffusors, can be used to generate special beam shapes like top-hat geometries or randomly-varying light fields [70].

While the gradient force is exploited to impose extended modulated potentials, whose amplitude is typically controlled by the laser power, the scattering force or radiation pressure will also affect the sample. The radiation pressure determines the distance of the particle from the cover slip, which will thus depend on the laser power. Due to hydrodynamic interactions, the distance to the cover slip affects the diffusion of the particle, which typically is reduced compared to free diffusion [103–105]. The experimental data presented in the following are corrected for this effect.

3 Dynamics of individual colloids in periodic and random potentials

Individual colloidal particles have been exposed to different potential energy landscapes (Fig. 1, top): sinusoidally-varying periodic potentials $U(y) = \varepsilon \sin(2\pi y/\lambda)$ with amplitude ε and wavelength λ (Fig. 1(A)), as well as one- and two-dimensional random potentials with a Gaussian distribution of potential values with (full) width 2ε (Fig. 1(B),(C)). For the one-dimensional random potential, figure 1B also shows the histogram of values of the potential, $p(U)$, which follows a Gaussian distribution $p(U) \propto \exp\{-(U - \langle U\rangle)^2/2\varepsilon^2\}$. In the experiments, the periodic potentials were generated using crossed laser beams [54,60] and the random potentials using a spatial light modulator [52,53,68] (Sect. 2).

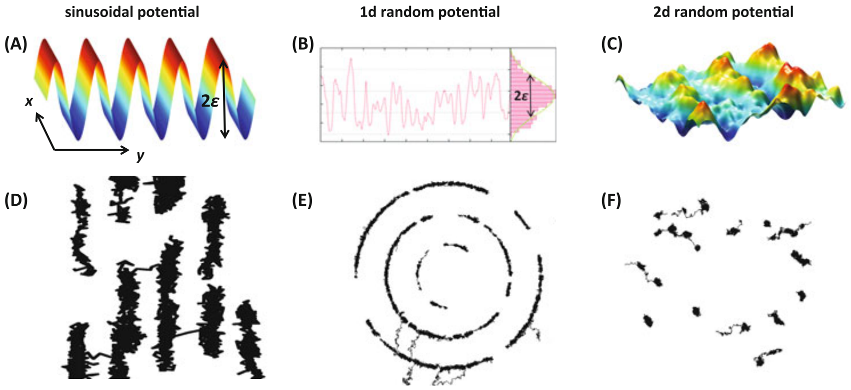

Fig. 1. (Top) schematic representations of the potential energy landscapes as felt by the particles and as reconstructed from experimental data (left to right): sinusoidally-varying periodic potential [54], one- and two-dimensional random potentials [52,53]. For the one-dimensional random potential, the histogram of values of the potential, $p(U)$, is shown and compared to a Gaussian distribution (green line). (Bottom) representative particle trajectories in these potentials. The one-dimensional random potential was arranged in large circles to obtain “periodic boundary conditions” and to improve the statistics by simultaneously investigating several circles.

The particle motions were monitored by video microscopy and the particle trajectories recovered by particle tracking algorithms [106,107]. In the absence of a light field, i.e. without an external potential, colloidal particles undergo free diffusion, thus exploring large areas. However, in the presence of external potentials, the particle dynamics are modified (Fig. 1, bottom). The trajectories and hence the excursions of the particles were limited with the particles remaining for extended periods at positions that correspond to local minima of the potential. In the periodic potential, anisotropic trajectories were observed (Fig. 1D). Particle motion along the valleys (x direction) was unaffected, while their motion across the maxima (y direction) was hindered by barriers of height 2ε.

In the one-dimensional random potentials, the particles remained for different periods of time at different positions, reflecting the randomly-varying potential values along the circular path (Fig. 1E). (The circular paths provided “periodic boundary conditions” and the simultaneous use of several circles helped to improve statistics.) Similarly,in the two-dimensional random potentials, the motion of the particles was limited due to the presence of local potential minima and saddle points (Fig. 1F). Upon increasing the amplitude of the roughness, ε, the particles were more efficiently trapped and hence explored an even smaller region.

Based on the particle trajectories, different parameters were computed to characterize the particle dynamics quantitatively in the presence of external potentials. The mean-squared displacement (MSD) is calculated according to

$$\langle \Delta x^2(t)\rangle = \left\langle [x_i(t_0+t) - x_i(t_0)]^2 \right\rangle_{t_0,i} - \langle\, [x_i(t_0+t) - x_i(t_0)]\,\rangle^2_{t_0,i}\,,$$

where the second term corrects for possible drifts. For both, experiments and simulations, the average is taken over particles i and waiting time t_0 to improve statistics. The average over t_0 affects the results [55,56], because initially the particles are randomly distributed while the distribution of occupied energy levels evolves toward a

Boltzmann distribution. To render the data independent of the specific experimental conditions, $\langle \Delta x^2(t) \rangle$ was normalized by the square of the particle radius R^2, and the time t by the Brownian time $t_\mathrm{B} = R^2/(2dD_0)$ with the short-time diffusion coefficient D_0 and the dimension d.

From the MSD, the normalized time-dependent diffusion coefficient $D(t)/D_0$ is calculated according to

$$\frac{D(t)}{D_0} = \frac{\partial \left(\left\langle \Delta x^2(t) \right\rangle / R^2 \right)}{\partial (t/t_\mathrm{B})} \quad , \tag{3}$$

while the slope of the MSD in double-logarithmic representation

$$\mu(t) = \frac{\partial \log \left(\left\langle \Delta x^2(t) \right\rangle / R^2 \right)}{\partial \log \left(t/t_\mathrm{B} \right)} \tag{4}$$

corresponds to the exponent in the relation $\left\langle \Delta x^2(t) \right\rangle \sim t^{\mu(t)}$ and quantifies deviations from diffusive behaviour: for free diffusion $\mu = 1$, while $\mu < 1$ for subdiffusion and $\mu > 1$ for superdiffusion. In addition, the non-Gaussian parameter [82]

$$\alpha_2(t) = \frac{\left\langle \Delta x^4(t) \right\rangle}{(1 + 2/d) \left\langle \Delta x^2(t) \right\rangle^2} - 1 \tag{5}$$

characterizes the deviation of the distribution of particle displacements from a Gaussian distribution and represents the first non-Gaussian correction [108]. In the two-dimensional case, the analogous equation based on $\langle \Delta r^2(t) \rangle$ and $\langle \Delta r^4(t) \rangle$ was calculated and has the corresponding meaning.

The effect of potential shape and amplitude on the particle dynamics was investigated in experiments [52–54], simulations [55,56] and theory [54,80], which all show consistent results (Fig. 2). Without an external potential ($\varepsilon = 0$), the MSD increases linearly with time and the diffusion coefficient $D(t)/D_0 \approx 1$, exponent $\mu(t) \approx 1$ and non-Gaussian parameter $\alpha_2(t) \approx 0$ are all independent of time, as expected for free diffusion. In contrast, in the presence of a periodic or random potential, the particle dynamics exhibit three distinct regimes which will be discussed in turn in the following. (Note that in the case of the sinusoidal potential, we only discuss the motion across the barriers, i.e. in y direction.)

At short times, the particle dynamics are diffusive and follow the potential-free case. This reflects small excursions within local minima and hence shows no significant dependence on the amplitude ε.

At intermediate times, the MSDs exhibit inflection points or plateaux, which become increasingly pronounced as ε increases. This corresponds to the decrease of the diffusion coefficients $D(t)/D_0$ from 1 to significantly lower values, the decrease of the exponent $\mu(t)$ and the increase of the non-Gaussian parameter $\alpha_2(t)$. The subdiffusive behaviour is caused by the particle being trapped in local minima for extended periods before it can escape to a neighbouring minimum.

In the case of the periodic potential, the barriers are all of equal height, 2ε, and thus the residence time distribution is relatively narrow. This is reflected in the reduced MSDs, the very pronounced and relatively quick decrease in $D(t)/D_0$ and $\mu(t)$ and increase in $\alpha_2(t)$. Thus, the minima in $\mu(t)$ and maxima in $\alpha_2(t)$ occur at relatively short times, $t_{\mu,\mathrm{min}}$ and $t_{\alpha,\mathrm{max}}$, respectively (Fig. 3, blue solid symbols). The minima in $\mu(t)$ occur earlier than the maxima in $\alpha_2(t)$. This is due to the fact that the minimum in $\mu(t)$ reflects the largest deviation from diffusive behaviour, i.e. when the probability to be (still) stuck in a minimum is largest and thus diffusion is most efficiently suppressed, whereas the maximum in $\alpha_2(t)$ indicates the largest deviation from the Gaussian distribution of displacements, i.e. the dynamics are maximally

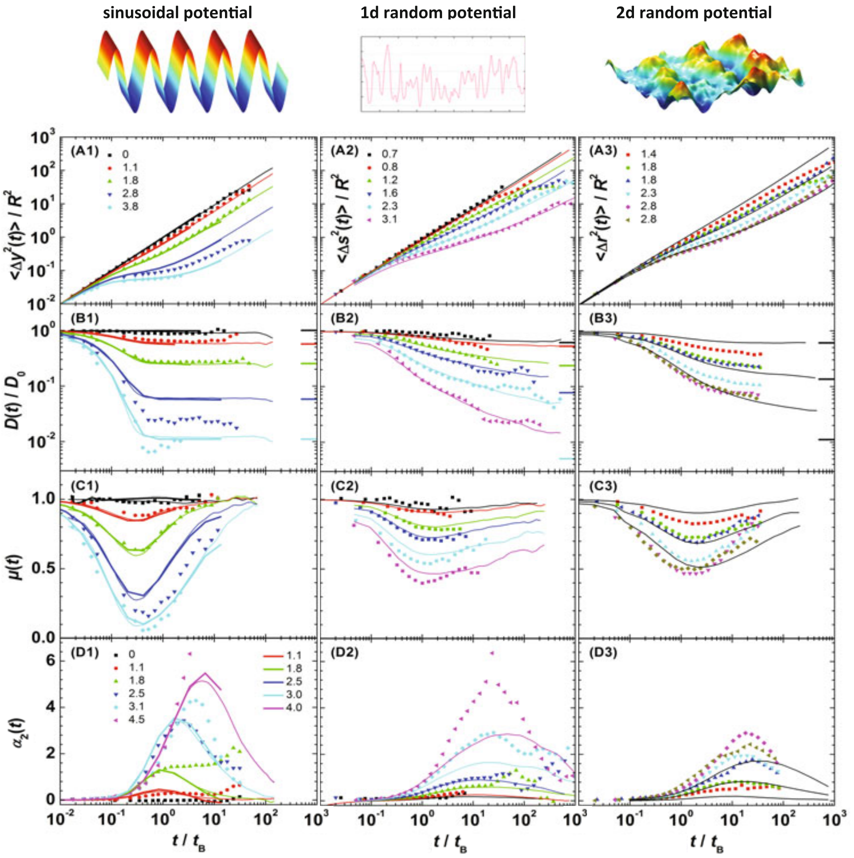

Fig. 2. Particle dynamics in (left to right) sinusoidally-varying periodic [54], one-dimensional random [52] and two-dimensional random potentials [53] as characterized by (top to bottom) the normalized mean-squared displacements, the normalized time-dependent diffusion coefficient $D(t)/D_0$, the exponent $\mu(t)$ in the relation $\langle \Delta x^2(t) \rangle \propto t^{\mu(t)}$, and the non-Gaussian parameter $\alpha_2(t)$ for different potential amplitudes and degrees of roughness ε (as indicated in the legends, in units of $k_\mathrm{B}T$). Experimental data are represented by symbols, simulations by solid lines, theoretical predictions (for the periodic potential) by thick lines. Theoretical predictions for D_∞/D_0 are indicated by horizontal lines.

heterogeneous with some minima having been left a long time ago, some only recently, with others yet to be left. The maximum in $\alpha_2(t)$ thus only appears once jumps have occurred, which happens after the minimum in $\mu(t)$, and hence $t_{\mu,\min} < t_{\alpha,\max}$. This also implies a weak ε dependence of $t_{\mu,\min}$ and a significant ε dependence of $t_{\alpha,\max}$ since ε determines the height of the barrier which has to be crossed. Similarly, the intermediate regime ends once the particle escapes the minima and performs a random walk between different minima with the diffusion coefficient $D(t)/D_0$, $\mu(t)$ and $\alpha_2(t)$ tending toward the plateaux values, 1 and 0, respectively. Again, since all barrier heights are identical, this occurs within a short period of time. Nevertheless, the time required to reach the end of the intermediate regime and hence the long-time diffusive

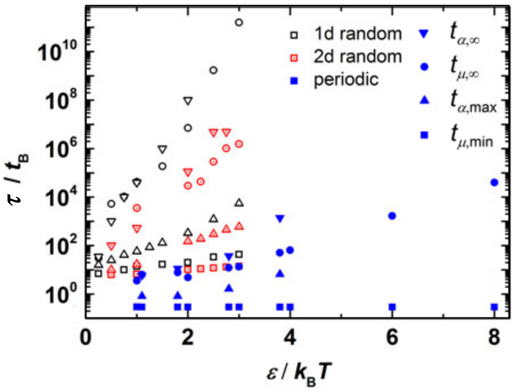

Fig. 3. Characteristic time scales τ in sinusoidally-varying periodic, one-dimensional and two-dimensional random potentials (as indicated and explained in the text). Data for the periodic potential are extracted from theoretical results. For the random potentials, data are retrieved from simulation data not averaged over waiting times t_0 [55,56].

limit, quantified either by $\mu \to 1$, i.e. $t_{\mu,\infty}$, or by $\alpha_2 \to 0$, i.e. $t_{\alpha,\infty}$, strongly depends on ε.

In the other case, i.e. in the presence of a random potential, there exists a wide range of barrier heights and thus residence times. This is reflected in the less pronounced plateaux or rather inflection points in the MSDs, a very slow decrease of $D(t)/D_0$ with very slow approaches to the long-time plateaux as well as a slow decrease and increase of $\mu(t)$ and $\alpha_2(t)$, respectively, and in particular an extremely slow return of $\mu(t)$ and $\alpha_2(t)$ to 1 and 0, respectively. Therefore, the intermediate subdiffusive regime, as indicated by the range from $t_{\mu,\min}$ and $t_{\alpha,\max}$ to $t_{\mu,\infty}$ and $t_{\alpha,\infty}$, occurs relatively late and in particular extends over a broad range of times with a strong ε dependence (Fig. 3), where the particular ε dependence of $t_{\mu,\infty}$ and $t_{\alpha,\infty}$ is discussed in [53,81]. For the one-dimensional random potential, subdiffusion is more pronounced than for the two-dimensional random potential, since in two dimensions maxima can be avoided and only saddle points need to be crossed. For the same reason, in one dimension, the ε dependence appears stronger and the intermediate regime extends to longer times. Thus, in the one-dimensional random potential the intermediate subdiffusive regime covers a longer time period than in the two-dimensional case, which in turn is longer and shows a stronger ε dependence than in the periodic potential. Moreover, increasing amplitude ε has similar effects for all potential shapes: First, the subdiffusive behaviour becomes more pronounced. Second, the intermediate regime extends to longer times, indicated by the slow returns of $\mu(t)$ and $\alpha_2(t)$ to 1 and 0, respectively. However, the beginning of the intermediate regime, characterized by the maxima in $\mu(t)$ and minima in $\alpha_2(t)$ and the corresponding times $t_{\mu,\min}$ and $t_{\alpha,\max}$, remains at about the same time with a weak ε dependence since no or only a few barrier crossings are involved.[1] Extrapolations of the characteristic times τ to vanishing potential amplitudes results in different values $\tau(\varepsilon \to 0)$ for the different potential shapes. Although unexpected, this might be related to the definitions of the amplitude ε for the periodic and random potentials, respectively, and to the fact that without an external potential, i.e. $\varepsilon = 0$, $\mu(t) = 1$ and $\alpha_2(t) = 0$

---

[1] Note that the amplitude ϵ characterises the amplitude of the oscillations in the case of the periodic potential, while it represents the amplitude of the roughness, namely the width of the Gaussian distribution of values of the potential, in the case of the random potentials.

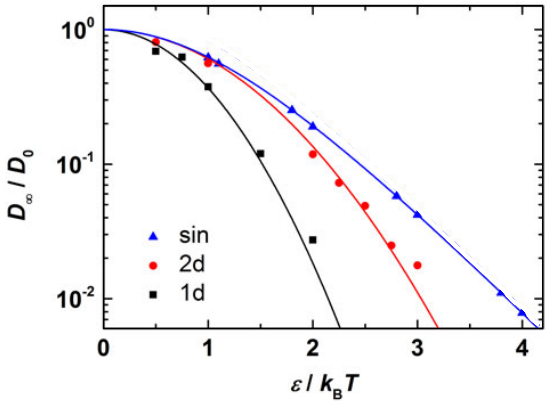

Fig. 4. Normalized long-time diffusion coefficient $D_\infty(\varepsilon)/D_0$ in one- and two-dimensional random potentials and sinusoidally-varying periodic potentials (left to right). Solid lines indicate theoretical predictions [7,46,80], symbols simulation results that have not been averaged over waiting times t_0 [54–56].

and thus no minimum in $\mu(t)$ and no maximum in $\alpha_2(t)$ exist and hence $\tau(\varepsilon = 0)$ is not defined.

At very long times, again diffusive behaviour is observed with constant, but much smaller D_∞/D_0 and $\mu(t)$ returning to 1 and $\alpha_2(t)$ to 0. On long time scales, hopping between minima becomes possible and, once more, the dominant process is a random walk, now between minima. The return to diffusion is fast in the case of the periodic potential, since very deep minima are absent, but slow in the two- and especially the one-dimensional random potential. With increasing amplitude ε, one notices increasingly long times to reach the asymptotic long-time limit (Fig. 3) and a decrease of the long-time diffusion coefficient $D_\infty(\varepsilon)$ (Fig. 4), which has been calculated for different potential shapes. For a periodic sinusoidal potential [54,80]

$$\frac{D_\infty(\varepsilon)}{D_0} = J_0^{-2}\left(\frac{\varepsilon}{k_\mathrm{B}T}\right) \approx 2\pi\left(\frac{\varepsilon}{k_\mathrm{B}T}\right) \mathrm{e}^{\left(\frac{-2\varepsilon}{k_\mathrm{B}T}\right)} , \tag{6}$$

where J_0 is the Bessel function of the first kind of order 0 and the approximation holds for $\varepsilon \gg k_\mathrm{B}T/2$ [54]. In the case of one- and two-dimensional random potentials one finds [7,46,109–111]

$$\frac{D_\infty(\varepsilon)}{D_0} = \mathrm{e}^{-\frac{1}{d}\left(\frac{\varepsilon}{k_\mathrm{B}T}\right)^2} . \tag{7}$$

In the case of a two-dimensional random potential, $D_\infty(\varepsilon)$ is larger because maxima can be avoided and only saddle points have to be crossed. Nevertheless, the exponential dependence on $-(\varepsilon/k_\mathrm{B}T)^2$ remains, which is the ratio of the equilibrium energy of a Gaussian distribution, $-\varepsilon^2/k_\mathrm{B}T$, and the thermal energy $k_\mathrm{B}T$. The first term describes the equilibrium energy and dominates the dependence of the activation barriers on temperature, because the typical barrier energies to be overcome when moving between different regions are essentially independent of the thermal energy, as suggested by the percolation picture [112]. The theoretical predictions and simulation as well as experimental data agree except at large ε where deviations are noticeable. Figure 4 shows the theoretical predictions and simulation results, the latter agreeing

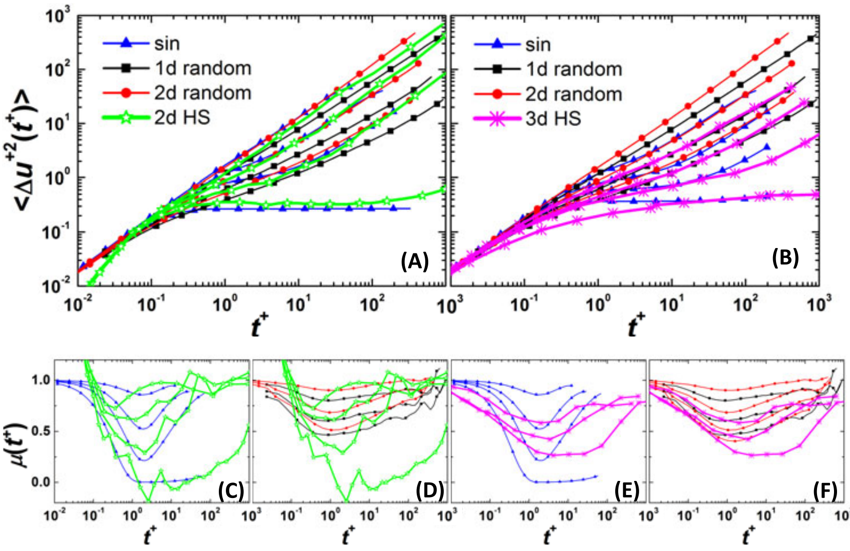

Fig. 5. Effect of particle-particle and particle-potential interactions on the particle dynamics. The dynamics of individual particles in sinusoidally-varying periodic and one- and two-dimensional random potentials (thin lines with symbols as indicated) [52–54] are compared to (A,C,D) (quasi) two-dimensional concentrated hard discs [83] and (B,E,F) three-dimensional concentrated hard spheres [29], the latter two in the absence of an external potential (thick lines as indicated). (A,B) Dimensionless mean squared displacements and (C–F) exponent $\mu(t)$ as function of dimensionless time. To allow for a comparison, both the mean squared displacement and the time have been normalized by typical length scales of the corresponding systems, indicated by the parameters $\langle \Delta u^{+\,2}(t^+)\rangle$ and t^+. Shown are the theoretical predictions for individual particles in periodic potentials with amplitude (A,C) $\varepsilon/k_\mathrm{B}T = 1, 2, 3, 8$ and (B,E) $2, 3, 4, 6$ [54], simulation results for individual particles in one-dimensional random potentials with amplitude $\varepsilon/k_\mathrm{B}T = 1.2, 2.3, 3.1$ [56] and in two-dimensional random potentials with amplitude $\varepsilon/k_\mathrm{B}T = 1.0, 2.0, 3.0$ [53,55], simulation results for concentrated hard discs with surface fractions $\sigma = 0.68, 0.69, 0.70, 0.715$ in the absence of an external potential [83], experimental data for concentrated hard spheres with volume fractions $\Phi = 0.466, 0.519, 0.558, 0.583$ in the absence of an external potential [29] (all top to bottom).

with the experimental data (Fig. 2). The slightly higher data are due to the fact that even for the longest investigated times the asymptotic long-time limit is not quite reached for the largest ε (Fig. 2).

The particle dynamics in periodic and random potentials as discussed above, resemble the dynamics of concentrated systems, whose subdiffusive behaviour has been associated with caging by neighbouring particles [113–115]. Thus particle-potential and particle-particle interactions seem to have similar effects on the particle dynamics. Their effects lead to characteristic signatures especially in the intermediate regime, which was described above. We hence can compare the dynamics of individual particles in external potentials and concentrated interacting particles without external potential (Fig. 5), namely experimental data from a three-dimensional bulk system containing hard spheres of different volume fractions [29] and experimental as well as simulation data from (quasi) two-dimensional systems of hard discs with different surface fractions [83,84]. The dynamics of the concentrated two-dimensional system

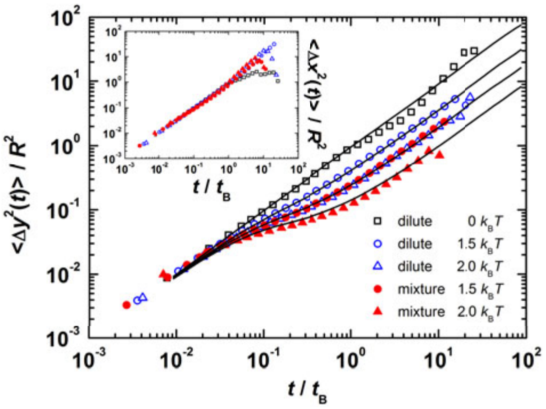

Fig. 6. Particle dynamics, namely MSD across the barriers, i.e. in y direction (main figure), and along the valleys, i.e. in x direction (inset), of an individual dilute large particle ($R_1 = 2.5$ μm, open symbols) and concentrated large particles in a binary mixture ($R_1 = 2.5$ μm, $R_2 = 1$ μm, total surface fraction $\sigma \approx 0.57$ with an about equal number of large and small spheres, filled symbols), both in sinusoidally-varying periodic potentials with wavelength $\lambda = 5.2$ μm and different amplitudes (as indicated). Lines represent Brownian Dynamics simulations of individual particles in a periodic potential with $\varepsilon/k_\mathrm{B}T = 0.0, 1.5, 2.0, 2.5$.

and the individual particles in the periodic potential are strikingly similar (Fig. 5A, C), while the dynamics in the random potentials appear different (Fig. 5A, D). In contrast, the dynamics of the concentrated three-dimensional system seem different from the individual particles in the periodic potential, for example the intermediate MSD is broader (Fig. 5B, E), while it resembles the dynamics in the random potentials (Fig. 5B, F).

4 Dynamics of interacting colloids in periodic and random potentials

So far the dynamics of individual colloidal particles in periodic and random potentials were considered. It shows striking similarities with the dynamics of concentrated suspensions without external potentials [29,83,84]. The combined effect of particle-potential and particle-particle interactions is hence briefly discussed. An increase of the particle concentration in a one-dimensional channel leads to single file diffusion with $\langle \Delta x^2(t) \rangle \sim t^{0.5}$ [116], which becomes more complex if a periodic potential is present along the channel [42]. Also in two-dimensional potentials an interplay between the particle-potential and particle-particle interactions was observed [41], which, under the investigated conditions, may be linked to changes in the particle arrangement, caused by laser-induced freezing and melting [71–73]. More complex potential-induced disorder-order and disorder-disorder transitions have been theoretically investigated in mixtures, namely colloid-polymer mixtures and binary hard discs [117–119]. The dynamics of binary colloidal mixtures with large size disparity have been investigated without the presence of an external potential [120,121]. Here, we focus on the dynamics of concentrated binary hard sphere mixtures in a periodic potential, with the mixture in the modulated liquid state. The MSDs of individual particles (similar to those in Sect. 3) and of interacting particles in the presence of smaller particles in a periodic potential are determined (Fig. 6). No signature of single-file diffusion could be observed in the MSDs along the valleys, i.e. in x direction (Fig. 6, inset). Across the barriers, i.e. in y direction, the MSDs of the interacting large particles in the binary mixture (in a periodic potential with amplitude ε) resemble the MSDs of individual large particles (in a periodic potential with a larger amplitude ε'). For the present conditions, in particular surface fraction $\sigma \approx 0.57$, we found $\varepsilon' \approx \varepsilon + 0.5\, k_{\mathrm{B}}T$. Moreover, the MSDs of the individual and interacting particles in a periodic potential agree with Brownian Dynamics simulations of an individual particle in a periodic potential (Fig. 6, lines). Similar observations have been made for interacting single-component systems in periodic and random potentials [79,122].

5 Conclusion

Optical devices, such as spatial light modulators and acousto-optic deflectors, can be exploited to create a large variety of modulated light fields. Due to the polarizability of colloidal particles, this translates into potential energy landscapes of almost any shape. The large flexibility, together with the possibility to observe and track colloidal particles by video microscopy, provides an ideal experimental tool to systematically and quantitatively investigate fundamental questions in statistical physics. Here we focused on individual Brownian particles, but also briefly mentioned interacting particles, in periodic and random potentials. The experimental findings were compared to simulation results and theoretical predictions. While the latter mainly concerns the long-time asymptotic limit, the experiments and simulations also provide detailed quantitative information on the intermediate dynamics, which exhibit subdiffusive behaviour. This was compared to the distinct intermediate dynamics of concentrated colloidal suspensions, thus relating particle-potential and particle-particle interactions. The interplay between these interactions was also illustrated using concentrated binary mixtures in external potentials. The dynamics of concentrated interacting particles in potential energy landscapes deserve further work, which will also be extended to time-dependent potentials.

We gratefully acknowledge support by the Deutsche Forschungsgemeinschaft (DFG) through the SFB-Transregio TR6 “The Physics of Colloidal Dispersions in External Fields” (project C7), the Research Unit FOR 1394 “Nonlinear Response to Probe Vitrification” and the International Helmholtz Research School “BioSoft”. C. D.-F. thanks the Humboldt foundation for the award of a fellowship. We thank H.E. Hermes, J. Horbach, M. Laurati, H. Löwen, K.J. Mutch, P. Nielaba, K. Sandomirski, M. Schmiedeberg, D. Wagner, and A. Yethiraj for very helpful discussions.

References

1. J.-P. Bouchaud, A. Georges, Phys. Rep. **195**, 127 (1990)
2. M. Sahimi, Rev. Mod. Phys. **65**, 1393 (1993)
3. J. Sancho, A. Lacasta, Eur. Phys. J. Special Topics **187**, 49 (2010)
4. J. Haus, K. Kehr, Phys. Rep. **150**, 263 (1987)
5. S. Havlin, D. Ben-Avraham, Adv. Phys. **36**, 695 (1987)
6. P.G. Wolynes, Acc. Chem. Res. **25**, 513 (1992)
7. D.S. Dean, I.T. Drummond, R.R. Horgan, J. Stat. Mech., P07013 (2007)
8. J.M. Sancho, A.M. Lacasta, K. Lindenberg, I.M. Sokolov, A.H. Romero, Phys. Rev. Lett. **92**, 250601 (2004)
9. R.M. Dickson, D.J. Norris, Y.-L. Tzeng, W.E. Moerner, Science **274**, 966 (1996)
10. G. Seisenberger, M.U. Ried, T. Endress, H. Büning, M. Hallek, C. Bräuchle, Science **294**, 1929 (2001)

11. M. Weiss, M. Elsner, F. Kartberg, T. Nilsson, Biophys. J. **87**, 3518 (2004)
12. I.M. Tolić-Nørrelykke, E.-L. Munteanu, G. Thon, L. Oddershede, K. Berg-Sørensen, Phys. Rev. Lett. **93**, 078102 (2004)
13. D.S. Banks, C. Fradin, Biophys. J. **89**, 2960 (2005)
14. F. Höfling, T. Franosch, Rep. Prog. Phys. **76**, 046602 (2013)
15. E. Barkai, Y. Garini, R. Metzler, Phys. Today **65**, 29 (2012)
16. A. Byström, A.M. Byström, Acta Crystallogr. **3**, 146 (1950)
17. A. Heuer, S. Murugavel, B. Roling, Phys. Rev. B **72**, 174304 (2005)
18. P. Tierno, P. Reimann, T.H. Johansen, F. Sagués, Phys. Rev. Lett. **105**, 230602 (2010)
19. P. Tierno, F. Sagués, T.H. Johansen, T.M. Fischer, Phys. Chem. Chem. Phys. **11**, 9615 (2009)
20. P. Tierno, F. Sagués, T.H. Johansen, I.M. Sokolov, Phys. Rev. Lett. **109**, 070601 (2012)
21. F.-R. Carminati, M. Schiavoni, L. Sanchez-Palencia, F. Renzoni, G. Grynberg, Eur. Phys. J. D **17**, 249 (2001)
22. M. Šiler, P. Zemánek, New J. Phys. **12**, 083001 (2010)
23. K.M. Douglass, S. Sukhov, A. Dogariu, Nat. Phot. **6**, 833 (2012)
24. K. Harada, O. Kamimura, H. Kasai, T. Matsuda, A. Tonomura, V.V. Moshchalkov, Science **274**, 1167 (1996)
25. A. Heuer, J. Phys.: Condens. Matter **20**, 373101 (2008)
26. P.G. Debenedetti, F.H. Stillinger, Nature **410**, 259 (2001)
27. C.A. Angell, Science **267**, 1924 (1995)
28. W.C.K. Poon, J. Phys.: Condens. Matter **14**, R859 (2002)
29. W. van Megen, T.C. Mortensen, S.R. Williams, J. Müller, Phys. Rev. E **58**, 6073 (1998)
30. A. Heuer, B. Doliwa, A. Saksaengwijit, Phys. Rev. E **72**, 021503 (2005)
31. R.B. Best, G. Hummer, Phys. Chem. Chem. Phys. **13**, 16902 (2011)
32. C.M. Dobson, A. Sali, M. Karplus, Angew. Chem. Int. Ed. **37**, 868 (1998)
33. J.D. Bryngelson, J.N. Onuchic, N.D. Socci, P.G. Wolynes, Proteins **21**, 167 (1995)
34. M.D. Haw, J. Phys.: Condens. Matter **14**, 7769 (2002)
35. E. Frey, K. Kroy, Ann. Phys. **14**, 20 (2005)
36. J. Klafter, I.M. Sokolov, Phys. World **18**, 29 (2005)
37. I.M. Sokolov, Soft Matter **8**, 9043 (2012)
38. M. Schmiedeberg, J. Roth, H. Stark, Eur. Phys. J. E **24**, 367 (2007)
39. C. Emary, R. Gernert, S.H.L. Klapp, Phys. Rev. E **86**, 061135 (2012)
40. K. Lichtner, A. Pototsky, S.H.L. Klapp, Phys. Rev. E **86**, 051405 (2012)
41. S. Herrera-Velarde, R. Castañeda-Priego, Phys. Rev. E **79**, 041407 (2009)
42. E.C. Euán-Díaz, V.R. Misko, F.M. Peeters, S. Herrera-Velarde, R. Castañeda-Priego, Phys. Rev. E **86**, 031123 (2012)
43. J. Bernasconi, H.U. Beyeler, S. Strässler, S. Alexander, Phys. Rev. Lett. **42**, 819 (1979)
44. J.W. Haus, K.W. Kehr, J.W. Lyklema, Phys. Rev. B **25**, 2905 (1982)
45. H. Scher, M. Lax, Phys. Rev. B **7**, 4491 (1973)
46. R. Zwanzig, Proc. Natl. Acad. Sci. **85**, 2029 (1988)
47. W. Dieterich, I. Peschel, W. Schneider, Z. Phys. B Condens. Matter **27**, 177 (1977)
48. P. Reimann, C. Van den Broeck, H. Linke, P. Hänggi, J.M. Rubi, A. Pérez-Madrid, Phys. Rev. E **65**, 031104 (2002)
49. F. Höfling, T. Franosch, E. Frey, Phys. Rev. Lett. **96**, 165901 (2006)
50. V. Krakoviack, Phys. Rev. Lett. **94**, 065703 (2005)
51. F. Sciortino, J. Stat. Mech., P05015 (2005)
52. R.D.L. Hanes, C. Dalle-Ferrier, M. Schmiedeberg, M.C. Jenkins, S.U. Egelhaaf, Soft Matter **8**, 2714 (2012)
53. F. Evers, C. Zunke, R.D.L. Hanes, J. Bewerunge, I. Ladadwa, A. Heuer, S.U. Egelhaaf, Phys. Rev. E **88**, 022125 (2013)
54. C. Dalle-Ferrier, M. Krüger, R.D.L. Hanes, S. Walta, M.C. Jenkins, S.U. Egelhaaf, Soft Matter **7**, 2064 (2011)
55. I. Ladadwa, F. Evers, A. Heuer, S.U. Egelhaaf (in preparation) (2013)
56. R.D.L. Hanes, S.U. Egelhaaf, J. Phys.: Condens. Matter **24**, 464116 (2012)

57. T.O.E. Skinner, S.K. Schnyder, D.G.A.L. Aarts, J. Horbach, R.P.A. Dullens, Phys. Rev. Lett. **111**, 128301 (2013)
58. X. Ma, P. Lai, P. Tong, Soft Matter **9**, 8826 (2013)
59. A. Ashkin, Science **210**, 1081 (1980)
60. M.C. Jenkins, S.U. Egelhaaf, J. Phys.: Condens. Matter **20**, 404220 (2008)
61. K. Dholakia, T. Cizmar, Nat. Phot. **5**, 335 (2011)
62. K. Dholakia, P. Reece, M. Gu, Chem. Soc. Rev. **37**, 42 (2008)
63. R.W. Bowman, M.J. Padgett, Rep. Prog. Phys. **76**, 026401 (2013)
64. K.C. Neumann, S.M. Block, Rev. Sci. Instrum. **75**, 2787 (2004)
65. J.E. Molloy, M.J. Padgett, Contemp. Phys. **43**, 241 (2002)
66. A. Ashkin, Proc. Natl. Acad. Sci. **94**, 4853 (1997)
67. D.G. Grier, Nature **424**, 810 (2003)
68. R.D.L. Hanes, M.C. Jenkins, S.U. Egelhaaf, Rev. Sci. Instrum. **80**, 083703 (2009)
69. M.P.N. Juniper, R. Besseling, D.G.A.L. Aarts, R.P.A. Dullens, Opt. Express **20**, 28707 (2012)
70. J. Bewerunge, A. Sengupta, S.U. Egelhaaf (in preparation)
71. Q.-H. Wei, C. Bechinger, D. Rudhardt, P. Leiderer, Phys. Rev. Lett. **81**, 2606 (1998)
72. K. Loudiyi, B.J. Ackerson, Physica A **184**, 1 (1992)
73. C. Bechinger, Q.H. Wei, P. Leiderer, J. Phys.: Condens. Matter **12**, A425 (2000)
74. A. van Blaaderen, J.P. Hoogenboom, D.L.J. Vossen, A. Yethiraj, A. van der Horst, K. Visscher, M. Dogterom, Faraday Discuss **123**, 107 (2003)
75. M. Brunner, C. Bechinger, Phys. Rev. Lett. **88**, 248302 (2002)
76. B.V.R. Tata, R.G. Joshi, D.K. Gupta, J. Brijitta, B. Raj, Curr. Sci. **103**, 1175 (2012)
77. E. Jaquay, L.J. Martínez, C.A. Mejia, M.L. Povinelli, Nano Lett. **13**, 2290 (2013)
78. J. Mikhael, J. Roth, L. Helden, C. Bechinger, Nature **454**, 501 (2008)
79. R. Castañeda-Priego, S. Herrera-Velarde, C. Dalle-Ferrier, S.U. Egelhaaf (in preparation)
80. R. Festa, E. d'Agliano, Phys. A: Stat. Mech. Appl. **90**, 229 (1978)
81. R.D.L. Hanes, M. Schmiedeberg, S.U. Egelhaaf, [`arXiv 1309.4801`] (2013)
82. B. Vorselaars, A.V. Lyulin, K. Karatasos, M.A.J. Michels, Phys. Rev. E **75**, 011504 (2007)
83. R. Zangi, S.A. Rice, Phys. Rev. Lett. **92**, 035502 (2004)
84. B. Cui, B. Lin, S.A. Rice, J. Chem. Phys. **114**, 9142 (2001)
85. C. Hyeon, D. Thirumalai, Proc. Nat. Acad. Sci. **100**, 10249 (2003)
86. H. Janovjak, H. Knaus, D.J. Muller, J. Am. Chem. Soc. **129**, 246 (2007)
87. M.P. Lettinga, E. Grelet, Phys. Rev. Lett. **99**, 197802 (2007)
88. E. Grelet, M.P. Lettinga, M. Bier, R. van Roij, P. van der Schoot, J. Phys.: Condens. Matter **20**, 494213 (2008)
89. K. Dholakia, W. Lee, Adv. Atom. Mol. Opt. Phys. **56**, 261 (2008)
90. A. Ashkin, Biophys. J. **61**, 569 (1992)
91. A. Ashkin, J.M. Dziedzic, J.E. Bjorkholm, S. Chu, Opt. Lett. **11**, 288 (1986)
92. M. Kerker, *The Scattering of Light and other Electromagnetic Radiation* (Academic Press, 1969)
93. Y. Harada, T. Asakura, Opt. Comm. **124**, 529 (1996)
94. K. Svoboda, S.M. Block, Ann. Rev. Biophys. Biomol. Struct. **23**, 247 (1994)
95. S.M. Barnett, R. London, J. Phys. B.: At. Mol. Opt. Phys. **39**, S671 (2006)
96. C. Zunke, R.D.L. Hanes, F. Evers, S.U. Egelhaaf (in preparation)
97. T. Tlusty, A. Meller, R. Bar-Ziv, Phys. Rev. Lett. **81**, 1738 (1998)
98. D. Bonessi, K. Bonin, T. Walker, J. Opt. A: Pure Appl. Opt. **9**, S228 (2007)
99. R.D.L. Hanes, C. Zunke, F. Evers, S.U. Egelhaaf (in preparation)
100. A. Chowdhury, B.J. Ackerson, N.A. Clark, Phys. Rev. Lett. **55**, 833 (1985)
101. W. Köhler, R. Schäfer, Adv. Polym. Sci. **151**, 1 (2000)
102. S. Wiegand, J. Phys.: Condens. Matter **16**, R357 (2004)
103. E.S. Pagac, R.D. Tilton, D.C. Prieve, Chem. Eng. Comm. **148–150**, 105 (1996)
104. J. Leach, H. Mushfique, S. Keen, R. Di Leonardo, G. Ruocco, J.M. Cooper, M.J. Padgett, Phys. Rev. E **79**, 026301 (2009)

105. P. Sharma, S. Ghosh, S. Bhattacharya, Appl. Phys. Lett. **97**, 104101 (2010)
106. J.C. Crocker, D.G. Grier, J. Coll. Interf. Sci. **179**, 298 (1996)
107. M.C. Jenkins, S.U. Egelhaaf, Adv. Coll. Interf. Sci. **136**, 65 (2008)
108. W. van Megen, T.C. Mortensen, S.R. Williams, J. Müller, Phys. Rev. E **58**, 6073 (1998)
109. D.S. Dean, I.T. Drummond, R.R. Horgan, J. Phys. A: Math. Gen. **30**, 385 (1997)
110. D.S. Dean, I.T. Drummond, R.R. Horgan, J. Phys. A: Math. Gen. **37**, 2039 (2004)
111. C. Touya, D.S. Dean, J. Phys. A: Math. Theor. **40**, 919 (2007)
112. J.C. Dyre, Phys. Rev. B **51**, 12276 (1995)
113. P.N. Pusey, W. van Megen, Nature **320**, 340 (1986)
114. K.S. Schweizer, Curr. Opin. Coll. Interf. Sci. **12**, 297 (2007)
115. K.S. Schweizer, E.J. Saltzman, J. Chem. Phys. **119**, 1181 (2003)
116. C. Lutz, M. Kollmann, C. Bechinger, Phys. Rev. Lett. **93**, 026001 (2004)
117. I.O. Götze, J.M. Brader, M. Schmidt, H. Löwen, Mol. Phys. **101**, 1651 (2003)
118. K. Franzrahe, P. Nielaba, Phys. Rev. E **76**, 061503 (2007)
119. K. Franzrahe, P. Nielaba, Phys. Rev. E **79**, 051505 (2009)
120. A. Imhof, J.K.G. Dhont, Phys. Rev. E **52**, 6344 (1995)
121. T. Voigtmann, J. Horbach, Phys. Rev. Lett. **103**, 205901 (2009)
122. J. Bewerunge, C. Zunke, S. Glöckner, F. Evers, S.U. Egelhaaf (in preparation)

This page has been left intentionally blank.

A FURTHER PUBLICATIONS

This page has been left intentionally blank.

A.1 Colloids exposed to random potential energy landscapes: From particle number density to particle-potential and particle-particle interactions

Journal: The Journal of Chemical Physics

Reference: *J. Chem. Phys.* **145**, 044905 (2016)

Impact factor: 2.965

Authors: Jörg Bewerunge, Ankush Sengupta, **Ronja F. Capellmann**, Florian Platten, Surajit Sengupta, and Stefan U. Egelhaaf

3rd author

Chosen as Editors' Choice 2016

J. B. performed the measurements and analysed the data. A. S. and S. S. performed theoretical calculations. J. B. and S. U. E. conceived, designed and discussed the experiments. All authors including R. F. C. discussed the results, contributed to their interpretation and the writing of the manuscript.

5% contribution of R. F. C.

Reproduced from [Bewerunge, J.; Sengupta, A.; Capellmann, R. F.; Platten, F.; Sengupta, S.; Egelhaaf, S. U.; *J. Chem. Phys.* **145**, 044905 (2016)], with the permission of AIP Publishing.

This page has been left intentionally blank.

THE JOURNAL OF CHEMICAL PHYSICS **145**, 044905 (2016)

Colloids exposed to random potential energy landscapes: From particle number density to particle-potential and particle-particle interactions

Jörg Bewerunge,[1] Ankush Sengupta,[2] Ronja F. Capellmann,[1] Florian Platten,[1]
Surajit Sengupta,[3] and Stefan U. Egelhaaf[1]
[1]*Condensed Matter Physics Laboratory, Heinrich Heine University, 40225 Düsseldorf, Germany*
[2]*Department of Chemical Physics, Weizmann Institute of Science, 234 Herzl St., Rehovot 7610001, Israel*
[3]*TIFR Centre for Interdisciplinary Sciences, Hyderabad 500075, India*

(Received 10 May 2016; accepted 1 July 2016; published online 28 July 2016)

Colloidal particles were exposed to a random potential energy landscape that has been created optically via a speckle pattern. The mean particle density as well as the potential roughness, i.e., the disorder strength, were varied. The local probability density of the particles as well as its main characteristics were determined. For the first time, the disorder-averaged pair density correlation function $g^{(1)}(r)$ and an analogue of the Edwards-Anderson order parameter $g^{(2)}(r)$, which quantifies the correlation of the mean local density among disorder realisations, were measured experimentally and shown to be consistent with replica liquid state theory results. *Published by AIP Publishing.* [http://dx.doi.org/10.1063/1.4959129]

I. INTRODUCTION

The potential energy landscape (PEL) of a system depends on the coordinates and/or other parameters of its constituents.[1] The concept of a PEL is successfully used in many fields of science to determine the properties and behavior of systems ranging from small, large and polymeric molecules, proteins and other biomolecules to clusters, glasses, and biological cells.[1] It is also applied to describe the transport over atomic surfaces,[2–4] in materials with defects (e.g., ions in zeolites[5] or charge carriers in conductors with impurities[6]), in inhomogeneous media[7,8] (e.g., porous gels,[9] cell membranes[10] or cells[11–14]), or in the presence of fixed obstacles as in a Lorentz gas.[15] They are also used to determine the rates of (bio)chemical reactions,[1,16] the folding of proteins and DNA,[17–23] as well as the particle dynamics in dense suspensions close to freezing,[24] in glasses[4,25–35] or, more general, in crowded systems.[12]

We focus on random potential energy landscapes (rPEL), which have been used in the interpretation of several experimental observations. For example, rPEL with a Gaussian distribution of energy values with a width of about the thermal energy have been used to describe the behavior of RNA, proteins, and transmembrane helices.[19,36,37] Although a rPEL might only represent a crude approximation for many experimental situations, it often provides a very useful initial description of the effect of disorder on the dynamics.[5,35,38]

The PEL is experimentally realised by exploiting the interaction of light with colloidal particles,[39,40] which was already applied to realise, e.g., sinusoidal[41–45] or random landscapes.[46–51] (See Ref. 49 for a review.) Here we investigate how a rPEL modifies the spatial arrangement of ensembles of colloidal particles.[1,7,52] Local density variations occur, which are related to the distribution of energy levels $p(U)$ and the spatial correlation function $C_U(r)$ of the underlying potential. For various disorder strengths, controlled through the laser power P, and particle concentrations, i.e., mean particle number densities ρ_0, we track particle positions and calculate the local density $\rho(\mathbf{r},t)$ at each time t, based on which different correlation functions are obtained: the disorder-averaged pair distribution function or pair density correlation function $g^{(1)}(r)$,[53] and, to characterize the quenched disorder, the density correlation $g^{(2)}(r)$,[52,54] similar to the Edwards-Anderson order parameter,[55–57] which is intensively used in the context of spin glasses and has been proposed in the context of pinned vortex liquids[54] and calculated in computer simulations.[52,58] However, as yet it has never been measured in an experiment. In this paper, we proceed to do precisely that. This analysis provides the main characteristics of the effect of the disorder, i.e., the rPEL, with respect to particle-potential as well as pair and higher order inter-particle interactions and can easily be extended to other systems, such as magnetic bubble arrays in a disordered potential,[59–61] particles on patterned surfaces,[62] and vortex liquids as well as glasses in the presence of random pinning.[58,63]

II. MATERIALS AND METHODS

A. Optical setup

A random intensity distribution, i.e., a speckle pattern, was created by directing an expanded laser beam (Laser Quantum, Opus 532, wavelength 532 nm, maximum intensity $P_{\max} = 2.6$ W) onto a microlens array (RPC Photonics, Engineered Diffuser™ EDC-1-A-1r, diameter 25.4 mm)[64,65] and subsequently focussing the modified beam into the sample plane of an inverted microscope. This results in a macroscopically uniform beam with a so called top-hat intensity distribution. However, the wavefronts from the randomly distributed microlenses interfere in the sample plane. This leads to microscopic intensity variations, so-called laser speckles, to which the particles were exposed. The

A.1 Colloids exposed to random potential energy landscapes: From particle number density to particle-potential and particle-particle interactions

interaction of the particles with the speckle pattern can be described by a rPEL. The particle size roughly matches the speckle size, but is much larger than the laser wavelength. Moreover, the laser intensity is spread over a large field of view. Thus, we neither expect nor observe optical binding effects[66,67] or light field-induced dispersion forces.[68] The colloidal particles were observed using the inverted microscope (Nikon, Eclipse Ti-U) with a 20× objective (Nikon, CFI S Plan Fluor ELWD, numerical aperture 0.45). A detailed description of the optical setup and a statistical analysis of both the intensity pattern and the resulting rPEL can be found in Ref. 51, where the present conditions correspond to "BE 5×".

B. Samples

Samples consisted of spherical polystyrene particles with sulfonated chain ends (Invitrogen, diameter $D = 2.8$ μm, polydispersity 3.2%) dispersed in purified water (ELGA purelab flex, electrical resistivity 18.2×10^4 Ωm). Three glass cover slips (#1.5) and a microscope slide (all from VWR) were assembled to form a small capillary.[69] After the capillary was filled with the dispersion, it was sealed with UV-glue (Norland, NOA61). Due to the density difference between particles and water, the particles sedimented and formed a quasi-two-dimensional layer at the bottom of the sample cell.

C. Data acquisition

Each measurement consisted of $K \approx 27\,000$ images, which were recorded at 3.75 frames per second using an 8-bit camera (AVT, Pike F-032B with 640 × 480 pixels and pixel pitch of 0.372 μm). Particle positions were determined using standard procedures.[70] Because the system evolves from a quenched random distribution towards its equilibrium distribution, care was taken that the correlation functions are not affected by the relaxation process, i.e., do not show a time dependence.[71]

Based on the particle positions, we determined the number of particles $\mathcal{N}(x_m, y_n, t, l)$ in each region at $\mathbf{r} = \mathbf{r}_{mn} = (x_m, y_n)$ at each time t for a particular realisation of the potential l (out of L different realisations), and calculated the local particle density as

$$\rho(x_m, y_n, t, l) = \frac{\mathcal{N}(x_m, y_n, t, l)}{\Delta x \Delta y}, \tag{1}$$

where $\Delta x = x_m - x_{m-1}$ and $\Delta y = y_m - y_{m-1}$, with $\Delta x = \Delta y$ for all $m = 1 \ldots M$, $n = 1 \ldots N$. Hence the quadratic regions all have the same size of 0.186 μm, which is well above the uncertainty of the particle positions, about 0.05 μm.[70] It is noteworthy that these regions do not coincide with pixels of the camera. The distance r between two regions at $\mathbf{r}$ and $\mathbf{r}'$ is $r = |\mathbf{r} - \mathbf{r}'|$, which depends on the location of both regions and thus on m, m', n, and n'. It was divided into bins of $\Delta r = 0.2\Delta x$, which represents a compromise between good statistics and high resolution.

III. RESULTS AND DISCUSSION

A. Random potential energy landscape (rPEL)

The colloidal particles were exposed to a rPEL by exploiting the interaction of light with particles having a refractive index different from the one of the dispersing liquid. Their interaction usually is described by two forces:[39,40] a scattering force, which pushes the particles along the beam, and a gradient force, which pulls particles with a larger refractive index than the one of the solvent towards regions of high intensity. This effect is typically applied in optical tweezers which are used to trap or manipulate colloidal particles.[39,40,72,73] Rather than single focused beams,

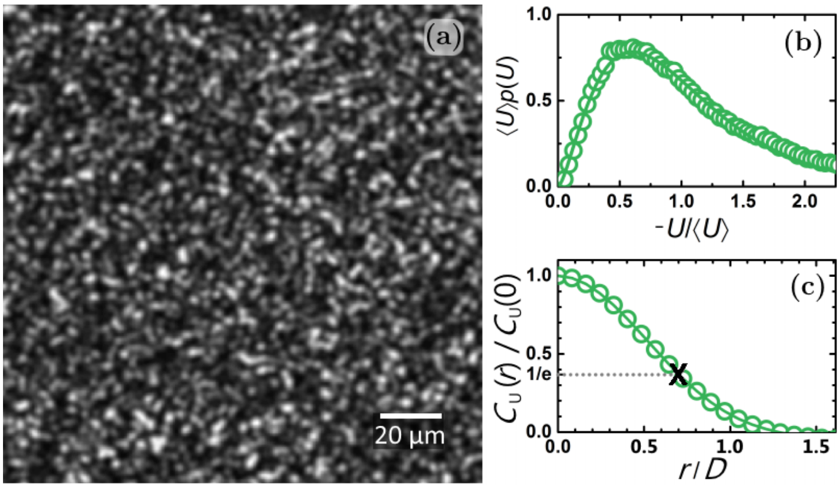

FIG. 1. (a) Random potential energy landscape (rPEL), i.e., $U(\mathbf{r})$, as calculated by convolving the measured intensity pattern $I(\mathbf{r})$ with the projected volume of a particle of diameter $D = 2.8$ μm, (b) its normalized probability density of energy values $p(U)$, and (c) its normalized spatial correlation function $C_U(r)/C_U(0)$ with 1/e-width $0.69D$ indicated by a cross.

an extended light field can be used to create a PEL.[49] To predict not only the shape of the PEL but also its amplitude, the particles' susceptibility or polarizability needs to be known, which typically is not the case. Nevertheless, it is possible to calculate the typical characteristics of the PEL by integrating the local intensity $I(\mathbf{r})$ over the particle's projected volume, thus taking the particle volume traversed by the light beam into account.[74] This results in an estimate of the potential $U(\mathbf{r})$ imposed on a particle, which then is considered to be point-like.[51]

Fig. 1(a) shows one realisation of the rPEL, i.e., $U(\mathbf{r})$, as a grey scale image which was obtained by convolving a recorded intensity pattern with the projected volume of a particle. The rPEL was characterized by the distribution of energy values $p(U)$, which follows a gamma distribution[75] with shape parameter $M = 2.6$ (Fig. 1(b), for details see condition BE5× in Table II of Ref. 51). The length scale of the fluctuations was described by the normalized spatial covariance function $C_U(\mathbf{r}) = \langle U(\mathbf{r}')U(\mathbf{r}' + \mathbf{r})\rangle_{\mathbf{r}'}/\langle U(\mathbf{r}')\rangle^2_{\mathbf{r}'} - 1$, whose azimuthal average can be described by a Gaussian distribution $C_U(r) = \exp(-(r/\xi)^2)$ with $\xi = 0.69D$ (Fig. 1(c)).

B. Particles in the rPEL

In the experiments, the particle concentration, i.e., the mean particle number density ρ_0 or the particle area fraction $\phi_{\mathrm{A}} = \pi(D/2)^2\rho_0$, as well as the laser power P, and hence the mean potential value $\langle U\rangle$ and the disorder strength, were varied, whereas the shape of the distribution, $p(U)$, and the spatial correlation function, $C_U(r)$, remain unchanged (Fig. 2). We consider three different ρ_0 (C1: $\rho_0 = 0.007\ \mu\mathrm{m}^{-2}$, C2: $\rho_0 = 0.041\ \mu\mathrm{m}^{-2}$, C3: $\rho_0 = 0.072\ \mu\mathrm{m}^{-2}$, corresponding to area fractions $\phi_{\mathrm{A}} = 0.045$, 0.25, and 0.45, respectively) as well as four different P (L0: 0 mW, L1: 917 mW, L2: 1640 mW, L3: 2600 mW), and indicate conditions by CiLj.

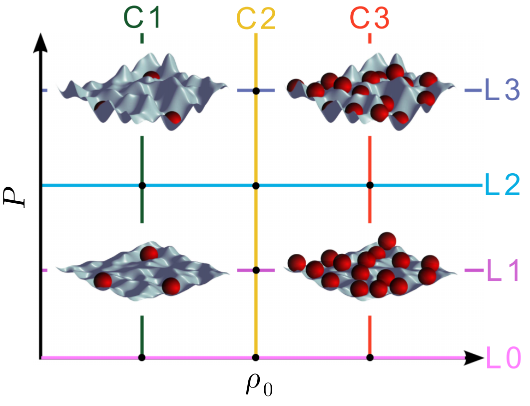

FIG. 2. Different laser powers P (L0 to L3), corresponding to different mean potential values $\langle U\rangle$ or disorder strengths, and mean particle densities ρ_0 (C1 to C3) are investigated. For four conditions sketches showing particles in a rPEL are shown.

Fig. 3 shows images of colloidal particles (top) and their trajectories (bottom) for two different mean particle densities ρ_0 (C1, C3) and increasing laser power P and hence disorder strength (L0, L1, L3), where L0 corresponds to the absence of a laser field and hence free diffusion. (For images at other combinations of mean particle density and laser power see Fig. 11 in Appendix A.) Neither for the low nor for the high mean particle density an effect of the potential is immediately visible in the images. However, there is a clear effect of the rPEL on the trajectories. For the low mean particle density C1, as the disorder strength is increased, the motion of the particles is restricted to small areas and a few particles even stay in one potential minimum for the entire measurement time. At high mean particle density C3 and low laser power L1 (Fig. 3(f)) almost the whole field of view is sampled by the particles. This indicates that the particles are very

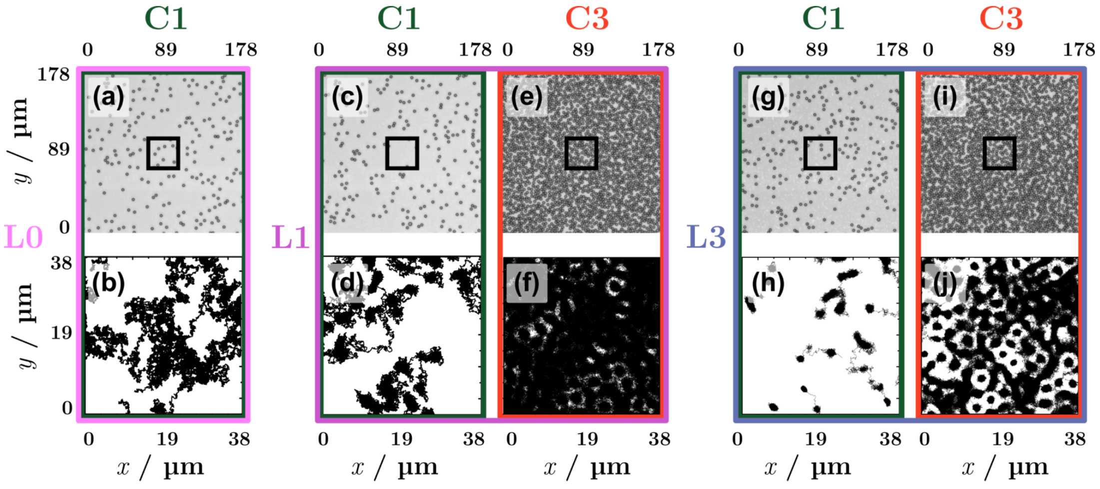

FIG. 3. (Top) Micrographs of parts of the samples ($178\times178\ \mu\mathrm{m}^2$) and (bottom) particle trajectories in a central region ($38\times38\ \mu\mathrm{m}^2$, indicated in the micrographs) during a time $\Delta t = 7200$ s after the micrograph has been taken, for different laser powers L0, L1, L3 (left to right) and mean particle densities C1 and C3.

mobile and exchange positions. In contrast, for high potential roughness L3 (Fig. 3(j)) some particles appear stuck in potential minima. This prevents other particles from exploring their neighbourhood and leads to regions depleted of particle centres.

The dynamic behaviour has important consequences on how particles sample a PEL. Since experiments have a limited measurement time, sampling can be incomplete and hence local information can only be partially accessible. The completeness of sampling determines whether time-averaged quantities might hold reliable local information and describe all points in a PEL, or whether only spatially averaged quantities might provide reliable information. Very low mean particle densities result in only limited information on some locations of the PEL. Upon increasing the mean particle density, sampling can become more complete (e.g., C3L1). However, higher mean particle densities also enhance particle-particle interactions, which hence might dominate particle-potential interactions. This reduces correlations with the underlying potential. Moreover, a strongly varying potential can also result in an "under-sampling" of energetically unfavourable areas, i.e., potential maxima, since they are avoided by the particles. The unexplored areas might depend on the initial positions of the particles, due to the quenched disorder of the potential. An average over different disorder realisations might help, but excludes the determination of local quantities, which lose their relevance.

C. Time-averaged particle density

First, we consider the time-averaged (or thermal-averaged) local particle density

$$\langle \rho(\mathbf{r},t,l)\rangle_t = \frac{1}{K}\sum_{k=1}^{K} \rho(x_m, x_n, t, l). \qquad (2)$$

Its ensemble and disorder average gives the mean particle density $\rho_0 = [\langle \rho(\mathbf{r},t,l)\rangle_{t,\mathbf{r}}]_l$, where $\langle\ldots\rangle_t$, $\langle\ldots\rangle_{\mathbf{r}}$, and $[\ldots]_l$ denote time, ensemble and disorder averages, respectively. In the experiments presented here, the large field of view provides a sufficient disorder average within a single rPEL realisation. Thus here the total number of disorder realisations $L = 1$ and the sample average imply an ensemble and disorder average.

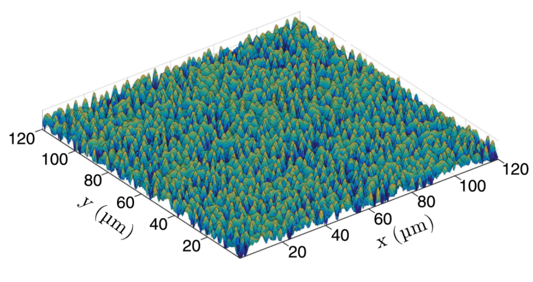

FIG. 4. Time-averaged local particle density $\langle\rho(\mathbf{r},t)\rangle_t$ for high laser power L3 and large mean particle density C3. The logarithmic colour scale indicates low ($\rho_0 = 1\times10^{-4}$ µm^{-2}) to high ($\rho_0 = 0.63$ µm^{-2}) local densities by dark blue to red colours.

Fig. 4 shows the time-averaged local particle density $\langle\rho(\mathbf{r},t)\rangle_t$, for large laser power L3 and high mean particle density C3 (cf., Figs. 3(i) and 3(j)). (For further examples see Fig. 12 in Appendix B.) For dilute samples in equilibrium, $\langle\rho(\mathbf{r},t)\rangle_t$ is related to $U(\mathbf{r})$ (Fig. 1(a)) by the Boltzmann distribution. At mean particle densities which result in reasonable statistics, however, $\langle\rho(\mathbf{r},t)\rangle_t$ is affected by both $U(\mathbf{r})$ and particle-particle interactions.

The local time-averaged particle density $\langle\rho(\mathbf{r},t)\rangle_t$ is characterized by the two-dimensional density autocovariance function $C(\mathbf{r})$, i.e., the density autocorrelation function of $\langle\rho(\mathbf{r},t)\rangle_t$ around the mean ρ_0, which is, making use of the Wiener-Khinchin theorem,[76] given by

$$\begin{aligned} C(\mathbf{r}) &= \left[\langle\langle\rho(\mathbf{r}',t)\rangle_t\langle\rho(\mathbf{r}'+\mathbf{r},t)\rangle_t\rangle_{\mathbf{r}'}\right]_l - \rho_0^2 \\ &= \left[\mathcal{F}^{-1}\left(\mathcal{F}\{\langle\rho(\mathbf{r},t)\rangle_t - \rho_0\}\ \mathcal{F}^*\{(\langle\rho(\mathbf{r},t)\rangle_t - \rho_0)\}\right)\right]_l, \end{aligned} \qquad (3)$$

where $\mathcal{F}$, $\mathcal{F}^{-1}$, and * indicate the Fourier transformation, inverse Fourier transformation, and complex conjugation, respectively. Since isotropic samples are considered, an azimuthal average is carried out:

$$C(r) = (1/2\pi)\int_0^{2\pi} C(r,\Theta)\,\mathrm{d}\Theta.$$

In Fig. 5, the azimuthally averaged density autocovariance function $C(r)$ is shown for different laser powers. It shows similar behaviour for all investigated experimental conditions since varying the laser power only changes the disorder strength but not the shape or statistics of the rPEL. A pronounced peak is located at the origin which is well described by a Gaussian distribution $C(r) = \sigma^2\exp(-(r/l_c)^2)$ (inset of Fig. 5). Its amplitude $\sigma^2 = C(0) = \langle\langle\rho(\mathbf{r},t)\rangle_t^2\rangle_{\mathbf{r}} - \rho_0^2$ is the variance of the local particle density and describes the probability to find a, not necessarily the same, particle

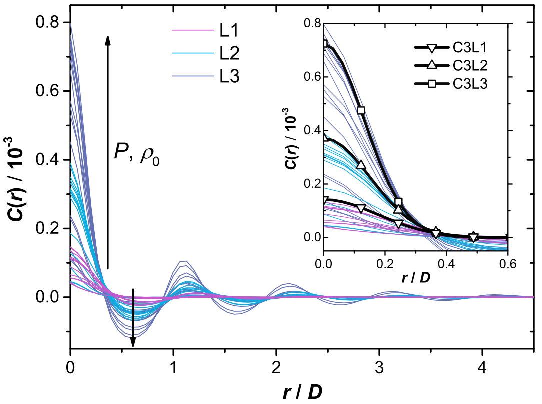

FIG. 5. Azimuthally averaged autocovariance or spatial autocorrelation function $C(r)$ of the time-averaged particle density $\langle\rho(\mathbf{r},t)\rangle_t$ as a function of normalized distance r/D for different laser powers P (L1-L3, indicated by colours) and increasing mean particle density ρ_0 (indicated by arrows). Inset: Same data with Gaussian fits to data corresponding to mean particle density C3 as black lines with symbols representing different laser powers (as indicated).

in a specific region for the entire measurement time. Thus the amplitude σ^2 characterizes the mean depth of the potential minima as sampled by the particles. It increases with potential strength about linearly and also increases with ρ_0 (Fig. 6(a)). With increasing ρ_0, the particles occupy increasingly higher potential values thus broadening the range of occupied values and increasing σ. The correlation length l_c (Fig. 6(b)) characterizes the width of the potential minimum as sampled by the particles. It decreases with laser power P, i.e., disorder strength, reflecting the tighter pinning. It also depends on the mean particle density ρ_0. For low ρ_0, particle-potential interactions dominate, whereas with increasing ρ_0, the particles occupy increasingly higher potential values within the same minimum and hence l_c increases. In contrast, for high ρ_0, particle-particle interactions dominate and the area fraction occupied by particles becomes important. Then l_c is mostly determined by the particle diameter D rather than the speckle size and hence slightly decreases before reaching a constant level. The height of this level decreases with potential strength, since the smaller the particles' excursions the smaller l_c.

The primary peak of $C(r)$ is followed by a minimum, which is more pronounced as the laser power increases (Fig. 5, indicated by arrow). It occurs at a distance comparable to the correlation length of the potential, $0.69D$ (Fig. 1), independent of both P and ρ_0. In contrast, the minimum becomes more pronounced with P and ρ_0. It is caused by particles pinned in potential minima, which exclude particles from their vicinity (Figs. 3(f) and 3(j)). The higher order minima (and maxima) are roughly spaced by multiples of the particle diameter D. These oscillations are caused by either particle-potential or, in the case of high ρ_0, multiple-particle interactions and thus reflect spatial arrangements of neighbouring particles, such as those caused by depletion and caging.

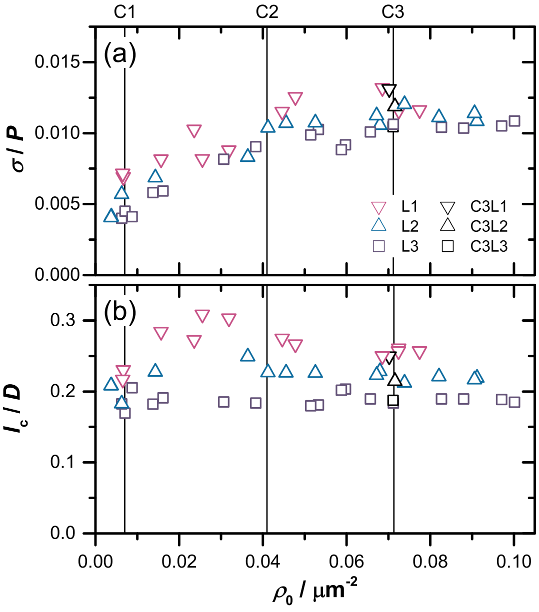

FIG. 6. (a) Standard deviation σ and (b) correlation length l_c of the time-averaged particle density $\langle\rho(\mathbf{r},t)\rangle_t$ as a function of mean particle density ρ_0 shown for different laser powers P (L1-L3, as indicated).

D. Correlation functions

To characterize the particle-potential and particle-particle interactions, based on the measured time-averaged local particle density $\langle\rho(\mathbf{r},t)\rangle_t$ we determine the pair distribution or pair density correlation function $g^{(1)}(r)$, the off-diagonal density correlation function $g^{(2)}(r)$, and the total correlation or Ursell function $h(r)$ which all are normalized by ρ_0^2.

The off-diagonal density correlation function $g^{(2)}(r)$ is an analogue of the Edwards-Anderson order parameter.[52,77] It is defined by

$$g^{(2)}(\mathbf{r}) = \frac{1}{\rho_0^2}\left[\left\langle\langle\rho(\mathbf{r}',t,l)\rangle_t\langle\rho(\mathbf{r}'+\mathbf{r},t,l)\rangle_t\right\rangle_{\mathbf{r}'}\right]_l \tag{4}$$

and hence is the normalized spatial correlation function of the mean local density among disorder realisations. It quantifies the probability for a particle to be pinned by the rPEL, i.e., it quantifies whether a certain location is still occupied by a particle after an arbitrarily long time period.[77] Therefore it describes a coupling between spatial disorder of pinning sites and particle positional ordering in time as well as multiple-particle interactions. Without an external potential, i.e., vanishing disorder strength, and for low enough mean particle densities, where particle-particle interactions are not important, $g^{(2)}(\mathbf{r}) = 1$. Application of an external quenched disorder, here in the form of the speckle pattern of the external laser field, disrupts this conservation law locally and thereby breaks the corresponding symmetry. This phenomenon is directly observed in the form of the real space inhomogeneities introduced in the density profile. The off-diagonal density correlation function $g^{(2)}(\mathbf{r})$ characterizes the order parameter of this symmetry-broken disordered state. Furthermore, for a large field of view and hence disorder averaging in one single realisation of the rPEL, $g^{(2)}(\mathbf{r}) = C(\mathbf{r})/\rho_0^2 + 1$. We consider the azimuthal average $g^{(2)}(r)$. It is calculated from the experimental data by

$$\begin{aligned} g^{(2)}(r) = {} & \frac{1}{\rho_0^2}\frac{1}{L}\sum_{l=1}^{L}\frac{1}{MN}\sum_{m',n'=1}^{MN}\frac{1}{N_\mathrm{r}} \\ & \times\sum_{m,n}\left[\left\{\frac{1}{K}\sum_{k=1}^{K}\rho(x_{m'},y_{n'},t,l)\right\}\right. \\ & \left.\times\left\{\frac{1}{K}\sum_{k=1}^{K}\rho(x_{m'+m},y_{n'+n},t,l)\right\}\right], \end{aligned} \tag{5}$$

where m and n are chosen such that regions with their centres in an annulus between radii $r - \Delta r/2$ and $r + \Delta r/2$ are included with N_r the number of such regions.

Fig. 7(a) shows $g^{(2)}(r)$ for different mean particle densities ρ_0 (C1-C3) and laser powers P (L1-L3, indicated by arrows). (Further conditions are shown in Fig. 13 in Appendix C.) For large distances r the time-averaged particle density is uncorrelated and thus $g^{(2)}(r\to\infty) = 1$.

A.1 Colloids exposed to random potential energy landscapes: From particle number density to particle-potential and particle-particle interactions

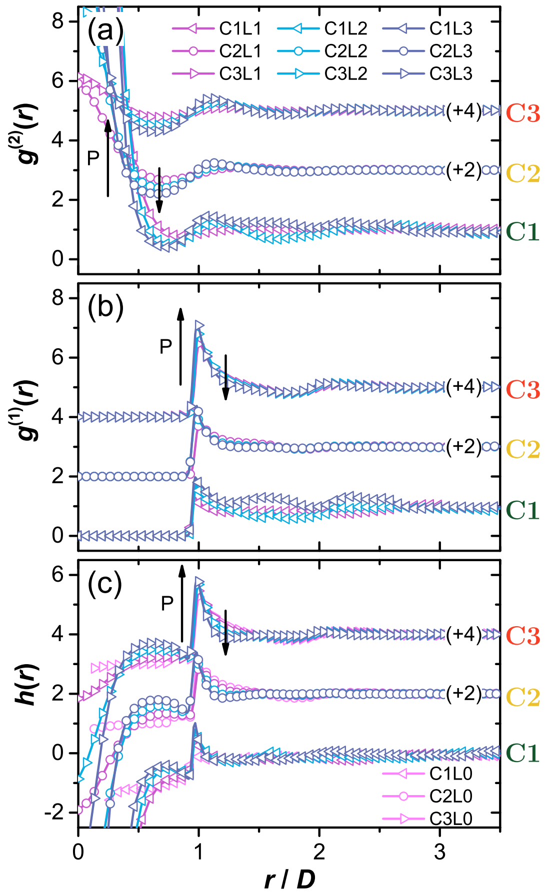

FIG. 7. (a) Azimuthally averaged off-diagonal density correlation function $g^{(2)}(r)$, (b) pair density correlation function $g^{(1)}(r)$, and (c) total correlation function $h(r)$ as a function of the normalized distance r/D for different laser powers P (L1-L3, indicated by arrows) and mean particle densities ρ_0 (C1-C3, as indicated). The data corresponding to C2 and C3 were shifted along the y-axis by +2 and +4, respectively.

By contrast, correlations between high local densities, reflecting potential minima, lead to deviations from unity. For small distances $r \to 0$, a pronounced peak is observed, consistent with the observations in connection with the density autocovariance function $C(r)$ (cf., Fig. 5). For distances larger than the minimal particle-particle distance $r > D$, no clear r dependence of the fluctuations is visible for the lowest ρ_0 (C1). This is attributed to the irregular distribution of the small number of particles in the random potential, in particular the potential minima, and hence the limited sampling (see Sec. III B). For medium and high ρ_0 (C2, C3) maxima occur around multiple integers of D. In the absence of a rPEL no such fluctuations are present in $g^{(2)}(r)$ (Fig. 13 in Appendix C). This indicates the interplay of particle-particle and particle-potential interactions.

The correlation function $g^{(1)}(\mathbf{r})$, which is the disorder-averaged analogue of the pair distribution function or pair density correlation function, is defined by[52]

$$g^{(1)}(\mathbf{r},l) = \frac{1}{\rho_0^2}\left[\langle \rho(\mathbf{r}',t,l)\,\rho(\mathbf{r}'+\mathbf{r},t,l)\rangle_{t,\mathbf{r}'}\right]_l - \frac{1}{\rho_0}\delta(\mathbf{r},l), \qquad (6)$$

where $\delta(\mathbf{r},l)$ is the Dirac delta function and the time average for the disordered system has to be taken prior to the disorder average. Note that the time-average of the product of the densities is taken in Eq. (6), whereas the product of the time-averaged densities is considered in Eq. (4). In the canonical ensemble the last term vanishes. The azimuthal average can be determined from the experimental data by

$$g^{(1)}(r) = \frac{1}{\rho_0^2}\frac{1}{L}\sum_{l=1}^{L}\frac{1}{MN}\sum_{m',n'=1}^{MN}\frac{1}{N_r}\sum_{m,n}\frac{1}{K} \times \sum_{k=1}^{K}\rho(x_{m'},y_{n'},t,l)\rho(x_{m'+m},y_{n'+n},t,l), \qquad (7)$$

where, again, m and n are chosen to include regions with their centres in an annulus between radii $r - \Delta r/2$ and $r + \Delta r/2$. It describes the spatial variance in the time-averaged local particle density.[53]

For $r < D$, $g^{(1)}(r) = 0$ whereas $g^{(1)}(r) = 1$ for $r \gg D$ for all conditions (Fig. 7(b)), which resembles a hard sphere system. At intermediate r, oscillations similar to the ones found for $g^{(2)}(r)$ are observed. For large ρ_0 they hardly depend on the laser power P. At low ρ_0 the fluctuations are more pronounced but appear at random distances. This is attributed to the limited sampling of the rPEL due to the small number of particles (see Sec. III B).

The peak at $r = D$, the contact value $g^{(1)}(D)$, is linked to the compressibility and thus the equation of state[78–80] (Fig. 8). The contact value $g^{(1)}(D)$ increases with ρ_0 and P. The experimentally determined $g^{(1)}(D)$ is very sensitive to the number of particles and their localization errors as well as the histogram parameters, i.e., bin positions and size. In particular at higher densities ($\rho_0 > 0.06\ \mu\text{m}^{-2}$), the peak of $g^{(1)}(r)$ at $r \approx D$ is very sharp compared to the bin size and the

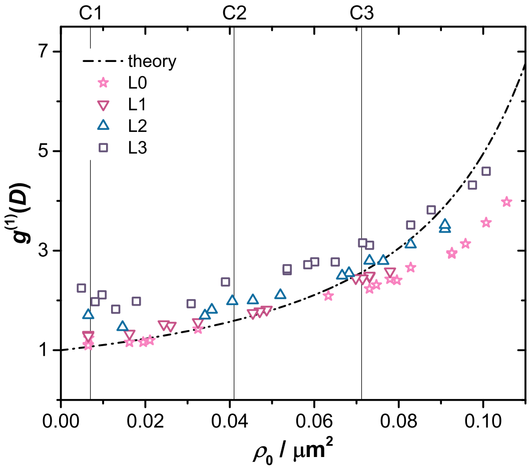

FIG. 8. Contact value of the pair density correlation function $g^{(1)}(D)$ as a function of the mean particle density ρ_0 for different laser powers P (L0-L3, as indicated). The dashed line represents the prediction by the Henderson equation of state.[79]

uncertainty of our tracking procedure and therefore $g^{(1)}(D)$ is expected to be underestimated. A theoretical prediction for hard spheres,[79,80] $g^{(1)}(D) = (1 - 7\phi_A/16)/(1 - \phi_A)^2$ (Fig. 8), agrees with the experimental data obtained in the absence of a rPEL (L0, indicated by pink stars) for low densities ($\rho_0 \lesssim 0.06\ \mu\text{m}^{-2}$) but differs at higher densities. This is possibly caused by the above mentioned uncertainties involved in the determination of $g^{(1)}(D)$.

The total correlation or Ursell function $h(r)$ is given by

$$h(r) = g^{(1)}(r) - g^{(2)}(r). \tag{8}$$

The contributions of particle-potential interactions to $g^{(1)}(r)$ are taken into account by $g^{(2)}(r)$ and hence $h(r)$ mainly describes the disorder-, ensemble-, and time-averaged density fluctuations caused by particle-particle and multiple-particle interactions. Therefore, $h(r)$ appears as a pair distribution function which hardly contains correlations due to the potential, in particular for $r > D$. For a homogeneous, isotropic fluid in the absence of an external potential, and hence $g^{(2)}(r) = 1$, it becomes $h(r) = g^{(1)}(r) - 1$, resembling the pair correlation function.

The total correlation function $h(r)$ is shown in Fig. 7(c) for different mean potential densities ρ_0 (C1-C3) and laser powers P (L0-L3). In the absence of a rPEL (L0), $h(r)$ is approximately -1 for $r < D$, shows a peak at $r \approx D$, and is about zero beyond the peak for $r \gg D$. In the presence of a rPEL, the behaviour for $r < D$ differs due to the strongly increasing $g^{(2)}(r)$. The height of the peak at $r \approx D$ increases with increasing mean particle density and its width decreases with increasing laser power. Remarkably, beyond this peak $h(r)$ is almost constant and takes a value of about zero for all investigated mean particle densities and laser powers. This is due to the balance between $g^{(1)}(r)$ and $g^{(2)}(r)$ which is illustrated in Fig. 9 by a direct comparison of all three functions. The above-mentioned concurrence of the oscillations of $g^{(1)}(r)$ and $g^{(2)}(r)$ results in an almost flat $h(r)$ beyond the first peak. The remaining maximum of $h(r)$ at $r \approx 2D$ is rather attributed to particle-particle and multiple-particle interactions than particle-potential interactions. (For a comparison of $g^{(1)}(r)$ and $g^{(2)}(r)$ at all measured combinations of mean particle density ρ_0 and laser power P see Fig. 13 in Appendix C.)

E. Replica liquid state theory

For a deeper understanding of our results, we compare the experimentally obtained correlation functions $g^{(1)}(r)$ and $g^{(2)}(r)$ to predictions of liquid state theory,[53] generalised to include the effects of an external rPEL, i.e., quenched disorder. While the details of this theory have been described previously,[52,54] they are briefly mentioned for completeness.

The colloidal particles are assumed to interact with each other through a hard sphere pair potential $V(r)$ and are exposed to a random potential $U(\mathbf{r})$ with the distribution of energy values $p(U)$ being Gaussian and the short ranged spatial correlations quantified by $C_U(r)$ as in the experiments. To obtain the free energy of this system, the disorder-average of the logarithm of the partition function, $[\ln Z]_l$, is calculated using the replica trick,[55]

$$[\ln Z]_l = \lim_{q \to 0} \int dU p(U) \frac{Z^q - 1}{q},$$

where Z^q is the partition function of a set of q non-interacting realisations of the same system, i.e., "replicas." The partition function of N particles replicated q times and averaged over the disorder distribution $p(U)$ is identical to the partition function of $N \times q$ particles interacting with the potential $V^{\alpha\beta}(r) = V(r)\delta_{\alpha\beta} + C_U(r)$.[54] The liquid state theory for such a system is now constructed assuming replica symmetry where all liquid state correlation functions, such as the pair correlation function, share the symmetry $g^{\alpha\beta}(r) = g^{\beta\alpha}(r) = g^{(1)}(r)\delta_{\alpha\beta} + g^{(2)}(r)(1 - \delta_{\alpha\beta})$. In the $q \to 0$ limit, the Ornstein-Zernike relation is[53]

$$\begin{aligned} h^{(1)}(k) &= \frac{c^{(1)}(k) - (c^{(1)}(k) - c^{(2)}(k))^2}{(1 - c^{(1)}(k) + c^{(2)}(k))^2}, \\ h^{(2)}(k) &= \frac{c^{(2)}(k)}{(1 - c^{(1)}(k) + c^{(2)}(k))^2}, \end{aligned} \tag{9}$$

where $h^{(1)}(k)$ is the Fourier transform of the (diagonal) pair correlation function $h^{(1)}(r) = g^{(1)}(r) - 1$ and $c^{(1)}(r)$ the corresponding direct correlation function. The off-diagonal correlations, with superscript (2), are defined analogously. The Ornstein-Zernike relation needs to be complemented with a closure relation in order to solve for the correlation functions. We have used two sets of closure relations to try to reproduce the measured correlation functions. Firstly, the analogue of the Percus-Yevick (PY) equation modified for the replicated case,

$$\begin{aligned} c^{(1)}(r) &= \left(e^{-\beta(V(r)+C_U(r))} - 1\right)\left(1 + y^{(1)}(r)\right), \\ c^{(2)}(r) &= \left(e^{-\beta C_U(r)} - 1\right)\left(1 + y^{(2)}(r)\right), \end{aligned} \tag{10}$$

where $y^{(1)}(r) = h^{(1)}(r) - c^{(1)}(r)$ and similarly $y^{(2)}(r)$ are the indirect correlation functions. These relations are solved using the method of Gillan.[81]

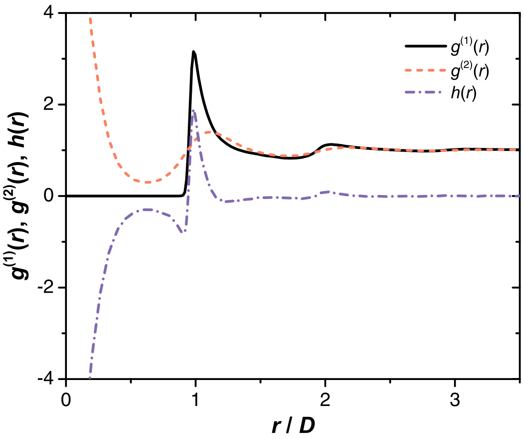

FIG. 9. Comparison of the azimuthally averaged pair density correlation function $g^{(1)}(r)$, off-diagonal density correlation function $g^{(2)}(r)$, and total correlation or Ursell function $h(r)$ as a function of normalized distance r/D for high laser power L3 and mean particle density C3.

The results from the replicated PY liquid state theory are compared to the experimental results for C3L1, i.e., a mean particle density $\rho_0 = 0.56\,D^{-2}$ (Fig. 10). Fitting yielded for the strength of the disorder $\langle U^2\rangle^{1/2} = 1.8\,k_BT$ with the thermal energy k_BT, consistent with experimental expectations, and for the correlation length $\xi = 0.43\,D$, which is somewhat lower than the experimental value $\xi = 0.69\,D$. While the $g^{(2)}(r)$ agree remarkably well, the PY approximation overestimates correlations in $g^{(1)}(r)$. This is a well known feature of the PY closure. To correct for this, we propose and solve a hybrid set of closure relations where the first equation of the set in Eq. (10) is replaced with

$$c^{(1)}(r) = e^{-\beta(V(r)+C_U(r))+y^{(1)}(r)} - 1 - y^{(1)}(r) \qquad (11)$$

and the second equation is kept the same. This results in much better agreement of the $g^{(1)}(r)$ while the $g^{(2)}(r)$ is almost unchanged. Thus, with the hybrid set of closure relations quantitative agreement between experimental data and replica liquid state theory predictions are obtained.

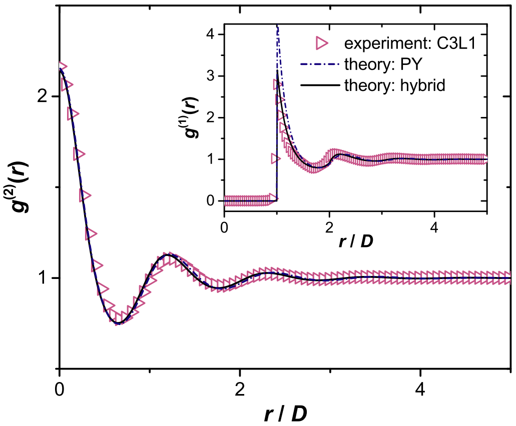

FIG. 10. Comparison of the experimentally determined azimuthally averaged off-diagonal density correlation function $g^{(2)}(r)$ and the pair density correlation function $g^{(1)}(r)$ (inset) with results obtained from liquid state theory, as a function of normalized distance r/D for low laser power L1 and high mean particle density C3.

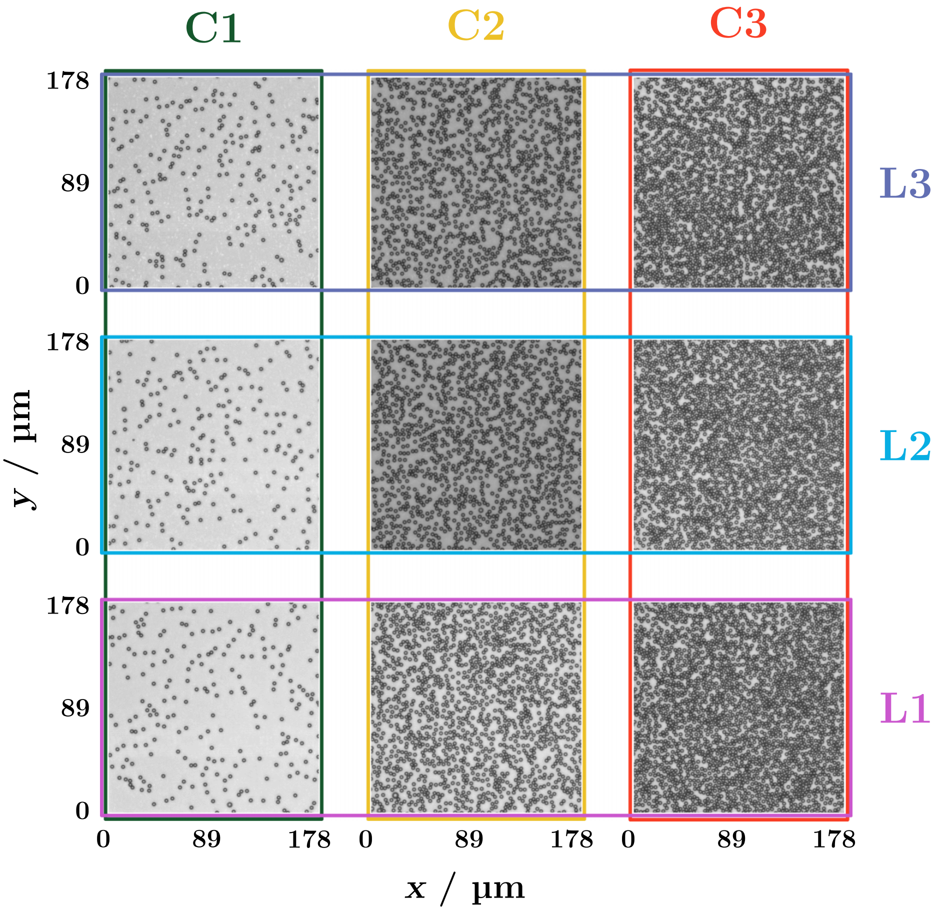

FIG. 11. Micrographs of parts of the samples (178 × 178 µm^2) for increasing laser power (L1-L3) and mean particle density (C1-C3, as indicated).

For experiments with the same laser power P, also the strength of the disorder $\langle U^2\rangle^{1/2}$ and the correlation length ξ remain constant, independent of the mean particle density ρ_0. Ideally, the results from our replica liquid state theory should follow these expectations. However, at large laser powers Eqs. (10) and (11) begin to give unphysical results. Also the fitted values, especially for ξ, depend on ρ_0. This indicates that the validity of the simple closure relations used in our theory is limited if the disorder is strong. Moreover, it is important to ensure that the whole landscape is sampled by the particles, which is particularly difficult for dilute systems within a reasonable measurement time. This can only be resolved by further experiments on a larger set of densities ρ_0 and laser powers P and/or by a better liquid state theory.[82]

Finally, the time-averaged local particle density in the presence of the rPEL is given by[52,53]

$$\langle \rho(\mathbf{r},t,l)\rangle_t = \rho_0 - \frac{\rho_0^2}{k_B T}\int d\mathbf{r}' h(|\mathbf{r}-\mathbf{r}'|)U(\mathbf{r}') + \cdots \qquad (12)$$

which links the time-averaged local particle density $\langle \rho(\mathbf{r},t,l)\rangle_t$ to the disorder potential $U(\mathbf{r})$. This analytical relationship can be used to determine $U(\mathbf{r})$ from a measurement of $\langle \rho(\mathbf{r},t,l)\rangle_t$ or to predict $\langle \rho(\mathbf{r},t,l)\rangle_t$ from $U(\mathbf{r})$ and $h(r)$.[52]

IV. CONCLUSIONS

We investigated colloidal particles in a random potential energy landscape (rPEL) with energy values distributed according to a gamma distribution. It was imposed by a laser speckle pattern. The rPEL affects the distribution of particles which, at higher mean particle densities, is also modified by particle-particle interactions. Therefore, local particle density variations occur, which are correlated in time and space. The time-averaged local particle density was determined and analysed as a function of mean particle density ρ_0 and laser power P, i.e., disorder strength. The off-diagonal density correlation function $g^{(2)}(r)$ not only reflects the potential roughness, but also spatial correlations in the local density caused by pinned particles. Thus it reflects particle-potential and particle-particle interactions. The pair density correlation function $g^{(1)}(r)$ is also influenced by spatial correlations of the rPEL. As a result, the total correlation or Ursell function $h(r) = g^{(1)}(r) - g^{(2)}(r)$ hardly reflects particle-potential interactions, but characterizes particle-particle and multiple-particle interactions. To our knowledge, this is the first time these correlation functions have experimentally been determined in the presence of disorder. Furthermore, they have successfully been compared to results from replica liquid state theory. This results in quantitative agreement, but also points towards deficits in the existing liquid state theory and calls for further experiments.

ACKNOWLEDGMENTS

We thank Manuel Escobedo-Sanchez, Jürgen Horbach, Hartmut Löwen, Gautam Menon, and Christoph Zunke for very helpful discussions and suggestions. We acknowledge funding by the Deutsche Forschungsgemeinschaft (DFG)

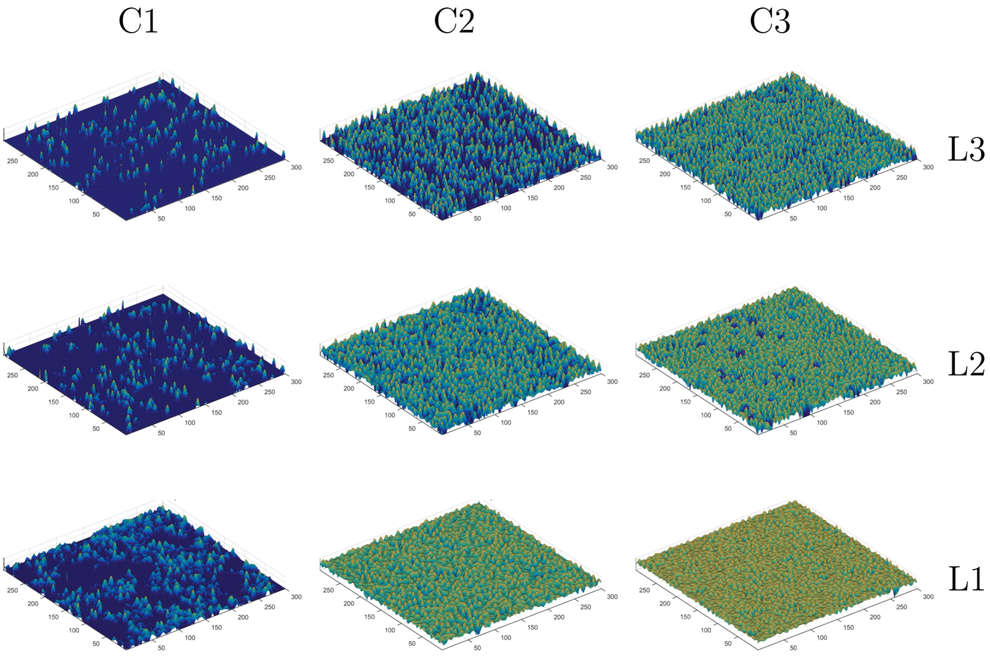

FIG. 12. Time-averaged local particle density $\langle \rho(\mathbf{r},t)\rangle_t$ for increasing laser power (L1-L3) and mean particle density (C1-C3, as indicated). Colour scale indicates low to high densities by blue to red colours, where different scales are used for the different conditions.

(Grant No. EG269/6-1) and the FP7-PEOPLE-2013-IRSES (Grant No. 612707, DIONICOS).

APPENDIX A: PARTICLE ARRANGEMENTS

Fig. 11 shows micrographs of colloidal particles for three different mean particle densities ρ_0 (C1-C3) and increasing laser power P, i.e., disorder strength, (L1-L3). Neither for low nor for high mean particle density and/or laser power an effect of the potential is immediately visible in the images.

APPENDIX B: TIME-AVERAGED LOCAL PARTICLE DENSITY

The time-averaged local particle density $\langle \rho(\mathbf{r},t)\rangle_t$ for three different laser powers P, i.e., disorder strengths, (L1-L3) and mean particle densities ρ_0 (C1-C3) is shown in Fig. 12. For dilute samples trapping of particles in deep potential minima during the entire measurement time leads to a discretisation of the density landscape. This becomes stronger with increasing laser power. At higher mean particle densities, $\langle \rho(\mathbf{r},t)\rangle_t$ is affected by both particle-potential and particle-particle

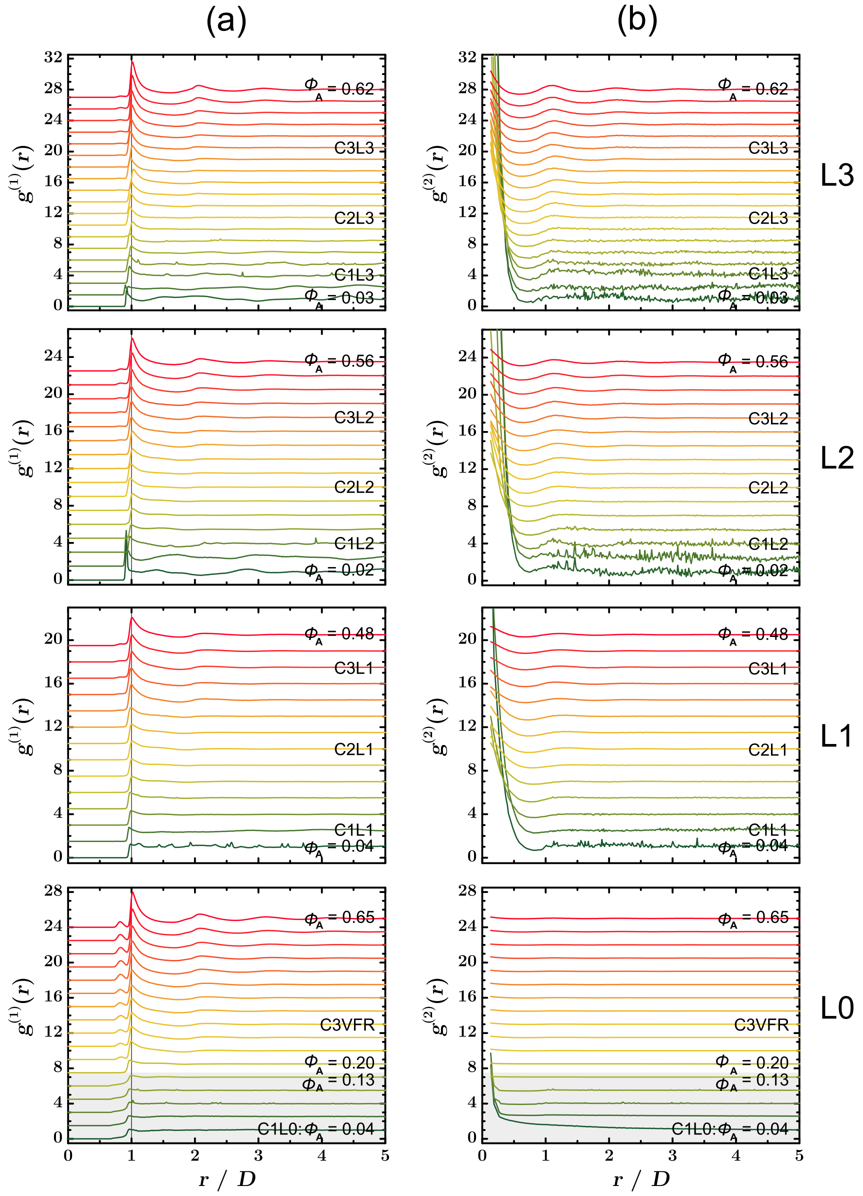

FIG. 13. (a) Azimuthally averaged pair density correlation function $g^{(1)}(r)$ and (b) off-diagonal density correlation function $g^{(2)}(r)$ for increasing laser power (L0-L3) and mean surface fraction ϕ_A or particle density (C1-C3, as indicated by colour gradient from green to red). Data are shifted vertically for clarity.

interactions, resulting in a smoothed density landscape. This becomes more apparent with a decrease in the laser power.

APPENDIX C: CORRELATION FUNCTIONS

The azimuthally averaged pair density correlation function $g^{(1)}(r)$ and off-diagonal density correlation function $g^{(2)}(r)$ at all measured combinations of mean particle density ρ_0 and laser power P (L0-L3) are shown in Fig. 13. For very large distances r the time-averaged local particle density is uncorrelated, and thus $g^{(1)}(r \to \infty) = 1$ and $g^{(2)}(r \to \infty) = 1$ independent of the mean particle density ρ_0 and the laser power P, i.e., disorder strength. By contrast, correlations at finite distances r between high local density values reflect pinning sites, i.e., particle cages or potential minima, and can be identified by deviations from this value. In the absence of a rPEL (L0), $g^{(1)}(r)$ shows a strong dependence on the mean particle density whereas $g^{(2)}(r) \approx 1$ for all mean particle densities, except for very few low mean particle densities ρ_0 which is attributed to insufficient statistics. However, in the presence of a rPEL (L1-L3) and for medium to high mean particle densities ρ_0, for both correlation functions maxima are observed around integer multiples of D, which increase with mean particle density ρ_0 and laser power P and indicate the interplay of particle-particle and particle-potential interactions.

[1] D. J. Wales, *Energy Landscapes* (Cambridge University Press, England, 2004).
[2] J. Barth, Surf. Sci. Rep. **40**, 75 (2000).
[3] A. P. Jardine, S. Dworski, P. Fouquet, G. Alexandrowicz, D. J. Riley, G. Y. H. Lee, J. Ellis, and W. Allison, Science **304**, 1790 (2004).
[4] D. Nguyen, J. Mallek, A. N. Cloud, J. R. Abelson, G. S. Girolami, J. Lyding, and M. Gruebele, J. Chem. Phys. **141**, 204501 (2014).
[5] L. Chen, M. Falcioni, and M. W. Deem, J. Phys. Chem. B **104**, 6033 (2000).
[6] A. Heuer, S. Murugavel, and B. Roling, Phys. Rev. B **72**, 174304 (2005).
[7] M. B. Isichenko, Rev. Mod. Phys. **64**, 961 (1992).
[8] H. Scher and M. Lax, Phys. Rev. B **7**, 4491 (1973).
[9] R. M. Dickson, D. J. Norris, Y.-L. Tzeng, and W. E. Moerner, Science **274**, 966 (1996).
[10] C.-L. Hsieh, S. Spindler, J. Ehring, and V. Sandoghdar, J. Phys. Chem. B **118**, 1545 (2014).
[11] M. Weiss, M. Elsner, F. Kartberg, and T. Nilsson, Biophys. J. **87**, 3518 (2004).
[12] F. Höfling and T. Franosch, Rep. Prog. Phys. **76**, 046602 (2013).
[13] I. M. Tolić-Nørrelykke, E.-L. Munteanu, G. Thon, L. Oddershede, and K. Berg-Sørensen, Phys. Rev. Lett. **93**, 078102 (2004).
[14] P. C. Blainey, G. B. Luo, S. C. Kou, W. F. Mangel, G. L. Verdine, B. Bagchi, and X. S. Xie, Nat. Struct. Mol. Biol. **16**, 1224 (2009).
[15] F. Höfling, T. Franosch, and E. Frey, Phys. Rev. Lett. **96**, 165901 (2006).
[16] W. Min, X. S. Xie, and B. Bagchi, J. Chem. Phys. **131**, 065104 (2009).
[17] R. L. Baldwin, Nature **369**, 183 (1994).
[18] S. D. Durbin and G. Feher, Annu. Rev. Phys. Chem. **47**, 171 (1996).
[19] H. Janovjak, H. Knaus, and D. J. Muller, J. Am. Chem. Soc. **129**, 246 (2007).
[20] A. Arcella, G. Portelly, R. Collepardo-Guevara, D. Chakraborty, D. J. Wales, and M. Orozco, J. Phys. Chem. B **118**, 8540 (2014).
[21] H. Frauenfelder, S. G. Sligar, and P. G. Wolynes, Science **254**, 1598 (1991).
[22] K. A. Dill, Biochemistry **24**, 1501 (1985).
[23] J. D. Bryngelson and P. G. Wolynes, J. Phys. Chem. **93**, 6902 (1989).
[24] A. V. Indrani and S. Ramaswamy, Phys. Rev. Lett. **73**, 360 (1994).
[25] T. R. Kirkpatrick, D. Thirumalai, and P. G. Wolynes, Phys. Rev. A **40**, 1045 (1989).
[26] A. Heuer, J. Phys.: Condens. Matter **20**, 373101 (2008).
[27] W. Götze, J. Phys.: Condens. Matter **11**, A1 (1999).
[28] C. A. Angell, Science **267**, 1924 (1995).
[29] F. Sciortino, J. Stat. Mech.: Theory Exp. **2005**, P05015 (2005).
[30] M. Goldstein, J. Chem. Phys. **51**, 3728 (1969).
[31] S. Sastry and P. G. Debenedetti, Nature **393**, 554 (1998).
[32] P. Charbonneau, J. Kurchan, G. Parisi, P. Urbani, and F. Zamponi, Nat. Commun. **5**, 3725 (2014).
[33] M. D. Ediger, C. A. Angell, and S. R. Nagel, J. Phys. Chem. **100**, 13200 (1996).
[34] F. H. Stillinger, Science **267**, 5206 (1995).
[35] C. P. Royall and S. R. Williams, Phys. Rep. **560**, 1 (2015).
[36] C. Hyeon and D. Thirumalai, Proc. Natl. Acad. Sci. U. S. A. **100**, 10249 (2003).
[37] I. Goychuk and V. O. Kharchenko, Phys. Rev. Lett. **113**, 100601 (2014).
[38] P. G. Wolynes, Acc. Chem. Res. **25**, 513 (1992).
[39] A. Ashkin, J. M. Dziedzic, J. E. Bjorkholm, and S. Chu, Opt. Lett. **11**, 288 (1986).
[40] A. Ashkin, Biophys. J. **61**, 569 (1992).
[41] B. J. Ackerson and A. H. Chowdhury, Faraday Discuss. **83**, 309 (1987).
[42] C. Bechinger, M. Brunner, and P. Leiderer, Phys. Rev. Lett. **86**, 930 (2001).
[43] M. C. Jenkins and S. U. Egelhaaf, J. Phys.: Condens. Matter **20**, 404220 (2008).
[44] C. Dalle-Ferrier, M. Krüger, R. D. L. Hanes, S. Walta, M. C. Jenkins, and S. U. Egelhaaf, Soft Matter **7**, 2064 (2011).
[45] M. P. N. Juniper, R. Besseling, D. G. A. L. Aarts, and R. P. A. Dullens, Opt. Express **20**, 28707 (2012).
[46] K. M. Douglass, S. Sukhov, and A. Dogariu, Nat. Photonics **6**, 834 (2012).
[47] R. D. L. Hanes, C. Dalle-Ferrier, M. Schmiedeberg, M. C. Jenkins, and S. U. Egelhaaf, Soft Matter **8**, 2714 (2012).
[48] R. D. L. Hanes and S. U. Egelhaaf, J. Phys.: Condens. Matter **24**, 464116 (2012).
[49] F. Evers, R. D. L. Hanes, C. Zunke, R. F. Capellmann, J. Bewerunge, C. Dalle-Ferrier, M. C. Jenkins, I. Ladadwa, A. Heuer, R. Castañeda-Priego, and S. U. Egelhaaf, Eur. Phys. J.: Spec. Top. **222**, 2995 (2013).
[50] G. Volpe, L. Kurz, A. Callegari, G. Volpe, and S. Gigan, Opt. Express **22**, 18159 (2014).
[51] J. Bewerunge and S. U. Egelhaaf, Phys. Rev. A **93**, 013806 (2016).
[52] A. Sengupta, S. Sengupta, and G. I. Menon, Europhys. Lett. **70**, 635 (2005).
[53] J.-P. Hansen and I. R. McDonald, *Theory of Simple Liquids*, 3rd ed. (Academic, London, 2006).
[54] G. I. Menon and C. Dasgupta, Phys. Rev. Lett. **73**, 1023 (1994).
[55] S. F. Edwards and P. W. Anderson, J. Phys. F: Met. Phys. **5**, 965 (1975).
[56] H.-J. Sommers, J. Phys. Lett. **43**, 719 (1982).
[57] G. Parisi, "An introduction to the statistical mechanics of amorphous systems," in *Field Theory, Disorder and Simulations* (World Scientific, 2012), Chap. 12, pp. 195–244.
[58] C. Dasgupta and O. T. Valls, Phys. Rev. B **74**, 184513 (2006).
[59] R. Seshadri and R. M. Westervelt, Phys. Rev. Lett. **70**, 234 (1993).
[60] R. Seshadri and R. M. Westervelt, Physica D **66**, 223 (1993).
[61] R. Seshadri and R. M. Westervelt, Phys. Rev. B **47**, 8620 (1993).
[62] H.-J. Wu, W. N. Everett, S. G. Anekal, and M. A. Bevan, Langmuir **22**, 6826 (2006).
[63] C. Dasgupta and D. Feinberg, Phys. Rev. B **57**, 11730 (1998).
[64] T. R. M. Sales, Opt. Eng. **42**, 3084 (2003).
[65] *Laser Beam Shaping: Theory and Techniques*, 2nd ed., edited by F. M. Dickey (CRC Press, Inc., 2014).
[66] M. M. Burns, J.-M. Fournier, and J. A. Golovchenko, Phys. Rev. Lett. **63**, 1233 (1989).
[67] R. W. Bowman and M. J. Padgett, Rep. Prog. Phys. **76**, 28 (2013).
[68] G. Brügger, L. S. Froufe-Pérez, F. Scheffold, and J. J. Sáenz, Nat. Commun. **6**, 7460 (2015).
[69] M. C. Jenkins and S. U. Egelhaaf, Adv. Colloid Interface Sci. **136**, 65 (2008).
[70] J. C. Crocker and D. G. Grier, J. Colloid Interface Sci. **179**, 298 (1996).
[71] J. Bewerunge, I. Ladadwa, F. Platten, C. Zunke, A. Heuer, and S. U. Egelhaaf, Phys. Chem. Chem. Phys. **18**, 18887 (2016).
[72] D. G. Grier, Nature **424**, 810 (2003).
[73] K. Dholakia, P. Reece, and M. Gu, Chem. Soc. Rev. **37**, 42 (2008).
[74] F. Evers, C. Zunke, R. D. L. Hanes, J. Bewerunge, I. Ladadwa, A. Heuer, and S. U. Egelhaaf, Phys. Rev. E **88**, 022125 (2013).
[75] J. W. Goodman, *Speckle Phenomena in Optics: Theory and Applications* (Roberts & Co., Englewood, Colorado, 2007).
[76] E. G. Steward, *Fourier Optics: An Introduction* (Courier Corporation, 2004).
[77] D. L. Stein and C. M. Newman, *Spin Glasses and Complexity* (Princeton University Press, 2013).
[78] E. Helfand, H. L. Frisch, and J. L. Lebowitz, J. Chem. Phys. **34**, 1037 (1961).
[79] D. Henderson, Mol. Phys. **30**, 971 (1975).
[80] X. Guo and U. Riebel, J. Chem. Phys. **125**, 144504 (2006).
[81] M. J. Gillan, Mol. Phys. **38**, 1781 (1979).
[82] F. J. Rogers and D. A. Young, Phys. Rev. A **30**, 999 (1984).